Heavy metal ion sensors based on organic microcavity lasers

Sergii Lozenko

ENSC-2011 N° 285

THESE DE DOCTORAT

DE L'ECOLE NORMALE SUPERIEURE DE CACHAN

Présentée par

Sergii LOZENKO

pour obtenir le grade de

DOCTEUR DE L'ECOLE NORMALE SUPERIEURE DE CACHAN

Domaine :

SCIENCES PHYSIQUES

Sujet de la thèse :

Heavy metal ion sensors based on organic microcavity lasers

Thèse présentée et soutenue à Cachan le 04/11/2011 devant le jury composé de :

GAVIOT Etienne	Professeur (L'Université du Maine)	Président
CHEN Yong	Directeur de Recherches (ENS)	Rapporteur
BENISTY Henri	Professeur (IOGS)	Rapporteur
BLAU Werner	Professeur (Trinity College Dublin)	Examinateur
LERAY Isabelle	Directrice de Recherches (ENSC)	Examinatrice
LEBENTAL Melanie	Maître de Conférences (ENSC)	Directrice de thèse
ZYSS Joseph	Professeur (ENSC)	Directeur de thèse

Laboratoire de Photonique Quantique et Moleculaire
ENS CACHAN/CNRS/UMR 8537
61, avenue du Président Wilson, 94235 CACHAN CEDEX (France)

Abstract

Monitoring of environmental pollutants present at low concentrations requires creation of miniature, low-cost, and highly sensitive detectors that are capable to specifically identify target substances. In this thesis, a detection approach based on refractive index sensing with polymer micro-lasers is proposed and its application to the detection of heavy metal pollutants in water (mercury – Hg^{2+}, cadmium – Cd^{2+} and lead – Pb^{2+}) is studied. The resonance frequencies of the microcavity are highly sensitive to the refractive indices of the resonator surrounding: the resonances shift by a small amount when the surface refractive index changes, resulting from the interaction of the mode evanescent field with the surrounding medium. This permits label-free detection by coating the resonator with a suitable recognition species.

The originality of this work lies in the utilization of active microcavities, or microlasers, created of the dye-doped polymers. Active microcavities offer an enhanced signal/noise ratio as compared to the passive ones and very narrow resonance peaks even at moderate quality factors ($Q \geq 6000$). The choice of polymers as an active medium is connected with a number of advantages they offer: as opposite to semiconductors, polymers can be easily functionalized, integrated in microfluidic circuits and are cheaper in processing. Moreover, the use of porous polymer matrices may allow accumulation of analyte ions inside the microcavity and thus enhance the sensitivity.

Two possible applications of microlasers are investigated in the thesis: refractive index variation sensing with non-functionalized cavities and heavy metal ion detection with functionalized cavities. In the first case, the sensitivity values have been obtained, comparable with the reported in literature for planar passive microresonators. In the second case, the experimental proofs of specific detection of mercury ions in liquid at 10^{-6}M concentration are presented. The ways of sensitivity improvement are discussed and verified and a foundation is layed for the creation of integrated Lab-on-Chip microfluidic biochemical detector.

Resume

Le contrôle des polluants environnementaux présents à faible concentration a conduit à la création de détecteurs miniaturisés, à bas coûts et ultra-sensibles, capables d'identifier spécifiquement certaines substances. Dans cette thèse, la méthode de détection explorée repose sur la sensibilité de micro-lasers polymères à une variation d'indice de réfraction. Cette approche a été mise en application pour détecter des métaux lourds (mercure – Hg^{2+}, cadmium – Cd^{2+} et plomb – Pb^{2+}) dans l'eau potable. En effet les fréquences de résonance de ces micro-cavités sont particulièrement sensibles à l'indice de réfraction du milieu extérieur et se déplacent lorsque celui-ci est modifié. Ce système permet ainsi une détection sans marqueur (« label ») en recouvrant la cavité d'une couche de reconnaissance spécifique de l'espèce recherchée.

L'originalité de ce travail repose sur l'utilisation de micro-cavités actives, ou micro-lasers, fabriquées avec des polymères dopés par des colorants lasers. En effet les micro-lasers permettent d'augmenter le rapport signal/bruit et de profiter de pics de résonance étroits, même pour des facteurs de qualité de l'ordre de quelques milliers seulement. Le choix de matériaux organiques comme milieu à gain a été dicté par les nombreux avantages qu'ils offrent. Contrairement aux semi-conducteurs inorganiques, les polymères peuvent être fonctionnalisés de manière relativement aisée et l'utilisation de matériaux poreux devrait augmenter la sensibilité en faisant circuler le fluide à tester à l'intérieur même du résonateur. De plus le protocole de fabrication des micro-lasers organiques reste d'un coût modéré et permet une intégration aisée en micro-fluidique.

Deux voies différentes ont été explorées dans cette thèse : détection d'une variation d'indice de réfraction avec des cavités non-fonctionnalisées et détection d'ions lourds avec des cavités fonctionnalisées. Dans le premier cas, la sensibilité obtenue est comparable à ce qui est publié pour des micro-résonateurs passifs. Dans le second cas, nous avons réussi à mettre en évidence la présence d'ions mercure jusqu'à 10^{-6} M. Quelques approches ont été envisagées pour diminuer encore le seuil de détection dont certaines ont été vérifiées expérimentalement. Ainsi, cette étude propose un prototype de composant sur puce pour la détection d'espèces chimiques ou biologiques.

Acknowledgments

First of all I would like to thank my advisors – Melanie Lebental and Joseph Zyss for offering me this interesting research subject at LPQM and d'Alembert Institute. I thank Joseph Zyss for all the fruitful and enriching discussions, which helped to advance the work. I owe to Melanie Lebental, for guiding me through with patience and enthusiasm, giving hints if the work seemed to reach a deadlock and encouraging when the success seemed within a step away.

I would like also to express my gratitude to Henri Benisty and Yong Chen, who have accepted to be my referees, to read and evaluate my manuscript, as well as to Etienne Gaviot, the chair of the jury, Werner Blau, who made a long trip to be at my defense and Isabelle Leray.

I can't but thank my colleagues-chemists from PPSM department – Isabelle Leray, Jacques Delaire, Jean-Pierre Lefevre, Djibril Faye, Emma and Cylia who greatly helped me in this interdisciplinary domain. Their experience, support, participation and devotion brought me to where I am now in this research and let me accomplish my thesis. I thank as well Isabelle Ledoux, the head of LPQM department, always ready to help and advice in any situation.

I should mention also Christian Ulysse from LPN laboratory for his precious contribution - e-beam fabrication of microcavities, and Joseph Lautru for managing the clean-room of ENS Cachan and providing technological support. I thank also the administration of LPQM and d'Alembert Institute.

At last (which is not the least) I would like to thank all my colleagues of LPQM and PPSM departments who contributed to the creative and friendly atmosphere which is indispensable for work and life. I thank Nadia Djellali, Iryna Gozhyk, Clement Lafargue, Bassam Hajj, Marcin Zielinski, Camille Delezoide and everyone else who made these three years of life an unforgettable experience.

Table of Contents

Chapter I

General Introduction

Introduction

The subject of this PhD thesis lies at the interface of two rapidly and extensively developing domains of research and technology: photonics and Lab-on-Chips. The term photonics, which appeared initially in 1960s-1970s with the development of semiconductor light emitters and optical fibers nowadays generalizes the research on emission, generation, transmission and detection of light as well as utilization of light in the areas traditionally occupied by electronics, such as signal processing and data transfer. From the research of distinct functional elements: laser diodes, optical fibers, light detectors photonics evolved into an area embracing complex, all-optical signal processing systems. That's why the term photonics is sometimes used as an analogy to term electronics. Optical signal transfer and amplification systems has already become a reality since 1980s with the invention of erbium-doped fibers, while nowadays numerous (and fruitful) investigations are carried out to create all-optical binary logic elements [1-3], optical memory [4-7] and, by analogy with electronic integrated circuits, optical integrated circuits [8-11].

The second broad domain of research, widely known as Lab-on-Chips, focuses on the development and integration on a single substrate of miniaturized devices that possess broad functionality that would typically require an entire biological laboratory [12, 13]. Through a network of microfluidic channels very small volumes (micro- to nanoliters) of biological samples can be transported, mixed, separated, and analyzed with significant advantages in terms of high sensitivity, speed of analysis, low sample and reagent consumption, and measurement automation and standardization. Applications of LOCs may range from chemical synthesis and drug developments [14] to environmental monitoring and detection of chemical and biological threats.

The present thesis was performed within the "microFLUID" project (THEME ICT-2007.3.6) which is a part of the 7th Framework Programme, supported by the European Comission. The aim of the project is creation of polymeric Lab-on-Chips for bio- and chemical sensing purposes using femtosecond laser processing. The ***main goal*** of our work is the development of a prototype of a sensor based on polymer microlasers that is able to detect heavy-metal ions in water for environmental monitoring purposes.

The choice of polymeric materials for the microlaser fabrication is based on a number of considerations. First of all, many polymeric materials, as opposite to semiconductors, can be easily functionalized biochemically in order to attach target biomolecules for specific detection. At the same time they are perfectly compatible with microfluidics thus allowing excellent optofluidic integration of chemical and bio-sensors [15-19]. The second reason is that polymers possess the advantage of low-cost mass production owing to different technological processes of fabrication that we will use and discuss in this thesis. Due to their intrinsic physic-chemical properties they offer many advantages for processing and conditioning in comparison with inorganic materials. Techniques like molding or nanoimprint lithography [20-24] may be applied to fabricate polymer structures, which ensure high throughput and resolution at low fabrication cost, impossible with semiconductor microstructures. Polymers are also compatible with mass-production using traditional UV lithography technique. It should be noted however that the lithography utilized for polymer-based photonic devices fabrication, although

directly derived from that of semiconductor fabrication technology, does not require heavy and expensive equipment. In this thesis, novel approaches to fabrication of microcavities, like laser ablation and 2-photon polymerization will also be considered. Another advantage is a large possibility of integration with different inorganic materials such as semiconductor, glass, sol-gel, ceramics [25], thus allowing simple construction of lab-on-chip for biochemical sensing applications. Finally, the third reason is the low refractive index of polymers resulting in low scattering loss on optical waveguide surfaces and in efficient coupling between these waveguides and optical fibers. Though in this project we didn't utilize the waveguides, we foresee the possibility of their integration in LOCs to collect the emission of microlasers.

The sensing principle that we implement is detection of the wavelength shift $\Delta\lambda$ in the lasing spectrum due to the influence of the refractive index change Δn of the medium surrounding the cavity. Generally, we may mark out two possible applications of microcavities as sensors. The first one is the refractive index variation sensing with non-functionalized cavities. In this case it is desirable to achieve the maximum possible spectral shift in response to the variation of index of the surrounding medium. The second one is the detection of analyte molecules with functionalized cavities. In the ideal case, the spectral shift should be observed only when the analyte molecules are bound by specific ligands and cavity spectrum should not be sensitive to the refractive index of the liquid carrying the molecules that we want to detect. However as the sensitivity to the analyte molecules is usually interconnected with the sensitivity to the bulk refractive index variation, a correct reference should be carefully chosen in the sensing experiments.

The thesis is split over 5 chapters. In this first chapter the general introduction is given, the motivation and novelty of the work are explained and a short review of the principles of sensor functioning and the state of art is presented. The second chapter introduces the theoretical ground necessary for understanding the work. In the last three chapters the original results obtained within the thesis are presented. Chapter 3 is entirely devoted to the technological aspects and explains the properties of the chosen materials and process of fabrication of microcavities. In the chapter 4 we talk about the sensing principle employed in this thesis, the design of microfluidic circuits, various aspects that influence the sensitivity of the cavity to refractive index variation. Experimental results of refractive index variation sensing and mercury detection in water are presented in this chapter. Chapter 5 is devoted to the novel cavity architectures – pedestal and pillar cavities – which are introduced in chapters 3 and 4. Experimental proofs of enhanced sensitivity of these cavity types are presented at the end of the chapter and their advantages and drawbacks are discussed. The descriptions of numerical simulations performed within the thesis are postponed to the Annex 1.

1.1. Motivation and scientific interest.

Screening of water for contamination is a very important task for preserving the environment and improving human health. Mercury (Hg^{2+}), cadmium (Cd^{2+}) and lead (Pb^{2+}) are the most toxic heavy metal ions, causing adverse environmental and health problems as they are responsible for a wide variety of diseases [26-29]. The release of these detrimental ions into the environment originates from numerous natural and man-made sources, such as fossil fuel combustion and the electronic industry. For these reasons, the level of heavy metal ions in drinking water is the object of strict health official norms and must not exceed 1μg/L for Hg^{2+},

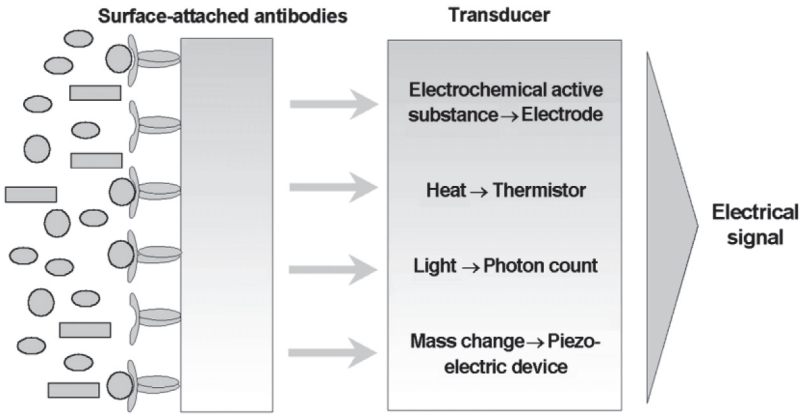

Fig.1-1. Generals scheme of a sensor, depicting the analyte-ligand binding and a transducer, converting binding event into a detectable signal.

10µg/L for Pb^{2+} and 5µg/L for Cd^{2+} [30]. While sophisticated analytical techniques (atomic absorption or atomic emission spectroscopies for instance) are currently used in applications relevant to environmental contamination, there is still a significant need to provide inexpensive and real-time monitoring methods that can detect the presence and, preferably, concentration of pollutants. There exist only rare examples of mobile sensors for heavy metal detection based on electrochemical techniques [31] such as ion-selective electrodes and voltammetry and some optical/colorimetric methods [32, 33]. The advantage of a portable Lab-on-Chip system becomes obvious, as it may allow performing in-field analyses also by not-specialized personnel with reduction of time and cost of the analysis and use a small quantity of reagents to perform the tests.

Historically, the research in active polymer microcavities or microlasers is one of the main research directions of LPQM laboratory (Laboratoire de Photonique Quantique et Moleculaire) of ENS de Cachan. Alongside with fundamental aspects and experimental study of the cavity emission properties [34, 35] various practical applications of microlasers are being investigated. In my thesis, we explore the applications of the microcavity lasers to bio- or chemical sensing. As it has been demonstrated in the theses of my perdecessors, the relatively high quality factors (≥6000) in such resonators lead to very narrow resonances. We expect the resonance frequencies to be highly sensitive to the refractive indices of the resonator and surroundings: the resonances will shift by a small amount when the surface refractive index changes, resulting from the interaction of the mode evanescent field with the surrounding medium. This permits label-free detection [36] by either coating the resonator with a suitable recognition species or by making the microresonator from a species-selective material such as a molecularly-imprinted polymer (MIP). Moreover, the integration of optical sensing in microfluidic Lab-on-Chips will significantly increase the device compactness and portability.

1.2. Approaches to chemical- and bio- sensing.

Fundamentally, a sensor can be represented as a coupling of a ligand-receptor binding reaction to a signal transducer, which converts the binding event into a "readable" signal: electrical, optical, etc. (Fig.1-1) [37]. Much research has been devoted to the evaluation of various signal transduction methods: radioactive, electrochemical, optical, piezoelectric, magnetic, micromechanical, mass-spectrometric.

Among the advantages of optical sensors is the sensitivity, real-time detection of biomolecular interactions and simplicity of response interpretation allow them to be applied widely. Optical sensing techniques are based on various sensing transduction mechanisms, for example, chemiluminescence, fluorescence, light absorption and scattering, reflectance, surface plasmon resonance (SPR) and Raman scattering. A very wide-spread approach in optical sensing is based on the use of fluorescent labels. The idea of labeling is rather simple, and can be schematically illustrated by the Fig.1-2. Specific ligands that capture the analyte molecules are immobilized on the surface of a sensor which is brought in contact with the analyte solution. The surface is washed to remove the molecules, not captured by the ligands. Afterwards fluorescent labels that specifically attach to the analyte molecules are immobilized, thus "marking" the molecules already present on the surface. Now, by measuring the intensity of fluorescence or radioactivity level, one may discover the presence or absence of the analyte molecules and their approximate concentration. Various modifications of this technique may be applied based for example on fluorescence quenching: once the analyte molecule is captured by the ligand the fluorescence signal is generated. However all these approaches require a use of additional chemical compounds and/or multiple steps in detection process (exposure of a sensor to analyte, washing, labeling). A simpler solution would be to use a label-free method, when the analyte binding event is directly converted into a detectable signal.

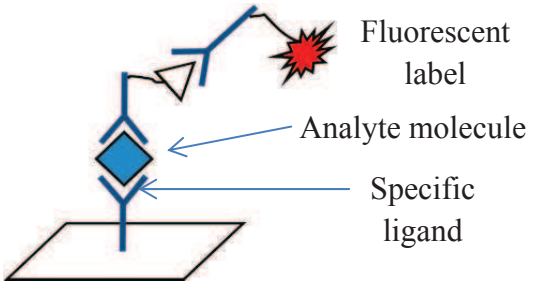

Fig.1-2. Schematic explanation of detection with fluorescent labeling.

In this thesis we will focus on the optical detection scheme, based on a polymer microlaser. The use of optical microresonators for the detection of biological molecules or chemical substances represents an emerging technology which is now intensively developed. The principle involved in these sensors is based on the detection of the change in environment close to the sensor surfaces, which means a local change in the refractive index, using an optical evanescent wave [15, 17, 36, 38-44]. Such devices can thus carry out label-free biochemical sensing and are able to provide highly specific detection owing to characteristic modification at the microresonator surfaces [15, 16, 18, 36, 38, 42, 44-49]. They are also compatible with microfluidic techniques [15, 17, 19, 36, 38-44, 50, 51].

	Microspheres	**Planar microresonators**	**LCORR**
Sensitivity ($\Delta\lambda / \Delta n$)	26 nm/RIU	200 nm/RIU	> 30 nm/RIU
Photonics integration	Very challenging	Easy	Difficult, under investigation
Microfluidics integration	Very challenging	Good (needs to be fabricated seperately)	Excellent
Mass production	Very difficult	Excellent	Good, under investigation
Multiplexed detection	Very challenging	Excellent	Good, under investigation

Table 1-1. Comparison of performance of sensors based on optical microresonators.

Transparent microspheres were the first microresonators used as optical sensors [39], followed by planar waveguides [44, 49, 52] and microresonators such as microdisks or microrings [36, 38, 40-42, 50, 51, 53]. The recent development of the Liquid Core Optical Ring Resonator (LCORR), which allows construction of an integral optofluidic circuit, constitutes an alternative and novel means of constructing bio- or chemical sensors [17, 19, 43, 54]. The Table 1-1 shows a comparison [19, 44] of performance of some recently developed sensors based on optical microresonators.

It must be pointed-out that all the cavity-based techniques mentioned here are optically passive, i.e. are based on the modification of linear optical properties, the material involved in the process lacking any nonlinear or laser properties. In this thesis however, we investigate a novel approach based on active microresonators, constructed of a polymer matrix doped with a laser dye. The advantage of this active component is the improvement of the signal/noise ratio due to the absence of any incident signal in the optoelectronic circuit. Moreover, the use of porous polymer matrices may allow the accumulation of analyte ions inside the material of the microresonator, thus enhancing the refractive index variation and consequently sensitivity. To our knowledge, there exist very few works were active microcavities (or microlasers) are employed for sensing purposes, for example [55-60].

Another popular and highly develop label-free biosensing approach is based on surface plasmon resonance (SPR). Firstly applied for bio-sensing and gas detection in 1982 [61, 62], SPR-based detection and analysis sensors made their way into the market, resulting into a series of commercial systems (manufacturer: Biacore, Horiba, Xantec, etc.). Majority of available SPR systems are based on spectroscopy of surface plasmons excited in thin metal (most often gold) films [63-67] and a refractive index resolution of the order of $1 \cdot 10^{-7}$ RIU has been achieved [68]. The applications of SPR to heavy metal ions detection in drinking water have been studied as well [69]. While being highly sensitive, existing SPR systems are bulky and poorly compatible with LOC technology. Therefore alternative strategy based on the localized surface plasmon resonance (LSPR) in metal nanostructures is widely explored [70, 71], which provides high parallelization and integration capacity. Multiple architectures of LSPR sensors are described in literature [72-77] with sensitivities reaching 1150nm/RIU [78].

Conventional planar strip and rib waveguides [79], including a novel slot waveguide [80, 81], introduced by Almeida et al in 2004 [82] can be used in biochemical sensors. For different slot waveguide configurations, sensitivities up to 490nm/RIU are reported in literature [83].

1.2.1. *Sensor performance*

The main characteristics of a sensor are of course its sensitivity and selectivity, or if we talk about the detection of water pollution, the ability to specifically detect a very low concentration of target molecules in liquid. In optical sensors, where the resonance spectra (this may be emission or absorption spectra) of various structures are studied, the parameter characterizing the sensitivity is very often the spectral shift of a resonance peak. The change of emission intensity may as well be a marker of analyte binding. However often the primary consequence of the analyte binding by a ligand is the shift of a resonance peak and various sophisticated techniques may be applied to the spectrum to convert the spectral shift into intensity change, as will be discussed in section 4.1. A spectral shift caused by the local change of refractive index of the

medium is usually measured in nanometers / refractive index units (RIU) and higher values mean the sensor is capable to detect lower concentrations of analyte.

In Table 1-1 the comparison of sensitivity of different microresonator types is given, evidencing that planar microresonators, the ones that will be studied in this thesis, demonstrate higher sensitivity in comparison with other resonator types. In this work we are focusing on active microcavities and study the emission spectra, therefore the Q-factor of the cavity does not play the crucial role. First of all, highly confined modes are less likely to be observed in the emission of a microlaser. Secondly, the width of the resonance peaks in this case is defined not only by the quality factor of the passive cavity but also by nonlinear processes connected with lasing.

Another important parameter of the performance of a bio- or chemical sensor is its response time. While not crucial for the heavy metals detection in this work, response time may be important for some biological applications. In many existing optofluidic devices, the time constant of the microfluidic flow limits the response of the sensors for continuous monitoring. Worse, this time constant is even more prolonged if regeneration of the sensing surfaces is required because of the generally complicated rinsing sequence that is introduced [15, 16, 38, 39, 45-48, 50]. This limitation is fundamental, however the intrinsic response of the optical sensor is crucial because it influences the overall response time of the device. In the present project, the microlaser response to the change of its surrounding is expected to be very fast, of the order of milliseconds, allowing observation of fast occurring processes, like for example conformational changes of biological macromolecules.

Finally for the construction of a mobile sensing device, its compatibility with mass production techniques is crucial and possibility of integration of multiple components on a single chip is a very important criterion. In this aspect, planar microresonators are again the leaders among the optical resonators, as they are inherently compatible with the existing planar fabrication techniques developed in semiconductor industry. On the contrary, mass fabrication of spherical or any other "3-dimensional" structures may be very difficult and integration with other photonic or microfluidic components even more challenging, as separate fabrication may be needed.

In traditional experimental setups used in conjunction with LOCs, both excitation and detection are performed using bulk optical equipment to focus the excitation light into a tiny measurement volume and to collect the resulting emission. Several efforts have been performed in order to improve integration [84-88]. In particular, optical waveguides allow confinement and transport of light in the chip, directing it into a small volume of the microfluidic channel and collecting the incident and transmitted/emitted light. The integration on the same substrate of optical and microfluidic components has far-reaching scientific and technological implications; to define this new field, the terms "optofluidics" has been recently introduced in the scientific literature [89-91]. Integration of multiple components on a single chip may require complicated multi-stage manufacturing processes, therefore much research is devoted as well to the development of microfabrication techniques. In this thesis, we will use traditional laboratory equipment, including lasers and spectrometers; however the architecture of our microlaser allows easy integration of waveguides or other photonic components on a single wafer. The ways also exist to integrate a compact detection system, which is based on the

conversion of a wavelength shift into intensity change and subsequent detection with a photodiode.

Conclusions

During this thesis we will fabricate active organic microcavities (or microlasers) based on polymer matrix doped with a laser dye. Cavities will be functionalized with specific ligands and experiments of mercury ions detection in liquid will be performed by recording the wavelength shift in the microlaser emission spectrum. The ways of sensitivity improvement will be proposed and experimentally proven with the novel pedestal and pillar microcavities.

The work on this interdisciplinary project was carried out in close collaboration with the chemists at PPSM laboratory, ENS Cachan. Our colleagues are responsible for the part of the work dealing with synthesis of specific ligands capable of binding heavy metal ions, as well as development and optimization of ligand grafting process on the polymer microresonators. The research on porous polymers as active medium is also carried out in close cooperation.

Chapter II

Theoretical basics

Introduction

The purpose of this chapter is to give a short general introduction to the principles of light confinement and guiding. First of all we will consider the total internal reflection which is a key phenomenon that makes light guiding possible. Light guiding will be explained on the example of a dielectric slab waveguide and the effective index model will be introduced, that significantly simplifies description of 3D waveguides and resonators. Afterwards, main parameters that characterize a resonator will be described and active resonators are introduced. Experimental setup and data treatment technique will be detailed in section 2.3 and at the end we will discuss the influence of polarization of the pump laser on the cavity spectra.

2.1. *Planar waveguides and cavities.*

We will start by a brief explanation of the principles of wave confinement and guiding. The key phenomenon that makes guiding of light possible in waveguide or optical fibers is total internal reflection (TIR). Total internal reflection occurs when a ray of light falls at the medium boundary at an angle θ_1 larger than a certain critical angle θ_c with respect to the normal to the surface (Fig.2-1). If $\theta_1 < \theta_c$ the ray will split into a refracted one, passing through the interface, and a reflected one. If $\theta_1 = \theta_c$ the refracted ray will be tangent to the boundary at the point of incidence. And finally, when $\theta_1 > \theta_c$ there is no refraction and the ray is reflected back.

The value of the critical angle χ_c can be calculated from the Snell-Descartes law:

$$n_1 Sin\theta_1 = n_2 Sin\theta_2 \qquad (2\text{-}1)$$

where n_1, n_2 are the refractive indices of the media, and θ_1, θ_2 are the incidence and refraction angles. By putting $\theta_2 = 90°$ we obtain:

$$\chi_c = ArcSin\left(n_2 / n_1\right) \qquad (2\text{-}2)$$

As it is obvious from the expression, total internal reflection may occur when light falls from the medium with the higher index into the medium with lower index.

In this thesis we work with planar dielectric cavities fabricated of polymer material with the refractive index of $n \approx 1.5$, surrounded by air (n_2=1). The value of critical angle for the reflection at polymer/air interface is therefore $\chi_c \approx 42°$ and, in case of polygonal resonator shape (number of sides ≥4), optical rays propagating at certain angles can remain confined inside by multiple total internal reflections at the resonator boundaries. The illustration of light confinement in a square-shaped dielectric resonator is given on Fig.2-1, where the so-called diamond periodic orbit is formed by the rays, incident at an angle of $45° > \chi_c$ [92]. For the polygons with the number of sides larger than 4 there will always exist a periodic orbit in form of an inscribed polygon, confined by total internal reflection.

In case when a cavity is immersed in liquid (n_2=1.33), the value of critical angle changes, and becomes $\chi_c \approx 62.5°$ for the reflection at polymer/water interface. The inscribed polygon orbit is therefore no longer confined for polygons with the number of sides ≤6. We will go into more details about the orbits in various cavity shapes in §4.4.2.

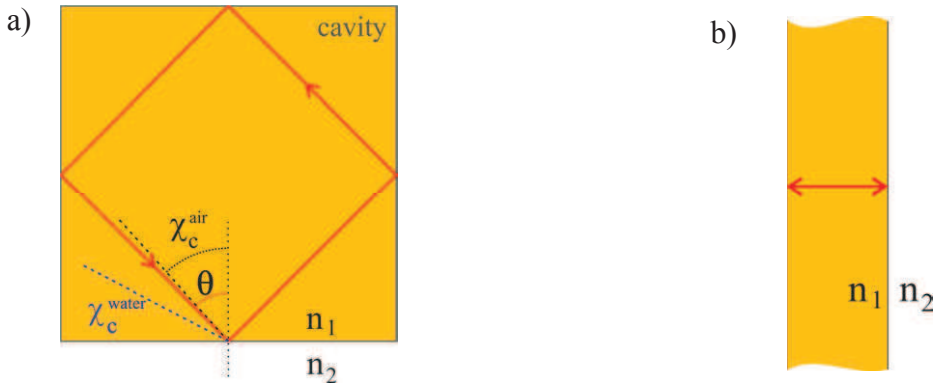

Fig.2-1. (a) Schematic illustration of light ray confinement in a square-shaped cavity (a), Fabry-Perot cavity (b).

The reflection coefficients for the light incident at the interface of two media are given by Fresnel formulas:

$$R_{TE} = \frac{n_e^2 Cos\theta - n\sqrt{n_e^2 - n^2 Sin^2\theta}}{n_e^2 Cos\theta + n\sqrt{n_e^2 - n^2 Sin^2\theta}} \qquad R_{TM} = \frac{nCos\theta - \sqrt{n_e^2 - n^2 Sin^2\theta}}{nCos\theta + \sqrt{n_e^2 - n^2 Sin^2\theta}} \qquad (2\text{-}3)$$

where the case when electric field (resp. magnetic field) lies in the plane of the cavity is called TE (resp. TM) polarization.

In the thesis we also work with simpler cavity shapes, like a Fabry-Perot cavity, shown on Fig.2-1b. In this case light is confined by reflections between two parallel edges of a polymer stripe with the reflection coefficient (in intensity) of approximately 0.04 at polymer/air interface and 0.005 at polymer/water interface.

Two approaches may be applied to the analysis of resonators and waveguides. If the characteristic dimensions (thickness of a slab) of the waveguide are much larger than the wavelength, a ray optics approach may be used. While it is useful to explain the existence of waveguide modes and determine their possible number, ray approach cannot determine the energy transferred by each of the modes and provide the distribution of electromagnetic fields. To get a complete description of the waveguide modes, the use of electromagnetic theory is required.

2.1.1. *Ray optics approach*

To better understand the principle of guiding we will use a ray optics approach and examine a simplest model waveguide formed by a dielectric slab with refractive index n_1, infinite in the (x, y) plane and having thickness d in z-axis direction. The slab is surrounded by a cladding: a substrate and a cover with refractive index n_1, $n_3 < n_2$. A ray of light travelling in the y-direction will remain confined inside the slab if it undergoes multiple total internal reflections at the core/cladding interfaces. The incidence angle θ should therefore be larger than the critical angle θ_c. Rays incident at larger angles will refract, lose part of their power at each reflection and consequently vanish.

A simple approach to carry out analysis of such guide would be to associate each ray with an electromagnetic plane wave and the total electromagnetic field would be a superposition of these

waves. We would consider a monochromatic wave with a wavelength $\lambda = \lambda_0 / n_2$ which has wavevector components $k_x = 0, k_y = k_0 n_2 Sin\theta, k_z = k_0 n_2 Cos\theta$.

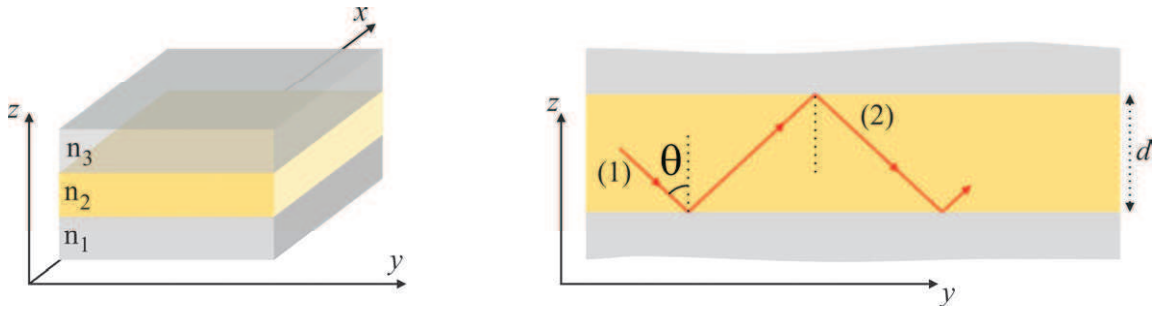

Fig.2-2. Planar dielectric waveguide of thickness d. Rays incident at angles $\theta > \chi_c$ are guided by total internal reflection.

For the wave to be guided in the dielectric slab, a condition of constructive interference must be satisfied, which means that the twice reflected wave ((2) on Fig.2-2) in the waveguide should be in phase with the initial wave ((1) on Fig.2-2):

$$2k_z d - 2\varphi = 2\pi m, \quad m = 0,1,2... \tag{2-4}$$

Where φ is the phase shift acquired by the wave upon reflection at the dielectric boundary, which depends on the incidence angle θ and can be calculated from the Fresnel formulas for TE and TM polarization. Solution of the guiding condition (2-4) yields a discrete set of angles θ_m lying in the range $0 < \theta_m < \pi/2 - \chi_c$ and the electromagnetic fields that correspond to the waves incident at angles θ_m are called the *m*-th guided modes. The *y*-components of the wavevectors of those waves are the propagation constants:

$$\beta_m = n_2 k_0 Sin\theta_m \tag{2-5}$$

A very important quantity, characterizing the wave in a waveguide or a resonator is the effective refractive index, which is defined as a ratio between the wavevector in the medium in the direction of propagation to the free space wavevector: $n_{eff,m} = \beta_m / k_0$. This quantity depends not only on the wavelength but also on the mode in which light propagates and therefore sometimes called modal index. Effective index is used widely within this thesis to describe modes in the cavities, treat experimental spectra and the way of its calculation will be presented in the following paragraph.

2.1.2. *Wave approach.*

To determine the distribution of fields and profiles of the modes the problem should be solved from the electrodynamical point of view, by writing the system of Maxwell equations with the corresponding boundary conditions and solving it. The system of Maxwell's equations forms the foundation of classical electrodynamics. Established by J.C. Maxwell in 1865, it establishes a connection between electric charges, currents, and electromagnetic fields. Also it describes how time varying electric fields gives birth to time varying magnetic field and vice versa. Solution of a system of Maxwell's equations gives complete description of electromagnetic fields for any problem.

In the absence of free charges or currents, as it is the case with our cavities, Maxwell's equations can be written as:

$$\nabla \cdot \vec{D}(\vec{r},t) = 0 \qquad \nabla \times \vec{E}(\vec{r},t) = -\frac{\partial \vec{B}(\vec{r},t)}{\partial t}$$
$$\nabla \cdot \vec{B}(\vec{r},t) = 0 \qquad \nabla \times \vec{H}(\vec{r},t) = \frac{\partial \vec{D}(\vec{r},t)}{\partial t} \tag{2-6}$$

where $\vec{D}(\vec{r},t) = \varepsilon(\vec{r})\vec{E}(\vec{r},t)$ and $\vec{B}(\vec{r},t) = \mu(\vec{r})\vec{H}(\vec{r},t)$ are linear constitutive relations connecting electric displacement $\vec{D}$ with electric field and magnetic induction $\vec{B}$ with magnetic field through the dielectric permittivity ε and magnetic permeability μ which are tensors in the most general case. Taking the curl of the equation $\nabla \times \vec{E}(\vec{r},t) = -\frac{\partial \vec{B}(\vec{r},t)}{\partial t}$, a wave propagation equation can be derived which becomes Helmholtz equation, when time dependency of the fields has harmonic form $\exp(-i\omega t)$:

$$\Delta\vec{E}(\vec{r}) + k_0^2 n^2(\vec{r})\vec{E}(\vec{r}) = 0 \tag{2-7}$$

where k_0 is a free space wavevector and $n^2(\vec{r}) = \varepsilon(\vec{r})/\varepsilon_0$ – refractive index of the medium.

In the case of the slab waveguide, shown on Fig.2-2, it can be proven mathematically that two wave polarizations – TE and TM may propagate. We will remind that we call TE (TM) polarization orientation of the $\vec{E}$ vector in the plane (perpendicular to the plane) of the waveguide. Taking into account that polymer is an isotropic and non-magnetic material (μ=1, ε is scalar), equation (2-7) for TE polarization may be rewritten as:

$$\Delta E_x(y,z) + k_0^2 n_i^2 E_x(y,z) = 0 \tag{2-8}$$

where n_i (i=1,2,3) is the refractive index of the dielectric layer (core or claddings) where wave propagation is considered. We will look for the solutions of equation (2-8) in the form:

$$E_x(y,z) = A_m u_m(z) e^{-j\beta_m y} \tag{2-9}$$

where A_m is a numerical constant, β_m is a propagation constant, and $u_m(z)$ is an unknown function. By substituting solutions (2-9) into (2-8) we obtain:

$$\frac{\partial^2 u_m}{\partial z^2} - \gamma_{i,m}^2 u_m = 0, \;\; \gamma_{i,m}^2 = \beta_m^2 - n_i^2 k_0^2 \tag{2-10}$$

Solution of this equation depends on the sign of $\gamma_{i,m}^2$. For the guided modes inside the core $n_i = n_2$, $\beta_m < n_2 k_0$ and consequently $\gamma_{i,m}^2 < 0$. In this case, (2-10) is satisfied by periodic oscillating functions in the form $u_m \sim \exp(\pm j\gamma_{2,m} z)$. For electric fields inside the cladding $n_i = n_{1,3}$, $\beta_m > n_{1,3} k_0$ and $\gamma_{(1,3),m}^2 > 0$. There is no propagation in the claddings and electric field decays exponentially along the z-axis. In this case equation (2-10) is satisfied by solutions in the form of decaying exponents $u_m \sim \exp(\pm\gamma_{(1,3),m} z)$. Therefore, an arbitrary TE field in the dielectric waveguide can be represented as a superposition of m modes:

$$E_x(y,z) = \sum_m A_m u_m(z) e^{-j\beta_m y} \tag{2-11}$$

where A_m is the amplitude of the mode m. Electric field distribution for several guided modes in a dielectric slab waveguide is displayed on Fig.2-3a. Field distribution of the magnetic field H and also in the case of TM polarization can be found similarly.

The dispersion relation for the waveguide modes can be obtained from the constructive interference condition (2-4) [93]. The phase shifts upon reflections at the core/substrate and core/cover interfaces are calculated from (2-3) where cosines and sines of angle θ are expressed through the components of the wavevector k_y and k_z and substituted into (2-4). The following expression may be obtained:

$$\frac{2\pi d}{\lambda}\sqrt{n_2^{\,2}-n_{eff}^2} = Arctg\left(\eta_1\frac{\sqrt{n_{eff}^2-n_3^2}}{\sqrt{n_2^{\,2}-n_{eff}^2}}\right)+Arctg\left(\eta_2\frac{\sqrt{n_{eff}^2-n_1^2}}{\sqrt{n_2^{\,2}-n_{eff}^2}}\right)+\pi\cdot l,\quad l=0,1,2... \qquad (2\text{-}12)$$

where $\eta_1=\frac{n_2^{\,2}}{n_3^2}$, $\eta_2=\frac{n_2^{\,2}}{n_1^2}$ for TM polarization, $\eta_1=\eta_2=1$ for TE polarization; n_2 – is the index of the cavity material and n_{eff} is the effective index. The advantage of introduction of effective index, is that the vertical component of the wavevector k_z is now hidden inside n_{eff} and therefore we may consider the waveguide as a two-dimensional, lying in (x,y) plane while effective index takes into account the vertical z-dimension.

It is convenient to plot the effective index as a function of d/λ which is made on the Fig.2-3b for n_1=1.45, n_2=1.54, n_3=1 – refractive indices of the silica substrate and polymer guiding layer, that are used to fabricate microcavities studied in this thesis. As it is seen from the plot, the values of effective index lie in the range limited from below by the index of a substrate or a cover (n_1 or n_3, whichever is higher) and from above by the index of a guiding layer $n_{eff,m}\in[\sup(n_1,n_3),n_2]$. There exists certain limiting d/λ ratio, below which no wave confinement and guiding is possible. For a fixed value of wavelength (λ=600nm) this means that the waveguide has a cutoff thickness, which in our case equals approximately $d_{\min}^{TM}=208\,nm$ and $d_{\min}^{TE}=255\,nm$ for TM and TE polarizations. For the ratio $d/\lambda\approx 1$, which is typical for the cavities studied in this thesis, only one mode (l=0) may be confined in the guiding layer along

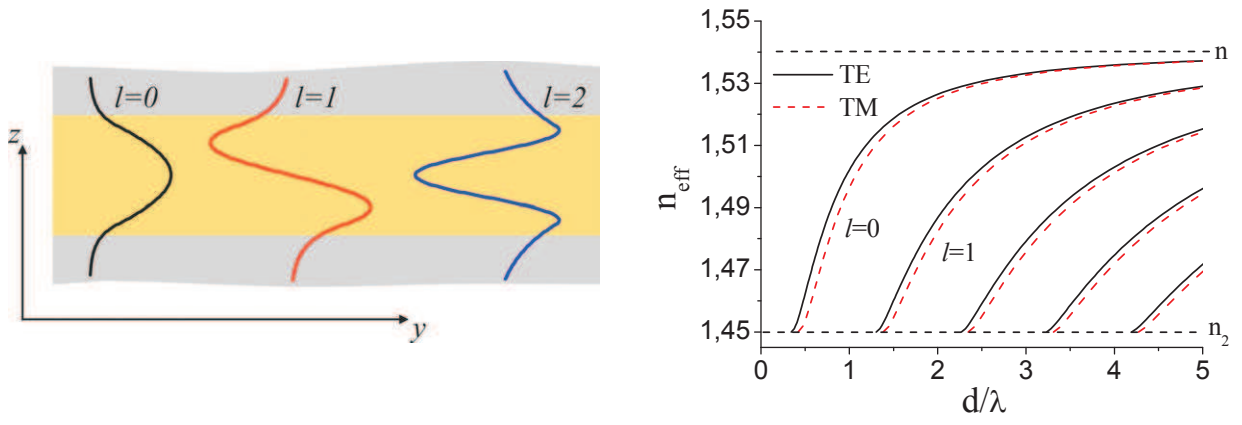

Fig.2-3. (a) Field distributions E(z) for several TE guided modes in a planar waveguide. (b) Effective refractive index of a guiding layer as a function of h/λ for constant substrate indices

the *z*-axis [94]. With the increase of d/λ ratio, higher order modes ($l \neq 0$) appear.

While planar waveguides as the one described here has limited practical use, it serves as a convenient model structure to explain the principles of wave confinement and guiding and to introduce an important concept of effective refractive index, that will be used later to analyze dielectric cavities and treat experimental spectra.

2.2. *Dielectric cavities.*

In the previous example of an infinite slab waveguide, light was confined along the *z*-axis and could freely propagate in x and y directions. If we limit the width and the length of a slab, we will obtain a structure in which light is confined in all 3 dimensions[1]. The configuration of the electromagnetic fields and frequencies at which confinement is possible depend on the shape of a cavity and properties of material.

In this thesis we work with quasi 2D dielectric cavities made of planar polymer structures of various shapes lying on a substrate with a lower refractive index (e.g. SiO_2, n=1.45). The transverse dimensions (along *z*-axis) of a cavity are of the order of a wavelength (λ=600nm), in order to obtain a cavity supporting only one mode in vertical direction. This should significantly simplify the treatment and explanation of observed emission spectra. The lateral dimensions of the cavities are of the order of 100λ, and are chosen to have sufficient gain in the active medium to achieve lasing. Due to the high substrate losses, the cavities smaller than approx. 50µm x 50µm require high pumping fluence in order to observe lasing emission, which bleaches the laser dye very quickly.

Taking into account that the cavities are fabricated of a dielectric polymer material, the mode energy is radiated in the surrounding space and therefore they belong to the class of open electrodynamical systems. In open resonators, as opposite to closed ones (i.e. radiofrequency resonators with perfectly conducting walls) electromagnetic fields do not vanish at its borders but may extend far behind the resonator's boundaries. Theoretical description of open systems is a very complicated task and, in case of planar dielectric cavities, a disk is the only system for which exact solutions of Maxwell equations exist [95]. Numerical modeling is therefore often applied for their analysis [96-99]. In this thesis, we will use Finite-Difference Time Domain (FDTD) method and Finite Element method (FEM) in order to analyze the electromagnetic field distribution in the cavity and predict the influence of the external medium on the cavity resonance spectra.

In this section we will briefly introduce main parameters characterizing the cavities, while planar cavities of various shapes used in this work and their suitability for sensing applications will be described in more details in §4.4.

2.2.1. *Cavity characteristics.*

In order to introduce the main parameters characterizing a cavity, we will revert to the ray optics approach and consider a resonator formed by *N* mirrors, placed in such a way that once

[1] Strictly speaking, expression (2-12) used to calculate the effective index is only valid for an infinite (in lateral dimensions) waveguide and becomes paradoxical near the edges of a planar resonator. However, it serves a good approximation and effective index calculated by (2-12) allows proper treatment of experimental results (calculation of periodic orbit lengths from emission spectra).

the ray of light is injected inside, it may travel in a closed loop between them. Similar as before, each ray with may be associated with a plane wave. A wave will be confined inside such resonator, if after completing one roundtrip (*N* reflections), it is identical to the initial injected one, which means it is in phase:

$$r_1 r_2 .. r_N e^{ik_m L n_{eff}(k_m)} = 1 \qquad (2\text{-}13)$$

Where $r_1 ... r_N$ are the reflection coefficients of the mirrors, n_{eff} is the effective index of the cavity medium, L is the length of a roundtrip distance. Condition (2-13) will be satisfied for a discrete set of wavenumbers k_m, which forms the resonance spectrum of the cavity. We will call *periodic orbit* the optical path of light inside the cavity which satisfies (2-13).

Quality Factor

One of the basic characteristics of a resonator is its quality factor, which is defined in words as the ratio of the time-averaged energy stored in the cavity to the energy loss per cycle. The quality factor can be measured experimentally from the spectrum of the cavity and is defined as:

$$Q = \frac{\lambda}{\Delta\lambda_{1/2}} \qquad (2\text{-}14)$$

where λ is the wavelength of the resonance and $\Delta\lambda_{1/2}$ is the width of the resonance peak at half of its magnitude. For sensing applications when the spectral shift is detected, we are interested to have narrow resonance peaks, therefore high quality factor is a very important characteristics of microcavities. Quality factor is also connected with the lifetime τ of the photon inside a cavity, which can be expressed as:

$$\tau = Q / 2\pi\nu \qquad (2\text{-}15)$$

where ν is the resonance frequency.

Finesse and Free Spectral Range

By definition, the free spectra range (FSR) is a wavelength spacing $\Delta\lambda_{FSR}$ (or frequency spacing $\Delta\nu_{FSR}$) between the adjacent resonances of a cavity. It is illustrated on Fig.2-4, on the example of a typical emission spectrum, registered from a planar microcavity. In general, the FSR becomes larger when the physical dimensions of the resonator decrease. A large FSR allows development of single mode microlasers and may be advantageous for the development of spectral shift detection schemes when a wavelength shift is converted into intensity change (see §4.1)

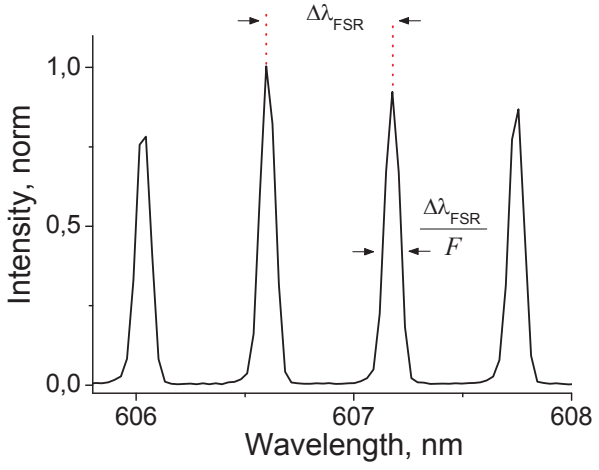

Fig.2-4. Resonance peaks of a lossy resonator (Fabry-Perot), illustrating the free spectral range and the finesse.

The strict condition on the frequencies of optical waves that are permitted to exist inside a resonator is

relaxed when the resonator has losses. The two principal sources of loss are: 1) losses due to absorption and scattering in the resonator medium; and 2) losses due to imperfect reflection at the mirrors. Presence of losses leads to the broadening of resonances so that in a real cavity resonance peaks always have some finite width, as different from the ideal no loss resonator, where the resonance peaks are delta functions. The quantity that connects the width of a resonance peak with the free spectral range is called *finesse* and is defined as:

$$F = \frac{\Delta\lambda_{FSR}}{\Delta\lambda_{1/2}} \tag{2-16}$$

When the finesse is large ($F >> 1$) the resonator spectral response features sharp peaks around the resonance frequencies.

2.2.2. *Whispering Gallery Modes*

The name "whispering gallery" originates from acoustical features of certain architecture shapes: it was noticed that a word pronounced by whisper near the wall of the dome can be clearly heard at the opposite side of the dome, but not in the middle of the building, even though the distance between the speaker and the listener is large. The fact that sound in a closed space seems to propagate not along the shortest path but along the concave wall was first studied and explained by Lord Rayleigh in 1910 [100]. The same physical effect is observed also for the radio and optical frequency waves, when due to multiple total internal reflections wave propagates along the concave boundary of a body. For historical reasons, such modes bear the name "whispering gallery modes" (WGM). The employment of WGMs in an axially-symmetric dielectric body for the creation of a high quality factor electromagnetic resonator was first proposed by Richtmyer in 1939 [101].

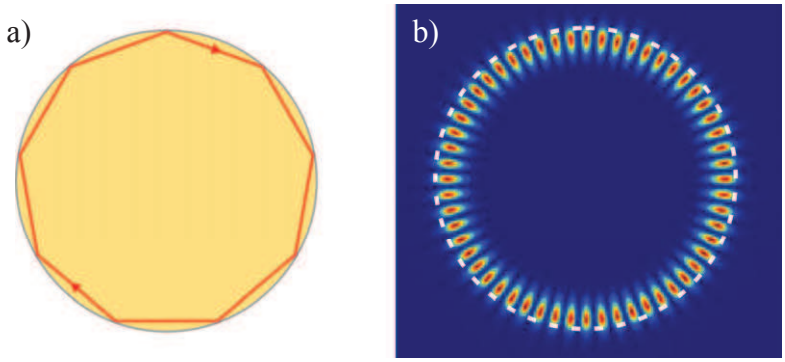

Fig.2-5. Geometrical optics (a) and wave optics (b) representation of a whispering gallery mode in a planar disc cavity. Cavity contour is shown in white dash on (b).

The most common resonator shapes where WGMs are observed are spheres or, in case of planar cavities studied in this work - disks. From the ray optics point of view, the light is trapped inside the disk by continuous total internal reflections at the curved boundary surface (Fig.2-5). Such modes possess high quality factors (experimentally up to 10^{11} [102]) leading to very narrow resonances. Moreover, high localization of the modes in a narrow region close to the cavity boundary, promotes nonlinear effects and leads to low lasing threshold if active cavity is considered. The main interest of WGMs in sensing application is their localization close to the boundary of the cavity, and therefore higher sensitivity to the changes in the medium

surrounding the cavity. The advantage of WGM-supporting cavity over other planar cavity shapes will be grounded in §4.4 with the experimental proofs presented in §4.5.

2.3. *Active cavities*

Until now in this introduction we talked about passive dielectric cavities. In this work however, we study cavities fabricated of a material with gain, or active cavities, in which laser generation is possible under appropriate conditions. To create a microlaser we introduce a laser dye homogeneously mixed inside the polymer that forms the cavity body. The dye molecules are pumped with a laser. Their emission is trapped inside the microcavity, amplified due to the multiple passes of light inside the cavity and stimulated emission, and emitted through the cavity boundaries. Up to now it seems that the spectral features are largely determined by the passive cavity resonances. It is important therefore to have laser dye emission in the spectral range, where passive cavity features sharp resonances.

Laser dyes are extensively studied since the beginning of the laser era (60s-70s) and possess a number of advantages: ease of manipulation, low cost, wide fluorescence band [103]. Laser dyes are traditionally considered as a 4-level system [104] (see Fig.2-6), which is in fact two levels S_0 and S_1, broadened by molecular vibrations. Absorption is accompanied by transition from the fundamental state S_0 to the first excited state S_1. Afterwards, molecules relax quickly (~300fs) and in a non-radiative way to the bottom of S_1 band. The fluorescence is observed as the molecules relax from the bottom of S_1 band to the S_0 band. Once again, fast non-radiative relaxation occurs to the bottom level of S_0 band. This process is very efficient and fluorescence quantum yield could reach 70% depending on the solvent or the matrix [105, 106].

At the same time, dye molecules exhibit effects that lead to extinguishment fluorescence, namely *bleaching* and *blinking*. Bleaching consists in the degradation (change of the chemical structure) of a dye molecule that makes fluorescence impossible. Bleaching may be promoted by numerous factors: reaction of a molecule with air oxygen, which is believed to be a very important factor [107, 108], reaction with other molecules, decomposition of molecule due to heating, etc [109, 110]. Bleaching of laser dye molecules in different polymer matrices and under long-time pumping will be studied in §3.3.

Blinking is connected with the presence of a triplet state T_1. Once trapped in the triplet state, the molecule may remain there for a long time (lifetime of the order of μs) and relax to S_1 in a non-radiative way. If dye molecules are pumped continuously, the T_1 level is populated and fluorescence emission stops. As the transition $S_1 \rightarrow T_1$ involves the rotation of spin, it is relatively long (~10ns) while $S_1 \rightarrow S_0$ is fast (~1ns). Pumping the molecules with short laser pulses (shorter than 1ns) allows generation of stimulated emission before the T_1 metastable state is populated [103, 111]. For this reason, we use a nanosecond laser (pulse length ≈1ns) in our experimental setup to pump the cavities.

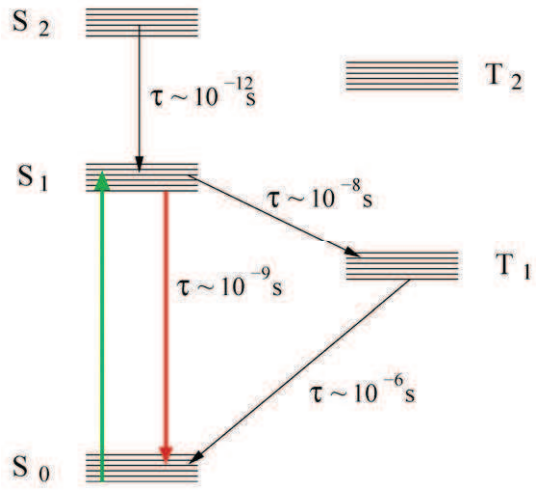

Fig.2-6. Energy levels diagram of a standard laser dye.

2.3.1. *Experimental setup for spectra recording.*

The experimental setup used to record lasing spectra of the microcavities is schematically presented on the Fig.2-7. The microlasers are optically pumped with a frequency doubled Nd:YAG laser (Teem photonics, λ=532nm, 10 Hz, τ=500ps) from the top, in the direction perpendicular to the cavity plane (see Fig.2-7b). The size of the beam spot on the sample can be varied with the help of a lens (L1) by slightly focusing or defocusing a beam and is adjusted to uniformly illuminate the cavity (spot diameter ≥ 2*size of the cavity). The intensity of the pumping beam is smoothly adjusted using a half wavelength plate (W1) and a polarization splitting cube (P1). The output of the laser is linearly polarized, so by turning the polarization plane with a λ/2 plate, the beam intensity varies after passing through the cube (P1), which transmits only vertical polarization. The half-wave plate (W2) serves to change the orientation of polarization of the pumping beam. Direction of polarization of the pumping beam significantly influences the spectra of certain cavities - Fabry-Perot, square shaped, while it seems to have no influence on the whispering gallery mode cavities (stadiums, discs). This subject requires deeper attention and more details will be mentioned in paragraph 2.3.3.

The sample is placed on a rotating mount that allows orienting the sample so that the direction of the maximum emitted intensity coincides with the direction of detection. The cavity that will be investigated is chosen with the help of the optical microscope (Leica WILD M10). By translating the stage in (*x*,*y*) plane the chosen cavity is aligned with the pumping beam. The rotation axis of the stage is centered at the point, where the beam falls on the sample. Thus 360-degree angular emission diagrams of microlasers can easily be recorded, by rotating the sample

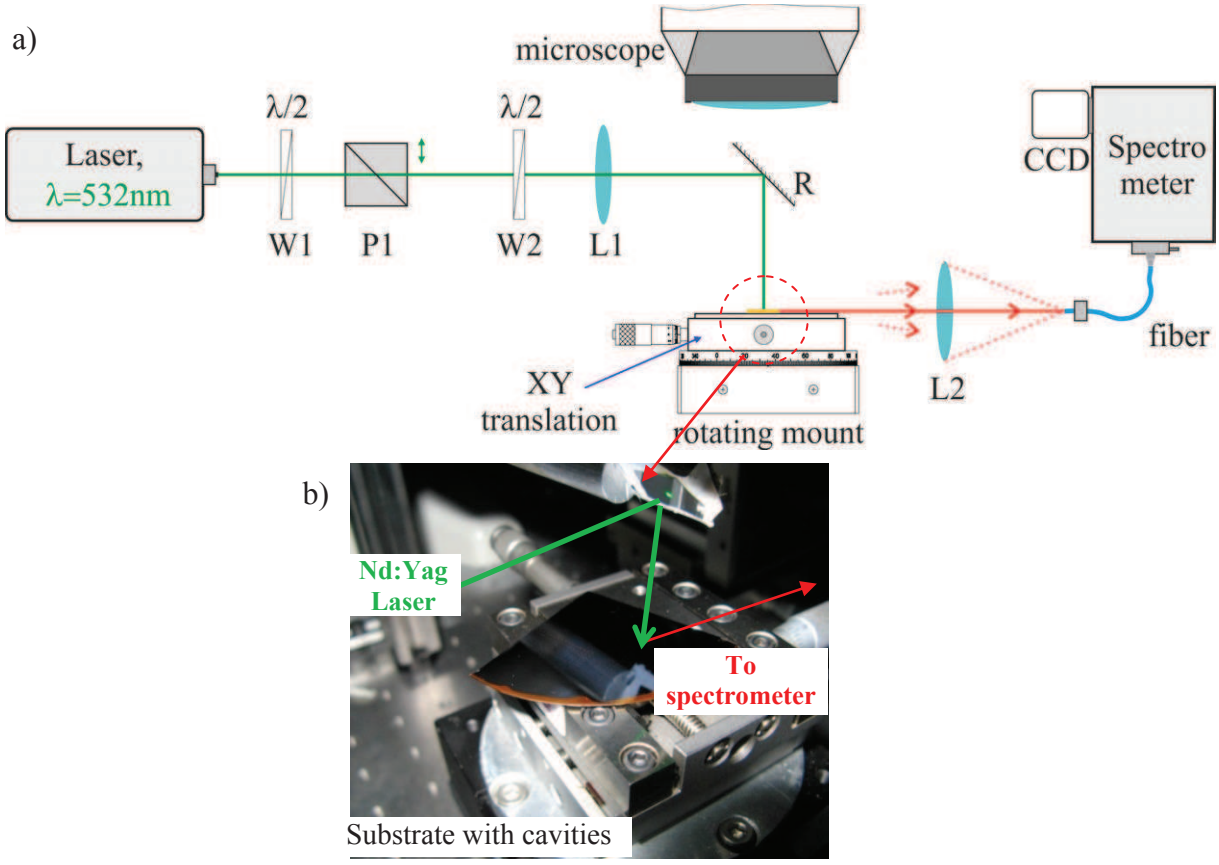

Fig.2-7. a) Scheme of the experimental setup. b) A photograph of the sample with microcavities on the stage, pumping and emission directions.

in its plane and recording the spectra at needed angular step. The emitted light coming out of the cavity in the lateral direction is collected in the far-field with a lens L2 (collection angle ~6º) that focuses the emission into an optical fiber, connected to an Acton SpectraPro 2500i spectrometer (F/6.5, 500mm focal length) equipped with a Princeton Instruments PIXIS 100 cooled CCD camera (resolution: 1340 x 100; pixel size: 20µm x 20µm). In the spectrum captured by the camera, one pixel corresponds to 0.029nm when converted to a wavelength scale. The spectra of the cavities are normally registered at a laser pulse repetition rate of 10Hz and an integration time of 3s, which corresponds to 30 pump pulses per one recorded spectrum (CCD camera shutter is synchronized with the pumping laser pulses). Integration time is chosen to achieve an optimal signal/bleaching ratio.

In its current configuration, our setup allows making only "2-dimensional" observations. Only the emission coming out of the cavities in their plane can be collected and studied, the detector cannot be placed at a certain angle relative to the cavity plane, as well as the excitation beam is always perpendicular to the cavity plane. We have noticed that the angle between the excitation beam and the cavity plane significantly influences the observed lasing spectra therefore perpendicularity of the beam was carefully controlled. This dependence on perpendicularity, similarly to dependence on the pumping beam polarization, is probably explained by the change of efficiency of excitation as well as the change of prevailing emission direction of the dye molecules in the polymer matrix. Such in-plane measurements were sufficient for most of the tasks of studying the traditional thin single vertical mode cavities (thickness ≤ wavelength) on the plane substrate, like measuring lasing thresholds, emission diagrams, assessment of sensitivity. However for novel cavity geometries, like pedestal cavities, described in Chapter 5 or 3D cavities (thickness > wavelength) it becomes necessary to observe the emission patterns not only in the cavity plane but also at a various angles to the plane. This necessity will become obvious after the properties of pedestal cavities will be explained in more details. The 3D setup that will allow full control over the pump beam incidence angle and the observation angle is being currently developed by Clement Lafargue at LPQM and will be described in his PhD thesis.

2.3.2. *Experimental data treatment*

Emission spectra of microlasers bear the geometrical features of the cavities and analysis of the spectra gives insight into the excited modes. In a simplified geometrical view, the light confined in the active cavity reflects on the cavity borders and travels along the closed loop which leads to the amplification and generation of a lasing spectrum, whose typical pattern is shown on Fig.2-8a. The length of the path traveled by the light during a roundtrip in the cavity can be recovered from the spectrum. To easily understand the procedure we use to treat the spectrum, we will explain it on the example of a Fabry-Perot cavity, which features only one periodic orbit.

The cavity consists of a long dye-doped polymer bar, as displayed on the inset of Fig.2-8a, pumped uniformly (the diameter of the pump laser spot is larger than the width of the cavity). The periodic orbit with the length $L=2a$ gives birth to a Fabry-Perot resonance between the two parallel walls of the cavity, and laser emission (marked by red arrows on the figure) is registered in one of the directions perpendicular to the cavity edges. The resonance condition states that the

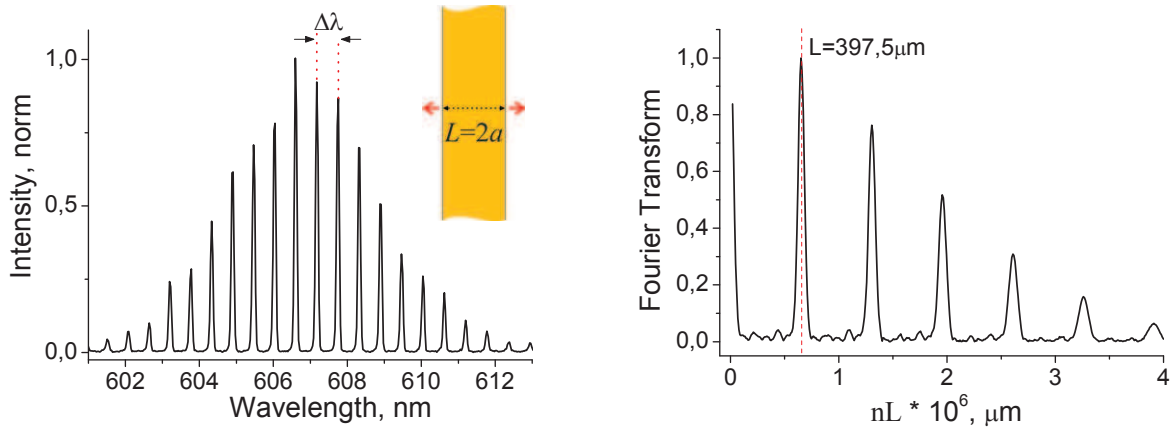

(a) (b)

Fig.2-8. The typical spectrum of a Fabry-Perot cavity (width=200μm) (a) and a corresponding Fourier transform (b). Inset on (a) shows emission directions of a Fabry-Perot cavity.

round trip distance L of the wave in the cavity, must be equal to an integer number of wavelengths λ :

$$k_m nL = 2\pi m \tag{2-17}$$

where n is the refractive index of the cavity material, m is an integer. The spectral peak positions k_m are therefore defined by this condition and the peaks are spaced periodically in the wavenumber space. In the wavelength space the periodicity is approximate, due to the fact that $\Delta k = \Delta\lambda/\lambda^2$, where $\Delta\lambda$ is a free spectral range. To extract the periodic orbit length L we can either measure $\Delta\lambda$ directly or use a Fourier transform of the spectrum, as shown on the Fig.2-8b. As the spectrum is registered as a function of a wavelength λ, before applying a Fourier transform it is converted to the wavenumbers 1/λ. The resulting Fourier transform consists of peaks centered at the optical length nL and its multiples mnL. The position of the first peak shows directly the length of the periodic orbit L (as the index n is known) and lets us easily recover the length of the lasing periodic orbit for different cavity shapes. In the example of the Fabry-Perot cavity, we obtain the length of the periodic orbit L = 397 ± 23μm, which agrees well with the dimension of the cavity $2a$ = 400μm. The spectrum treatment procedure is explained in more details in [94].

The measurement error of the orbit length is given by the width of the Fourier transform peak and may be determined by the pixel size of the CCD detector, signal/noise ratio in the spectrum, coexistence of multiple orbits with close length. To avoid systematic measurement errors, the spectrometer and a CCD camera need to be duly calibrated, as if the correspondence between the wavelength values and camera pixel coordinates is wrong the treatment of the spectrum will be false. The calibration is performed by the spectrometer and camera software, using a mercury lamp doublet as a reference source and the error in $\Delta\lambda$ measurement is estimated to be not larger than 0.01nm.

It was found in [34] that if the index of the bulk polymer (n=1.54 for PMMA+DCM) was used in calculation, obtained orbit length was always underestimated for approximately 10%. As it was figured out, the dispersion of the refractive index should be taken into account, which

compensates for the missing 10%. The total refractive index which is also called a group index therefore becomes:

$$n_{total} = n_{eff}(\lambda_0) - \lambda_0 \frac{\partial n_{bulk}}{\partial \lambda} - \lambda_0 \frac{\partial n_{eff}}{\partial \lambda} \tag{2-18}$$

TM	$n_e = 1.0$	n_{total} =	1.496	–	-0.10	–	-0.059	=	1.65 ± 0.01
	$n_e = 1.33$	n_{total} =	1.502	–	-0.10	–	-0.048	=	1.65 ± 0.01
TE	$n_e = 1.0$	n_{total} =	1.502	–	-0.10	–	-0.049	=	1.65 ± 0.01
	$n_e = 1.33$	n_{total} =	1.505	–	-0.10	–	-0.043	=	1.65 ± 0.01

Here the first term in the formula (2-18) is the effective refractive index calculated at the wavelength of interest λ_0, the second term is the dispersion of the index of bulk polymer (retrieved from ellipsometry measurements) and the third term is the calculated dispersion of the effective refractive index. The calculation is performed for the wavelength $\lambda_0 = 600nm$ and two values of medium refractive index: 1 and 1.33, corresponding to the cavity in air and in water. The values of effective index and dispersion of effective index are given with precision of 3 digits after decimal point in order to underline the difference between them. However the dispersion of the bulk material is measured only with the precision of two digits after decimal point, consequently the final result is rounded. Another source of error comes from the fact that the value of effective refractive index may vary substantially for different cavity modes but we neglect this variation and always use the value calculated for a fundamental mode of a guiding layer surrounded by infinitely thick claddings.

The values of the group index were found to be equal (within the error range) for different medium indices. While the value of effective refractive index of the cavity in water increases, the dispersion becomes lower and the group index remains almost unchanged. Therefore the same value of n_{total} can be applied for extraction of periodic orbit length both for the cavities in air and in water.

2.3.3. *Polarization influence.*

Laser dye molecules, due to their 3-dimensional shape, exhibit sensitivity to the polarization of the incident emission. Depending on the molecule orientation, light of one polarization may be absorbed more efficiently than another one. Direction of molecule's emission will also depend on its orientation. As molecules are introduced inside the cavity, the direction of molecule's emission may play a very important role in the efficiency of excitation of cavity modes. The influence of polarization on the spectra of cavities is a complicated issue that requires a separate deep study, which is not the subject of this thesis, however it can be visually explained by the 2D example of a Fabry-Perot cavity (Fig.2-9b) if we consider dye molecules as linear dipoles lying in the plane of the cavity. Such simplified representation is of course imprecise, but allows us to qualitatively explain the observed changes in the lasing spectra. When polarization of the pumping beam, incident from the top, is parallel to the cavity walls ($P_{\parallel}$), the dye molecules with the dipoles oriented along the polarization direction are effectively

pumped, and the dipoles emit in the direction, perpendicular to the cavity walls, therefore exciting a Fabry-Perot cavity mode. However, if the polarization is oriented perpendicularly to the cavity walls ($P_\perp$), the dipoles emit mainly in the direction along the cavity, thus decreasing the efficiency of FP mode excitation. This is clearly evidenced in the lasing spectra (Fig.2-9a): there ratio of emission intensities reaches 150 for the orthogonal polarizations in Fabry-Perot cavities under same pumping energy.

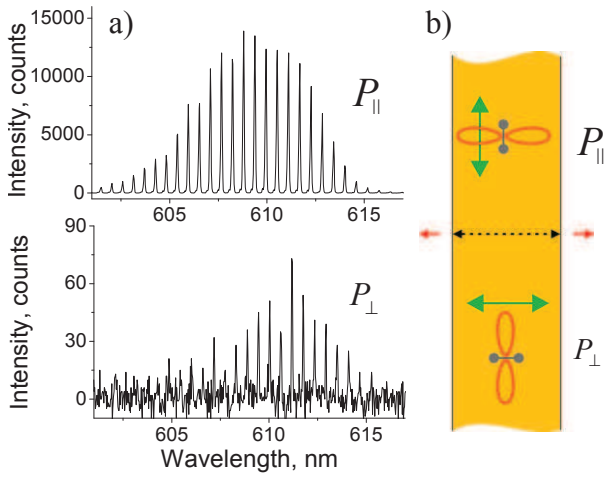

Fig.2-9. (a) Lasing spectra of a Fabry-Perot microcavity (width=200μm) under same pumping energy (70 μJ/cm²) for $P_\parallel$ and $P_\perp$ polarizations of the pumping beam. (b) Illustrative explanation of polarization influence.

In the case of square-shaped cavities, the influence of polarization is more complex. Difference in lasing spectra in this case originates from cavity modes of different symmetry classes that are excited depending on the polarization of the pumping beam. The origin of this phenomenon is still not clarified and is being studied.

For the cavities, supporting whispering gallery modes (discs, stadiums) we didn't see any influence of polarization on the lasing spectra, that are attributed to the WGMs. At the same time, for those cavity shapes, polarization orientation may either inhibit or promote the Fabry-Perot component in the observed spectrum. For example, in the case of a disc (Fig.5-8), if the polarization is directed along the *y*-axis, and the emission spectra are recorded in the *x*-axis direction, a strong Fabry-Perot component is present in the spectrum which may be observed along with WGM or completely outshine it. If the polarization is oriented along the *x*-axis and the emission spectra are recorded in the *x*-axis direction, then only the WGM component is seen in the generation spectrum (a FP mode in this case is excited along the *y*-axis, and is not registered). The same considerations apply to the stadium-shaped cavities.

To fully understand the influence of polarization on the lasing spectra of the cavities, the 2D approximation of the cavity is insufficient and a full 3D problem needs to be solved, where the laser dye molecules must be represented with adequate models and a question of dye molecule orientation in the polymer matrix should be studied. Polarization influence on the spectra as well as the polarization of the microcavity emission will be studied in more details in the thesis of Iryna Gozhyk, LPQM.

In this chapter we reminded the basics of wave confinement and guiding in dielectric waveguides and mentioned the main parameters characterizing resonators. The principle of functioning of active cavities doped with laser dyes was explained and the description of our experimental setup that allows recording cavity emission spectra is provided. The concept of effective refractive index was explained as well, which, as was shown in [34], is a convenient way to describe wave propagation in the waveguide or a cavity and allows reducing the complex 3-dimensional problem to a 2 dimensional one. The use of effective index allows correct

treatment of experimental results and lets us extract the length of periodic orbit from the lasing spectrum of a cavity. Obtained orbit lengths are in good agreement with physical dimensions of a cavity.

Chapter III

Technology: creating a microlaser.

Introduction

Elaboration and optimization of technological processes are the important factors on the way of creation of a portable microcavity-based sensor, therefore current chapter will be entirely devoted to technological aspects and description of material properties. At the beginning we will talk about the materials that have been chosen for cavity fabrication – PMMA and porous polystyrene-based polymers doped with different laser dyes, and ground the choice by comparing their properties and characteristics. Photodegradation of the laser dyes in the chosen polymer matrices, which is an important issue affecting the polymer microlaser performance, will be studied. Later on, fabrication process of polymer microcavity lasers based on conventional UV and e-beam lithography will be thoroughly described as well as different novel approaches to fabrication of micrometer-scaled polymer components (such as 2-photon polymerization and femtosecond laser ablation) will be discussed. Finally, we will propose and discuss the ways of further development of existing microcavity design: cavities on pedestal as well as pillar cavities on low-index polymer substrate will be introduced. This new cavity design is expected to enhance the performance of cavities both as laser generators as well as sensitive detectors. The properties of the cavities and sensing results will be discussed in the following chapter, while this chapter is entirely devoted to the fabrication technology.

3.1. *Materials: polymers and dyes.*

In our research we have investigated microcavity lasers created on the basis of organic polymer materials: a polymer matrix with a laser dye introduced in it. We have worked with several commercially available polymers (non-porous: PMMA; porous: PS-b-PAA, PS-b-P4VP, PS-Co-PAA) and various laser dyes (DCM, Pyrromethene, Rhodamine) trying to find the best solution adapted to sensing (as will be detailed below) however the fabrication process remains almost identical in all the cases.

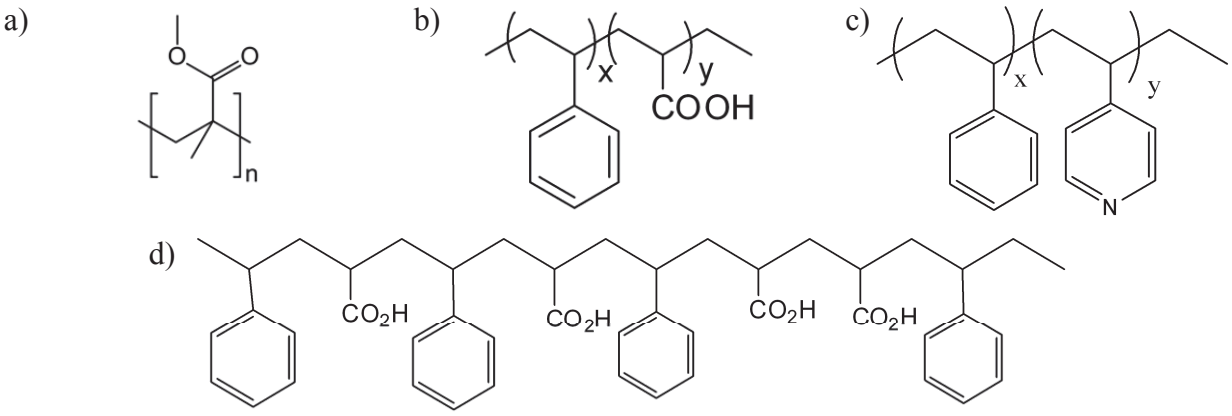

Fig.3-1 The structure of PMMA molecule (a), PS-b-PAA (b), PS-b-P4VP (c) and PS-Co-PAA (d).

From the beginning of the research project we utilized a PMMA polymer – Poly(methyl methacrylate), whose structural formula is depicted on Fig.3-1a. Microlasers made of PMMA have been well-tested previously in our laboratory and they are used as a "reference" in experiments. The PMMA polymer was purchased from Microchem (495K Microchem PMMA A6, 6%wt solution in anisole).

More widely known in everyday life as Plexiglass, PMMA turned out to be a very convenient material for fabrication of light guiding and confining devices. Its high mechanical

rigidity, solubility in various solvents, transparency and low cost make it an ideal material for fabrication of various photonic elements. A low glass transition temperature (lying in the range 95-106ºC for the PMMA type that we used[1]) makes it possible to perform thermal reflow[2] steps in manufacturing process without destroying laser dye molecules thus creating perfectly smooth surfaces and/or certain special cavity shapes [112].

We have also worked with porous polymers, provided by our colleagues chemists (PPSM department, ENS Cachan) – polystyrene-based PS-b-PAA, PS-b-P4VP and PS-Co-PAA (Fig.3-1b,c,d). The difference between the non-porous PMMA and porous cavities reveals at the stage of functionalization with ligands. In the case of a non-porous PMMA cavity, ligands can be immobilized only at the surface at the last step of manufacturing process with relatively low percentage of surface coverage. However in the case of the porous polystyrene polymers, ligands are introduced directly into polymer solution, before spin-coating, thus all of the cavity volume is functionalized. Due to the cavity porosity, we expected that analyte molecules may diffuse and bind to the ligands inside the pores which may potentially lead to a higher sensitivity.

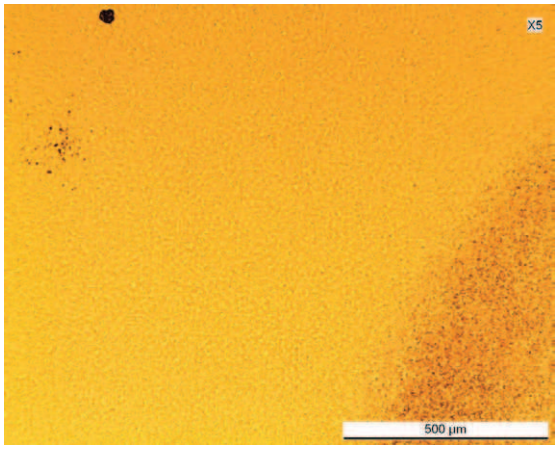

Fig.3-2. A microscope photograph of the spin-coated layer of a PS-Co-PAA polymer demonstrating micrometer-scale aggregates.

In case of PS-b-PAA and PS-Co-PAA polymers solution, we had to optimize the concentration and chose an appropriate solvent in order to fabricate a layer which is sufficiently flat and doesn't contain aggregates. The quality of the layer is critical to achieve lasing in microcavities as even minor aggregates may lead to strong scattering losses. Usually, only layers that looked smooth under the microscope allowed fabrication of microcavities and presence of impurities or aggregates rendered the microlasers inoperative. After testing different solvents (dioxane, toluene, anisole, THF) we chose for PS-b-PAA an anisole/dioxane 1:1 solvent combination and polymer concentration of 125mg/ml as giving the best results for a smooth layer preparation. For PS-Co-PAA the final choice of the solvents was the same however we didn't succeed in obtaining a layer of appropriate quality. Substantial aggregate formation prevented us from proceeding to microlaser fabrication and PS-Co-PAA was dismissed from further work (Fig.3-2).

The list of the tested dyes and solvent combinations for each polystyrene-based polymer type is given in Table 3-1. The "bad quality" mark in the results column means that aggregates of various sizes were present in spin-coated layers, or other defects were observed. The "ASE" mark signifies the intensity of amplified spontaneous emission observed from the layer, as explained below. Even if ASE emission is intense, presence of aggregates renders the layer

[1] Glass transition temperature provided by manufacturer.

[2] Thermal reflow is a process of thermal treatment of a solid polymer structure by heating is slightly above the glass transition temperature. The softened polymer surface will seek to minimize its surface energy by transforming into a spherical shape. Depending on the treatment time and temperature this approach may either be used to create very smooth, defect-free surfaces or polymer hemi-spheres or some other shapes.

Dye	Solvent	Conc, mg/ml	Result
PS-b-PAA			
DCM-OH 1% , 2%	Dioxane/toluene 1:1	150	**Quality**: fine. **ASE**: very weak.
DCM-OH 1%	Anisole/THF 1:1	150	**Quality**: bad. **ASE**: intense.
DCM-OH 1% , 2%, 5%	Anisole/Dioxane 1:1	125	**Quality**: fine. **ASE**: very weak.
DCM 2%, 5%	Anisole/Dioxane 1:1	125	**Quality**: fine. **ASE**: intense.
Rhod640 2%	Anisole/Dioxane 1:1	125	Rhodamine partly insoluble
Pyr605 2%, 5%	Anisole/Dioxane 1:1	125	**Quality**: fine. **ASE**: intense.
PS-Co-PAA			
DCM 2%	Anisole/Dioxane 1:1	125	**Quality**: bad.
Rhod640 2%	Anisole/Dioxane 1:1	125	**Quality**: bad + Rhodamine insoluble
PS-b-P4VP			
DCM 2%	3-pentanone/cyclohexane	200	**Quality**: bad. **ASE**: intense.
DCM 2%	3-pentanone/cyclohexane	150	**Quality**: bad. **ASE**: intense.

Table 3-1. Tested laser dyes, solvent combinations, polymer concentration in solvent for each polymer type.

unusable for cavity fabrication. For example, in the case of Anisole/THF solvent combination for PS-b-PAA, the resulting layer was very non-uniform in thickness as a result of high solvent volatility: solution started to dry before wafer was fully covered with polymer, however observed ASE emission was strong. For the PS-b-P4VP polymer, aggregation can be explained taking into account the polymer structure, which is a combination of hydrophilic and hydrophobic parts. Probably, a self-organization of these two components in solution occurs that leads to formation of micelles, rendering the dried polymer layer unusable.

3.2. *Material characterization: Amplified Spontaneous Emission and ellipsometry.*

In order to verify whether a dye-doped polymer layer is suitable for microlaser fabrication we record its amplified spontaneous emission (ASE) spectra. ASE by definition is a process of amplification of spontaneous emission during its propagation in a medium with gain. To record an ASE spectrum, a doped polymer layer is pumped from the top, close to the cleaved edge, as shown on Fig.3-3. A spontaneous emission in the lateral direction that has been amplified during single pass in the active medium with a large gain is captured and recorded by spectrometer. A signature of amplified spontaneous emission is an intense and narrow peak, dominating over the luminescence spectrum. An intense ASE peak signifies high active medium gain, efficiency of the laser dye and good waveguiding properties of the polymer layer – absence of aggregates or other scattering centers.

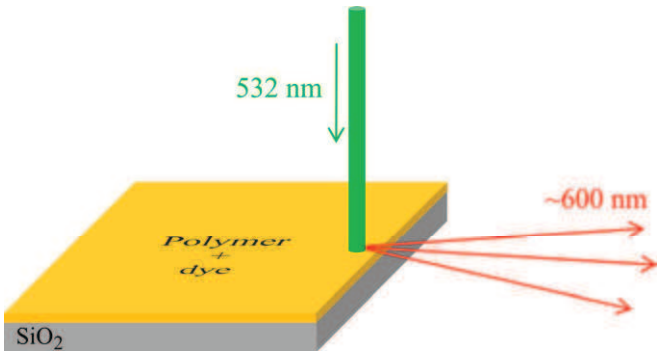

Fig.3-3. A schematic representation of ASE spectra recording.

We have performed spectral ellipsometry measurements (Sopra GES 5 ellipsometer, performed by Nguyen Chi Thanh, LPQM) to determine the refractive indices of pure and dye-doped PMMA

and PS-b-PAA layers at $\lambda \approx 610$ nm. A good refractive index contrast is necessary between the polymer layer and a substrate in order to ensure good wave confinement and prevent mode leakage into the substrate. Moreover, the knowledge of the refractive index and its dispersion is necessary to analyze the lasing spectra of cavities and to calculate the optical path of light inside [94].

For a PMMA layer (non-doped) we have measured a refractive index in the range of 1.484 - 1.495 units. For a PMMA+DCM 5% layer, the estimated value is $n = 1.54$. For the layer of PS-b-PAA + Pyrromethene 2% measurements gave the refractive index value of $n \approx 1.75$. Measurements of indices of doped layers are complicated due to the dye absorption that adds resonant peaks in the measured data and makes it difficult to interpret the results.

3.3. *Materials: choice of a laser dye.*

A choice of the appropriate laser dye is very important to create an efficient, long-lasting microlaser with stable emission intensity. Initially we have worked with a DCM laser dye. DCM (4-dicyanomethylene-2-methyl-6-p-dimethylaminostyryl-4H-pyran) is a commercial dye with a fluorescence spectrum centered around 600nm. Besides relatively low cost (purchased from Exciton) and availability, the main assets of DCM are a good fluorescence quantum yield and a large Stokes shift (~100nm) (Fig.3-4a) which prevents from reabsorption of the emitted light. However, the DCM dye is subject to fast photobleaching under continuous pumping.

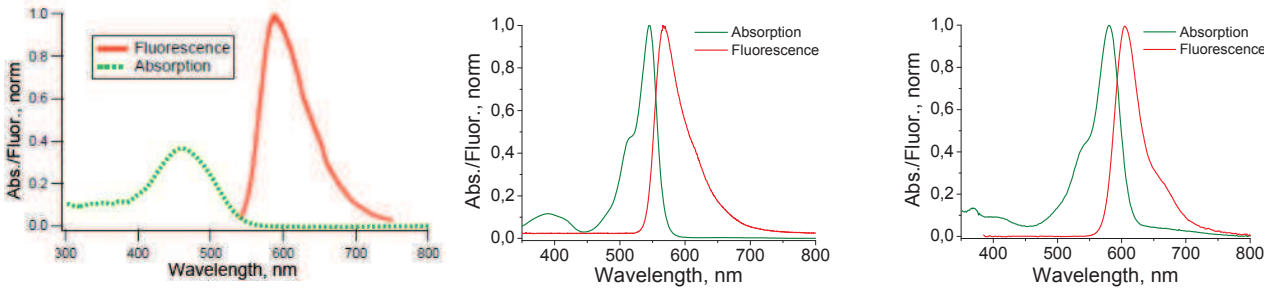

(a) (b) (c)

Fig.3-4. Absorption and fluorescence spectra of a layer of (a) PMMA+DCM 5%, (b) PMMA+Pyr605 5% and (c) PMMA+Rhod640 5%.

While talking of the dye instability one needs to distinguish two different aspects. The first one is the stability in time, which means the ability of polymer/dye combination to preserve its properties during a long storage time. The second one is the photostability, or the behavior of the dye under continuous exposure to pumping emission or ambient light. We have also experimented with Pyrromethene 605 ($\lambda_{max,abs} = 543$ nm in ethanol) and Rhodamine 640 ($\lambda_{max,abs} = 575$ nm in ethanol) laser dyes, purchased from Exciton, which are both known to be more photostable than DCM. Their absorption and fluorescence spectra are given in Fig.3-4b,c. As it is obvious from the spectrum, absorption maximum of Pyrromethene 605 in PMMA matrix ($\lambda \approx 545$nm) lies much closer to the pumping laser wavelength (532nm) thus more efficient pump energy conversion is expected.

Introduction of different laser dyes into the non-porous PMMA matrix creates a material that preserves its emissive properties for ages – the cavities prepared in PMMA-DCM were stored for years without any noticeable ageing and change in their emission intensity. At the same time,

when the dyes were introduced inside the porous PS-b-PAA matrix, the cavities stopped functioning after just 2-3 months of storage at room temperature and atmosphere which may be explained by the penetration of the oxygen inside the polymer matrix due to porosity and consequent dye degradation.

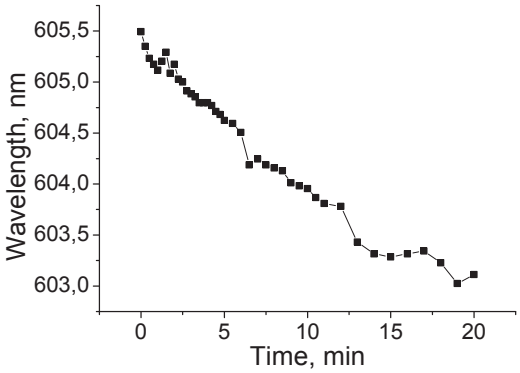

Fig.3-5. A blue-shift of the ASE maximum peak of PS-b-PAA+Pyr605 2% during 20 minutes exposure to the pump laser (700ps, 10Hz repetition rate, 6.2μJ pulse energy).

Dye photobleaching doesn't only lead to the decrease of emission intensity, but also to the blue-shift of the emission maximum. For example, Fig.3-5 shows the blue shift of the maximum of an ASE spectrum of a porous PS-b-PAA polymer layer doped with pyrromethene dye. For a laser microcavity this means that in a continuous series of measurements, each subsequent spectrum is blue-shifted relative to the previous one. This effect was observed and quantified in [35]. For a PMMA-DCM cavity the blue-shift rate of the lasing spectrum was estimated to be $\delta\lambda = 3.33 \cdot 10^{-4}$ nm/s while pumping with 700ps laser pulses at 10Hz repetition rate (4μJ pulse energy). The values of the blue-shift vary depending on the polymer-dye combination and pump fluence and may become very significant for the microcavities. In case of sensing applications, where we aim at detecting certain analyte presence by a spectral shift, parasitic blue-shift creates significant interference and complicates results interpretation. This stimulated us to experiment with different dyes that combine high quantum yield with an improved photostability in the used polymer matrices. High quantum yield allows lower pumping intensity and improved photostability leads to a smaller value of a blue-shift.

An optimal laser dye concentration has to be found for each polymer to achieve maximum emission intensity while avoiding concentration quenching. ASE spectra were recorded from dye-doped polymer layer in order to estimate their lasing ability. Both Rhodamine 640 and Pyrromethene 605 dyes in PMMA matrix show significantly higher emission intensity than DCM (Fig.3-6a). We have investigated their photostability under long-time illumination of the layers by the pulsed pumping laser (pulse energy 9.3μJ, pulse duration 700ps, repetition rate 10Hz). The DCM dye turns out to be the less stable out of 3 competitors (Fig.3-6b, black) with the ASE intensity decrease of more than 30% after 15 minutes of continuous illumination, while Rhodamine 640 was found to be the less degrading dye.

In porous PS-b-PAA matrix Pyrromethene 605 at 2% concentration provides the maximum emission efficiency (Fig.3-6c), however the photostability of the dye is rather short, as can be seen on Fig.3-6d, – 60% of intensity decrease after 15 minutes of continuous excitation. For the microcavities doped with Pyrromethene 605, the photostability was found to be significantly lower than for doped layer, probably due to the smaller volume of the material that is excited (cavity lateral dimensions ~150μm). The Rhodamine 640 dye is an ionic species and is not well soluble in a weakly polar anisole/dioxane solvent combination which explains its low observed performance. Hence temporal intensity decay was not measured for Rhodamine in PS-b-PAA.

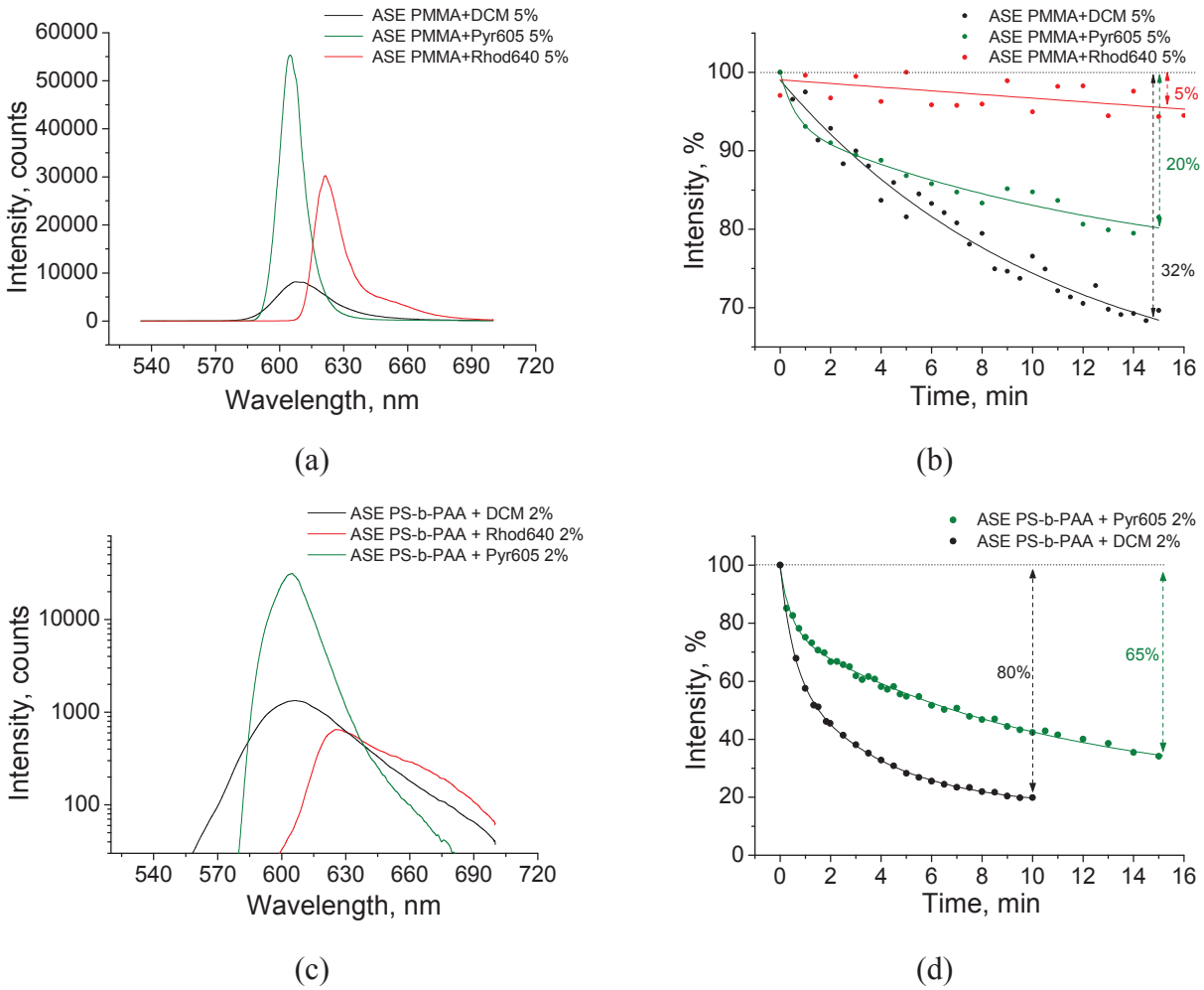

Fig.3-6. (a) ASE spectra of PMMA polymer layers with different laser dyes: DCM (black), Pyrromethene 605 (green) and Rhodamine 640 (red) laser dyes demonstrate high efficiency of Rhodamine and Pyrromethene (pump energy 9.3μJ). (b) Decay of the ASE intensity in PMMA under continuous exposure to the pumping laser pulses (9.3μJ, 700ps, 10Hz). (c) ASE spectra of PS-b-PAA layers with DCM, Pyrromethene 605 and Rhodamine 640 dyes on the logarithmic scale. (d) Decay of the ASE intensity in PS-b-PAA under continuous exposure to the pumping laser pulses (6.2μJ, 700ps, 10Hz)

According to the measurements results, for the cavity manufacturing in the case of PMMA polymer the dye concentration (DCM, Rhodamine 640 or Pyrromethene 605) is chosen to be 5% in weight. In the case of PS-b-PAA polymer, dye concentration (DCM or Pyrromethene 605) was chosen to be 2%.

3.4. *Microcavity fabrication technology.*

Several technological processes are available for laser microcavity fabrication in polymers. Cavities can be formed either by conventional lithography (UV or e-beam) or, as was supposed in the microFLUID project we were working on, by using novel approaches such as femtosecond laser ablation or 2-photon polymerization. Below we will briefly discuss the techniques and the results we obtained.

3.4.1. *Photolithography.*

Technology of organic micro-laser fabrication by optical lithography is relatively simple and easily reproducible. The process workflow is schematically depicted on Fig.3-7. The process starts with preparation of a polymer-dye solution. The necessary amount of dye is put inside the flask with a polymer solution and stirred using magnetic stirrer for 24 hours. Then a dye-doped polymer layer (thickness < 1μm) is spin-coated on a commercial SiO_2 2μm/Si substrate (2μm of SiO_2 formed by thermal oxidation), baked for 2 hours at 120ºC and slowly cooled down to a room temperature inside the oven to avoid layer cracking due to fast temperature change. A UV-light sensitive positive resist layer (Microposit S1805 or S1818) is spin-coated on top and microscopic cavities are formed using UV lithography (Fig.3-7a,b) through a positive chrome mask. The resist pattern is then transferred into the active polymer layer by oxygen plasma etching (Fig.3-7c) thus creating multiple cavities on one single substrate. The cross-section of a single cavity is demonstrated on Fig.3-7d and microscope photographs showing various cavity shapes can be seen on Fig.3-7e. To make sure that no resist remains on top of the cavity, oxygen plasma etching is performed slightly longer, thus removing up to 50μm of active layer. By adjusting the parameters of spin-coating and plasma etching, the thickness of cavities may be controlled with the precision of ±20μm.

We have successfully fabricated cavities in both PMMA and PS-b-PAA polymers, however in the case of PS-b-PAA an unexpected problem arises during etching step. A layer of PS-b-PAA cannot be completely removed by oxygen plasma etching – a thin (30 - 40 nm) residual layer remains on the wafer surface. Probably the structure of PS-b-PAA is changed under the influence of oxygen plasma leading to the formation of a different polymer species with a very low etching rate, approximately 10-20 nm/minute compared to ≈100 nm/minute for initial PS-b-PAA layer and ≈120 nm/minute for S1805 resist. Despite the presence of the residual layer the PS-b-PAA, microlasers worked fine and we recorded the spectra of both dry cavities and cavities in the microfluidic chip.

The main disadvantage of the conventional UV lithography in the context of this work is that extreme care must be taken to keep the mask clean. Whenever it may not pose a substantial problem while creating electric conductors of $10 \div 100$ micrometers resolution, in case of photonic components any wavelength-scale defects in the structure may severely affect its performance. In our case, even minor defects on the cavity borders that originate from dust or resist remains on the mask often led to a malfunction (Fig.3-8b). Therefore the mask was carefully cleaned after each series of exposures. Depending on the soiling level we performed either immersion in a hot acetone to dissolve resist remains, either oxygen plasma treatment or mechanical cleaning with a lens cleaning tissue while immersed in acetone (to minimize scratching).

The capabilities of UV-lithography are not limited to the creation of planar “2D” cavities. By using the photoresists that upon exposure can form high aspect-ratio structures (like SU-8 epoxy-based negative photoresist) it is possible to fabricate 3-dimensional cavities like cubes, cylinders or any other 3D shapes that have vertical sidewalls and flat top with existing binary lithographic masks. With more advanced approach, by using grey-scale masks, more sophisticated shapes like hemispheres or pyramids can be fabricated; however this falls beyond the scope of present work. Fabrication and characterization of “3-dimensional” cavities will be performed in the PhD thesis of Clement Lafargue, LPQM, ENS Cachan.

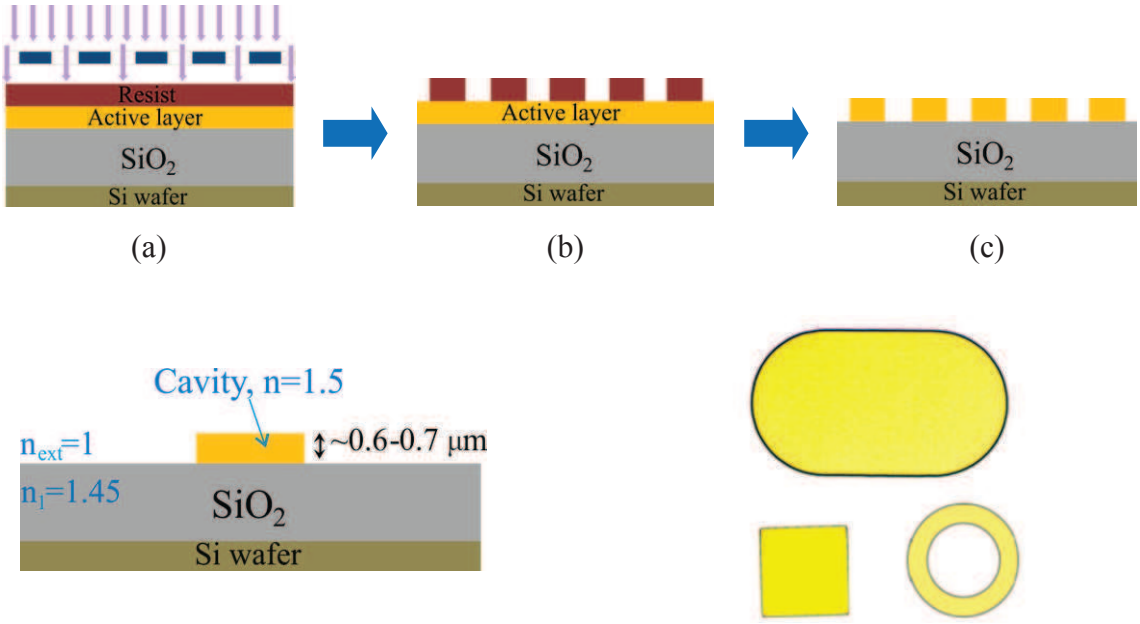

Fig.3-7. Schematic depiction of a microcavity manufacturing process. (a) Spin coating of an active polymer layer, optical resist layer and UV Lithography through a positive mask. (b) After resist development. (c) Formation of cavities by oxygen plasma etching. (d) Single laser microcavity on the substrate. (e) Photographs from an optical microscope of cavities of different shapes (real colors).

3.4.2. *E-beam lithography.*

One of the possible processes of cavity creation is fabrication by electron-beam lithography (performed by Christian Ulysse at LPN laboratory). The e-beam lithography allows achieving the highest quality of the cavity, as shown on Fig.3-8a. Due to the high resolution (of the order of 20-30 nm), cavity corners and sidewalls are highly sharp and free of defects that may degrade or completely diminish cavity performance. This is particularly important for the cavities

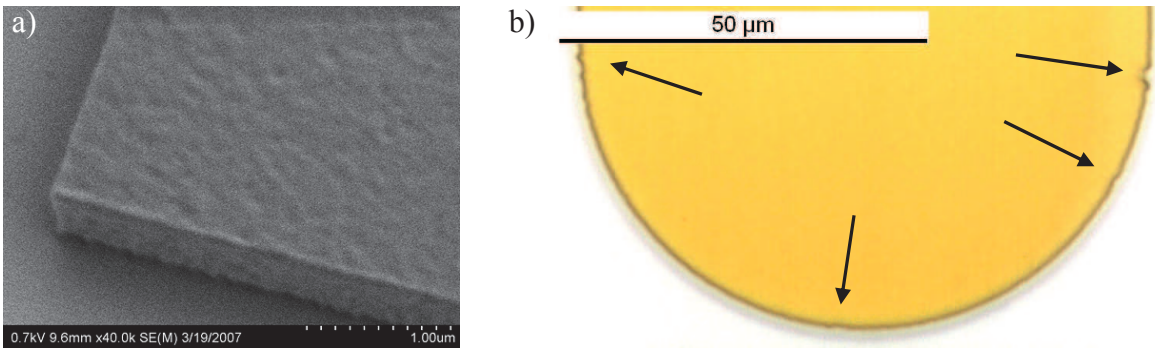

Fig.3-8. a) A scanning electron photograph of a cavity fabricated in PMMA with e-beam lithography. b) A microscope photograph of a part of PMMA cavity fabricated with UV lithography. Arrows point at occasional defects that appear due to mask soiling.

supporting whispering gallery modes, which are very sensitive to the quality of sidewalls due to the mode localization near to the rim. We have used e-beam lithography setup (Leica EBPG 5000+) for manufacturing cavities only in PMMA by directly exposing the active layer (PMMA + dye) by electron beam and subsequent development.

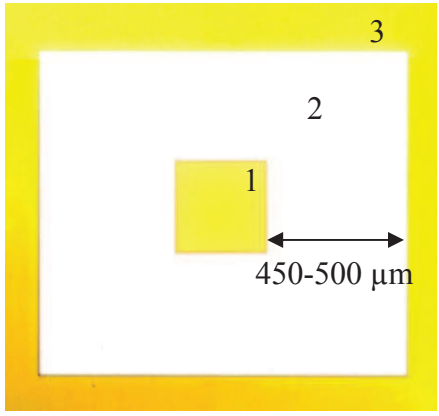

Fig.3-9. The photograph of the square cavity created by an electron-beam exposure. 1) A cavity; 2) The area exposed by electron beam and removed by developer; 3) surrounding polymer layer.

The PMMA polymer is well-known in microelectronics industry as a positive e-beam resist: the parts exposed with an electron beam become solvable in the developer. For PMMA microcavity fabrication this means that a negative mask must be prepared (area around the cavity is exposed) which leads to a very large areas that need to be exposed by electron beam and very long exposure times (up to 20 hours). The mask is designed in such a way (Fig.3-9), as to achieve a suitable compromise between the exposure time and a distance between the cavity and the surrounding polymer layer. We have chosen to surround each cavity by a free space approx. 450 ÷ 500µm wide, to ensure that the pumping laser beam will only excite the cavity and not the surrounding polymer layer. The electron-beam exposure also affects the laser dye and slightly modifies the refractive index of the doped PMMA layer along the cavity borders. Depending on the shape of cavity contour, the exposure dose varies and may be higher in some areas, for example, in the vicinity of the corners of a square. Due to the finite size of an electron-beam focal spot and presence of scattered electrons, a cavity may receive a dose of radiation which is on the one hand too low to render it soluble in the developer (so shape and dimensions are not affected) but on the other hand may be sufficient to slightly alter its refractive index. We have not investigated in details the influence of the electron beam exposure process on the material refractive index.

There exist several works, for example [113], where the SU-8 negative UV-photoresist is used as a negative e-beam resist [114]. Moreover, by varying the electron beam exposure dose across the resist layer, 3-dimensional structures and complex surface reliefs can be created with a single exposure [115, 116]. At the same time, SU-8 resist can be easily doped with various laser dyes. This approach allows thus incorporating Bragg gratings in laser microcavities within a single manufacturing step and for instance, creating distributed feedback resonators. Manufacturing of 3D cavities or reliefs was not attempted within this thesis, however this perspective pathway will be probably developed in future.

Possibility of utilization of polystyrene as an e-beam resist was demonstrated in the literature [117], however we didn't try to apply this process to the PS-b-PAA polymer.

3.4.3. *Fabrication by laser ablation and 2-photon polymerization.*

In the context of the microFLUID project it was supposed to manufacture microlaser cavities with novel approaches such as femtosecond laser ablation and/or 2-photon polymerization (2PP). The following results were obtained in cooperation with the partners at Laser Zentrum Hannover (LZH).

Laser ablation is a process of removal of a solid material by irradiating it with a focused laser beam. Ablated material heats rapidly in the focal point of a laser beam and instantly sublimates without passing through a liquid state. This process has several advantages over other structuring techniques: it is easy to automate and it doesn't involve any hazardous chemical compounds. Usually ablation is performed with pulsed lasers. For this project, LZH utilized a Newport Spectra-Physics Spitfire Pro XP Ti:Sapphire Regenerative Amplifier System (λ=800 nm, pulse duration ≈ 40 fs, repetition rate = 1 kHz).

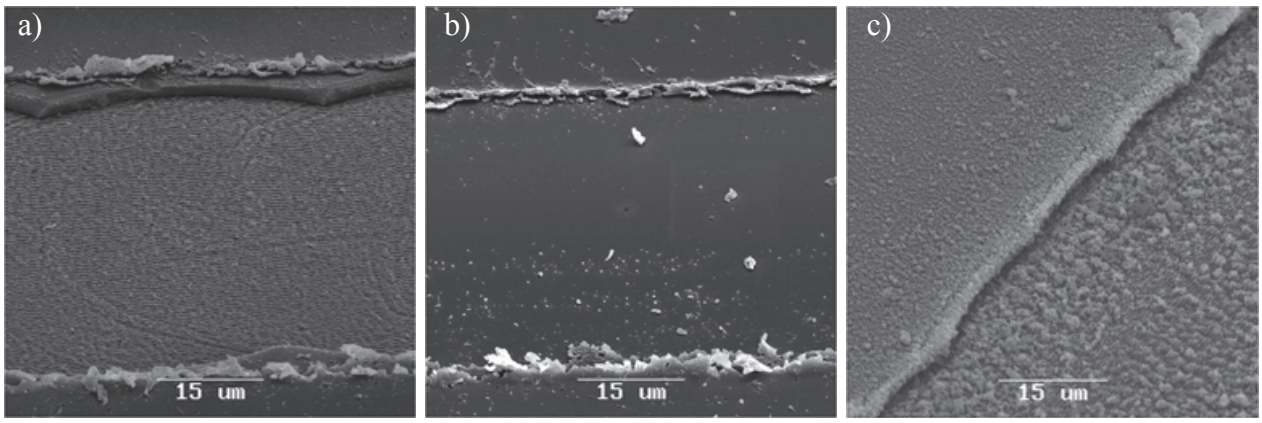

Fig.3-10. SEM images of the PMMA areas ablated with average power a) above and b, c) below ablation threshold of the Si/SiO2 substrate. Images provided by LZH.

Fabrication of microcavities by femtosecond laser ablation was reported a failure by LZH. While showing very good results for metals and plastics (on a macroscopic scale), this method is poorly compatible with organic materials when a wavelength-scale resolution (~500nm) is required. Laser ablation cannot provide the required quality of edges, producing edge roughness with feature size of more than 15 μm as seen on Fig.3-10. The surface of the substrate and the polymer layer are also contaminated by polymer nano-particles generated in the ablation process which can be clearly seen in Fig.3-10c.

Fabrication by 2-photon polymerization provides much more satisfactory results. Generally, 2-photon polymerization is a powerful technique that allows creating complex 3-dimensional structures, with the shape limited only by imagination. First attempts have been performed with a non-doped layer of negative SU8 photo-resist deposited on the Si/SiO_2 substrate. A SHG

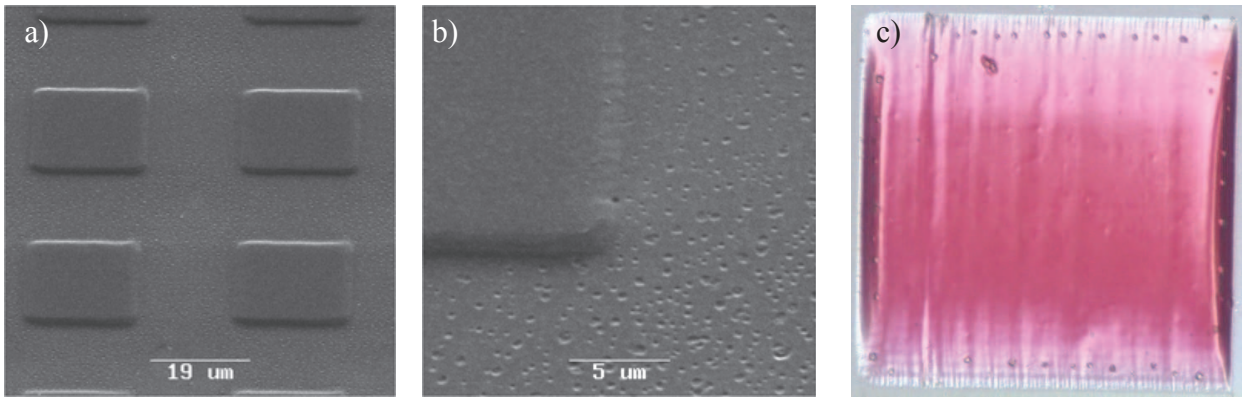

Fig.3-11. a, b) SEM images of the non-doped SU8 micro-cavities on the *Si/SiO_2* substrate *fabricated by 2PP. Images provided by LZH. c) Microscope photograph of a dye-doped cavity fabricated by 2PP in MAPTMS sol-gel material.*

Yb:Glass laser was used with λ=513nm, pulse duration = 150 – 200fs, and repetition rate of 1 MHz. The results, as shown on SEM photographs on Fig.3-11 have proven the capability of 2PP technique to achieve the desired resolution.

In LZH a reliable process of 2PP structuring have been developed for a sol-gel type of materials, like commercially available ORMOCER or methacryloxypropyltrimethoxysilane (MAPTMS, Polysciences Inc.) [118]. Cavity manufacturing was attempted in a layer of MAPTS doped with a derivative of Pyrromethene 605 synthesized at PPSM, ENS Cachan. Chemical modification of Pyrromethene was needed in order to ensure strong chemical bonding between the dye and MAPTMS molecules. When non-modified pyrromethene was used, the problems at the development stage arose: the dye was washed out from the sol-gel matrix by the developer. The first attempt of a cavity manufacturing was a success and, in spite of having an irregular shape as Fig.3-11c shows (approx. 100μm x 100μm x 7μm in the tallest part), the cavity exhibited lasing spectrum. The 2-photon polymerization approach to fabrication of microcavities shows promising results and will be developed further in the work of Clement Lafargue, LPQM.

3.5. *Alternative cavity geometry.*

In a pursuit of sensitivity enhancement and improvement of the microlaser charachteristics, we have developed and tested several microcavity configurations that may prove useful and offer one or another advantage depending on the application area.

3.5.1. *Transparent quartz substrate.*

The possibility of micro-laser fabrication on quartz (fused silica) substrates instead of SiO_2/Si wafer has been demonstrated. The manufacturing process remains exactly identical to the described above. The refractive index of the quartz plate is approx. 1.45 making it equivalent to the SiO_2/Si substrate, but with one difference: quartz plate is perfectly transparent. While this offers no obvious advantage for sensing applications at which we are aiming, it may be very useful for integrating the pump source and a laser microcavity onto one chip. A diode laser used for pumping can be mounted to the bottom of quartz substrate right under the microcavity and excite it from below, while leaving all the upper part of the chip for microfluidic circuitry and detection system. Alternatively, the cavity emission can be reflected at 90º by a micro-scale mirror and detected from below, after passing through a transparent substrate. In this configuration both excitation and detection systems can be mounted to the substrate right under the cavity thus isolating any electrical circuits from the microfluidic components.

Here, under the name “quartz” we understand fused silica substrates, fabricated from amorphous silica and therefore showing no anisotropy. The cavities can be fabricated on a plain glass substrate as well, which is less expensive than a quartz substrate, however in this case a transparent buffer layer is needed with the refractive index lower than that of the active layer, to ensure light confinement. Spin-on glass (SOG) or a polymer with a low refractive index (eg. CYTOP) can be utilized as a buffer layer.

3.5.2. *Pedestal cavities.*

We have fabricated “pedestal” cavities by utilizing a wet-etching of silica subtsrate. As it will be explained at the beginning of Chapter 5, we expect pedestal cavities supporting whispering gallery modes to be advantageous for sensing applications. Alongside with expected

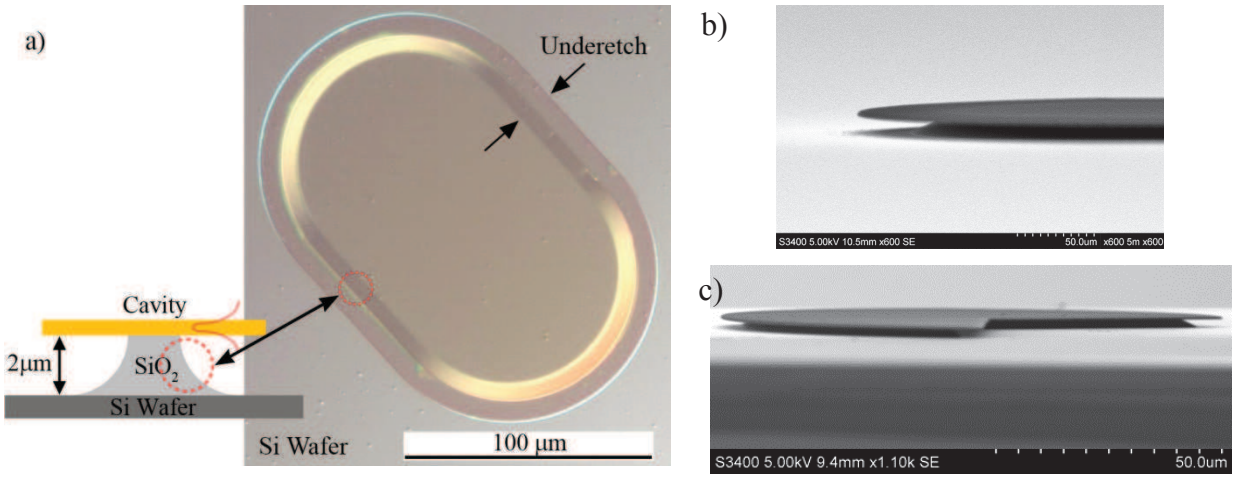

Fig.3-12. (a) Optical microscope image of a stadium-shaped micro-laser on pedestal and a schematic drawing. The underetch (approx. 10µm) and the slope of the SiO_2 pedestal are visible in the photograph. The PMMA-DCM layer is transparent. (b), (c) SEM images of different cavities after HF etching show a clearly visible under-etch.

sensitivity increase, we have discovered multiple interesting properties of pedestal microlasers as well. At the first stage, the cavities are created on a plane SiO_2/Si substrate as described above. Afterwards, to create a pedestal, the sample is immersed in a buffered hydrofluoric (HF) acid that isotropically etches the SiO_2 and subsequently rinsed in distilled water. The HF acid does not affect the doped polymer layer. Solution used for etching is VLSI Selectipur 87.5-12.5 containing ammonium fluoride (NH_4F) : HF in 87.5 : 12.5 proportion. The width of the under-etched part is monitored by the time of immersion (etching rate about 140 nm/minutes) and then measured with a duly calibrated optical microscope, benefiting from the transparency of the PMMA-DCM layer (see Fig.3-12). On the figure we see a stadium shaped cavity standing on a silica pedestal. The 2µm thick SiO_2 buffer layer is entirely removed around the cavity during the HF etching, exposing the Si wafer surface. In the underetch region (under the edge of the cavity) a silica pedestal is formed which has curved slopes as displayed on the schematic drawing on Fig.3-12a and partly seen on the SEM photographs (Fig.3-12b,c).

However the etch depth varies slightly from one cavity to another on the same sample, probably due to the lack of circulation of the etching solution in the thin under-etch region (SiO_2 thickness is 2µm). Another difficulty that arises, is air-bubbles that may be trapped in the under-etch region. If it is necessary to further etch a sample already containing pedestal cavities, one should make sure that there is no air trapped under the free-standing part upon immersion in HF. If bubbles are present, this will lead to asymmetrical pedestals and different under-etch depth for different cavities on one sample. Placing the beaker with HF etching solution in a ultrasonic bath may help to solve the problem, however for safety reasons we didn't do that and limited ourselves to accurately shaking the sample inside the beaker.

Mechanical rigidity of the PMMA layer of ≈ 600 nm thickness allows creating under-etches of up to 10µm without any issues. A deeper etch sometimes leads to a collapse of pedestal cavities, probably due to high mechanical strains created by capillary and surface tension forces of the liquid (etching solution and water) as it goes under, and pours out of the under-etch region. We have performed an attempt to manufacture free-standing Fabry-Perot cavities, however we found this impossible to achieve by a wet-etching process due to the aforementioned reasons.

After creating a pedestal, another oxygen plasma etching step may be used to adjust the thickness of the cavity and to obtain cavities of the order of or thinner that the cutoff thickness for the cavity on a plane SiO_2 substrate (≈300nm). This order of operations is preferable as wet-etching the thinner and therefore more fragile cavities may easily collapse them. The advantage of thinner cavities for sensing will be explained in paragraph 4.4.1.

3.5.3. *Low-index substrate cavities. Pillar cavities.*

We have successfully fabricated laser microcavities on a low-index, transparent polymer buffer layer. On the one hand, the transparent buffer layer may be indispensable if cavities are to be fabricated on a transparent glass substrate, when detection or excitation is performed through the substrate. On the other hand, the CYTOP polymer used as buffer has refractive index lower than that of the silica, therefore we expect it to have positive influence on the lasing properties of our cavities. Higher refractive index contrast means better mode confinement in the active layer and lower losses. Moreover, as it will become clear from Chapter 5, cavities on CYTOP pillars may be advantageous for sensing applications.

The fabrication process of the cavities on a low-index polymer substrate is generally similar but includes few additional steps. As a buffer layer we have used a CYTOP CTX-809A polymer (Asahi Glass Co. Ltd.) that belongs to the class of fluoropolymers [119, 120]. A 2µm thick layer of CYTOP is spin-coated on a commercial Si substrate (or on glass), baked for 2 hours at 180ºC and slowly cooled down to a room temperature. The measured refractive index of the layer was n ≈ 1.34 (ellipsometry performed by Nguyen Chi Thanh, LPQM). After baking, CYTOP forms a highly hydrophobic, transparent coating resistant to majority of organic solvents. In order to make PMMA (or any other polymer) adhesion possible, a CYTOP surface was activated by a

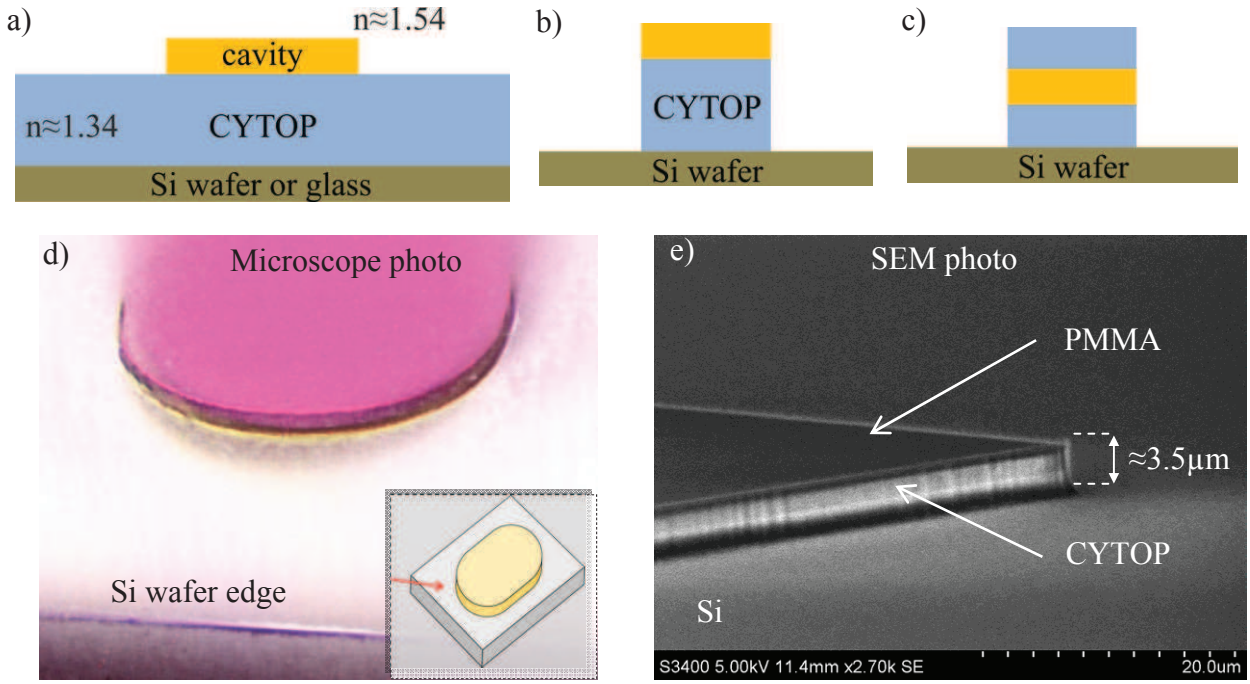

Fig.3-13. a) A schematic image of a polymer microcavity on a low-index CYTOP substrate. Inset shows the angle at which the cavity is photographed. b,c) Schematic depiction of correspondingly asymmetric and symmetric cavity on a CYTOP pillar. d,e) Microscope and SEM photographs of a working cavity on a CYTOP pillar (total thickness approx. 3.5µm).

short exposure to oxygen plasma. Immediately after, a dye-doped PMMA layer was spin-coated, and processed as was described above. The etching rate of CYTOP in the oxygen plasma (bias 300V, 50W RF power, 5mT O_2 pressure) is approx. 380nm/min which is substantially higher than for PMMA (≈180nm/min) and S1818 resist (≈120nm/min). It is difficult to precisely control the etching (which is a complex process and the rate may vary, in general, nonlinearly with time) to stop at exactly the right moment, so a PMMA cavity is always standing on a little CYTOP pillar as displayed on a scheme on Fig.3-13a.

While advantageous for various reasons (see Chapter 5.6) these cavities are not very well suited for sensing: a microfluidic chip cannot be attached to the CYTOP layer; a clean Si wafer surface would be preferable. A logical continuation of this process was the creation of CYTOP pillars (Fig.3-13b,d,e). By slightly increasing the resist thickness and oxygen plasma etching time, it is possible to entirely remove the CYTOP substrate and create a cavity on top of the pillar. Due to the big difference in etching rates, pillar height can be varied to a great extent and made as high as 7-10μm, which may be required by the lab-on-a-chip architecture.

Generally, utilization of a low-index polymer substrate layer enables us to easily create microlaser cavities on virtually any surface, where a smooth layer can be spin-coated. Thus all-polymer devices can easily be created by conventional lithographic techniques, if we replace quartz or silicon substrates by a plastic with a thin layer of low-index polymer spin-coated on top. Moreover, symmetrical cavities that have no cutoff thickness can be easily constructed, if another layer of CYTOP is spin-coated on the doped PMMA layer (Fig.3-13c).

3.5.4. *All-polymer pedestal cavities.*

As a further development of pillar cavity technology, we have attempted to combine the advantages of a pedestal and a low-index substrate and to create a cavity on a low-index CYTOP pedestal. This process is possible due to the fact that solvents that dissolve fluoropolymers are often chemically inert to other organic compounds making it possible to selectively dissolve the CYTOP substrate without affecting the cavity. We have used Perfluorodecalin (chemical formula: $C_{10}F_{18}$) purchased from Sigma-Aldrich as a solvent, which is a flammable but relatively non-toxic compound, much safer in handling than HF acid. It should be noted also that a wide range of fluorinated solvents are currently available on the market: 3M Fluorinert liquid, perfluoro(methyldecalin), perfluorokerosene, perfluoroheptane and its isomers and combinations [121, 122]. The choice of solvent is therefore not limited to perfluorodecalin and determined by the availability of one or another compound.

The process of CYTOP dissolution is substantially different from the oxide etching by HF. When immersed in acid, SiO_2 is completely dissolved with no residues remaining, however when CYTOP is immersed in the solvent, a combination of dissolution and lift-off processes occurs. Depending on the molecular weight, the CYTOP layer can be a very stable solid that will not entirely dissolve but will decompose in tiny fragments and peel off the surface.

First we have measured the dissolution/lift-off rate by immersing a spin-coated layer of CYTOP into perfluorodecalin and measuring the layer thickness before and after immersion. The layer was rinsed with distilled water immediately after solvent immersion. The etch rate was found to be ≈125nm/min, however a large number of tiny peeled of fragments were found on the layer surface after the rinse. Perfluorodecalin is an oily substance and is not easily washed away by water. So the alternative to the water rinse was to dip a sample for a few seconds in a pure

perfluorodecalin, not contaminated with peeled off particles, and to immediately dry it on a hot plate. Such approach allowed us to obtain a smooth layer, almost free of peeled fragments.

To create pedestals we immersed a sample with CYTOP pillar cavities in perfluorodecalin for 30 min, dipped for a few seconds in a pure perfluorodecalin and baked on the hot plate at 95ºC for 60 min, to ensure that all the solvent has completely evaporated. As expected, a CYTOP pillar was partially etched resulting in a pedestal cavities, as shown on Fig.3-14a, with an under-etch of approx. 2.7 µm. To facilitate the circulation of the solvent in the under-etch region and removal of peeled off fragments we tried to sonicate the solvent during etching. However most of the cavities were either entirely removed from the wafer, together with CYTOP pillars, or moved from their initial positions (Fig.3-14b). This can be explained either by insufficient adhesion between the CYTOP and a Si substrate so that sonication detaches the pillar or by diffusion of the solvent inside the whole volume of CYTOP pillars thus softening them. However, most probably, both effects take place. We can also see from the SEM images (Fig.3-14c,d) that the CYTOP pedestal is "inversed" with respect to the silica one: narrower at its base and thicker in the upper part. This may be due to a stronger adhesion of CYTOP to the upper PMMA layer and easier detachment from Si substrate.

The swelling of CYTOP after immersion in perfluorodecalin was not studied here, and we didn't verify whether the refractive index of the CYTOP layer after immersion in solvent and

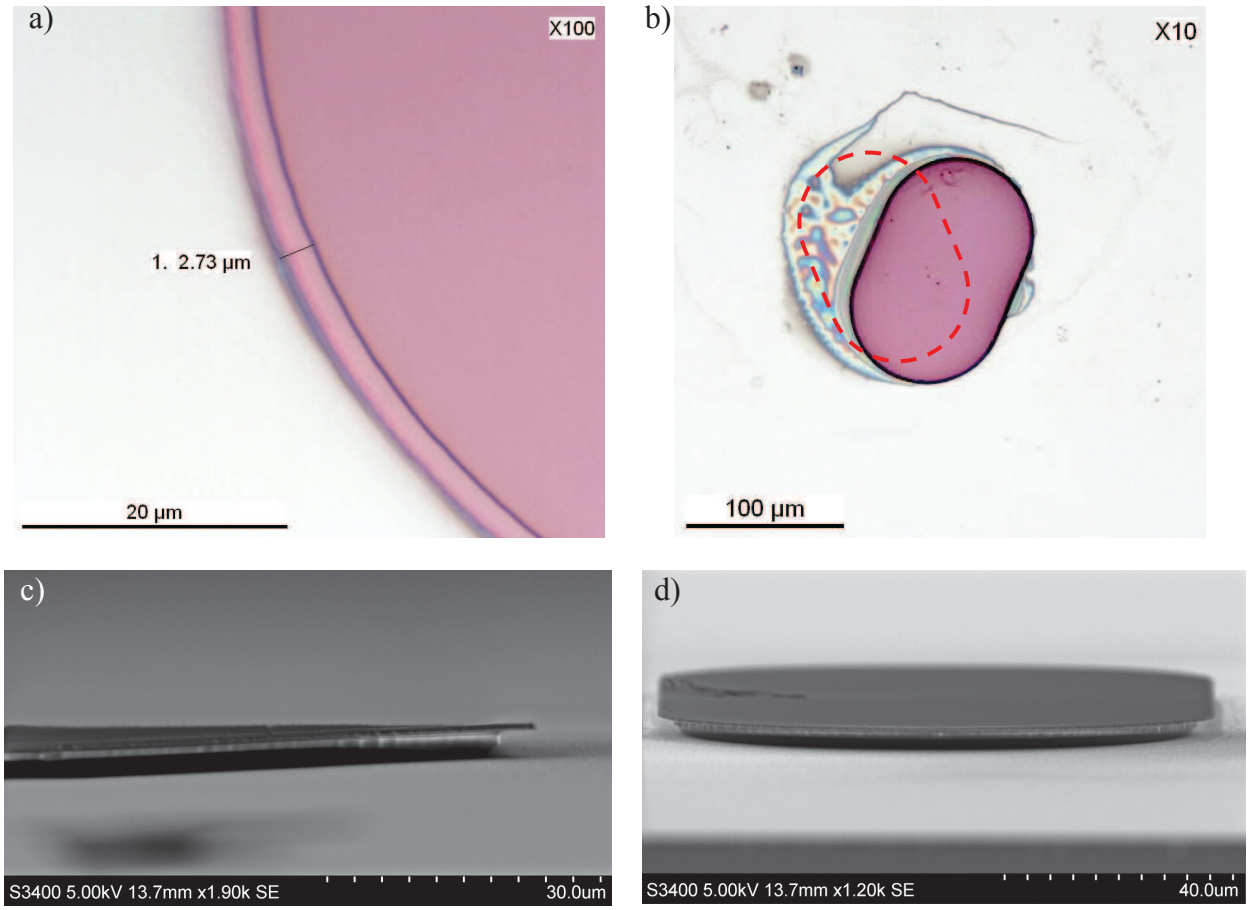

Fig.3-14. a) A microscope photograph of a pyrromethene doped PMMA cavity on a CYTOP pedestal. The under-etch of ≈2.7µm is clearly observed. b) Displacement of the pedestal cavity from its original position (dashed outline) due to sonication during etching. c, d) SEM images of the PMMA cavities on CYTOP pedestals.

drying remains the same as the index of a newly spin-coated layer. We have demonstrated the possibility of creating fully organic pedestal cavities, but the process still needs to be optimized.

Chapter IV

Microlaser as a refractive index sensor

Introduction

In this chapter I will describe how a microcavity laser transforms into a sensor that is capable to detect changes of the refractive index (RI) of the surrounding medium and, after certain modification, various chemical and biological species in liquids. Sensing becomes possible due to high sensitivity of the resonant frequencies of the microcavity to the refractive index of the cavity material and the surrounding. At the beginning of the chapter, the principle of RI change detection will be explained. Afterwards, the design of the microfluidic chip that brings analyte in contact with the cavity and the issue of selective and specific detection of various compounds will be discussed (§§ 4.2, 4.3). Cavity functionalization with specific ligands is utilized to achieve this goal. Sensitivity of the cavity spectrum to the external influence largely depends on the cavity shape and the optimal choice should be made for sensor development. The factors that influence the sensitivity will be studied and explained in § 4.4. The proof of sensing principle and sensitivity tests will be described in paragraphs 4.5 and 4.6. Afterwards we will discuss the possible ways of sensitivity improvement.

4.1. *Principle of refractive index change detection.*

The general aim of the work is to create a sensor based on a laser microcavity for the detection of heavy metal pollutants in drinking water. The principle that we implemented is based on the influence of the refractive index change of the medium surrounding the cavity on the lasing properties. The high quality factor of such microcavities leads to very narrow resonances, which are expected to shift by a small amount when the refractive index of the resonator surrounding changes.

Generally, we may mark out two possible applications of microcavities as sensors. The first one is the refractive index variation sensing with non-functionalized cavities. In this case it is desirable to achieve the maximum possible spectral shift in response to the variation of index of the surrounding medium. The second one is the detection of analyte molecules with functionalized cavities. In this case, it would be preferable to observe spectral shift only when the analyte molecules are bound by specific ligands. In the ideal case, the spectral shift should be observed only when the analyte molecules are bound by specific ligands and cavity spectrum should not be sensitive to the refractive index of the liquid carrying the molecules that we want to detect. However, the sensitivity to the analyte molecules is usually interconnected with the sensitivity to the bulk refractive index variation; therefore a reference should be carefully chosen in the sensing experiments, to avoid erroneous interpretation of the spectral shift, which may occur due to the index variation of the analyte solution and not due to the capture of analyte molecules.

The typical emission spectrum of an organic micro-laser, which is a comb of almost equally spaced peaks, is shown on Fig.4-1a. On Fig.4-1b, an individual spectral peak is depicted schematically, explaining the key principle of detection. As the refractive index of the environment in the vicinity of a cavity raises when the analyte molecules are bound to the surface, the evanescent wave of the cavity mode feels this change. The effective refractive index of the mode increases which is reflected as a red-shift of the cavity lasing spectrum. The spectral shift of the peak can be presented as a function of the refractive index change as $\delta\lambda = f(\Delta n)$. Therefore, the sensor can be calibrated by precise quantification of the spectral shift thus allowing for concentration measurements.

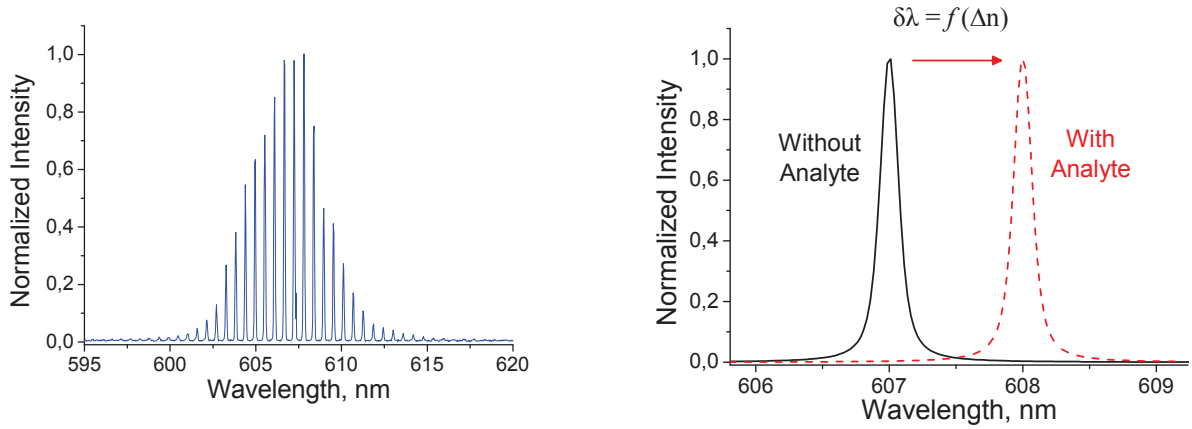

(a) (b)

Fig.4-1. (a) Typical experimental lasing spectrum of an active microcavity and (b) schematical explanation of chemical sensing based on a peak wavelength shift.

In this work, the wavelength shift was measured directly using a high-resolution spectrometer, as will be described later. However, every detection system has a finite resolution and the wavelength shift can only be measured with a certain precision, which introduces rounding errors and may be a limiting factor in sensing experiments. In the case of our experimental setup, one pixel on the spectrum corresponds to ≈0.03 nm on a wavelength scale, therefore imposing a limit on the spectral shift that can be measured. On the other side, the measured shift value will be a multiple of 0.03 nm and a rounding error occurs, if the real peak position is in between two recorded values. To minimize the effect of a rounding error, we can observe the spectral shift of several peaks of the comb (or all of them) and take an arithmetic mean as a shift value. For example, if after a binding event two spectral peaks out of three watched seem to remain at their initial position, however the third one has shifted for 0.03 nm, it means that the spectral shift was present in this experiment, however it was inferior to 0.03 nm. The arithmetic mean of ≈0.01nm would not be a precise and correct value; however it prevents one from drawing a wrong conclusion that there was no shift at all.

We can also think of resolution enhancement techniques, for example employing a vernier scale [123]. This approach is easy to understand with the help of illustration Fig.4-2a. The equidistant lasing spectrum (solid line) is passed through a filter with a comb-like transmission function (dash line), but a free spectral range tailored to be larger than the intermodal distance in a lasing spectrum. Initially, peak *n* of a lasing spectrum coincides with the transmission peak of a filter, and therefore emission is detected at a wavelength of, for example, 606 nm. When a shift occurs in a laser spectrum, the peak *n* moves out of the transmission line, however the lasing peak *n+5* now coincides with the next transmission peak of the filter and emission is now detected at 611.5nm. As a result the small and hard to detect spectral shift in a lasing spectrum may be amplified and converted to a several times larger shift due to the vernier scale effect.

If we think of miniaturization and integration of the sensor on a LOC, such bulky and expensive components as a spectrometer do not fit well in the scheme. It is much more advantageous both in terms of size and cost to perform measurements of intensity. A microlaser emission intensity may change as a result of analyte binding, and therefore registered by a photodiode, either by recording the total emission intensity (integrating over the whole spectrum), either by picking out and observing a single spectral peak. In our experiments we

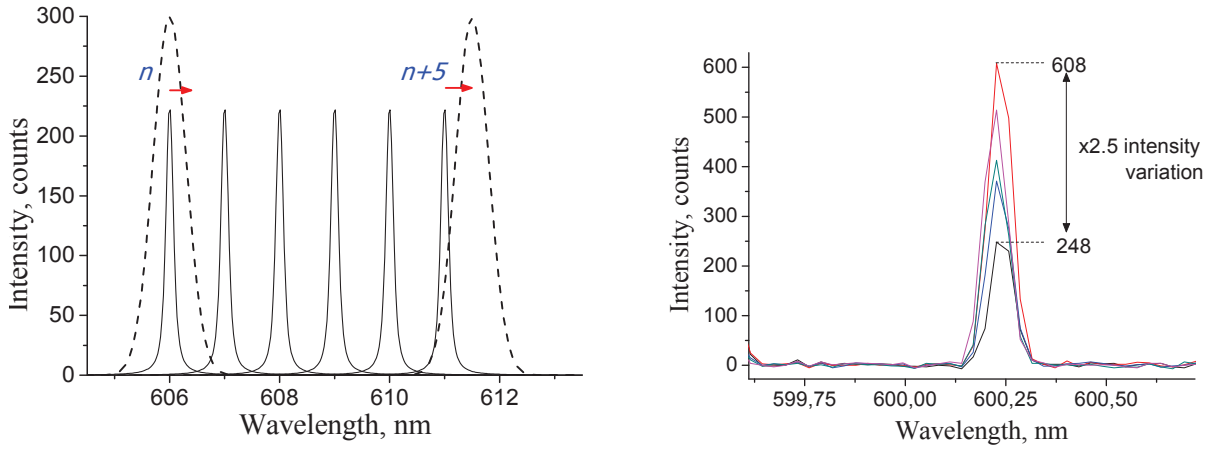

(a) (b)

Fig.4-2. a) An illustration demonstrating the vernier scale principle in spectral shift detection b) Intensity variation of the same peak within a series of spectra

couldn't determine any dependency in the intensity change as a result of analyte binding or refractive index change, therefore this approach was not applicable in our particular case (Fig.4-2b).

Other, indirect ways of measurement of wavelength shift are also possible, which should be advantageous for a miniature lab-on-a-chip (LOC) system. The wavelength shift can be converted into the change of intensity if we employ a filtering scheme that will isolate one single peak out of the lasing spectrum, or if a single-mode microlaser will be employed. Then, if the photodetector records laser emission intensity at the wavelength of this peak, any shift in the peak maximum will be detected with high precision as a change of emission intensity, assuming that the peak is narrow.

Alternatively, other configurations can be thought of, in which the intensity change is measured. If the direction of microlaser emission maximum depends on the refractive index of the medium, which is true for stadium-shaped cavities (as we will see later), then the change of emission direction can be recorded as a variation of intensity by a photodiode that collects laser emission at a certain narrow angle. One more possible mode of detection system functioning is the "binary" on/off action of the microlaser under certain conditions. In a case, when a lasing periodic orbit in a cavity becomes deconfined when the index of the surrounding medium bypasses a certain threshold value, the lasing spectrum will abruptly change. This change will be measured by a photodiode as either a jump in intensity or total absence of emission, depending on the cavity lasing orbit.

While the direct measurement of the spectral shift by a spectrometer was accomplished in this thesis as the simplest to implement for laboratory tests of micro-laser based detectors, the more sophisticated, integrable and compact detection schemes may be realized in future work on microcavity sensors.

4.2. *Designing a microfluidic chip.*

In order to transform a microcavity laser into a detection system, it must be somehow brought in contact with the analyte solution. The simplest solution that can be thought of is simply placing the drop of the analyte solution on top of the cavity. This approach, which is not

applicable for the integrated detection system, may seem sufficient for the intermediate experiments. However, the drop of liquid placed on the cavity acts as a lens both for the excitation beam and for the laser emission of the cavity itself, uncontrollably changing the conditions of experiment, deflecting the emission and rendering the results irreproducible.

Therefore, one of the priority tasks of the project is the integration of microcavities and possibly other photonic components into the microfluidic networks to address the sensing application. The ability to adequately manipulate fluids is essential for a LOC system. This can range from simple flow-through systems that require little interference from an operating device, to complex networks containing active elements for the control of movement of one or several drops of fluid.

Current task of heavy metals detection implies that the microfluidic chip must fulfill the following criteria: 1) it must ensure effective delivery/evacuation of analyte to/from the cavity surface; 2) it should allow easy pumping of the microlaser cavity and 3) microlaser emission spectra must be easily registered. Therefore a work has been performed in order to find a microfluidic network design that fulfills all the stated criteria.

The scheme of the microfluidic chip that was designed, made of Polydimethylsiloxane (PDMS) by molding technique is presented on Fig.4-6a,b with caption indicating liquid inlet and outlet channels. PDMS is a silicon-based organic polymer, used in a wide range of domains, from medicine to food industry and is a most common material for fabrication of microfluidic chips [124-127]. It is optically clear ($n \approx 1.41 \div 1.43$), and in general, is considered to be inert, non-toxic and non-flammable. For microfluidic chip fabrication it is supplied as a two-component kit: a liquid PDMS prepolymer and a cross-linking agent. Once mixed in appropriate proportions, cross-linking process starts under room temperature and PDMS cures to a hard rubbery state. Thanks to its properties, it is a perfect material for molding: a silicon wafer or a glass plate can be used as a mold on which a relief pattern of microfluidic channels is created. The liquid prepolymer is then poured into the mold and left to polymerize. When removed from the mold, even the smallest relief details are left imprinted in the PDMS slab.

For our microfluidic chip fabrication we purchased a two-part kit from Dow Corning: a pourable liquid SYLGARD 184 Silicone Elastomer (PDMS) and a curing agent. Polymerization of liquid PDMS is achieved by mixing the two components in a 10:1 ratio by volume. Once mixed, the cross-linking reaction starts and proceeds slowly: the cross-linking at a room temperature completes in 48hours. We fabricated a mold from a layer of SU-8 2025 photoresist (~25µm thick) spin-coated on a Si wafer and patterned by UV-lithography (Fig.4-3a). Prior to

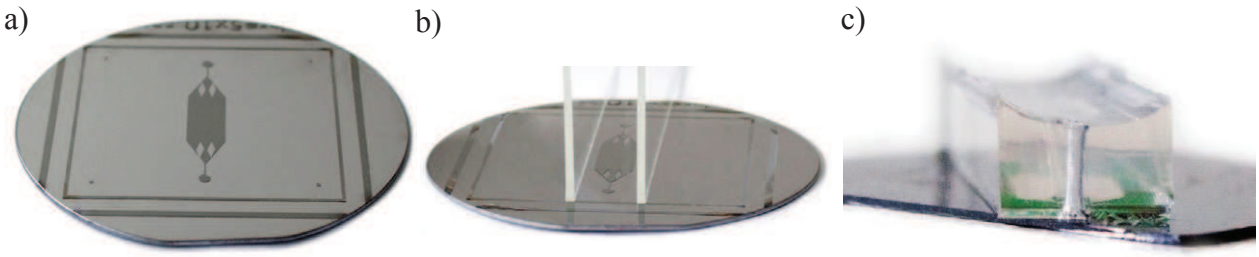

Fig.4-3. Explanation of the PDMS chip manufacturing process: a) A mold fabricated in SU-8 photoresist on Si wafer; b) A mold with two vertical glass plates fixed on it; c) A finished PDMS chip bonded to a wafer, showing a concave upper surface.

pouring the liquid PDMS prepolymer, the mold was treated by the vapor of HMDS (Hexamethyldisilazane), which silanizes the surface thus rendering it hydrophobic and facilitates PDMS detachment from the mold. The mold is placed in a closed container with a beaker of liquid HMDS inside for approximately 30 minutes. The volatile HMDS liquid evaporates inside the container and forms a very thin layer on the mold surface that is sufficient to prevent PDMS from sticking to the mold. To accelerate the polymerization process, heat treatment is applied that drastically increases cross-linking rate: we baked the mold with liquid PDMS inside the oven at 75ºC for 120min, which was sufficient for polymerization reaction to complete. During the process, the mold is rigidly fixed in a home-made Teflon holder that prevents liquid PDMS from leaking.

Afterwards, the ready-made chip – a polymerized PDMS slab with imprinted channels – is carefully detached from the mold. The needed parts of the slab can be easily cut out with a scalpel or a razor blade. The holes are cut through the slab using a thin metal tube with a sharpened section edge. The holes will be used later to connect flexible inlet and outlet pipes. The surfaces of the chip are protected from dust and soiling with a scotch tape (3M) up to the moment of attachment to the wafer.

The chip can be sealed to a clean, smooth glass or SiO_2 plate or silicon surface. The surface of a cured PDMS is hydrophobic, therefore oxygen plasma oxidation is used to activate the surface by disrupting surface bonds and creating SiOH groups. After the treatment, the PDMS is placed on a wafer with the activated side (the side with imprinted channels) down and once the bonds relax to their normal state, the slab is permanently sealed to the surface, thus creating a waterproof channel with inlet and outlet connectors. Oxidized PDMS surface remains stable in air, for a time largely sufficient to attach the slab to a wafer and, after a certain time hydrophobic recovery of the surface is inevitable, independently of the surrounding medium.

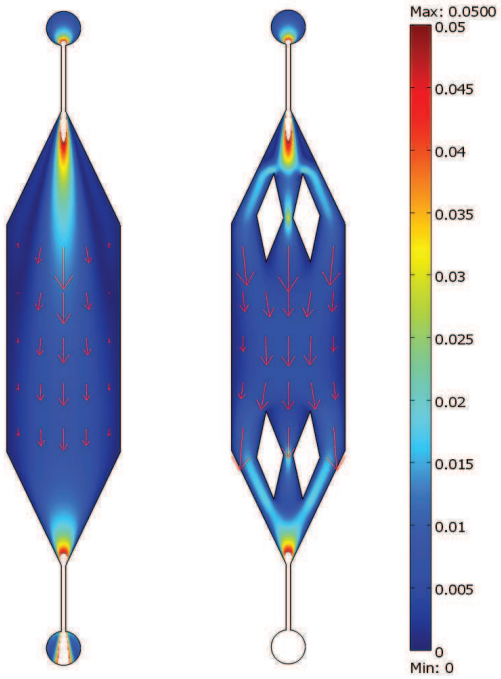

Fig.4-4. Numerical modelisation of the flow in a microfluidic chamber. Color code: flow velocity in m/s. Red arrow lengths is proportional to the flow velocity in a given area.

One of the tasks that needed to be solved is the effective circulation of the analyte solution inside the microfluidic chamber to ensure that the entire surface of the cavity is exposed to the analyte. After numerical modelisation (COMSOL Multiphysics) of the liquid flow inside the chamber, we came up with the solution to introduce rhombus-shaped mixers inside the chamber as displayed on Fig.4-4 (results obtained and presented in the thesis of Wu Ting, PPSM). Without the mixers the flow tends to concentrate in the central part of the chamber, whenever the sides are not sufficiently accessed by liquid. Introduction of mixers in front of the inlet channel leads to more uniform distribution of the analyte solution throughout the chamber at the flow velocity of 0.007 m/s and homogenizes the flow velocity distribution across the chamber.

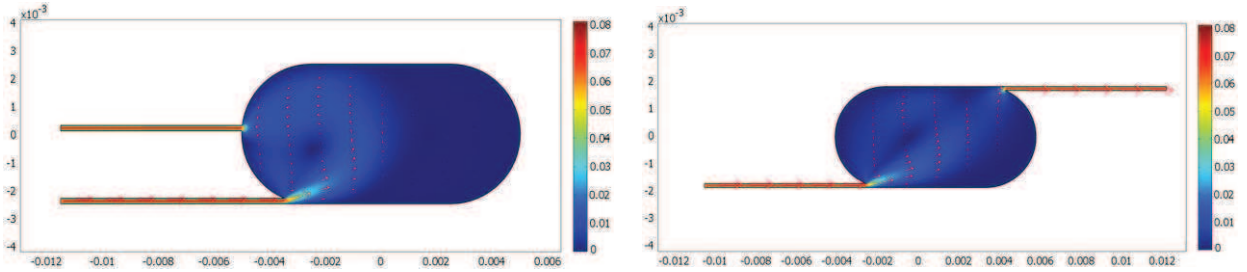

Fig.4-5. Numerical simulation results for liquid flow velocity distribution (m/s, shown in color) in stadium-shaped microfluidic chamber for 2 different configurations of inlet/outlet channels. Red arrow lengths is proportional to the flow velocity in a given area.

We have also investigated an alternative approach to achieve efficient liquid circulation and wetting the cavities in a microfluidic chamber without utilization of the mixers but just by modifying the shape of the chamber. Numerical simulations using COMSOL Multiphysics have been performed for the case of stadium-shaped chambers. The stadium-shaped billiard is known to be a chaotic system. It is thus an archetypal research object in quantum chaos physics. By analogy, we wanted to estimate the behavior of stadium-shaped chamber in microfluidics network. Results of simulations are presented on Fig.4-5. The figures show flow velocity distribution inside the chamber in meters/s with red color corresponding to the fastest and blue – to the slowest flow velocity. Several configurations of inlet/outlet channels have been considered. However, simulations proved that effective liquid circulation is achieved only at inlet flow velocity of about 0.055 m/s which is about ten times larger than in currently used system with mixers. Therefore the chamber design with rhombus-shaped mixers inside was preferred as simpler and ensuring the desired result.

In order to observe cavity's optical response the sidewalls of the PDMS chip must be highly flat and transparent to allow light to escape the chip and minimize losses due to light refraction and scattering on surface roughnesses. If the PDMS slab is cut with a scalpel after curing, the resulting side surfaces are rough and diffusing (Fig.4-6c), making it virtually impossible to observe microcavity emission through the chip. Such fabrication is appropriate if the emission is recorded through the transparent top side of the PDMS chip or through the bottom supporting glass plate. In our configuration, when emission is collected sideways, the recorded ASE intensity was more than 200 times lower than for the same sample without the PDMS chip.

Several ways of solving the issue were considered: we tried carefully cutting the PDMS with a thin razor blade, which didn't bring positive results as the edge remained diffusive; we considered modifying the mold by attaching two polished wafer pieces. However the simplest way to achieve highly transparent sidewalls was chosen. As it is shown on Fig.4-3b two parallel glass plates were fixed vertically on the mold during PDMS chip manufacturing. The contact of the liquid PDMS with the smooth glass surface ensures the necessary quality of the chip sidewalls after solidification (Fig.4-6c). We also exposed glass plates to HMDS vapor, however polymerized chip is easily detached from the plates even without this precaution. The Teflon mold holder, mentioned above (and not shown on the photographs), also serves to rigidly fix the glass plates.

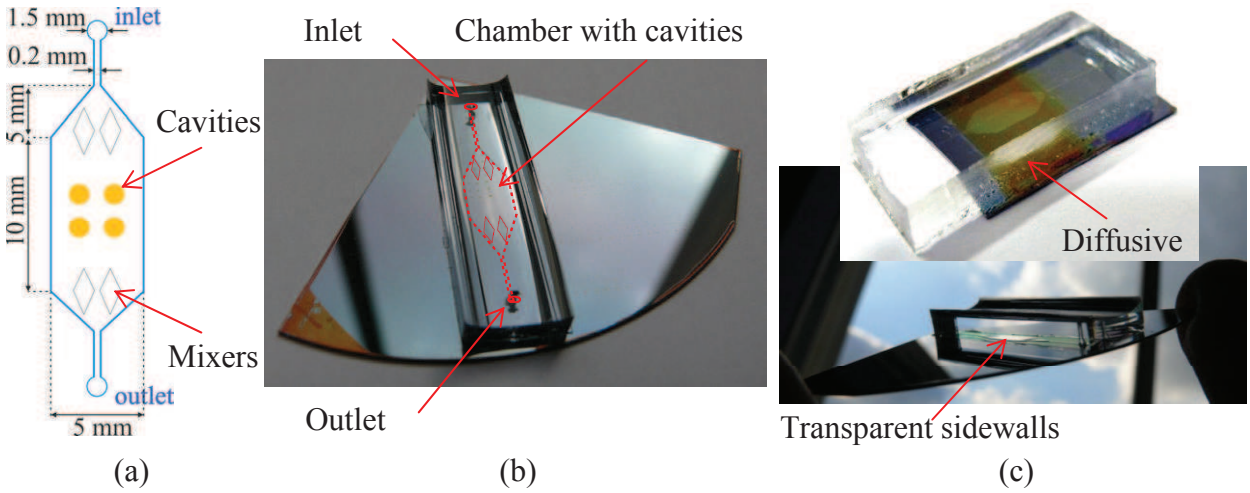

Fig.4-6. (a) A scheme of the microfluidic channel with microcavities inside it (view from the top). (b) Photograph of the working microfluidic sensor prototype: a molded PDMS cap with a microfluidic channel placed on top of the SiO_2/Si substrate with microlaser cavities on it. (c) Photograph demonstrating the transparent sidewalls of the final PDMS chip (bottom) in comparison with the diffusive sides of the first chip designs (top).

The drawback of this fabrication approach that immediately becomes obvious is that the top surface of the PDMS chip has a curved shape instead of being flat. The PDMS in its liquid phase, contained within two glass plates forms a concave meniscus, which we see in the chip after polymerization (Fig.4-3c). If the microcavity pumping is performed from the top, as it is realized in our experimental setup, the meniscus will play the role of a lens, deflecting the pump laser beam and complicating the alignment of the pump with the cavity. The simplest improvement to solve this issue would be to fix the third glass plate in a horizontal position, in between the two vertical ones, so that the liquid PDMS touches it when poured on the mold and doesn't form a concave meniscus. This would somewhat complicate the microfluidic chip production, however facilitating the beam alignment. We worked with the concave PDMS chips, as the alignment problem is not a crucial one at this stage and did not influence the measurement precision.

The second source of inaccuracy comes from the positioning of the two glass plates: they are neither ideally parallel nor ideally vertical (perpendicular to the mold). These features are transferred into a PDMS chip leading to deflection of the cavity emission that passes through the sidewalls, both in vertical and horizontal planes. A mold with precisely aligned holders for glass plates needs to be manufactured to avoid described defects; however the degree of influence of these inaccuracies was acceptable and didn't pose any significant problems in current experiments.

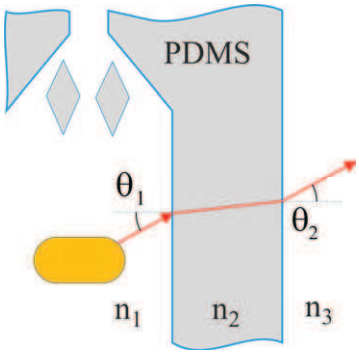

Fig.4-7. Schematic view of a cavity inside the microfluidic channel illustrating the case when cavity emission direction is not perpendicular to the PDMS wall.

Finally, the third difficulty comes from the fact, that the PDMS wall should be preferably perpendicular to the direction of maximum emission of the cavity. The situation is illustrated on Fig.4-7: if the cavity is in the air (n_1=1), refraction of cavity emission (red line) on two

PDMS interfaces ($n_2 \approx 1.43$ at 610nm [128]) will compensate each other ($\theta_2 = \theta_1$) and microfluidic chip will not change the angle at which the emission is observed in the far field. Once water is injected inside the microfluidic chip (n_1=1.33) refraction is no longer compensated and PDMS chip will deflect the cavity emission at a certain angle. For small incidence angles $\theta_1 \leq 5°$ the output angle is roughly equal to $\theta_2 \approx n_1 * \theta_1$ ($\theta_2 \approx 6.7°$ for $\theta_1 = 5°$). For larger values of θ_1 the angular emission maxima in the far field may be significantly displaced and needs to be found experimentally each time before performing measurements, therefore it is preferable to keep θ_1 minimal. For this purpose we have marked the orientation of the cavities on the wafer and then manually, by sight, aligned the PDMS chip prior to attaching it to the wafer, in order to have the θ_1 as small as possible. The alignment by sight produced an error in θ_1 of ±3º. In case when we needed to place cavities of various shape that emit at different angles on the same sample (Fabry-Perot and stadiums), all the cavities were positioned on the lithographic mask in a way to emit in the same direction.

The photos of the working microfluidic sensor prototype that was used in experiments are shown on the Fig.4-6b,c. The photographs show the microfluidic PDMS chip with transparent top and sidewalls, attached to the SiO_2/Si wafer with cavities on it. Such device prototype fully satisfied our needs and requirements.

4.3. *Sensing selectivity: specific ligand grafting.*

In the previous section we talked about refractive index variation detection with a non-functionalized laser microcavity. Now we will talk about the functionalization of cavities with specific ligands for selective detection of analyte molecules. First of all we will describe the functionalization attempts of the porous polystyrene based polymers. Then, the surface functionalization of PMMA will be described and the choice of functionalization pathway will be grounded. The estimation of refractive index change upon analyte binding to the ligands will be discussed.

If one wants to utilize the cavity for the detection of different species dissolved in liquid, they must be brought and accumulated in the immediate vicinity of the cavity surface. The presence of the analyte molecules bound to the cavity surface will modify the refractive index on the surface, which will influence the cavity mode and therefore induce shifts in the lasing spectrum. This can be achieved by either coating the cavity with suitable ligands that bind the molecules of interest or by making the cavity from a species-selective material such as a molecularly-imprinted polymer. The specificity of the cavity response will depend on the utilized ligands. Therefore once the laser spectrum detection system has been implemented, development of a cavity-based sensor becomes as well a “chemical” problem. The ligands must be synthesized that on the one hand can be easily grafted on the cavity surface with a large coverage ratio, and on the other hand ensure specific binding of the species of interest. Moreover, if the sensor is designed as reusable, the binding of the species to the ligands must be reversible. There should be developed a cleaning procedure that will quickly de-complex all the bound molecules from the ligands without damaging them and the cavity material. The same applies in the case when a cavity is fabricated directly from a species-selective material.

For the current project of heavy-metal ion sensing in drinking water, a series of specific ligands was synthesized at the PPSM laboratory of ENS Cachan. Those ligands are capable of

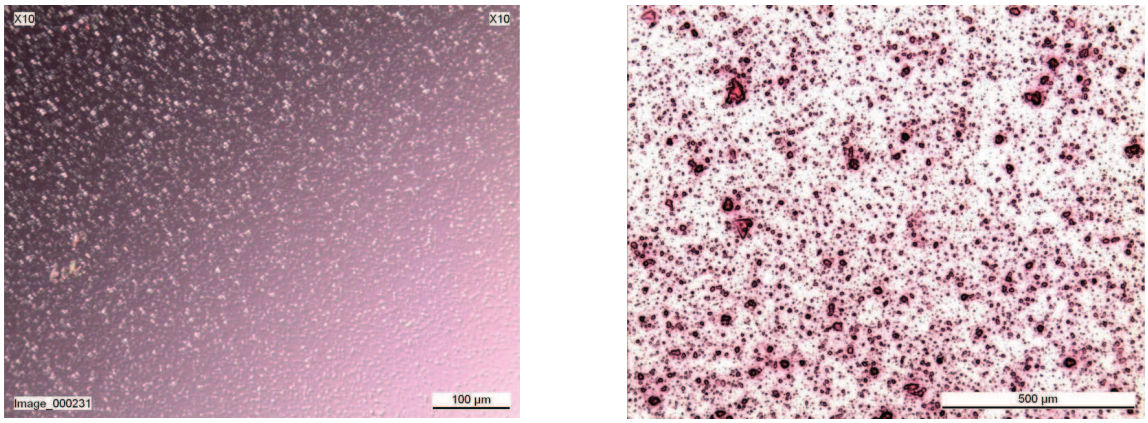

(a) (b)

Fig.4-8. Optical microscope photographs of spin-coated layers of a) PS-b-PAA with Pb^{2+} ligand (10% in weight); b) PS-b-PAA + Pyr 2% with Hg^{2+} ligand;

selectively binding Hg^{2+}, Pb^{2+} and Cd^{2+} ions in water [129-131] and releasing them after a proper treatment procedure.

Initially the work was focused on the porous polymers, described in the previous chapter (PS-b-PAA, PS-Co-PAA). It was expected that ligands will be introduced directly in the polymer solution prior to cavity manufacturing and therefore will be present in the whole cavity volume which should lead to a higher sensitivity. However, certain technological difficulties arose that forced us change the initial plans and switch to the surface functionalization of the non-porous PMMA cavities. While we have succeeded in fabrication of a layer of pure PS-b-PAA polymer, addition of the Hg^{2+} or Pb^{2+} ligands, 10% in weight, to the solution changed the solubility of polymer and led to strong aggregation. The problem lies in reticulation of the polymer: ligand molecules possess numerous bonds and may attach to several polymer molecules at a time thus creating a strongly interconnected network. In the case when a lead ligand was added (Fig.4-8a), aggregates <5µm size were observed in the spin-coated layer which makes it unsuitable for cavity fabrication. When a mercury ligand was introduced (Fig.4-8b), polymer was strongly agglomerated and spin-coating resulted in 5 ÷ 50 µm large clots spread over the wafer surface. In order to solve this problem, ligand molecules must be modified appropriately to avoid reticulation, which shifts the problem from the technological to the chemical domain. Therefore, after numerous attempts the decision has been taken to focus on surface functionalization of PMMA cavities.

Grafting the ligands on the non-porous PMMA cavity surface requires several additional steps in fabrication process. Ligands cannot be attached directly to the PMMA surface and therefore the surface needs to be modified. We considered two approaches: performing a short O_2-plasma treatment or depositing a thin auxiliary layer on top of the cavity. Plasma treatement creates free –OH groups on the surface of PMMA that form bonds with ligand molecules. It would be a simpler and faster solution that eliminates additional deposition/etching steps. However performed experiments, presented below, have shown lower efficiency of this approach. Therefore the auxiliary layer approach was accepted for further work. We have used a thin layer of PHEMA (polyhydroxyethylmethacrylate) deposited on the cavity as an auxiliary material. PHEMA is a polymer with a structure similar to that of PMMA, which however contains hydroxyl groups on the surface that are used for ligand grafting. Several ways were considered for depositing a layer, namely spin-coating and dip-coating.

We have found dip-coating to be the fastest and the most convenient approach, that allows to quickly obtain a layer with a good control of thickness. First of all, a finished sample with laser microcavities undergoes a short 20 seconds O_2-plasma treatment (Harrick PDC-002 plasma cleaner) to make PMMA surface more hydrophilic and to increase adhesion (30W RF power, 300 mT O_2 pressure). This step noticeably increases the smoothness and uniformity of deposited layer. In the test samples of PMMA spin-coated on a glass plate, O_2 plasma treatment let us reduce the surface roughness from almost 100nm (Fig.4-9d) to $7 \div 20$ nm (Fig.4-9e). The treatment was verified not to have any detectable influence on the cavity performance. Afterwards, a layer of PHEMA (0.5wt% solution in methanol) is dip-coated on top of the cavities, and the sample is dried in ambient conditions for 2 hours. Dip-coating parameters (40 mm/min dip; 5 mm/min pull-out) are adjusted in a way to obtain approximately 20nm thick PHEMA layer on top of PMMA cavity, as measured by profilometer (Dektak). Ellipsometry measurements confirmed that dip-coated PHEMA layer has a thickness of the order of $10 \div 25$ nm depending on the sample, and a refractive index of approximately 1.338. The layer is transparent and thus doesn't attenuate the cavity emission nor interferes with the excitation laser beam. It is visible in the optical microscope as a minor roughness on the surface of the cavity and the wafer (see Fig.4-9a,b). However on the cavities that are located closer to the edges of the wafer, significant accumulation of dried PHEMA polymer was observed (Fig.4-9c). Those dried PHEMA drops can be 100 – 150 nm in thickness, but despite their presence, we were still able to record a strong emission spectrum of the cavities. Once the cavity surface is prepared, one can proceed with ligand grafting. We have chosen to do the grafting immediately inside the

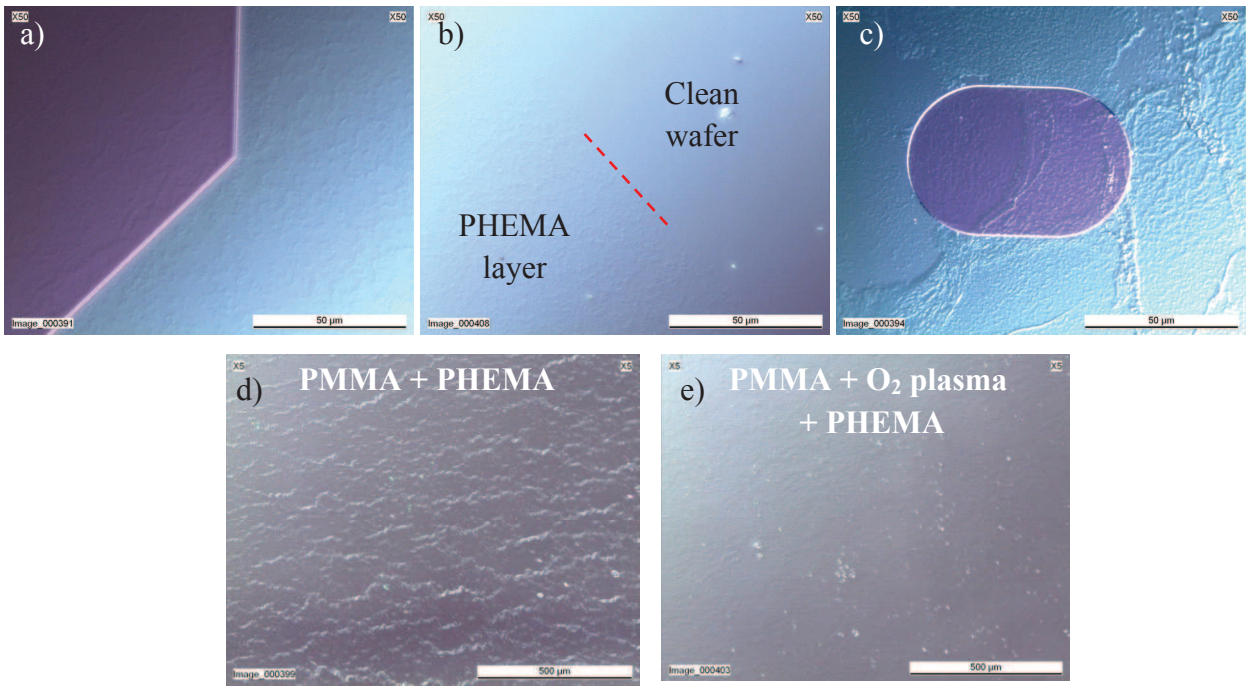

Fig.4-9. Optical microscope photographs of the dip-coated PHEMA layer on the PMMA + Pyrromethene cavities. a) Thin transparent PHEMA layer is seen as roughness on the cavity and wafer surfaces. b) The border between the PHEMA layer and a clean wafer surface after oxygen plasma etch. c) Dried accumulations of PHEMA on the cavities located close to the wafer edge. d) Dip-coated PHEMA on top of untreated PMMA layer (on glass substrate) demonstrating significant roughness. e) Dip-coated PHEMA on top of O_2-plasma treated PMMA layer.

microfluidic chip, by flowing the appropriate reagents through which is advantageous for several reasons. First of all, the quantity of reagents needed is significantly smaller as only the cavities of interest are exposed to solution. If not, the whole wafer should be immersed in the ligand solution. The second important point is that the ligand molecules may be damaged by the oxygen plasma treatment during attachment of PDMS microfluidic chip. We didn't test, whether plasma treatment affects the ligands, but proceeded immediately with the safer approach and grafted the ligands at the last step.

At this stage we have functionalized the cavities with thiol groups that are known to selectively bind mercury [132, 133]. We used a commercially available organosilane 3-MPTS (3-mercaptopropyltrimethoxysilane) as a source of thiol groups [134]. The preference was given for a commercial material due to a large number of tests that needed to be performed before the functionalization procedure and sensing experiment protocol were optimized. Synthesis of our own ligands for testing purposes is unjustified due to a high cost and large quantities needed for tests. The functionalization was performed as follows: pure 3-MPTS was injected in the microfluidic channel with the help of a syringe pump and left inside for 30 minutes; after channel is rinsed with water to remove the excess of unbound material and dried with nitrogen. Procedure is repeated 3 times.

We have performed AFM microscopy observation of the PMMA layers on glass substrate (without PDMS cover), functionalized with different approaches (Fig.4-11). The spin-coated PMMA layer represents a smooth surface with a minor nanometer-scale roughness. After O_2-plasma oxidation, we observe the increase of surface roughness (~8nm) and the picture changes slightly after grafting the thiol ligands. After PHEMA layer is deposited, we observe a significantly rougher surface (~40nm) that clearly evidences PHEMA presence. When thiol is grafted on PMMA/PHEMA layer, we observe even higher surface unevenness (up to 100nm). However these observations don't lead to any quantitative conclusions about the ligand presence on the polymer surface.

The presence of the thin PHEMA layer on the wafer surface around the cavities makes it impossible to attach a microfluidic chip, therefore all the unneeded PHEMA must be removed first. The PDMS sticks well to a clean surface, like glass or silica but the presence of any organic contamination prevents it from attaching. To clean the surface, the cavities that will be used in sensing experiment are selected and protected by a hard mask (covered by a small piece of wafer), and the sample undergoes another short-term oxygen plasma exposure in the Reactive ion etching machine (bias 300V, 50W RF power, 5mT O_2 pressure), that removes the unprotected PHEMA layer, leaving a clean wafer surface (Fig.4-9b). Afterwards, a microfluidic chip is attached to the wafer (as explained in § 4.2) and the cavity functionalization is performed inside the microfluidic channel (Fig.4-10a).

To quantitatively compare the efficiency of different functionalization pathways, thiol ligands were grafted on the surface of non-doped PMMA surfaces through both O_2-plasma treatment and PHEMA layer approaches. Afterwards ligands were labeled with 5-IAF fluorescein derivative (5-Iodoacetamidofluorescein) and grafting efficiency was evaluated by recording the fluorescence spectra (Fig.4-10b). The labeling was performed as follows: 4 mM/L 5-IAF solution in Na_2HPO_4 buffer (0.1M/L, pH=9.1) is injected in the microfluidic channel and left for 30 minutes; after channel is rinsed with water and dried with nitrogen. Procedure is

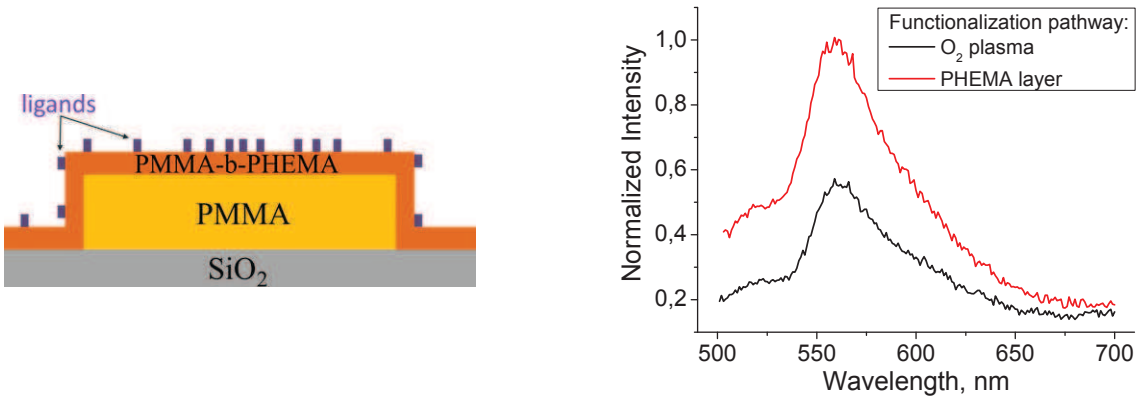

(a) (b)

Fig.4-10. a) Schematic view of a PMMA microcavity covered with a PHEMA layer (thickness ≈ 20nm) with ligands grafted on top. Scale not respected. b) Fluorescence spectra demonstrating higher ligand coverage in PHEMA-intermediated grafting process.

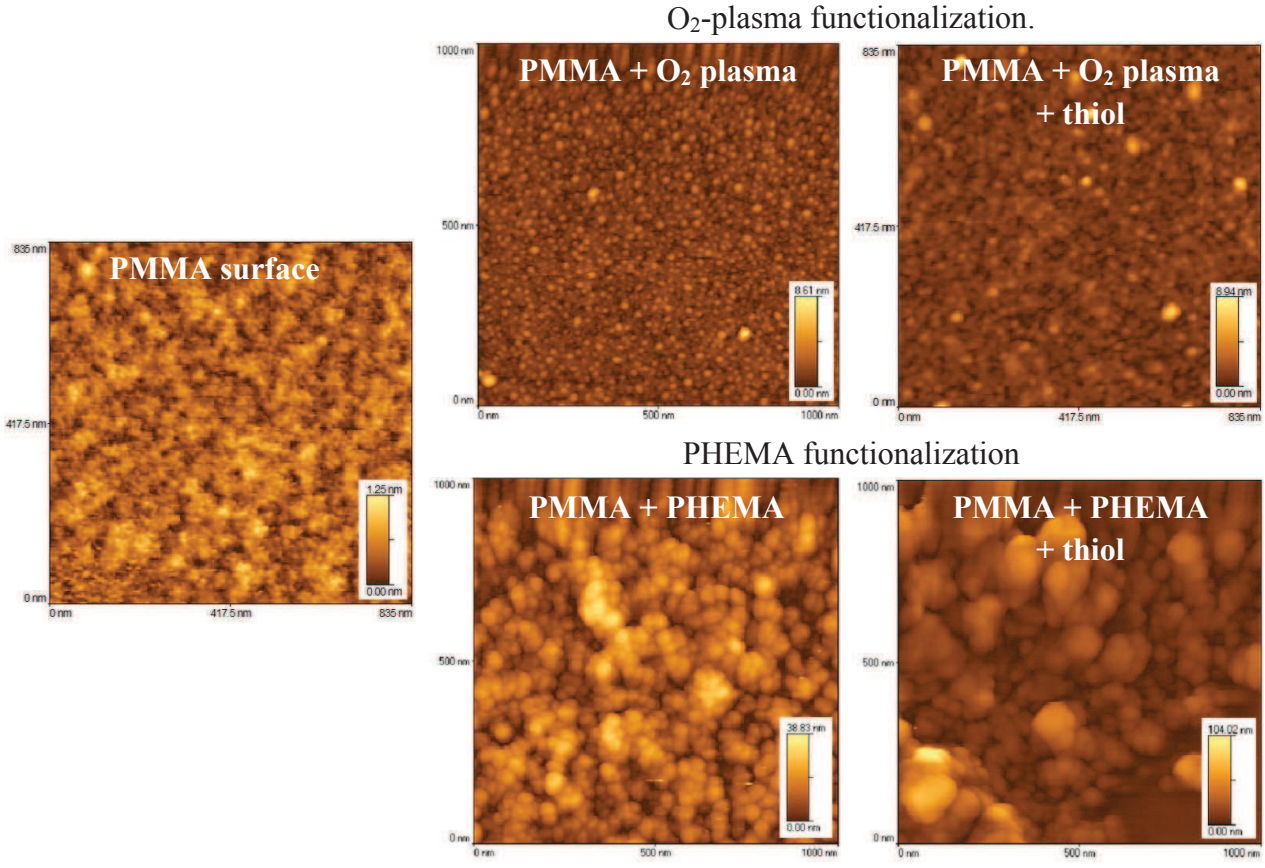

Fig.4-11. AFM images of the PMMA layers functionalized via O_2-plasma and PHEMA layer approaches.

repeated 3 times. Recorded spectra have revealed a stronger and more reproducible signal from the PMMA functionalized with the help of intermediate PHEMA layer, which evidences a higher number of ligand molecules on the surface. By recording corresponding fluorescence spectra, we made sure that fluorescein is grafted solely on the layer functionalized with thiol ligands, and not on the wafer surface or the walls of PDMS microfluidic chip.

Estimation of the coverage ratio of PMMA surface by thiol groups is a very difficult task. We didn't perform a detailed study of this question, but only verified the presence/absence of the grafted ligands on the surface with the help of fluorescence measurements, as mentioned above. The grafting of ligands, described above, as well as estimation of grafting efficiency for different processes was performed by our colleagues from PPSM laboratory. More details can be found in the thesis by Djibril Faye, PPSM.

We have attempted to estimate the order of refractive index change that occurs when mercury ions are bound by the ligands on the functionalized PMMA surface with the help of ellipsometry measurements. For this purpose we immobilized mercury ligands on a layer of PMMA polymer without a dye, immersed a sample in a concentrated 0.1M Hg^{2+} solution for 2 hours, washed the layer with water to remove any unbound mercury remaining on the surface and dried it. The doping of the layer with a dye significantly complicates the measurement and makes the result less precise: presence of the dye introduces absorption peaks in the measured dependencies and complicates fitting process. Therefore the polymer layers should be preferably undoped. We performed ellipsometry measurements of the refractive index of the polymer layer before and after immersion. However for correct interpretation of ellipsometry data, a uniform layer of the material must be present on the surface. According to the AFM and IR-spectroscopy measurements, in case of PMMA functionalization, Hg ligands do not form a uniform layer on the PHEMA layer, but are scattered on the surface with a low coverage ratio (~ 10 ÷15 %). Therefore we tried considering PHEMA + Hg^{2+} ligand as a single "effective" layer when interpreting ellipsometric measurement data. The measurement of PMMA – PHEMA – Hg^{2+} ligand stack before immersion gave the value of refractive index ~ 1.414 units and thickness ~ 40nm for the PHEMA + Hg^{2+} ligand layer. After the immersion, the index and thickness values were approximately 1.440 units and 50 nm. This is a very subtle difference that lies within the error range for such kind of measurements, taking into account inhomogeneity of the ligand layer. Therefore ellipsometric measurements couldn't provide us with any consistent conclusion about the refractive index change introduced by mercury ions absorption.

In this section we discussed different cavity functionalization pathways. Difficulties while functionalizing the porous PS-b-PAA polymer were encountered hence the surface functionalization of PMMA cavities was chosen for cavity fabrication. Two functionalization approaches (via oxygen plasma treatment and auxiliary PHEMA layer were studied and comparison of ligand grafting efficiency demonstrated the advantage of the PHEMA approach. Cavity functionalization process is described in details. The ellipsometry measurements of the refractive index variation upon mercury binding to functionalized PMMA surface did not yield reliable results.

4.4. *Sensing and various cavity shapes. Choice of the optimal shape.*

Once we have chosen the material for the cavity fabrication and constructed the microfluidic chip, we should understand which cavity geometry is best suited for sensing applications. In this

section, we will talk about the requirements that a microlaser should satisfy to be used as a sensor. A simple theoretical explanation of the cavity sensitivity to refractive index variation will be given in section 4.4.1 that allows predicting the expected spectral shift for the cavities of different shapes (Fabry-Perot, polygons). Numerical simulation will be employed to verify the model and to analyze the chaotic stadium-shaped cavities, where analytical solution is impossible. Afterwards in section 4.4.2, basing on the theoretical model and numerical simulation, we will chose the optimal cavity shape to be used in a sensor.

4.4.1. *Factors influencing sensitivity to refractive index variation.*

As we have already seen in the previous chapters, various microlaser shapes can be easily fabricated, each having its own emission features and characteristics. To better understand which cavity shape one should use for the sensing application, we will investigate the factors that influence the microlaser spectra. The medium surrounding the cavity may influence the lasing spectra by two different mechanisms:

- First of all, the thin cavity layer (in case of PMMA, $n_{bulk} \approx 1.54$) is surrounded by claddings with different refractive indexes (SiO_2 substrate, n = 1.45; air, n = 1). The wave confined and propagating in the cavity is described in terms of an effective refractive index that depends on the index of the active polymer layer, buffer layer and upper cladding (air). Once the index of the surrounding medium (upper cladding) changes, the cavity mode will inevitably feel this change. And this influence will be more pronounced, if the mode is partially deconfined, i.e. there exists a significant evanescent wave tail in the upper cladding layer.

  The term "effective refractive index" (also called modal index) can lead to confusion at this point. It is easy to believe, that effective index is some kind of an average between the indices of a guiding layer and the claddings, with the contributions depending on the mode energy localization. Though in many cases this intuitive logic seems to work, such interpretation would be wrong. Effective refractive index of the mode may differ substantially for the modes having very similar spatial localization.

- The second factor affecting the spectra is the phase incursion. As wave propagating in the cavity reflects at the cavity/surrounding medium interface it acquires a phase incursion ($\Delta\phi$) which will influences the spectrum.

From the resonance condition which states that the round trip distance L of the wave in the cavity, must be equal to an integer number of wavelengths λ

$$\frac{2\pi}{\lambda} nL + N \cdot \phi = 2\pi m \tag{4-1}$$

where n is the refractive index of the cavity material, N – number of reflections experienced by the wave along the roundtrip, ϕ – phase change upon one reflection. One can deduce the following relation for the wavelength shift, assuming that phase change and effective refractive index change influence the spectrum independently:

$$\Delta\lambda = \frac{\lambda^2}{2\pi}\frac{N}{nL}\Delta\phi\Big|_{\Delta n_{eff}=0} + \frac{\lambda}{n}\Delta n_{eff}\Big|_{\Delta\phi=0} \tag{4-2}$$

Let us consider these two factors in more details, and obtain a quantitative estimate of the cavity response. First of all, we will study the case when the phase of the wave doesn't change along the roundtrip inside the cavity: $\Delta\phi=0$. Then according to (4-2) spectral shift will only depend on the variation of effective refractive index. We will use the following formula derived in [34] to calculate the effective refractive index of a microcavity mode:

$$\frac{2\pi h}{\lambda}\sqrt{n^2-n_{eff}^2} = Arctg(\eta_1\frac{\sqrt{n_{eff}^2-n_e^2}}{\sqrt{n^2-n_{eff}^2}}) + Arctg(\eta_2\frac{\sqrt{n_{eff}^2-n_2^2}}{\sqrt{n^2-n_{eff}^2}}) + \pi\cdot l \qquad (4\text{-}3)$$

Here, $\eta_1=\frac{n^2}{n_e^2}$, $\eta_2=\frac{n^2}{n_2^2}$ for TM polarization and $\eta_1=\eta_2=1$ for TE polarization; n – is the index of the cavity material (1.54 for DCM-doped PMMA), n_e – index of the surrounding medium (whose variation we want to detect), n_2 – index of the buffer layer (1.45 for SiO_2), h - thickness of the cavity and λ - a free-space wavelength. On Fig.4-12b we plot the family of curves $n_{eff}=f(h/\lambda)$ for the constant indices n, n_2 and values of $l=0\ldots4$. The curves are limited below by the index of the SiO_2 cladding and above by the index of the doped PMMA polymer. The dependence of the effective index on the cavity thickness becomes clear: there exists a minimal cutoff thickness value, below which effective index is a complex number and light guiding in the cavity medium is no longer possible. For the average emission wavelength of our cavities λ=600nm, the cutoff thicknesses for TM and TE modes are $h_{\min}^{TM}=208\,nm$ and $h_{\min}^{TE}=255\,nm$. If we increase the thickness, vertical modes start to appear, that correspond to l=1,2…: $h_{\min,\,l=1}^{TM}=796\,nm$, $h_{\min,\,l=1}^{TE}=843\,nm$ and so on. Therefore, the cavity thickness should lie within the range thickness $260\text{ nm} < h < 800\text{ nm}$ for the cavity to be single-mode in vertical direction. In the case if the substrate and upper cladding indices are equal ($n_e=n_2$), there is no cutoff thickness and at least one vertical mode always exists in the layer. This fact can be exploited to create thin symmetric cavities (in a sense that $n_e=n_2$), not limited by the cutoff thickness, where a cavity mode would be less confined and therefore interact more with the surrounding medium. It should be noted also, that the calculation (4-3) is performed and valid only in the case of infinitely wide and thick dielectric layers (Fig.4-12a). In a real cavity, where a

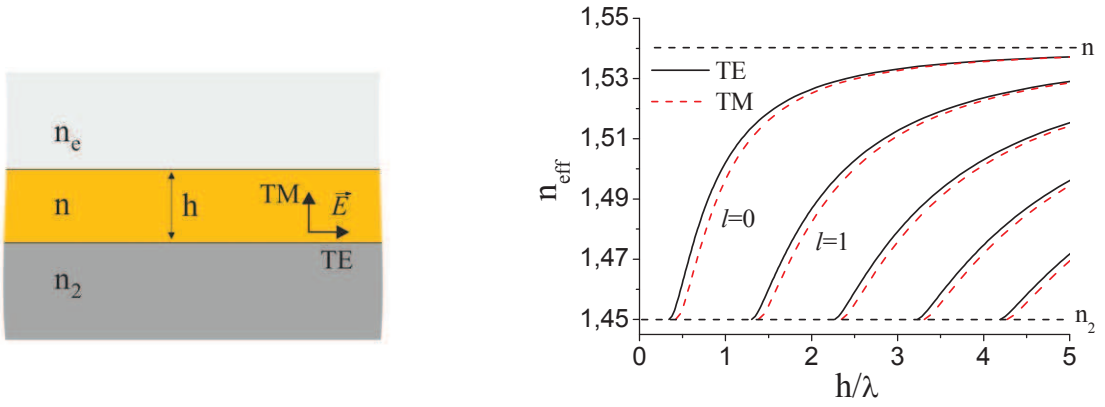

Fig.4-12. a) Effective refractive index model for infinite dielectric layers. b) Effective refractive index of a guiding layer as a function of h/λ for constant substrate indices.

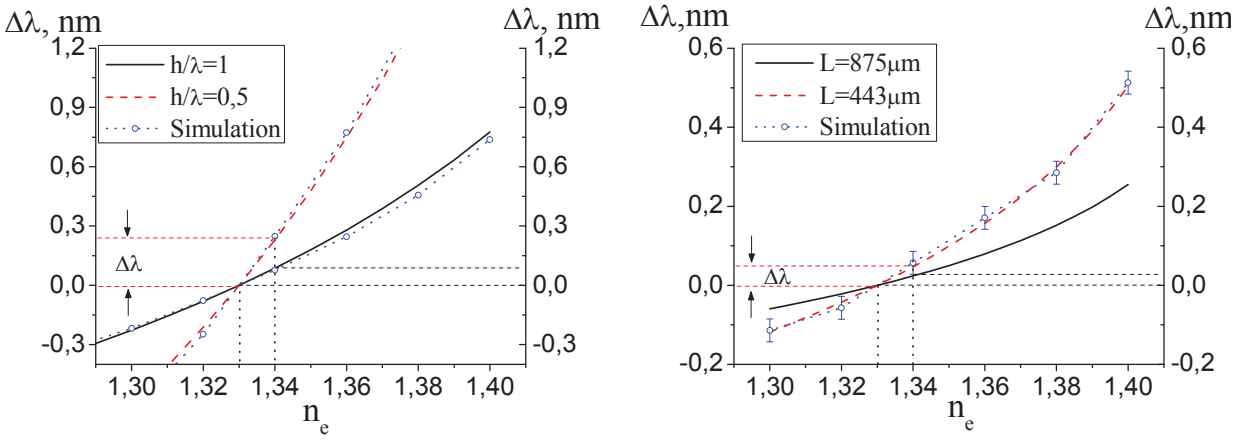

Fig.4-13. a) Calculated influence of the medium index variation (n_e) on the cavity spectral shift due to a) effective refractive index change; b) phase incursion in an octagonal cavity. Numerical simulation (FDTD) data displayed with dotted lines.

guiding layer is limited in lateral dimensions, the effective index felt by the mode near the cavity edge would be different from the one predicted by Eq. (4-3). It is difficult to precisely calculate the effective index value in this case and taking into account that the lateral dimensions of the cavity are much larger than the wavelength (typical cavity size ~ 100 - 200μm), we would assume effective index to be constant all along the cavity.

To get a clear understanding of how the index of the external medium influences the effective refractive index of the cavity mode and therefore the spectral shift, we will plot the $\Delta\lambda = f(n_e)$ dependence on Fig.4-13a from the Eq. (4-4) for the TE mode and two different h/λ ratios. The ordinate axes on Fig.4-13 represents wavelength shift $\Delta\lambda$ while $n_e = 1.33$ (index of water) is chosen to be the reference zero point. Therefore $\Delta\lambda$ is positive for the indices higher than that of water and negative for the lower ones. As the scale of the ordinate axes are different on the graphs, the $\Delta\lambda$ values from the right graph on Fig.4-13 should be divided by two to be visually compared with the left graph.

$$\Delta\lambda\big|_{\Delta\phi=0} = \frac{\lambda}{n}\Delta n_{eff} = \frac{\lambda}{n}\frac{\partial n_{eff}}{\partial n_e}\Delta n_e \qquad (4\text{-}4)$$

The TE mode is chosen as according to experimental data, emission of our microlasers is mostly TE-polarized, except some special cases which will be mentioned separately. Variation of the effective index $\frac{\partial n_{eff}}{\partial n_e}$ was calculated numerically from (4-3) with n=1.54, n_2=1.45, h/λ=1; 0.5 and l=0. A standard cavity configuration used in experiments is h/λ=1, the thickness being equal or slightly larger than the emission wavelength. It becomes immediately evident, that the influence on the spectral shift is larger, the thinner the cavity is, which is natural as the cavity mode is less confined in the latter case. Though this dependence is non-linear, the range of indices that we are interested in is rather narrow. The cavities are supposed to function as sensors in aqueous environment, therefore the medium index variation range is $1.33 < n_e < 1.35$ and we may assume with a high degree of precision that the response is linear in this domain. An estimate gives that for the change of the medium refractive index of $\Delta n_e = 0.001$ the expected spectral shift should be $\Delta\lambda$=0.01nm, which cannot be resolved with our spectral setup.

The most obvious way to improve the sensitivity would be to decrease the h/λ ratio: according to the plot, a ratio of 0.5 would increase the sensitivity more than 2 times. However from the practical experience we know that lower h/λ value are difficult to achieve. The thinner the cavity is, the smaller is the gain and the stronger is the coupling of the cavity mode to the substrate layer due to weak refractive index contrast. Therefore higher pumping energies are needed to achieve lasing which in turn leads to the fast bleaching of the laser dye and consequently decrease of emission intensity. In our experiments, we didn't detect any laser emission for the cavities on the plane substrate with the thicknesses lower than ~ 400 ÷ 450 nm ($h/\lambda \sim 0.7$). One of the ways to overcome this difficulty would be to use substrates with lower refractive indices for cavity fabrication, thus decreasing the substrate losses, lasing thresholds and making the cavity more sensitive to the change in n_e. This approach would be studied in Chapter 5 of this thesis. But if the materials and thickness remain unchanged, the sensitivity could be enhanced due to the phase incursion inside the cavity.

We have performed numerical simulation of a spectral shift in response to refractive index variation for a TE mode of a passive Fabry-Perot cavity with the help of FDTD method (Lumerical FDTD software package, see Annex 1). In a Fabry-Perot cavity the phase incursion upon light roundtrip equals zero, therefore we can verify the spectral shift value induced by the effective index variation with the theoretical values. As the spectral shift is expected to be independent of the size of the cavity, a cavity with the length of 15µm, significantly smaller than the one used in experiments, was chosen. To be able to compare the simulation with the calculus, the model was built without taking into account the Si wafer but with an infinitely thick SiO_2 buffer layer. The studied resonance wavelength and index of buffer layer remained the same as in calculations above. The simulation was performed on a 2D cavity cross-section that allows taking into account the change of refractive index above the surface of the cavity. The refractive index of the cavity surrounding was varied in the range 1.3 ÷ 1.4 units and we have obtained a close agreement (Fig.4-13a) with theoretical estimate, proving that the effective refractive index model adequately predicts cavity response in this range of indices. The error bars are not plotted on this graph for the simulated curve, because the error estimated as described in the Annex 1 equals ±0.007 and is not clearly visible at the scale of the graph.

Afterwards, to have a closer correspondence with the real cavities and to be able to compare the simulation data with the experiments, we performed the simulation with a Si wafer, taking into account the finite thickness of silica buffer (not displayed on the plot). There was virtually no difference between the two simulated curves in the h/λ=1 case, while in the h/λ=0.5 case a noticeable difference revealed. Being non-significant in the range of indices, displayed on the plot, the deviation increased for the lower index values, reaching its maximum at n_e=1. For example, for the variation Δn=0.001 around n_e=1.33 the simulated spectral shift $\Delta\lambda$ equals 0.03nm when the Si wafer is taken into account and 0.025nm when Si wafer is absent and SiO_2 is considered infinite. While not crucial for the sensing application taking into account the limited precision of measurements (~0.03nm), the nature of this difference was intriguing and stimulated further research. The most obvious explanation would be that when the cavity becomes thinner, the larger fraction of the guided mode propagates inside the SiO_2 substrate and feels the presence of the Si substrate. As the index above the cavity increases, the mode energy is repartitioned: the penetration of the mode in the substrate decreases, while larger percentage of the mode is localized on the cavity/medium interface.

The effective refractive index model used here is based on the assumption of infinite thickness of the upper and lower cladding layers. However in the h/λ=0.5 geometry the 2μm thickness of the SiO_2 layer is no longer sufficient to isolate the mode from the underlying Si wafer. To retrieve the correct spectral shift dependency, the effective refractive index needs to be calculated taking into account the finite thickness of a silica substrate. The close agreement between the calculation and a simulation in case when a SiO_2 buffer layer is infinite confirms the hypothesis.

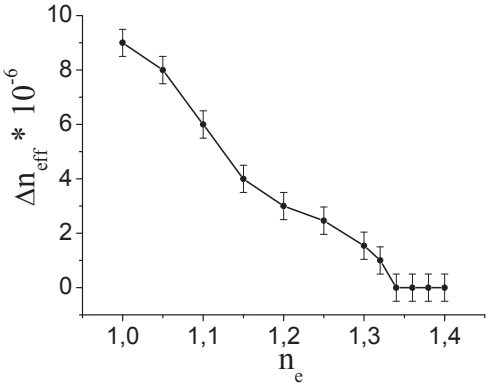

Fig.4-14. The difference between analytical and simulated values of effective index for a TE mode, demonstrating the influence of Si substrate.

We have also calculated numerically, using the FEM method, the effective refractive index n_{eff}^{Si} for a mode in a 4-layer stack: medium / cavity layer (0.3μm) / SiO_2 (2μm) / Si and visually estimated the penetration depth of a TE mode into the claddings (see Annex 1). The difference $\Delta n_{eff} = n_{eff} - n_{eff}^{Si}$ between the effective indexes calculated for a 3-layer stack, without the influence of Si wafer, and with 2μm of Si is plotted on Fig.4-14. The deviation is maximal for n_e=1 and gradually approaches zero as the medium index reaches 1.33 and the mode extends more into the medium above the cavity, proving the hypothesis. The calculated effective index values were rounded to the 6th digit after decimal point, therefore error bars on the graph represent the rounding error. For the case of 3 layers (SiO_2/cavity/medium), numerically predicted effective index values coincide with the analytical calculation by eq. (4-3) with the precision of at least 8 digits after decimal point. In the case of a less confined TM guided mode the difference in effective refractive indices was found to be significantly larger in h/λ=0.5 geometry.

More detailed information regarding the FDTD and FEM simulations, layout and sources of errors will be provided in Annex 1.

Now, we will analyze the second case, when the wave acquires a non-zero phase incursion ($\Delta\phi \neq 0$) along the round-trip in the microcavity, while assuming that effective refractive index remains constant:

$$\Delta\lambda\big|_{\Delta n_{eff}=0} = \frac{\lambda^2}{2\pi}\frac{N}{nL}\Delta\phi \qquad (4\text{-}5)$$

This case is realized for all the cavity shapes with periodic orbits, different from Fabry-Perot, where the incidence angle at the cavity facet is larger than the critical angle for total internal reflection. The phase change upon one reflection ϕ can be easily calculated using Fresnel reflection coefficient formulas (4-6), (4-7). In the case of a total internal reflection, $nSin\theta > n_e$ and reflection coefficients become complex numbers, which we will represent in the form $R_{TE,TM} = \left|R_{TE,TM}\right| e^{i\phi}$

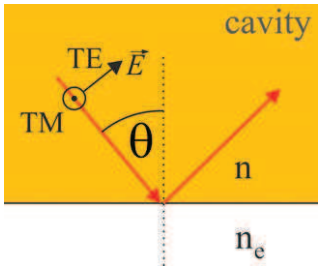

$$R_{TM} = \frac{nCos\theta - \sqrt{n_e^2 - n^2 Sin^2\theta}}{nCos\theta + \sqrt{n_e^2 - n^2 Sin^2\theta}} \tag{4-6}$$

$$R_{TE} = \frac{n_e^2 Cos\theta - n\sqrt{n_e^2 - n^2 Sin^2\theta}}{n_e^2 Cos\theta + n\sqrt{n_e^2 - n^2 Sin^2\theta}} \tag{4-7}$$

Fresnel reflection coefficients for TE and TM polarization in case of total internal reflection and a scheme explaining polarization orientation relative to the cavity border.

Then after separation of real and complex parts we will obtain from (5):

$$R_{TM} = \frac{a - i\cdot b}{a + i\cdot b} = \frac{\sqrt{a^2+b^2}\cdot e^{-i\cdot Arctg(b/a)}}{\sqrt{a^2+b^2}\cdot e^{i\cdot Arctg(b/a)}} = e^{-i\cdot 2\,Arctg(b/a)}$$

$$a = nCos\theta\,,\ b = \sqrt{n^2 Sin^2\theta - n_e^2}$$

$$\phi^{TM} = -2Arctg\left(\frac{\sqrt{n^2 Sin^2\theta - n_e^2}}{nCos\theta}\right) \tag{4-8}$$

and similarly,

$$\phi^{TE} = -2Arctg\left(\frac{n\sqrt{n^2 Sin^2\theta - n_e^2}}{n_e^2 Cos\theta}\right) \tag{4-9}$$

The dependence of $\Delta\lambda = f(\Delta\phi)$ from Eq. (4-5) is plotted on Fig.4-13b for TE cavity mode, two different orbit lengths L=875µm, 443µm and 8 reflections inside the cavity (N=8). This case corresponds to an octagonal cavity with the side length a=120µm and 60µm. The theoretical calculation of the orbit length yields L=886µm for an octagon with side length of 120µm, however the value of L=875µm is used here, as it was determined from experimental spectra. The rationale for the octagonal shape choice would be given later. The spectral shift in this case is proportional to the number of reflections N, phase shift ϕ and inversely proportional to the orbit length L; therefore small-size polygonal cavities with large number of sides should be advantageous for sensing purposes. However, similarly to the case of small h/λ ratio, the cavities cannot be made very small in lateral dimensions. Due to the high substrate losses, the cavities smaller than approx. 50µm x 50µm require a high pumping fluence in order to observe lasing emission, which bleaches the dye very fast. Therefore, either different substrate materials should be employed, or dyes with higher quantum yield should be used or cavities should be made larger.

The FDTD simulation was also performed for the TE mode in the octagonal cavity with side length 60µm (corresponds to L=443µm). The simulation (see Annex 1) takes into account only the phase shift upon reflections at the cavity facets and doesn't account for the effective refractive index change, thus allowing model verification (Fig.4-13b). Due to the very long simulation times we didn't model the larger octagon with 120µm side. Instead, to verify the dependency of sensitivity on the periodic orbit length we simulated a smaller octagon with the side length of 30µm (L=221µm) and compared with a calculated dependency. A very good

match again proves the validity of the model. Therefore, for any complex cavity shape where the precise calculation of the phase shift is not possible, the cavity sensitivity can be estimated by summation of the shape-independent effective refractive index contribution and a shape-dependent phase contribution obtained from numerical simulation.

Opposite to what we have expected, the influence on the cavity spectrum through the change of the effective refractive index turned out to be noticeably stronger than the influence due to the phase change. Our expectations were based on a simple estimation, that for the variation of the medium refractive index of Δn_e=0.001 the corresponding effective index change is of the order $\Delta n_{eff} \sim 10^{-5}$; we expected the mode to be well-confined (h/λ=1) and weakly sensitive to the exterior changes.

Taking into account the factors described above, we can conclude that the main mechanism influencing the spectral shift for the planar polygonal (≤ 8 sides) non-functionalized cavities with $h/\lambda \leq 1$ is the change of the mode effective refractive index. The expected sensitivity is of the order of 10nm/RIU and can be further enhanced in polygonal cavities due to the phase incursion mechanism.

It should be noted as well, that the Fresnel reflection formulas used above are only valid in the case of a plane wave falling on an infinite plane surface. We didn't study the applicability of phase change approach in the thin quasi-2D structures like our cavities, where reflection occurs not on an infinite wall but on a cavity facet, limited in vertical dimension.

4.4.2. *Optimal cavity shape*

Besides being sensitive to the exterior medium, the microlaser must also provide sufficiently intense emission, in order to facilitate detection in the microfluidic chip and possess low lasing threshold, to avoid excessive pumping and fast bleaching of the laser dye. Further on we will analyze various cavity shapes with respect to their lasing properties, describe the possible periodic orbits and talk of the ways to increase refractive index sensitivity.

Fabry-Perot

The simplest cavity shape that provides intense and directional laser emission is the Fabry-Perot cavity (Fig.4-19a). However, Fabry-Perot resonator is not entirely suitable for the sensing purposes in its current configuration ($h/\lambda \approx 1$) due to insufficient sensitivity to refractive index variations. Supporting experimental results which coincide quite well with the calculus will be presented in the next section. We shall seek another cavity shape, where light undergoes large number of reflections, so that phase incursion would play a supportive role.

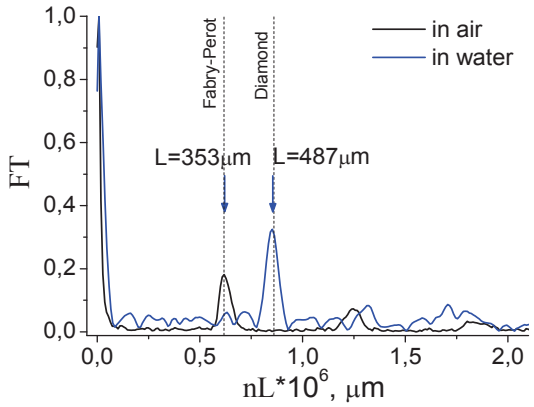

Fig.4-15. Normalized Fourier transform of the lasing spectra of a square microcavity (side = 175μm), demonstrating the change of a lasing periodic orbit.

Square

The next step in increasing the number of facets would be a square cavity (Fig.4-19b). This type of cavities features two lasing orbits: a diamond-like and a Fabry-Perot (two Fabry-

Perot resonances exist between 2 pairs of parallel cavity walls) that give 4 intense and directional laser emission lobes [35]. In air ($n_e = 1$), the diamond orbit is confined by total internal reflection (critical angle in air $\chi_c^{air} = 40.5°$), consequently having a higher quality factor than a Fabry-Perot resonances, which are lossy as the reflection coefficient for PMMA/air interface at a normal incidence angle is $R_{FP} = 0.045$. Once the cavity is immersed in water, the resonances experience changes: for a Fabry-Perot orbit the reflection coefficient decreases and becomes $R_{FP} = 0.005$ and the diamond orbit is no longer confined (critical angle in water $\chi_c^{water} = 59.9°$) with a reflection coefficient $R_{diam} \approx 0.03$. Though this value is higher than for the FP, the light in diamond orbit undergoes 4 reflections, and as the orbit closes, the light intensity would be proportional to $R_{diam}^4 \approx 8 \cdot 10^{-7} << R_{FP}^2 \approx 2.5 \cdot 10^{-5}$ which is two orders less than for the FP resonance. Therefore, both modes can exist in the cavity, but we expect the FP mode to be dominating in water. We have performed tests on the square cavities, and have evidenced the vanishing of a diamond periodic orbit once the cavity was immersed in water. The Fourier-transform of the lasing spectra of a square with the side=175µm, presented on Fig.4-15, illustrates the change of the lasing periodic orbit from a diamond (length $L \approx 487$µm), when a cavity is in the air to a Fabry-Perot one ($L \approx 353$µm) once the cavity is immersed in water. Thus, we find ourselves in the previous case of the Fabry-Perot microlaser, with insufficient sensitivity to the refractive index variation, which makes square microlasers not well suited for sensing.

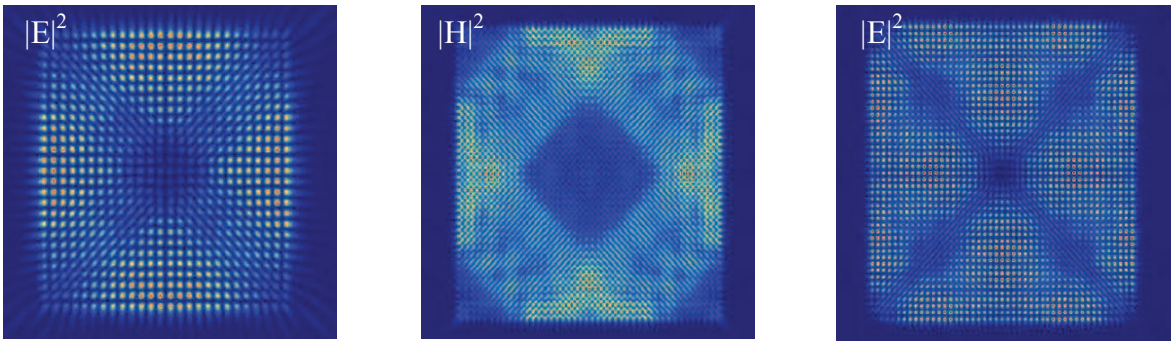

Fig.4-16. Electric and magnetic field distribution for several resonant modes in a square microcavity in air by FDTD simulation.

Visualization of several resonant modes in a square microcavity in air by FDTD simulation is presented on Fig.4-16. Here, the square with a 10µm side length was simulated, and the electromagnetic field distribution corresponding to several cavity resonances was plotted. The time apodization filter centered at 1000fs is applied to cut the transient processes occurring at the beginning of the simulation and to recover the stationary mode profiles. Detailed explanation of the mode visualization is given in Annex 1.

Octagon

We did not experiment with pentagonal and hexagonal cavities, but to increase the number of reflections, moved on to an octagonal shape (Fig.4-19c). For the octagon-shaped cavity, 3 orbit types exist: Fabry-Perot (4 resonances between parallel facets), inscribed square (2 orbits) and an inscribed octagon, two latter being confined by total internal reflection for the cavity in air [35]. Plot of the electric field intensity for two resonant modes, obrained by FDTD simulation, which resembles the inscribed square and inscribed octagon orbits, is shown on

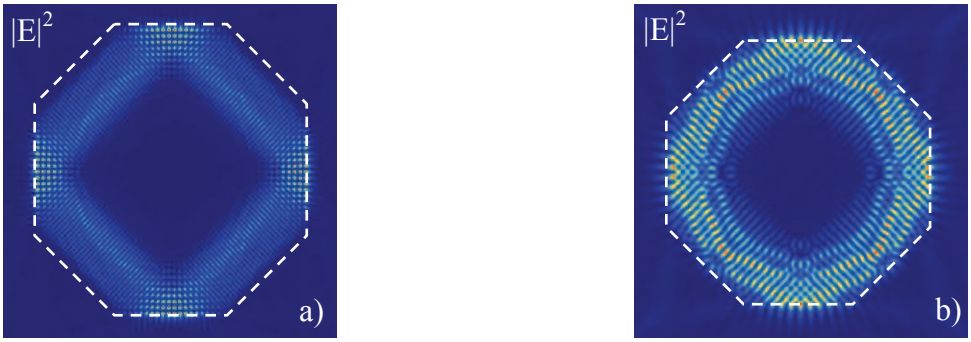

Fig.4-17. Electromagnetic field distribution (by FDTD simulation) for two resonances of an octagonal cavity in air, resembling a square-shaped (a) and octagon-shaped (b) periodic orbits. Cavity contour is showed with white dash line.

Fig.4-17. As before, time apodization filter has been set up at 1000fs to isolate the stationary cavity modes.

Once the octagon is immersed in water, the inscribed square orbit becomes lossy as in the case of a square cavity, but the octagonal orbit remains confined (reflection angle $\theta = 67.5° > \chi_c^{water}$) and according to our experimental observations, mostly dominating over the FP. The estimation of sensitivity for the octagons of two different sizes was already graphically presented before (Fig.4-13b) and showed an additional sensitivity improvement. Experimental data for the octagons will follow.

Disc

If we think of the way to increase the number of reflections inside the cavity, the whispering gallery modes may be a helpful solution. In the cavity shapes that support WGMs, the wave

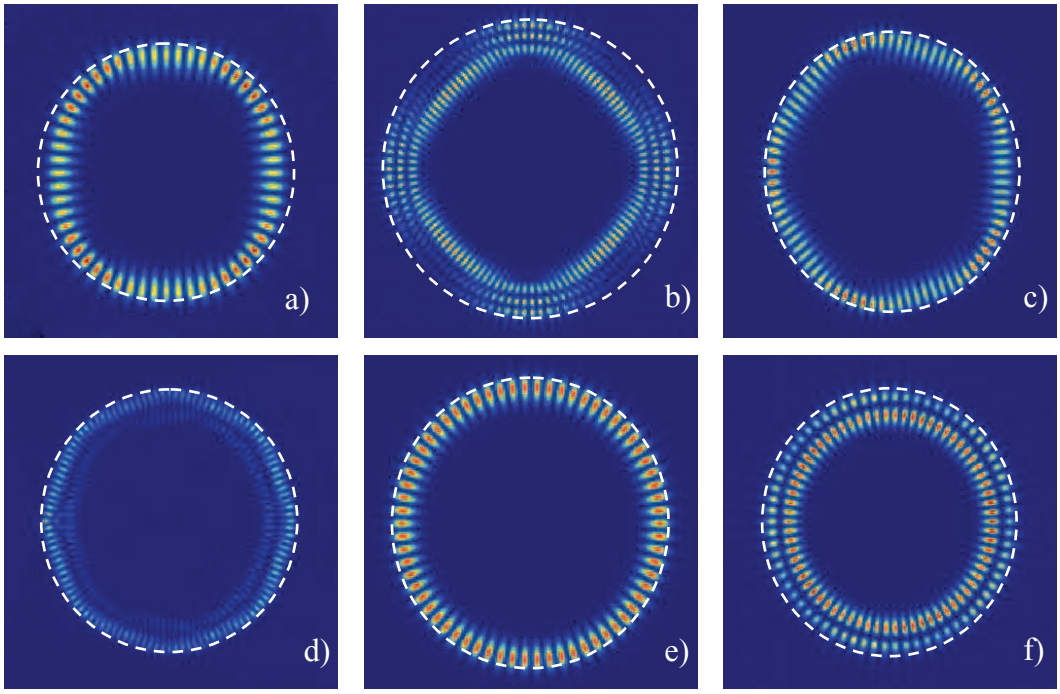

Fig.4-18. Visualization of several modes in a disc microcavity (r=2.5μm) by FDTD simulation. a-d) Electric field distribution resembling (a), (b) square-like; (c) pentagon; (d) octagon periodic orbits. e, f) Whispering gallery modes with different radial numbers. Plotted is electric field intensity $|E|^2$, cavity outline is shown with white dash.

Cavity shape	Emission Diagram	Periodic orbits

a)

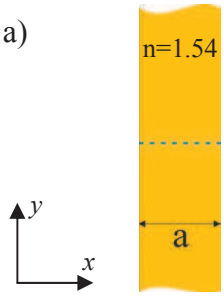

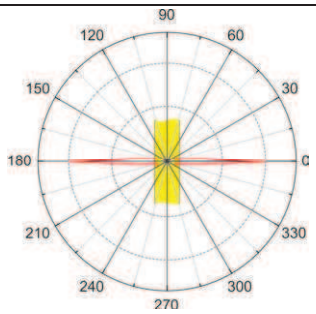

Orbit type	*Length*
Fabry-Perot	$L_{FP} = 2 \cdot a$

b)

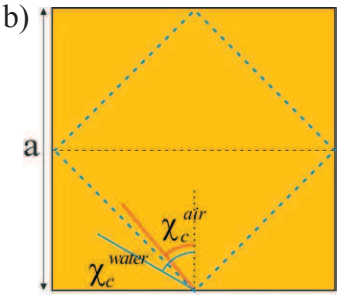

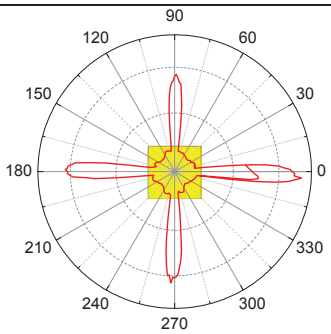

Orbit type	*Length*
Fabry-Perot	$L_{FP} = 2 \cdot a$
Diamond	$L_{diam} = 2\sqrt{2} \cdot a$

c)

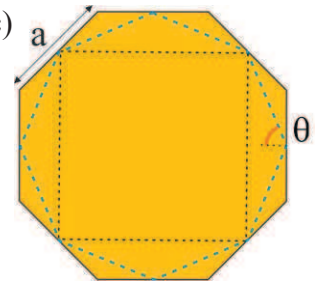

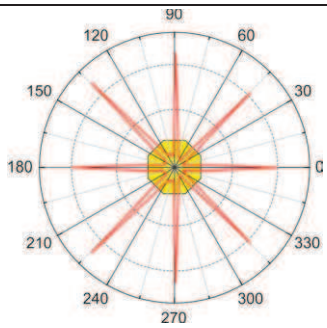

Orbit type	*Length*
Fabry-Perot	$L_{FP} = 2(\sqrt{2}+1) \cdot a$
Square	$L_{sq} = 4(1+\frac{1}{\sqrt{2}}) \cdot a$
Octagon	$L_{oct} = 8\cos(\theta/3) \cdot a$

d)

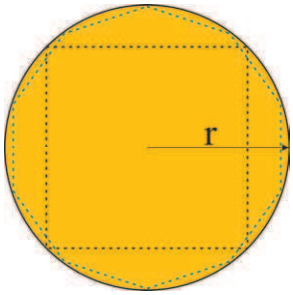

Orbit type	*Length*
Fabry-Perot	$L_{FP} = 4 \cdot r$
Square	$L_{sq} = 4\sqrt{2} \cdot r$
Higher order (<perimeter)	$L < 2\pi \cdot r$

e)

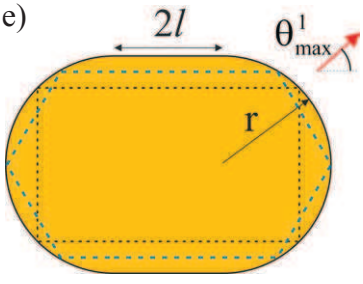

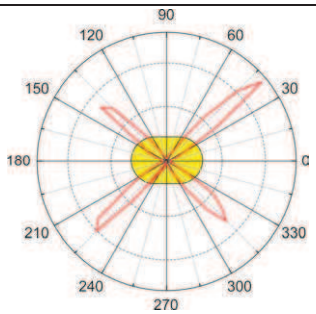

Orbit type	*Length*	
Fabry-Perot	$L^x_{FP} = 4(l+r)$	
Square	$L_{sq} \approx 7.66 \cdot r$	Only for
Hexagon	$L_{hex} \approx 8 \cdot r$	
Higher order (<perimeter)	$L < 8.28 \cdot r$	

Fig.4-19. Schematic images of a Fabry-Perot (a), square-shaped (b), octagonal (c), disc (d) and stadium-shaped (e) cavities with the corresponding emission diagrams and lengths of the most common periodic orbits (shown in dash lines). Periodic orbits that are more likely to exist when cavity is immersed in water are shown with blue dashed line.

undergoes numerous reflections as it propagates along the cavity circumference and therefore it may render such micro-lasers more sensitive to changes in the surrounding medium even in $h/\lambda \approx 1$ geometry. The simplest plane cavity shape supporting WGMs is a disc (Fig.4-19d). According to the trace formula [34, 135, 136], we expect to see the polygonal periodic orbits starting from the inscribed square, which is the first orbit confined by total internal reflection, followed by a pentagon, hexagon, etc. Some of the possible microdisk cavity modes are visualized on Fig.4-18: figures e, f show the whispering gallery modes, excited in the microdisk with a radius $r = 2.5\mu m$, while the time apodization is set up at 5000fs to capture the stationary cavity modes. At the same time, on Fig.4-19a-d, we observe the modes which resemble some of the periodic orbits – inscribed polygons. These modes are observed at simulation times smaller than 5000fs, as will be explained in Annex 1.

The higher-order polygon orbits are more confined and their coupling with exterior is less efficient, therefore they are unlikely to be observed in the lasing spectra. But the theoretical estimations apply only to a cavity with a perfect, defect-free sidewall. In our samples, the lasing orbit observed in experiments depends greatly on the quality of etching of the cavity. For the microdisks fabricated by e-beam lithography, when the sidewall is smooth and almost defect-free, the whispering gallery modes are well-confined and the laser emission that we observe mostly comes from a FP orbit (width of a FP cavity = 2*diameter of a disc). And when the cavity is manufactured by UV-lithography in our cleanroom, the sidewall is usually rougher, the number of defects is higher and therefore higher-order polygon orbits becomes less confined and are observed in laser spectra. The FP orbit is unlikely to contribute to lasing in this case.

The weak point of a microdisk cavity with regard to sensing is the isotropic emission, due to the rotational symmetry. As the disk emits uniformly in all the directions the emission intensity in a given direction of observation is relatively weak. Once such cavity is placed inside a microfluidic chip that additionally attenuates the emission, spectra recording becomes complicated and requires higher pumping energies which is very undesirable. To overcome this issue, it would have been preferable to find a cavity supporting WGMs and emitting the light directionally. Such cavity shape exists: a stadium-shaped cavity that exhibits four pronounced emission directions (Fig.4-18).

Stadium

A stadium shaped cavity is formed by two semi-circles with radii r attached to a rectangle with the side $2l$. This cavity shape is chaotic: any minor perturbation of the light orbit leads to a drastically different propagation path after a number of reflections. The periodic orbits of stadiums and their stability have been studied in details in [34]. Surprisingly, despite its chaotic

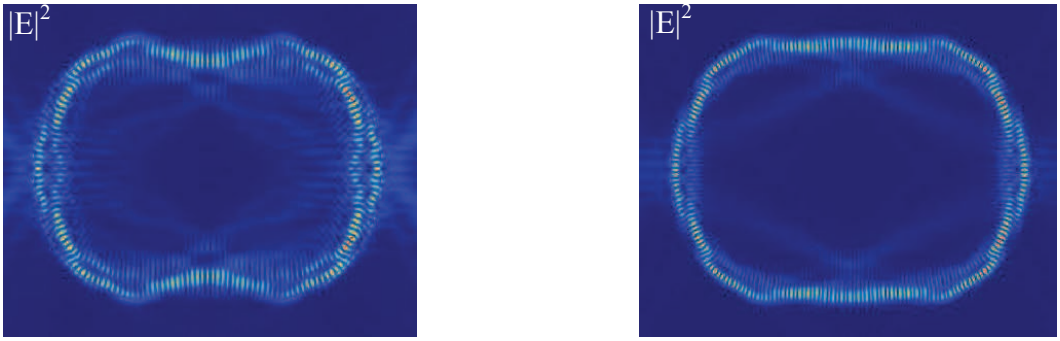

Fig.4-20. Visualisation of two modes of a stadium cavity (l/r = 0.5) by FDTD simulation.

nature, stadium cavities exhibit high directionality of emission that has been studied theoretically in [137, 138] and in [34] the lens models have been developed, that predicts and experimentally confirms the angular positions of the maxima and shows that these angles depend on *l*/r ratio (which is a stadium deformation parameter). In our sensing experiments we have used stadiums with the ratio *l*/r = 0.5, which exhibit four symmetrical emission maxima at the angles $\theta_{\max}^{1,2,3,4} \approx$ 42º, 138º, 222º, 318º. Distribution of electric field for two different modes of a stadium microcavity, calculated with FDTD, is shown on Fig.4-20.

Most of the refractive index variation sensing and heavy-metal detection results in this thesis were obtained with the stadium cavities. In order to make all the cavities (Fabry-Perot, squares, stadiums) emit in the same direction, perpendicular to the PDMS chip wall, the stadiums on the lithographic mask were rotated at 42º, so that two of their emission maxima are oriented in parallel with the emission of other cavity shapes.

The main drawback of the WGM cavities, which deals more with technology than physics, lies in the higher requirements for the cavity edge quality, as the mode is localized mostly in the region near the perimeter, undergoes numerous reflections at the sidewall and any minor fabrication defects may significantly affect lasing performance.

4.5. *Experimental proof of RI variation sensing and heavy metal ions detection.*

Before proceeding with detection of heavy metal ions with functionalized cavities, we needed to obtain an experimental proof of the medium influence on the cavity spectra in order to choose and work further with the best available solution. While making multiple trials at this stage of work is still acceptable, once functionalization with ligands is involved, each failed attempt is not only time and material consuming, but also expensive.

4.5.1. *First measurements of lasing spectra in liquids.*

Once the optimal cavity shape has been clarified, that should let us (at least in theory) achieve the highest sensitivity to changes in cavity surrounding, we can proceed with the experimental verification. The first attempts that we have performed were aimed to detect laser emission spectra of cavities in liquids. It was not evident, especially for the complex, non-integrable chaotic cavites like stadiums, how will the liquid environment with elevated refractive index influence their lasing properties. For the "simple" shapes, like Fabry-Perot, square... for which a closed periodic orbit can be plotted from geometric optics considerations (Fig.4-19a,b,c) one can try to predict the behavior of the cavity in water. For the Fabry-Perot, for example, the periodic orbit will not change, but will only become less confined due to lower index contrast with the environment. For the square cavity the influence is more significant: we have predicted and experimentally observed the change of the lasing periodic orbit from a diamond in air to a Fabry-Perot in water (Fig.4-15). In the octagonal cavities, the inscribed octagon orbit remains confined by total internal reflection. In other words, all the microlasers when immersed in liquid, continued to function properly.

However, once the stadium cavity is considered, we cannot predict its behavior so simply due to the cavity's chaotic nature. In the first experiments with stadiums, we noticed a sudden drop of detected emission intensity (to zero for some of the stadiums) at the observation angle of 42°, where the intensity should be maximal, once a cavity is immersed in water. The maximum was found to lie in the range 25º - 32° for different cavities, which was not expected. We

performed ray simulations, as described in [139], to predict the angular emission pattern, as shown on Fig.4-21 (code written and maintained by Iryna Gozhyk, LPQM). We have found that emission maxima change their position, and are located now closer to the x-axis, the first maximum being approximately at 25°, which coincides with the experimental data. The error in determination of the maximum comes partly due to the fact that emission was no longer perpendicular to the PDMS surface: the angle measured through PDMS chip is larger for approximately $\theta_2 - \theta_1 \approx 4 \div 5°$ (see Fig.4-7).

4.5.2. *Refractive index variation: preparation of sample solutions and first attempts.*

To assess the sensitivity of the lasing spectra to the variation of refractive index of the cavity surrounding, one needs to prepare a set of liquid solutions with precisely measured refractive indices, inject them into the microfluidic chip and record the changes in emission spectra (if any). Initially, we tried using the simplest available materials: common salt (NaCl) dissolved in distilled water in different concentrations in order to modify the refractive index. However these solutions are likely to produce sediment, which is very undesirable as it can easily block the microfluidic channels. Moreover, any deposit left on the cavity surface will permanently alter the mode confinement conditions and consequently lasing spectra of the cavities, up to the point when the cavity may become unusable.

The first RI variation sensing experiments performed on the octagon and stadium-shaped cavities, involving salt solutions were unsuccessful: we haven't detected any medium index-related shifts in the spectra. The spectral peaks either remained at exactly the same position, or were blue-shifted due to the laser dye bleaching, as was explained in § 3.3. As it became evident later, we have overestimated the sensitivity of the cavities at this stage and used too much diluted 0.9% salt solutions with insufficient refractive index variation (Δn=0.002).

When we tried to use more concentrated salt solutions, we have noticed that microfluidic chips started to leak frequently, at the point where input tube is connected. This indicates that, most likely, the 0.2mm thin input our output channel was blocked by accumulation of salt, sedimented on the walls. A leakage in the microfluidic chip renders the sample unusable, as the PDMS chip is strongly bonded to the wafer surface cannot be detached to be replaced. Attempts to wash the circuits, if the channel is (almost) completely blocked are also futile in most of the cases.

To prepare solutions with various refractive indices, we have chosen glucose (α-D-Methylglucoside, $C_7H_{14}O_6$) which is supplied as a powder and has a high solubility in water at a room temperature: 108 g/100 mL (20 ºC). The solutions that we used are far from saturation point and are unlikely to produce sediment during the relatively short utilization time (hours - few days). Glucose was dissolved in purified, deionized distilled water (resistance ~18MΩ/cm) to create solutions with various refractive indices. The concentration of glucose in the solutions was not controlled; instead the parameter controlled is the refractive index, measured

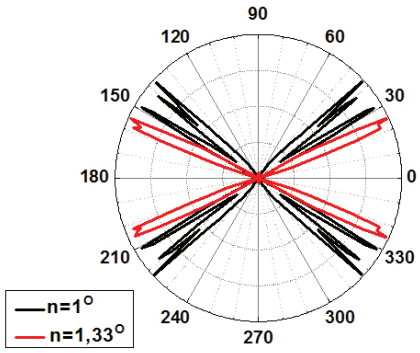

Fig.4-21. Simulated angular emission diagram of a stadium in air (black) and in water (red).

with Abby refractometer at ~643nm wavelength (HgCdZn lamp illumination) with ± 0.0002 precision.

4.5.3. *Proof of RI variation sensing principle.*

In this section the experimental results of refractive index variation sensing with different cavity shapes will be presented. The comparison with model predictions and numerical simulations will be carried out and temperature influence on the spectra of microlasers will be discussed.

Fabry-Perot

Taking into account the estimates for refractive index sensitivity obtained above, we have performed a series of refractive index variation sensing experiments on the cavities of various shapes. First of all, we experimentally observed the influence of the effective refractive index change on the spectral shift with the Fabry-Perot cavity (width=200μm, h/λ≈1). The lasing spectra (Fig.4-22) recorded in liquids with different refractive indices (Δn=0.0045) were nearly identical. Some of the spectral peaks are red-shifted for 0.029nm while others coincide, which, as was mentioned already before, means that there is a minor shift in the spectrum, most likely inferior to 0.029nm that can be attributed to the influence of effective refractive index change. The measured value reasonably agrees with the estimate, calculated with (4-4) and given in Table 4-1: for Δn=0.0045 index change the predicted spectral shift should be Δλ=0.039nm, which is near the limit of our setup resolution. A parasitic blue-shift due to the dye bleaching and variation of the real cavity parameters from the ones used in calculation may be responsible for the lower measured value. The measurement error was defined as 0.5*pixel size of a CCD camera, which corresponds to ±0.015nm. The variations of ±0.1 in h/λ ratio in the case when h/λ=1 lead to the change in the wavelength shift of roughly ±0.007nm which lies within the measurement error range.

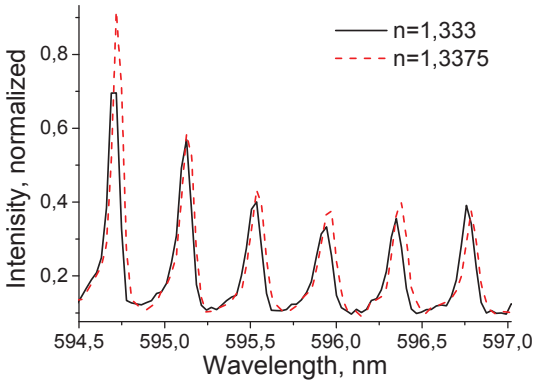

Fig.4-22. Normalized lasing spectra of a Fabry-Perot cavity (width=200μm) in liquids with different refractive indices (Δn=0.0045) show minor shift.

Calculations show as well, that for the thinner cavities (h/λ =0.5), variation of the effective refraction index, Δn_{eff} becomes more significant when index of the surrounding environment (n_e) changes. In particular, a two times thinner Fabry-Perot cavity should demonstrate almost 3 times higher sensitivity, though at the cost of higher lasing threshold and lower emission intensity at the similar pumping fluence.

Octagon

In an attempt to reach higher sensitivities for h/λ=1 geometry, we performed experiments with the octagonal cavities of two sizes: side length of 120μm and twice smaller, 60μm, where phase incursion is expected to bring enhancement. The twice smaller cavity size was chosen to verify the expected dependence of sensitivity on the phase incursion, which should be two times larger

Mode	h/λ =1	h/λ =0.5
TE mode	n_e = 1.333 / 1.3375; n_{eff} = 1.50558 / 1.50568; $\Delta n_{eff}=1\cdot10^{-4}$	n_e = 1.333 / 1.334; n_{eff} = 1.47085 / 1.47112; $\Delta n_{eff}=2.7\cdot10^{-4}$
	$\Delta\lambda^{index} \approx 0.038$nm	$\Delta\lambda^{index} \approx 0.102$nm
	$\Delta\lambda_{Experiment} \leq 0.029$nm	
	Sensitivity ≈ 8.5 nm/RIU	Sensitivity ≈ 23 nm/RIU
TM mode	n_e = 1.333 / 1.3375; n_{eff} = 1.50207 / 1.50221; $\Delta n_{eff}=1.4\cdot10^{-4}$	n_e = 1.333 / 1.3375; n_{eff} = 1.46464 / 1.46498; $\Delta n_{eff}=3.4\cdot10^{-4}$
	$\Delta\lambda^{index} \approx 0.055$nm	$\Delta\lambda^{index} \approx 0.130$nm
	Sensitivity ≈ 12 nm/RIU	Sensitivity ≈ 29 nm/RIU

Tab.4-1 Estimated influence of the cavity thickness on the effective refractive index for TE and TM modes; expected and experimental (for TE mode) wavelength shift for a Fabry-Perot cavity for $\Delta n=0.0045$ and extrapolated sensitivity to RI variation.

Mode	a=120μm (L_{oct}=875 μm)	a=60μm (L_{oct}=443 μm)
TE mode	n_e = 1.333; $\phi \approx 1.452$ / n_e = 1.342; $\phi \approx 1.516$	
	$\Delta\lambda^{phase} \approx 0.023$nm	$\Delta\lambda^{phase} \approx 0.045$nm
	$\Delta\lambda^{total} = \Delta\lambda^{index} + \Delta\lambda^{phase} = 0.1$nm	$\Delta\lambda^{total} = \Delta\lambda^{index} + \Delta\lambda^{phase} = 0.12$nm
	$\Delta\lambda_{Experiment} \approx 0.095 \pm 0.015$nm	$\Delta\lambda_{Experiment} \approx 0.116 \pm 0.015$nm
	Sensitivity ≈ 11 nm/RIU	Sensitivity ≈ 13 nm/RIU
TM mode	n_e = 1.333; $\phi \approx -1.402$ / n_e = 1.342; $\phi \approx -1.352$	
	$\Delta\lambda^{phase} \approx 0.018$nm	$\Delta\lambda^{phase} \approx 0.035$nm
	Sensitivity ≈ 14 nm/RIU	Sensitivity ≈ 33 nm/RIU

Tab.4-2 Estimated influence of the phase incursion on the wavelength shift in octagonal cavities with side length a=120μm and 60μm (h≈600nm) for TE and TM mode and extrapolated sensitivity to RI variation. L - periodic orbit length. Experimental data given for comparison.

in this case. We placed the cavities inside the PDMS microfluidic chip and recorded a series of lasing spectra (Fig.4-23a,b) in the following way. First, pure water (n=1.333) was injected inside the microfluidic chip with the help of a syringe pump, let to flow through for 1 minute, and the first lasing spectrum was recorded in water (black). Afterwards, a glucose solution with elevated refractive index (n=1.342) was injected, and let flow through for 1 minute, to make sure that all the water went out of the chamber and the cavity is uniformly covered by the new solution. The second spectrum is recorded (red). Finally, the cavity is washed by pure water for several minutes, to remove glucose solution, and the third spectrum is recorded in water (blue).

We have clearly detected the red-shift of 0.08 ± 0.015nm for the 120µm octagon (Fig.4-23a) and approx. 0.116 ± 0.015 nm for the 60µm octagon (Fig.4-23b), indicating the difference in the refractive indices. In the case of larger octagon, the 3rd spectrum, recorded in pure water after removal of glucose didn't restore to the initial position but is blue-shifted, probably due to the dye bleaching. Therefore red-shifted peak position should be corrected: we will assume that the blue-shift was linear during the 2nd and the 3rd measurements. Therefore actual peak position

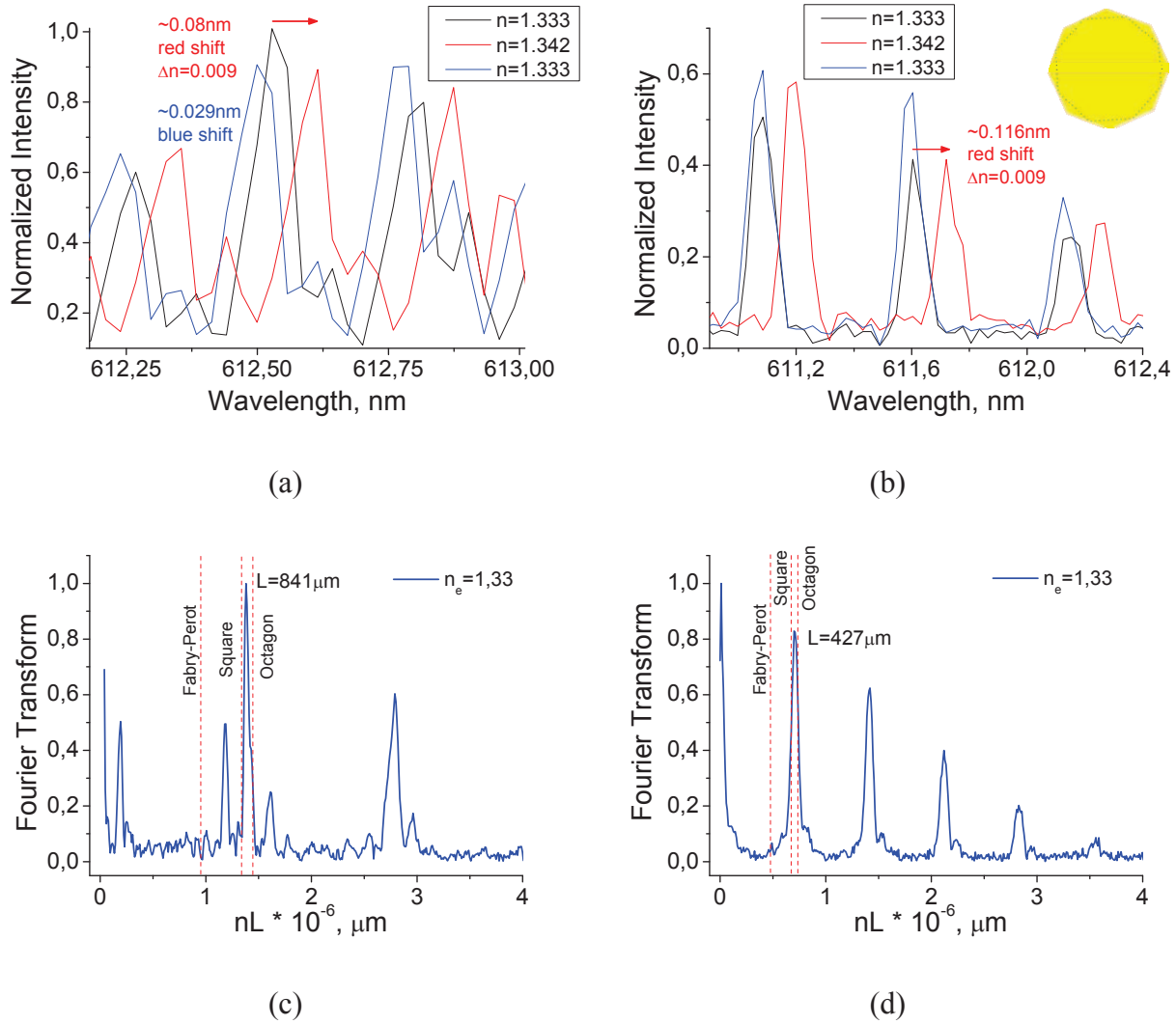

Fig.4-23. Lasing spectra of the octagonal cavity in water and glucose solution (Δn=0.009) for the octagon side length of 120µm (a) and 60µm (b) demonstrates a red-shift in the spectrum. The measurements were performed in the following chronological order: black, red, then blue. c, d) Fourier transforms showing the measured length of the periodic orbit for 120µm and 60µm stadiums correspondingly.

should be $(0.08 \pm 0.015) + ((0.029 \pm 0.015) / 2) = 0.095 \pm 0.022$nm. Taking into account that a blue shift amount depends on multiple factors: pump fluence, used dye and polymer and is, strictly saying, individual for each studied sample, we will consider the measurement error to be limited only by the CCD camera and to be therefore ±0.015nm for the cases when there is no explicitly detected shifts. To minimize the bleaching influence, the spectra should be recorded at the lowest possible pumping power.

The Fourier transform of the lasing spectra (Fig.4-23c,d) shows that the length of the observed periodic orbit for both octagons lies in the range between the inscribed square and the inscribed octagon. For the bigger octagon with the side of 120μm these length are $L_{oct} = 886\mu m < L_{mes} = 841\mu m < L_{square} = 820\mu m$ and for the smaller one with the side of 60μm – $L_{oct} = 443\mu m < L_{mes} = 427\mu m < L_{square} = 410\mu m$. These results agree well with the observations in [34], where the periodic orbit length was inferred from the lasing spectra of octagonal cavities of various sizes.

For the octagonal shape, the expected wavelength shift ($\Delta\lambda^{total}$) can be assessed as a sum of effective index-induced shift ($\Delta\lambda^{index}$), taken from Table 4-1 and a phase incursion contribution ($\Delta\lambda^{phase}$), calculated in Table 4-2. Here we assume that the variation of effective index $\partial n_{eff} / \partial n_e$ remains similar for various cavity modes possessing different effective indices. The experimental values, also included in Table 4-2 for easier comparison, are in a very good agreement with calculations, the difference being explained by the blue-shift and difference of real cavity parameters from the ones used in calculation. The extrapolated sensitivity, given in nanometers / Refractive Index Units is slightly higher than for the Fabry-Perot cavity, but still insufficient to resolve the refractive index variation of at least 10^{-3} units.

Stadium

The next step was to test the stadium-shaped cavities that support whispering gallery modes, and due to the high number of wave reflections at the cavity boundary we expected them to be more sensitive to the refractive index of the surrounding medium. Due to stadium's chaotic nature we cannot analytically predict the phase shift and the corresponding spectral shift due to the external index variation, as it can be done for the polygons; however we expect that the sensitivity will be reversely proportional to the stadium size (4-10) as it was observed for octagons. In equation (4-10) f denotes certain unknown non-linear function. A 2D FDTD numerical simulation was therefore employed to reveal the dependence of spectral shift on the index of the medium as well as on the size of the microcavity, while not taking into account the effective refractive index variation.

$$\Delta\lambda^{phase}\Big|_{\Delta n_{eff}=0} \sim \underbrace{f\left(\frac{1}{nL}\right)\cdot\frac{\partial\varphi}{\partial n_e}}_{a}\Delta n_e = a\cdot\Delta n_e \qquad (4\text{-}10)$$

We have numerically calculated the spectral shift $\Delta\lambda$ for a TE mode while varying the medium index n_e in the range $1.33 \div 1.34$ for different sizes of the stadiums. Refractive index of the cavity material was taken equal to that of the PMMA layer doped with DCM dye, n=1.54. The shift was assumed to be linear in the given range of indices. The slope a of the obtained dependencies for each stadium size is plotted on Fig.4-24, revealing a non-linear dependency of the resonance wavelength shift on the stadium size, resembling that of the exponential. The error bars on the plot correspond to the error of a linear fit of $\Delta\lambda = f(n_e)$ dependency. Taking into

account a good agreement between simulation and calculation for the octagons and Fabry-Perot cavities, we consider the obtained results to be trustworthy. Slow decrease of the sensitivity for the stadium radii $r > 30\mu m$ complicates experimental verification of this dependency, as spectral shift will lie within the error range of the experiment; and the stadiums with radii $r \leq 30um$ normally generate very weak or no emission and require high pumping energies. Once again, as in the case of the octagons, we will assume that the effective refractive index contribution to the spectral shift $\Delta\lambda^{index}$ remains independent of the cavity size, and the value of 0.038nm calculated above (Table 4-1) for the Fabry-Perot cavity is taken. The comparison with the experimental data for PMMA+DCM stadiums is presented in Table 4-3.

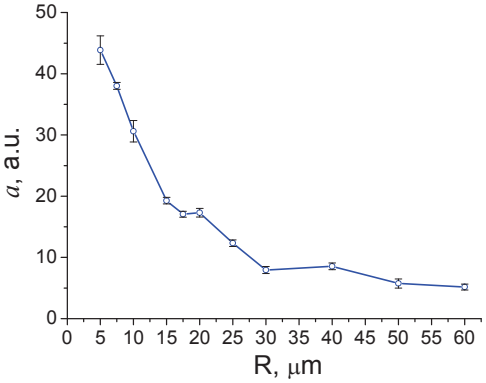

Fig.4-24. Simulated dependence of the spectral shift on the size for r/l=0.5 stadiums (r=2l) due to phase incursion. Plotted is the slope a from Eq. (4-10).

Refractive index sensitivity measurements have been performed for both non-porous PMMA and porous PS-b-PAA stadium-shaped cavities doped with DCM and Pyrromethene605 dyes respectively. The stadium size was $r=2l=40\mu m$ for PMMA (manufactured with e-beam lithography) and $r=2l=50\mu m$ for PS-b-PAA polymer (manufactured with UV lithography); experiment was performed as was described above. Among various cavity sizes present on the sample, we have chosen the ones exhibiting the most regular and intense spectra. The aim of the experiment was not to investigate the dependence of sensitivity on the cavity size but to prove the possibility of such sensing and to estimate approximate sensitivity. Prior to recording spectra at different index values the angle of maximum emission in water was found experimentally and all the following measurements were made at a certain fixed stadium orientation.

Similar refractive index sensitivity values have been obtained for both materials, as shown on Fig.4-25. In the case of PMMA (Fig.4-25a) the gradual shift of the spectrum with the increase of medium index is demonstrated. Upon analyte removal the lasing spectrum restored to the initial position, except for some peaks, for which the blue-shift was seen. The sensitivity values are similar in both cases, approximately 13nm/RIU for the PMMA and 10nm/RIU for PS-b-PAA

	PMMA + DCM r=2*l*=40μm	PS-b-PAA + Pyr605 r=2*l*=50μm
TE mode	$\Delta n_e = 0.009$	$\Delta n_e = 0.009$
	$\Delta\lambda^{phase} \approx 0.077\text{nm}$	
	$\Delta\lambda^{total} = \Delta\lambda^{index} + \Delta\lambda^{phase} = 0.038nm + 0.077nm = 0.115\text{nm}$	
	$\Delta\lambda_{Experiment} = 0.116 \pm 0.015\text{nm}$	$\Delta\lambda_{Experiment} = 0.088 \pm 0.015\text{nm}$
	Sensitivity ≈ 13 nm/RIU	Sensitivity ≈ 10 nm/RIU

Tab.4-3 Numerically estimated ($\Delta\lambda^{total}$) and experimentally measured spectral shift for stadium cavities (h/λ≈1) due to medium refractive index variation.

microlasers (Table 4-3). The simulation data results cannot be directly compared with the PS-b-PAA stadium experimental values as the refractive indices of these polymers differ. The Fourier transform of the lasing spectra of the PMMA stadium (Fig.4-25c) shows that the periodic orbit of the stadium in air and in water remains the same, within the error of calculation of refractive index by Eq. (2-18). The length of the lasing orbit, calculated from the spectrum (L=327μm), lies in between the lengths of the inscribed hexagon (L_{hex} = 320μm) and the perimeter of the stadium (L_{perim} = 331.2μm), thus proving that the observed orbit can be attributed to a whispering gallery mode.

We have experimentally confirmed the refractive index sensing principle with both traditional PMMA and porous polystyrene-based cavities: a clearly identifiable red-shift is seen in the cavity lasing spectra that depend on the refractive index of the cavity surrounding. The main contribution to the sensitivity comes from the change of the mode effective refractive index in response to the medium index variation. The additional shift caused by the phase incursion upon reflection at the borders of the cavity plays supportive role and allows further enhancement of the sensitivity. While the effective index contribution is independent on the size of the cavity,

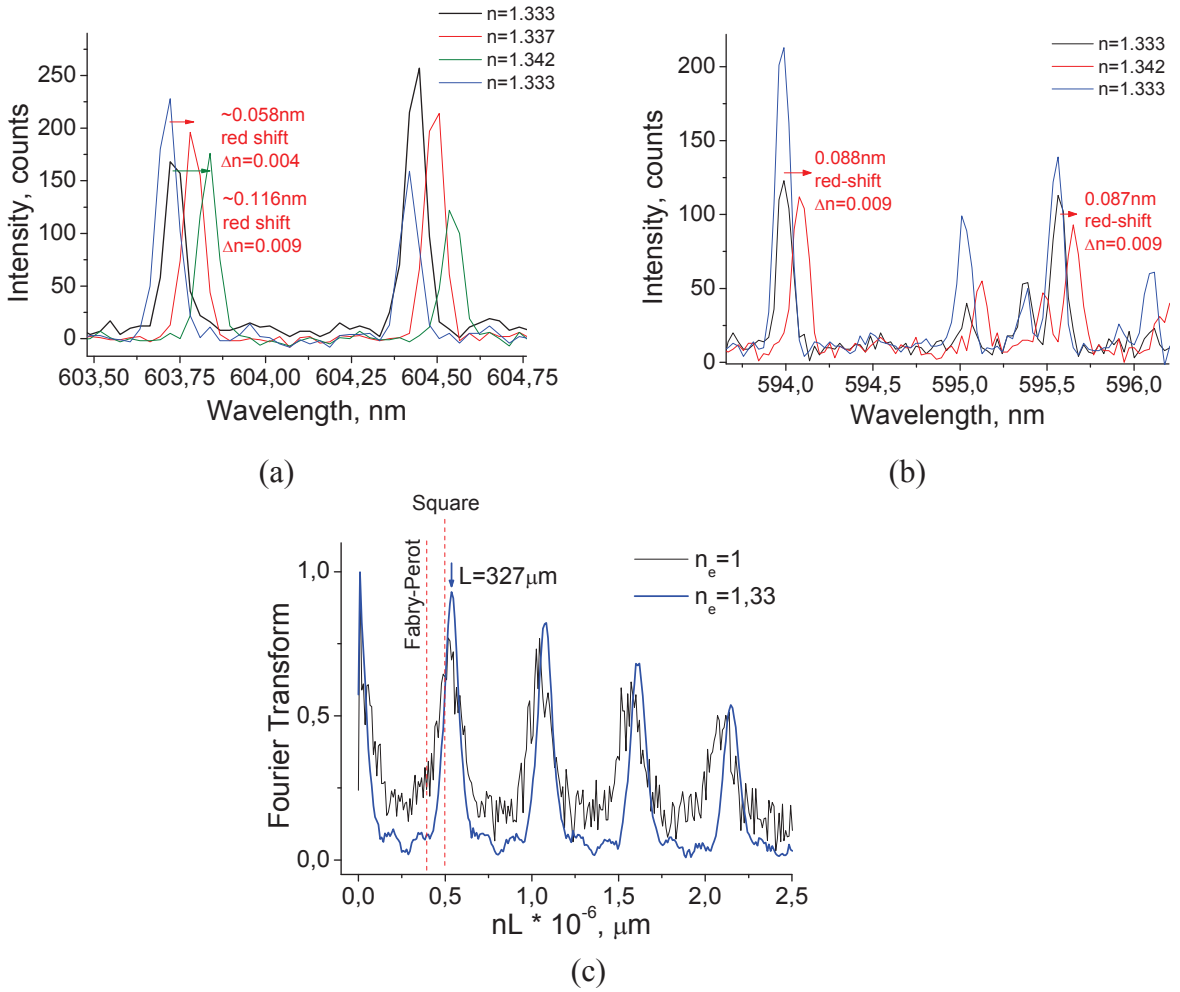

Fig.4-25. (a) Refractive index sensing with a stadium-shaped PMMA microlaser (sensitivity ≈ 13nm/RIU). A red shift of 0.058nm and 0.116nm is observed for the analyte refractive index change of Δn=0.004 and Δn=0.009 units. The spectrum restores its initial state upon analyte removal (blue). (b) RI sensing with a stadium-shaped PS-b-PAA microlaser (sensitivity ≈ 10nm/RIU). (c) Fourier transform of a lasing spectrum of PMMA stadium mirolaser.

the phase incursion part grows linearly with the decrease of the cavity size and increase of the number of reflections at the cavity border (at least for the polygonal shapes).

The experimental sensitivity values for the octagons (a = 60μm) and stadiums of the tested size (the shape that we expected to possess the highest sensitivity) were found to be very close, approximately 13nm/RIU (which approximately coincides with numerically predicted sensitivity). Further decrease of the lateral dimensions as well as cavity thickness, that is expected to improve the sensitivity, is problematic for the current cavity architecture as was already mentioned above. Therefore a novel cavity design described in Chapter 5 – cavity on a pedestal – has been implemented and investigated, that weakens the constraints on the cavity size and significantly enhances sensitivity.

4.5.4. *Temperature Influence*

An important question that has been omitted until now is the temperature dependence of the spectral shift. The essence of the problem lies in the dependency of the polymer refractive index on the temperature, due to thermal volume expansion. A smallest variation in the cavity refractive index will lead to the change in the optical path inside the cavity and consequent shift of the resonances. The dependency of effective refractive index on the temperature will therefore be constituted of the dependencies of indices of polymer and claddings:

$$\frac{dn_{eff}}{dT} = \frac{\partial n_{eff}}{\partial n_{polymer}} \frac{dn_{polymer}}{dT} + \frac{\partial n_{eff}}{\partial n_{SiO_2}} \frac{dn_{SiO_2}}{dT} + \frac{\partial n_{eff}}{\partial n_e} \frac{dn_e}{dT} \tag{4-11}$$

The following experimental values of temperature coefficient of refractive indices were taken for estimation: $\frac{dn_{PMMA}}{dT} \approx -1.2 \cdot 10^{-4}$ [140] , $\frac{dn_{SiO_2}}{dT} \approx 1 \cdot 10^{-5}$ [141], $\frac{dn_{H_2O}}{dT} \approx 1 \cdot 10^{-4}$ [142]. The contributions of indices of claddings and polymer into variation of effective index can be calculated using (3) and are approximately: $\frac{\partial n_{eff}}{\partial n_{PMMA}} \approx 0.9$, $\frac{\partial n_{eff}}{\partial n_{SiO_2}} \approx 0.1$, $\frac{\partial n_{eff}}{\partial n_e} \approx 0.02$. The temperature coefficient of effective refractive index is therefore estimated to be of the order 10^{-4}, two orders less than the influence of the medium refractive index that we are measuring:

$$\frac{dn_{eff}}{dT} \approx 10^{-4} \; < \; \frac{\partial n_{eff}}{\partial n_e} \approx 10^{-2} \tag{4-12}$$

In our experimental setup, no temperature stabilization was employed. Though variation of temperature of several degrees may give a measurable influence in the measurement results, we assume that this contribution is negligible. Moreover, within one experiment, all the liquids are kept at the same conditions and are let to flow through the microfluidic chip for a minute or two prior to performing actual measurement, therefore we do not expect to experience temperature variations during the time of experiment. The laboratory where experiment where performed is located in the basement and is air-conditioned, which practically eliminates temperature variations during the day.

4.6. *Detection of heavy-metal ions with microcavity sensors.*

Once we have proven the possibility of refractive index variation sensing with an organic laser microcavities, and found an optimal cavity shape that leads to the highest sensitivity, we can proceed with functionalization of the cavities with specific ligands and detection of heavy metal ions in liquids. The stadium-shaped cavities were verified to generate intense emission with a regular spectrum, corresponding to whispering gallery modes prior to functionalization with mercury-binding thiol groups that was performed as described in part 4.3. Due to the sensitivity of the thiol ligands to oxygen, functionalization was performed right before (at most two hours) performing the sensing experiments and sample was stored in an exsiccator under vacuum. This problem would be absent for the specific ligands synthesized at PPSM, ENS Cachan.

The experiment is performed similarly to the refractive index sensing experiment, but there exist two important differences. First of all, in the case of mercury solutions, the refractive index variation is created locally by the metal ions captured by the ligands, in the thin layer close to the cavity surface. We tried to estimate this variation with ellipsometry, as was described above, but did not obtain coherent results. The refractive index of the mercury solutions, measured by the Abbe refractometer is the same (within the precision of measurement) for all the concentrations and is equal to 1.3345, that of the MES (2-(N-morpholino)ethanesulfonic acid) buffer, used to prepare the solutions. The difference in refractive indices between the solutions of different concentration would complicate the result interpretation: it would be impossible to distinguish, whether the spectral shift comes from the presence of metal ions or from the difference in solution indices. In this case, each spectrum recorded in the analyte solution should be compared to the spectrum recorded in the reference solution with the same refractive index, which would slightly complicate the experiment. Secondly, in the case functionalized, chemical bonds are formed between the analyte ions and ligands. A technique to decomplex the analyte ions should be developed if the sensor is planned as reusable. We have experimentally verified two approaches for release of the bound mercury ions from the ligands: washing the cavities with acidic solutions (PH 1 or PH 3.5) or with dimercaptopropanol, which are known to release mercury from thiol groups [131]. However after treatment with acidic solution, we noticed the changes in the lasing spectra, which may probably occur due to protonation of Pyrromethene dye. Therefore we used dimercaptopropanol that didn't exhibit any negative effects on cavity performance. More details about mercury complexation will be presented in the PhD thesis of Djibril Faye, PPSM, ENS Cachan.

The set of analyte solutions and corresponding washing solutions were obtained from our colleagues. The analyte solutions contain mercury Hg^{2+} in MES buffer with linearly increasing concentration: from 10^{-6}M to 10^{-3}M with 10^{-1} step. The washing solutions contain 2,3-dimercapto-1-propanol at a concentration one order higher than that of a mercury. It has been shown in [154] that the most efficient decoupling of mercury from thiol ligands is achieved in the dimercaptopropanol solution with 50 times higher concentration than that of the mercury. This means, that after injection of $1 \cdot 10^{-6}$M Hg^{2+} solution in a microfluidic chip, washing was performed with $5 \cdot 10^{-5}$M dimercaptopropanol solution and so on.

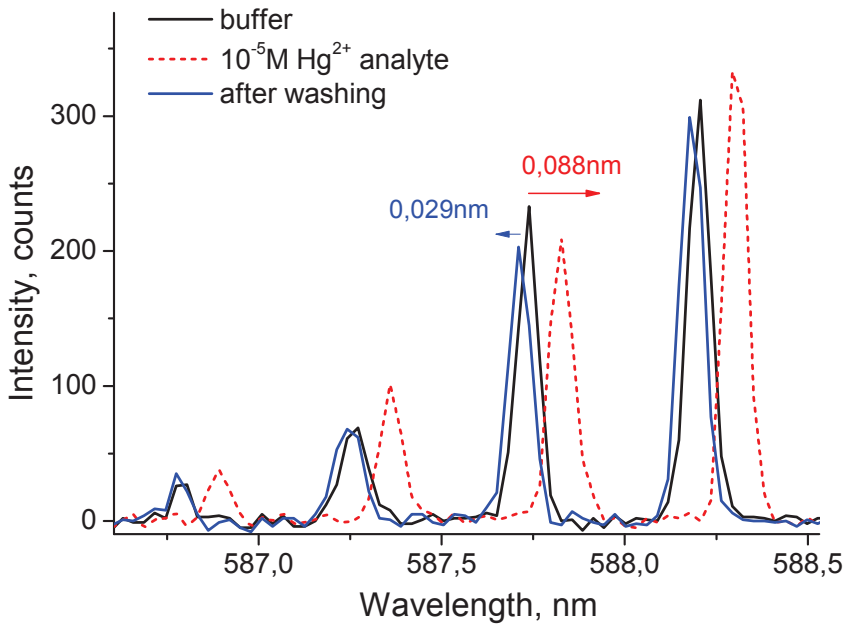

(a)

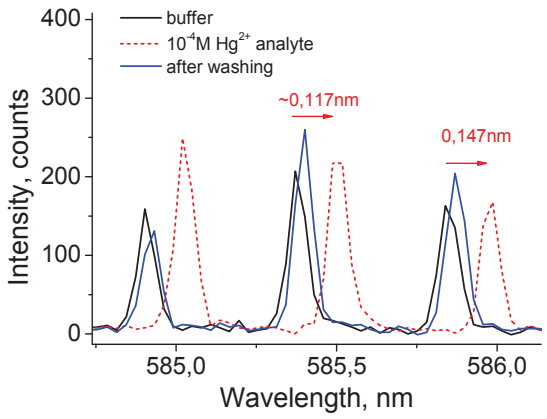

(b)

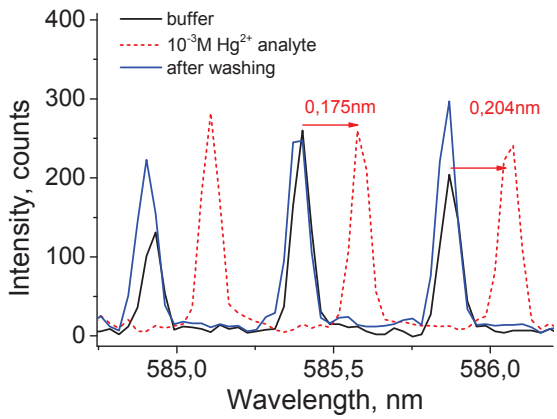

(c)

Fig.4-26. (a) Detection of a 10^{-5}M concentration of mercury ions in analyte solution with a stadium shaped microlaser. The red-shift of 0.088nm is observed in the lasing spectrum. (b), (c) Spectral shifts for 10^{-4}M and 10^{-3}M Hg^{2+} concentrations.

In order to avoid cavity pollution with mercury salts, we varied the mercury concentration from the lowest, 10^{-6}M to the highest, 10^{-3}M, while performing measurements. The solutions are injected inside the microfluidic chip with a pump at the flow rate of approximately 10ml/hour and in the case of a mercury analyte, let inside the chip for 8-10 minutes to increase the amount of ions captured by ligands. No separate study was performed on the rate of complexation/decomplexation of mercury ions by thiols.

Sensing experiments were performed on a stadium-shaped cavity (R=2*l*=50μm), fabricated in PMMA polymer doped with Pyrromethene 605 dye. For the 10^{-6}M Hg^{2+} concentration we didn't detect any changes in spectra. The results presented on Fig.4-26a evidence a clearly detectable red-shift of $\Delta\lambda \approx 0.088$nm between the lasing spectra in buffer solution and in the analyte with 10^{-5}M Hg^{2+} concentration, proving therefore the viability of the sensing approach. The cavity was washed with 3ml of $5 \cdot 10^{-4}$M dimercaptopropanol solution, the clean buffer was injected again and the lasing spectrum restored to its initial position with a slight blue-shift. The actual value of red-shift is slightly smaller if blue-shift correction is taken into account and is therefore approximately $\Delta\lambda = 0.088\text{nm} - 0.029\text{nm}/2 = 0.073$nm. For higher concentrations of mercury, 10^{-4}M and 10^{-3}M, the spectral shift was expectedly stronger, following an approximately linear dependence, and equal 0.146nm and $0.175 \div 0.204$nm correspondingly (Fig.4-26b,c).

Several cycles of washing/analyte injection were performed and similar spectral shifts were recorded for the same analyte concentration. In some cases, like on Fig.4-26b, spectra didn't restore to the initial state after washing but remained slightly red-shifted. Additional, longer washing with dimercaptopropanol led to complete mercury decomplexation (or below the detectable level) and restoration of the spectra. The reference experiment was performed with non-functionalized cavity and no spectral shift was detected, whatever the mercury concentration was.

The obtained results confirmed the possibility of heavy metal ions detection in liquids with concentrations down to 10^{-5}M, however to be competitive with other detection approaches, for instance fluorescence labelling, sensitivity needs to be increased for at least 3 orders of magnitude. In the next chapter we will present the results of mercury detection with pedestal microcavities, featuring enhanced sensitivity.

Chapter V

Pedestal Microcavities

Introduction

In this chapter we will discuss the prospective cavity design – pedestal cavities that should in theory lead to a significant sensitivity increase of a microlaser-based sensor. The technology of the pedestal cavity fabrication was detailed in Chapter 3. First of all the primary difference between the conventional and pedestal cavities will be outlined and the consequences on the lasing spectra and performance will be discussed and supported by numerical simulations. A striking influence of the pedestal geometry on the spectra has been discovered. Afterwards the sensing results will be presented, including refractive index variation sensing as well as mercury ions detection in liquid. Finally, cavities on a low-index CYTOP substrate and all-polymer pedestal cavities will be discussed.

5.1. *Plane substrate vs pedestal.*

The work on the pedestal microcavities started as a search of the ways to enhance sensor performance. Our expectations for higher sensitivity were based on the following two ideas, illustrated on Fig.5-1a:

- First of all, the mode localized in the free-standing region of the cavity will not experience coupling to the substrate, but will interact with the surrounding medium, which will lead to stronger influence on the effective refractive index and consequently sensitivity. The effect is expected to be the strongest for the whispering gallery modes, which are localized in the region close to the cavity circumference. In the case of functionalized cavities, pedestal structure can be considered as an increase of the effective sensing surface, covered by ligands.
- Secondly, the free-hanging cavity part can be considered as a symmetric waveguide: a cavity layer surrounded by two claddings (air) with equal refractive indices. For such a structure there exists no cutoff thickness: at least one vertical mode is always confined in a waveguide. For a whispering gallery mode cavity this means, that if the underetch is made deep enough so that the mode is located inside the freely-hanging part, the cavity can be made thinner (≤ cutoff thickness) than in case when it is supported by the substrate. This in turn will lead to lower mode confinement and higher interaction with the surrounding medium. In other words, geometries with $h/\lambda \leq 0.5$ are achievable (see section 4.4.1).

While the increase of the effective sensing surface is clearly seen from the scheme on Fig.5-1a the weakening of mode confinement in thinner cavities can be conveniently illustrated if we plot a profile of the guided mode in the cavity layer (Fig.5-2). The mode profile was calculated numerically, similar to as described in Annex 1. One can observe qualitatively, that in case of the thinner pedestal cavity (h/λ=0.5) in water (Fig.5-2b) the intensity of the electric field in the vicinity of the cavity surface is higher than in h/λ=1 pedestal case, being approximately 65% of the maximum field intensity compared to ~50% in the former case and ~40% for a cavity without a pedestal. Thus medium index variation or presence of analyte molecules captured by ligands is expected to significantly alter the cavity mode effective refractive index and consequently the lasing spectra.

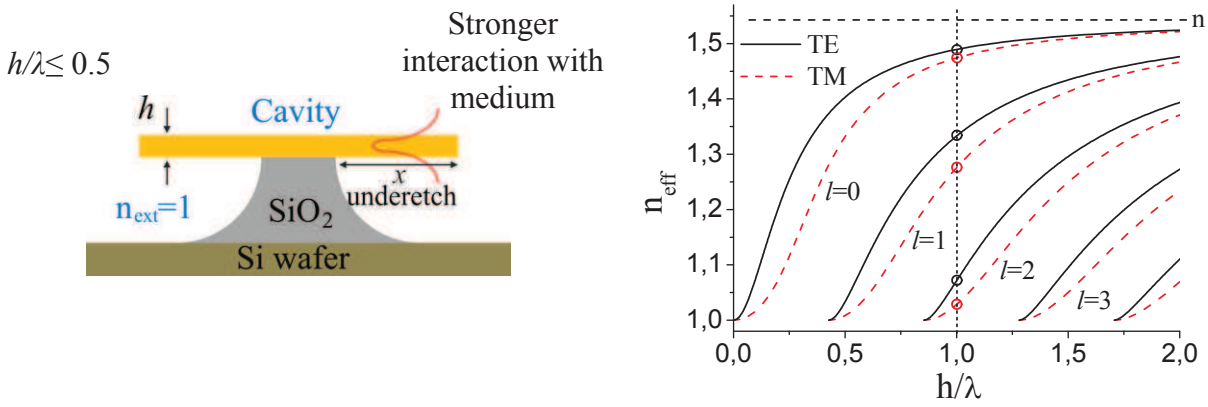

Fig.5-1. a) Illustration of pedestal geometry features. Scale not respected. b) Effective refractive index of a guiding layer as a function of h/λ for the case n_e=1.

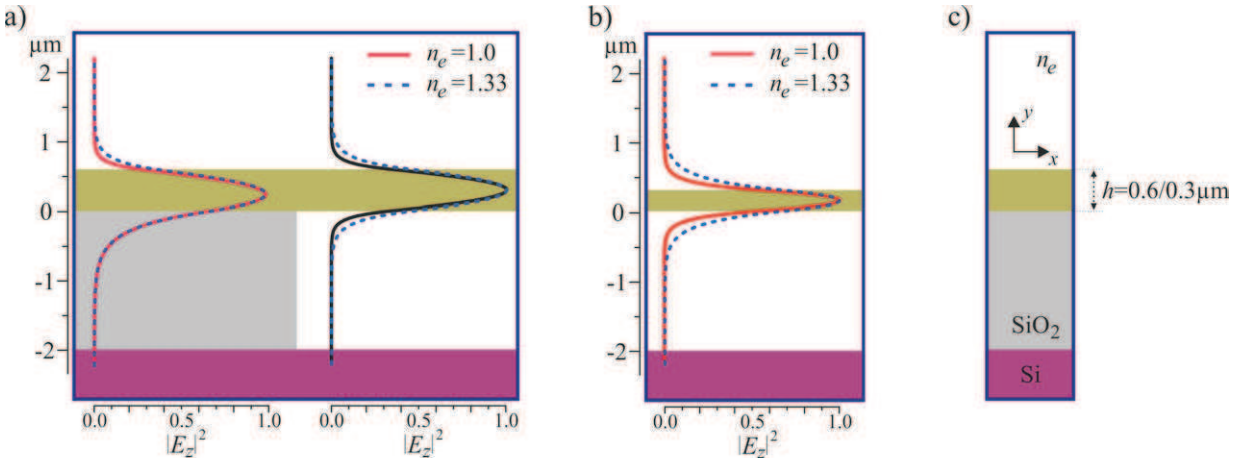

Fig.5-2. The profile of the TE mode propagating in the cavity layer for a) h/λ=1 geometry in the substrate region and in the underetch region; b) h/λ=0.5 geometry, underetch region. n_e - refractive index of the surrounding medium. c) The layout and dimensions of simulation region.

5.1.1. *Vertical modes.*

Another important difference between the pedestal cavities and the ones fully supported by the substrate is illustrated by the dispersion of an effective refractive index on Fig.5-1b. According to Eq. (4-3) the symmetric cavities or waveguides, where the upper and lower cladding indices are equal, can confine up to three TE and TM vertical modes ($l = 0,1,2$) if the layer thickness is equal to the wavelength (h/λ=1) and up to two when h/λ=0.5. The corresponding effective index values for the first three vertical TE modes (h/λ=0.5) are $n_{eff}^{l=0} \approx 1.49$, $n_{eff}^{l=1} \approx 1.33$ and $n_{eff}^{l=2} \approx 1.07$.

The question how the possibility of vertical mode existence will influence the lasing spectra is an interesting one, however difficult to answer. The cavity on the pedestal may be imagined as consisting of two parts: the part supported by the substrate, where only one vertical mode may exist and a free-standing one, where up to 3 vertical modes may be confined. The question

therefore is what will be the configuration of a resulting cavity mode and whether modes with different *l* numbers may coexist in different cavity parts.

The analytical solution of this problem is impossible; therefore we will apply the finite element numerical modeling in an attempt to discover the mode profile. On Fig.5-3a the profiles of the vertical TE modes with *l*=1,2 are plotted for a cavity part with an underetch (n_2=1). The profile of *l*=0 mode can be seen on Fig.5-2a. Now we will try to visualize the mode profiles in a pedestal waveguide structure, depicted on Fig.5-3b, where the left part of the waveguide is supported by a silica substrate and the right part has an underetch. To simplify the task, the simulation has been performed without taking into account the presence of a Si wafer. The depicted structure is a cross-section of an infinite waveguide, where wave propagates along the *z*-axis, and not a cross-section of a whispering gallery mode cavity (disc, for example). Therefore configuration of mode electromagnetic fields found in simulation would be different from the one existing in a WGM cavity. Also, obtained results are not directly applicable for the Fabry-Perot cavities, where resonance occurs along the *x*-axis (in connotations of Fig.5-3b), while here wave propagates along the *z*-axis.

We will try to find out, whether a vertical mode in the underetch part of a waveguide may coexist together with a mode in a substrate-supported part. For this purpose we will look for the guided modes of a pedestal waveguide with the effective indices close to the ones calculated theoretically from Eq.(4-3) for the following cases: 1) TE, *l*=0 mode in a waveguide on silica substrate, 2) TE, *l*=0 mode in a free-standing waveguide (n_2=1), 3) TE, *l*=1,2 modes in a free-standing waveguide. The discovered modes are displayed on Fig.5-3 c-1 – c-6. For the effective index value of n_{eff}=1.50171 close to that of the fully supported waveguide (TE, *l*=0; *n*=1.45; n_{eff}=1.50209) there exists a mode fully localized inside the part of a guide supported by a substrate and which doesn't extend into the right part with an under-etch (Fig.5-3 c-1). A number of transverse modes may also exist, fully confined in the left part of the waveguide with slightly lower effective indices (Fig.5-3 c-2). Here we name "transverse" a mode whose electric filed E_z has multiple maxima along the *x*-axis (Fig.5-3e) as opposite to the fundamental mode, whose E_z component doesn't vary along *x*-axis (Fig.5-3d). Afterwards at n_{eff}=1.48898, close to the index of a free-standing waveguide (TE, *l*=0; *n*=1.0; n_{eff}=1.48940) there appears a mode confined in the part of a waveguide with an underetch coupled to a transverse mode with multiple maxima along the *x*-axis, propagating in the substrate-supported waveguide part (Fig.5-3 c-3). A family of transverse modes with lower effective indices is excited, which are localized both in the supported cavity part as well as in the one with the underetch (Fig.5-3 c-4). Finally, for the n_{eff} values close to that of the first and second vertical modes in a free-standing waveguide, we find that in the right part, the field configuration indeed corresponds to that of the vertical mode with *l*=1 and *l*=2 (Fig.5-3 c-5, c-6), however no energy is guided in the waveguide part supported by the substrate. Instead, there exists a mode, propagating both in the PMMA guiding layer and in the silica substrate. Such mode should have high losses and is unlikely to exist in a real cavity, as the part of the energy coupled into a SiO_2 substrate is guided out of the cavity.

Concluding the results, it seems that the pedestal waveguide structure is most likely to be single-mode in vertical direction and supporting a family of transverse modes. An exception may be a whispering gallery mode cavity, where the underetch is made deep enough so that the mode is entirely localized inside the free-standing part and doesn't "feel" the part of the cavity supported by a substrate. In this case vertical excitations may be found.

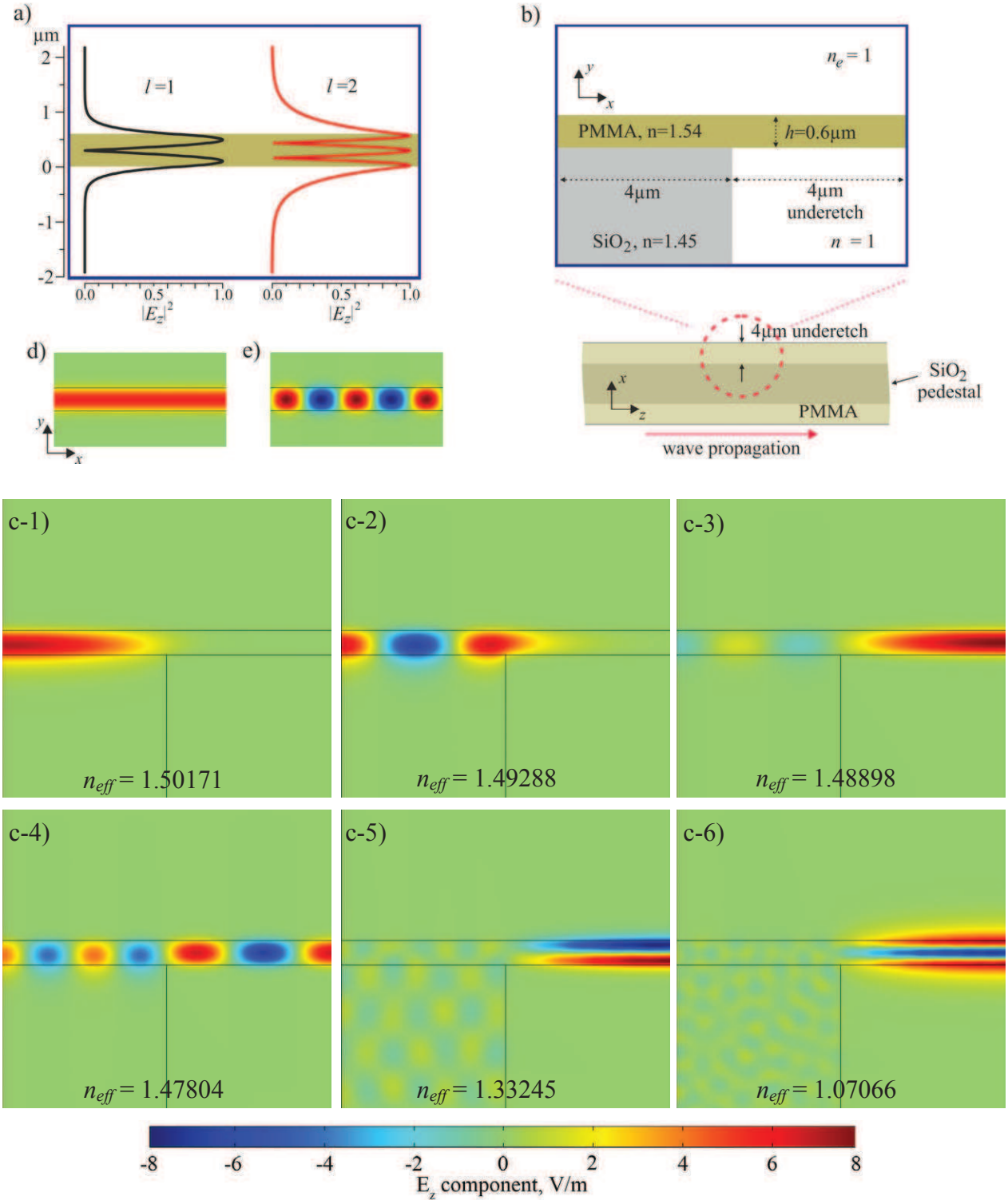

Fig.5-3. a) The profile of the vertical TE mode with l=1,2 propagating in a free-standing waveguide (h/λ=1) obtained from COMSOL FEM simulation. b) Simulation layout of a waveguide, partially supported by a silica substrate. Propagation along z-axis. c-1) – c-6) E_z component of the electric field of a guided mode in a partially supported waveguide. Field distribution for the modes with different effective indices is shown.

5.2. *Pedestal influence on emission properties.*

While studying the emission spectra of the pedestal cavities of various shapes we have discovered many interesting and intriguing effects that require deeper attention and would be described in the following parts, prior to presenting the results of refractive index and heavy-metal ion sensing at the end of this chapter. Alongside with emission intensity increase and lasing threshold diminution an important influence of the pedestal configuration on the cavity lasing spectra was observed, which will be described below on the example of disc and square microcavities.

5.2.1. *Enhanced intensity and lower lasing threshold.*

One of the most appealing effects of the pedestal configuration is a giant enhancement of the microlaser emission intensity, which was observed for all the studied cavity shapes. For instance, the emission spectra of the same Fabry-Perot cavity, fully supported by the substrate and then on a pedestal, are presented on Fig.5-4. Comparison of the spectra under equal pumping fluence evidences a 1000 increase in intensity when the cavity is set on a pedestal. Generally for the same cavity with and without a pedestal we observed intensity increase from 5 to 1000 times, depending on the cavity geometry.

Alongside with the striking intensity increase, we have noticed the diminution of lasing threshold, especially pronounced for the whispering gallery mode cavities. Lasing thresholds were measured with a precision of ±0.01 μJ and were reproducible for identical cavities even on different samples. For instance, thresholds of Fabry-Perot and stadium cavities with different underetch depths are presented on Fig.5-5. To record these dependencies we performed HF etching of the same sample in several steps and measured the underetch depth and lasing threshold for the same cavity after each step. For the Fabry-Perot we observe no significant dependency of the threshold on the underetch depth (Fig.5-5a). The threshold drops slightly after the first etching and almost doesn't change with further increase of the underetch. On the contrary, micro-lasers supporting whispering gallery modes, like stadiums, where modes are expected to be confined close to the edge of the cavity, exhibit threshold several times lower than the same fully sustained cavities. Moreover, with the increase of the underetch we noticed further diminution of the threshold.

We were able to explain these effects by diffraction of the wave at the border of the cavity without pedestal and consequent coupling into the substrate (Fig.5-6a, more details in the next section), thus being the dominant loss influencing lasing. For a Fabry-Perot cavity once an underetch is created the diffractional coupling to the substrate is eliminated thus lowering slightly the threshold (from approx.

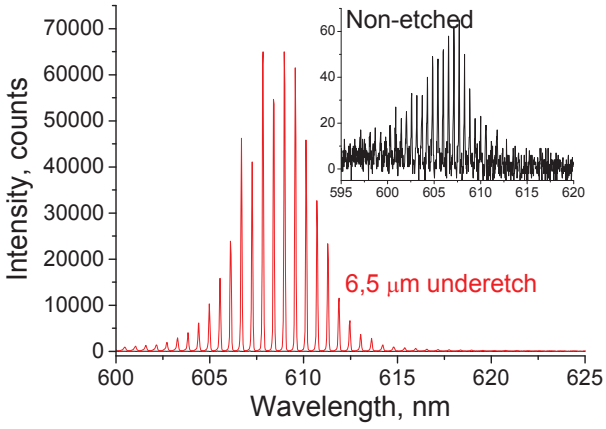

Fig.5-4. Lasing spectrum of the same Fabry-Perot cavity (width = 200 μm) on the plane substrate (inset) and then on a pedestal at an equal pump energy of 0.4 μJ.

0.35μJ to 0.27μJ) and increasing the emission intensity. The small increase of the underetch depth has no further effect on the lasing threshold as the cavity mode is localized all over the volume of the cavity – the underetch constitutes less than 10% of the width of the Fabry-Perot cavity.

On the contrary, for the whispering gallery mode cavities, the diffractional and evanescent coupling losses are reduced over the whole path of light along the cavity perimeter, thus modifying the lasing threshold more significantly than in a Fabry-Perot configuration (from approx. 0.37μJ to 0.14μJ). Further, the WGMs which are localized in the certain volume close to the cavity edge become more confined in the active layer when underetch increases, leading to more efficient conversion of pump energy into laser emission. This explains gradual lowering of the threshold with the increase of the underetch. We expect that once the underetch becomes deeper than the width of mode localization area, the threshold will achieve certain minimal value and will not change any further. Unfortunately, we couldn't verify this guess experimentally, due to the limitation on the underetch depth implied by the wet-etching process.

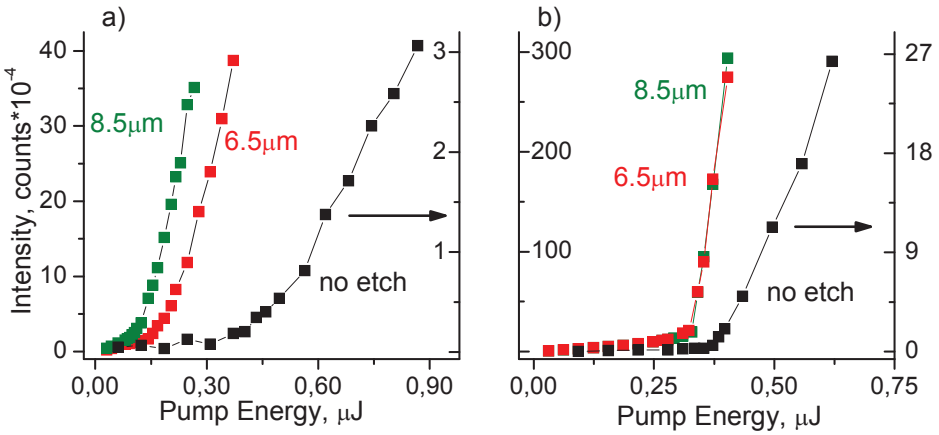

Fig.5-5. Influence of the etch depth (as written on the graph) on the laser threshold: (a) for the same stadium-shaped micro-laser (r = 60μm and r/l = 0.5), and (b) for the same Fabry-Perot micro-laser (width = 200 μm).

5.2.2. *Explanation with numerical simulations.*

Observed influence on intensity and thresholds were confirmed by numerical modeling of the corresponding passive resonators, which emphasizes the crucial role of the substrate coupling. First of all, using COMSOl finite element simulation we modeled the vertical slice of the edge of a Fabry-Perot cavity as a fragment of a 2D passive PMMA waveguide (n=1.54) lying on a SiO_2 (n=1.45)/Si (n=3.48) substrate (Fig.5-6). The plane wave (E_z-polarized) is injected from the left end of a waveguide. In the case of a cavity set on a solid substrate, strong coupling of the guided mode to the silica substrate is seen to occur at the edge of the PMMA waveguide (Fig.5-6a). When the buffer layer is etched, coupling to the substrate at the side of the cavity vanishes (Fig.5-6b).

On the one hand simulation shows that, in the air, wave diffraction at the cavity boundary is considerably reduced in the pedestal case. We monitored the power flow A and B through the segments whose length was chosen to correspond to the collection angle of ~6º of a lens in the experimental setup. The ratio of the power flow for the guides with and without an underetch

was found to be B/(A-C) ≈ 40 units[1], which is large but far from the enhancement by up to 3 orders of magnitude observed for Fabry-Perot resonators. Most probably, non-linear effects connected with lasing must be taken into account.

On the other hand, we observe, that reflection of emission from the Si substrate surface in the case of a pedestal generates a fringe pattern in the far-field (Fig.5-6c), which may significantly influence the intensity of the detected signal. From the simulated field distribution we see that in the case of the pedestal, there exist emission lobes that propagate almost parallel to the substrate and thus fall entirely into the 6° collection angle of the lens. We expect the detected emission intensity to be strongly dependent on the vertical alignment of the collecting lens, and therefore a full 3D emission diagram of the cavity needs to be recorded in order to observe and confirm the existence of fringes experimentally. This will be performed in the thesis of Clement Lafargue, LPQM.

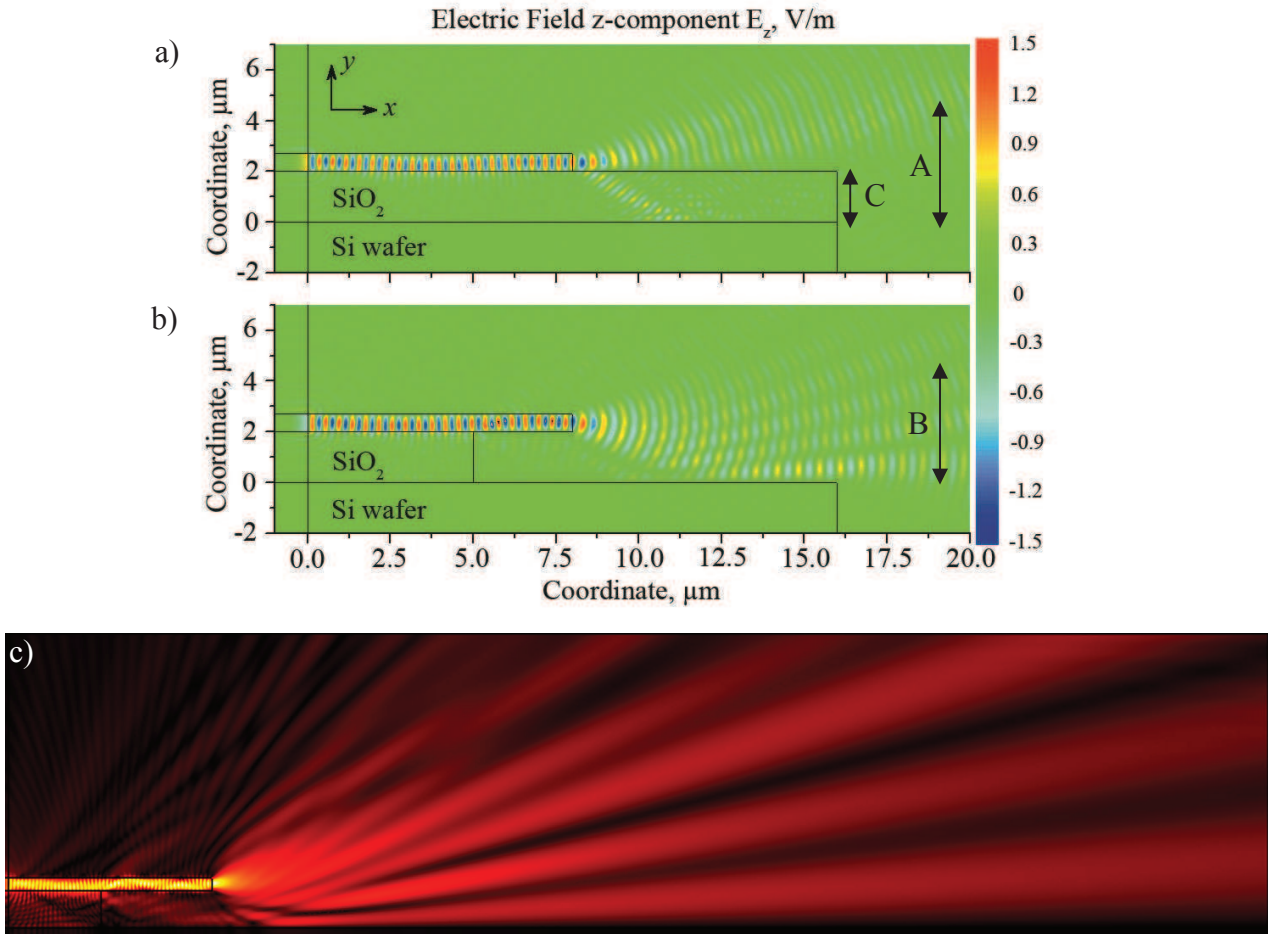

Fig.5-6. Numerical simulations to compare emission from the edge of a PMMA waveguide on a planar silica substrate (a) and on a substrate with a 3µm underetch (b). c) Fringes generated by the emission reflection from the substrate in pedestal configuration. Color gradient represents the z-component of the electric field, E_z [V/m].

[1] The power flow C through the edge of the silica substrate layer is subtracted from A, as the emission coupled into the substrate is attenuated and very unlikely to be detected in experiment.

5.2.3. *New spectral features: disk and square microcavities.*

While studying the emission spectra of various cavities on a pedestal, we noticed that for some cavity shapes the spectra were enriched and consisted of multiple combs of peaks. We studied more attentively the case of a disk and square microcavities.

Disks

In the case of microdisks we have noticed apparition of the whispering gallery modes in the spectrum of the pedestal cavity, while only Fabry-Perot resonances (with orbit along the diameter) are observed from a substrate-supported microlaser (Fig.5-7a). It should be noted, that the modes observed in the spectrum of a disk seem to depend on the quality of cavity etching: for the microlasers fabricated by e-beam lithography, the sidewalls are more vertical and well-defined, therefore FP modes are likely to be seen in the spectrum, while the WGMs remain well confined. On the contrary, for the UV-lithography process, when the cavity walls are more rough, mainly WGMs are observed in the spectrum [94] while FP resonances are suppressed.

Once the e-beam fabricated microdisk is set on a pedestal (underetch approximately 8.5μm), the spectral peaks corresponding to the WGMs are registered (Fig.5-7b). These new peaks are clearly red-shifted with respect to the FP modes and can be observed at the wavelength up to 700nm, although the DCM dye fluorescence is centered at 590nm. The orbit length L, calculated from this new part of spectrum, lies in between the Fabry-Perot orbit length (2*diameter = 500μm) and the perimeter of the cavity ($2\pi R$ = 785μm). Both spectra were registered at equal pumping energy of 0.775μJ and approximately 16 times intensity increase is seen for the pedestal cavity.

The polarization of the pumping beam was perpendicular to the direction of observation, $P_{\parallel}$ in notations of Fig.2-9, which promotes the excitation of a Fabry-Perot resonance that will emit in the direction of a detector. If the pump polarization is set to $P_{\perp}$, the Fabry-Perot resonance is excited along the axis perpendicular to the observation direction and therefore only whispering gallery modes are registered in the lasing spectrum, as displayed on Fig.5-8.

Apart of spectral features, we have also analyzed the polarization of microlaser emission. A linear polarizer plate has been mounted in front of the collecting lens, which allowed selecting either TE (E field in the plane of the cavity) or TM polarization. It turned out that the emission corresponding to WGMs is partly TE partly TM polarized (approximately 60% / 40%), while the part of the spectrum that corresponds to the Fabry-Perot resonance has almost 100% TE polarization, which was commonly observed for Fabry-Perot orbits whatever the cavity shape.

Squares

Similarly, we have observed the enrichment of the lasing spectra of a square microcavity. In the case of a square microlaser fully supported by a substrate, (Fig.5-9a) the spectral comb can be assigned to the diamond periodic orbit as evidenced by the Fourier transform in the inset. The difference in the predicted orbit length L for a given cavity size and obtained from experiment may be due to the slight diminution of the refractive index of PMMA polymer during e-beam exposure. Once the underetch is created (approx. 8.5μm), the spectrum looks very different (Fig.5-9b), featuring multiple superimposed combs, but the dominant periodic orbit remains the

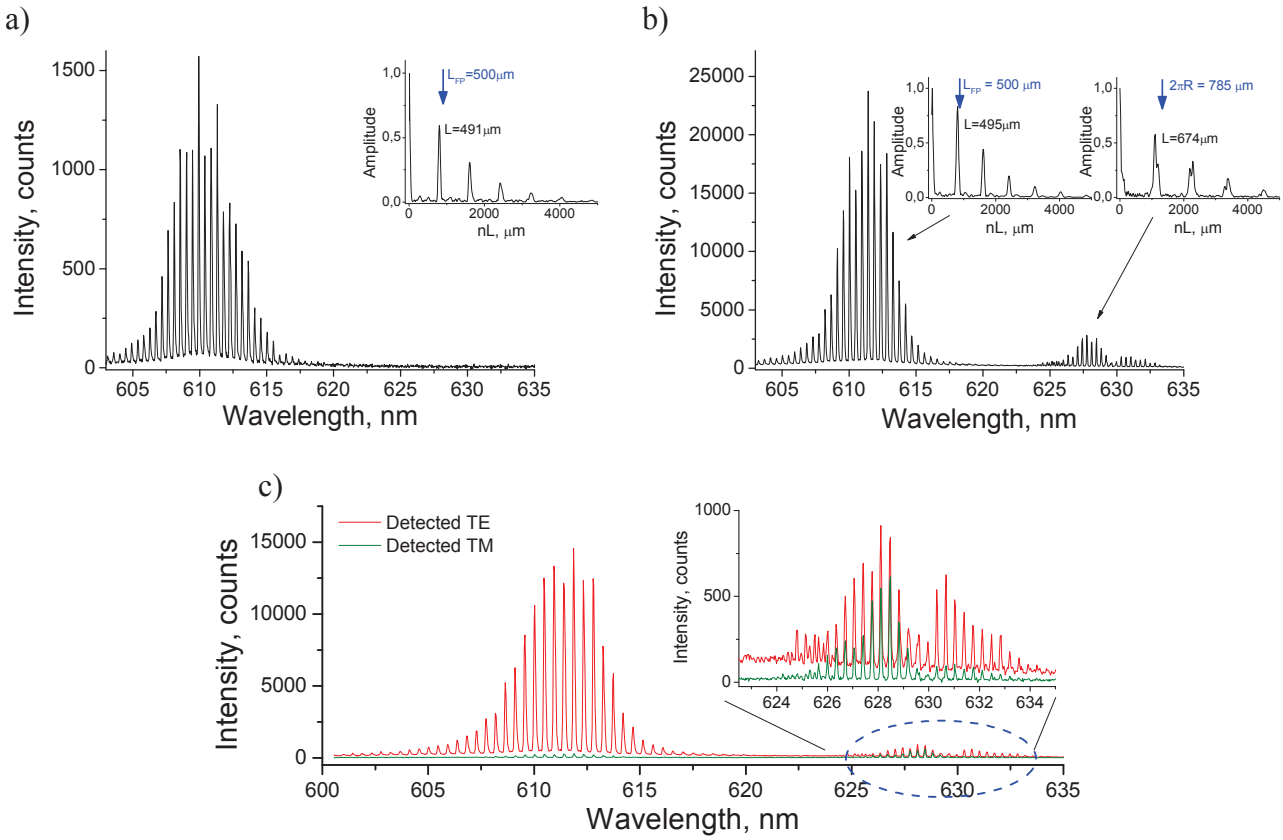

Fig.5-7. a, b) Experimental spectra of the same disk microlaser (r=125μm) without (a) and with (b) a pedestal. The normalized Fourier transforms are plotted in the inset. The blue arrow indicates the expected position of a periodic orbit. c) TE and TM polarization components of the experimental spectrum of the same microdisk on a pedestal.

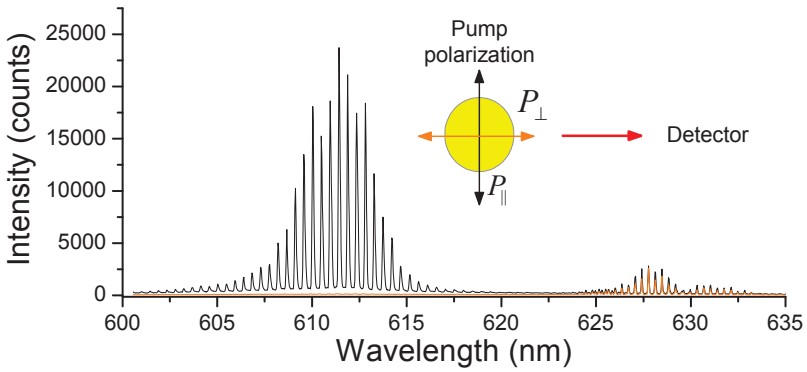

Fig.5-8. Experimental spectra of a disk microcavity (r=125μm) demonstrating the influence of the pump polarization on the disk emission.

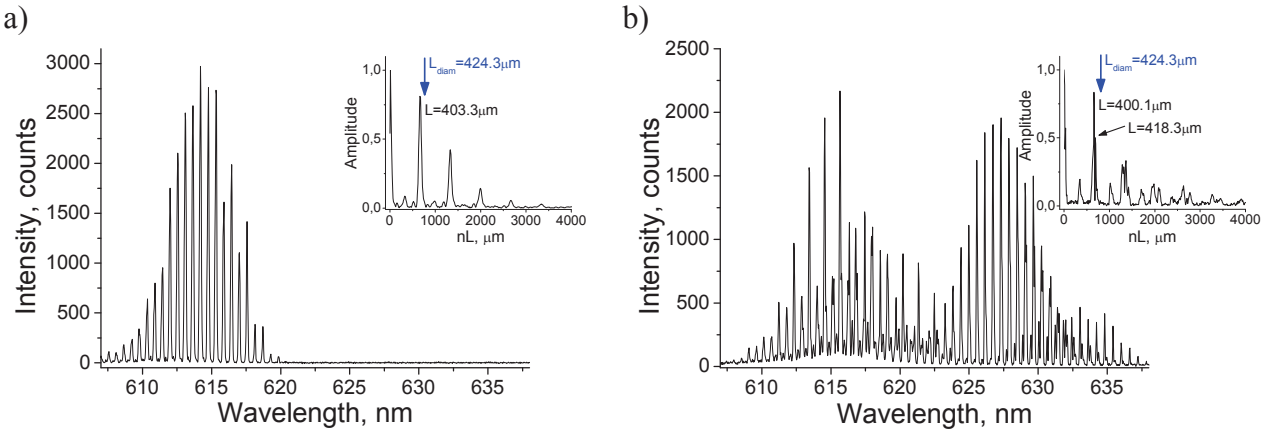

Fig.5-9. Experimental spectra of the same square microlaser (side = 150μm) without (a) and with a pedestal (b). The normalized Fourier transforms are plotted in the inset. Pump energy is 1.24μJ for a cavity without a pedestal (a) and 0.46μJ with a pedestal (b).

diamond one as confirmed by the Fourier transform (see inset). These new peaks may originate from transverse excitations of the diamond orbit as proposed in the superscar model [94] or from higher order vertical excitations that may exist in the free-standing cavity part.

The pedestal geometry was therefore evidenced to influence not only the microlaser emission intensity but also the composition of the spectrum. In the case of microdisks, the whispering gallery modes were observed in the emission spectrum of pedestal cavities, while only Fabry-Perot resonances dominated for the substrate-supported disks. In case of the squares, the spectrum was enriched, while the observed orbit remained a diamond one. The pedestal geometry is thought to influence both the modes excited in the cavity and the out-coupling processes, allowing us to see the modes that would be otherwise suppressed by the losses connected with the substrate presence.

5.2.4. *Hot-spots and angular emission diagrams.*

Another pointer at the importance of the 3D effects and light diffraction at the cavity boundary are the top-view photographs of the cavities under pumping (Fig.5-10). The photographs were taken by a digital photo camera, mounted on the optical microscope that is used to align the pump laser beam with the cavity. The scattered pump laser emission was filtered out with a rejection filter. The square microcavities are uniformly pumped, while for the Fabry-Perot, the pump beam diameter is larger than the width but smaller than the cavity length.

For a square microcavity without (Fig.5-10a) and with a pedestal (Fig.5-10b) bright hot-spots are observed at the cavity corners, designating the zones where cavities emit vertically and probably present a strong diffraction. While for the Fabry-Perot cavity, the emission (bright line) is distributed all along the boundary (Fig.5-10c). Due to constraints on the set-up, the microscope is slightly tilted and the field of view partially obstructed which leads to slight non-symmetry in photographs (different intensity of hot spots at square corners and Fabry-Perot edge). By rotating the cavities at 180º we made sure that the emission is indeed symmetrical.

A deeper study of the out-coupling mechanisms in square microcavities, probably employing near-field techniques, as well as 3D observation of emission patterns are needed to

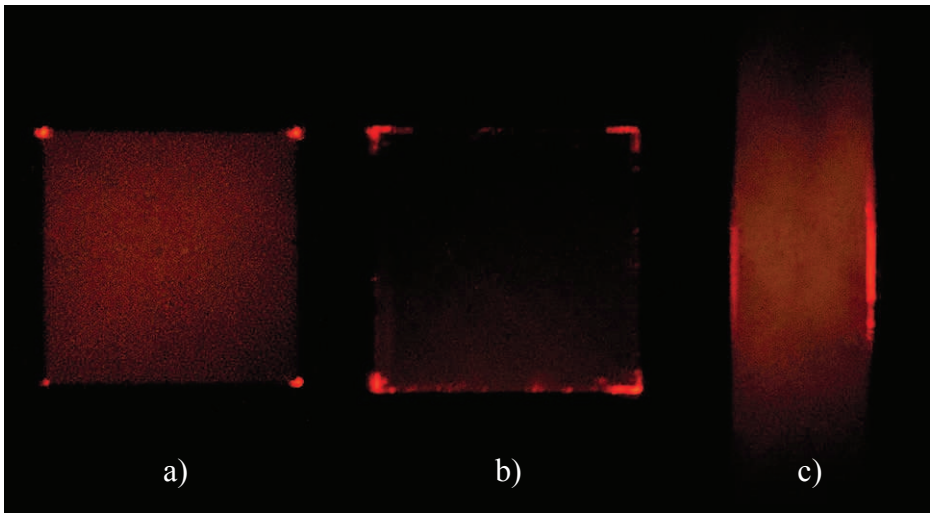

Fig.5-10. Top-view photographs of microlasers under pumping. a) Substrate-supported square micro-laser, side 120μm, pump 0.6μJ. b) Pedestal square micro-laser, side 150μm, pump 0.3μJ. c) Substrate supported Fabry-Perot microlaser, width 120μm, pump 0.8μJ.

explain the observed hot-spots and the difference between the pedestal and ordinary cavity geometry.

Finally, among the other manifestations of pedestal microcavity geometry, we have observed significant changes in the angular emission diagrams of microlasers of different shapes. Emission diagrams are the key pointers to the out-coupling processes [138, 139, 143-145] therefore changes in emission directions may provide a clue to deeper understanding of resonances existing in cavities of complex shapes and help explain influence of the pedestal geometry.

We have observed intriguing changes in the angular emission diagrams of the square-shaped and rectangular-shaped microcavities. For the cavities, fully supported by the substrate (Fig.5-11a,c), the emission was highly directional, featuring 4 symmetric lobes for the square microcavity and two lobes for a rectangular-shaped cavity (ratio of length to width is 2:1). Once on the pedestal, emission lobes broaden substantially and the high directionality is lost (Fig.5-11b,d). For the rectangular cavity, the direction of maximum emission was inversed and is now parallel to the long side. However the loss of directionality cannot be ascribed purely to the presence of the underetch or to the etching quality: the emission of the pentagon micro-laser remains highly directional both in the case of a substrate-supported cavity and in the pedestal case. The broadness of peaks in the case of substrate supported pentagon (Fig.5-11e) is explained by the noise: the signal to noise ratio can be improved by increasing the pump energy which eventually leads to the lobes as narrow as in Fig.5-11f but with a more significant dye bleaching. The intensity of emission lobes for a pedestal pentagon cavity varies from cavity to cavity.

The observed phenomena highlight the crucial issue of dynamical coupling between the amplifying medium and the passive modes of the resonator. The presence or absence of a substrate seems to play a determining role in shaping the emission of microcavity lasers. The pedestal configuration is as well a convenient way to improve the performance of microlasers, namely to increase emission intensity at a lower lasing threshold. The comprehensive explanation of the observed effects requires additional studies, and work is now in progress to

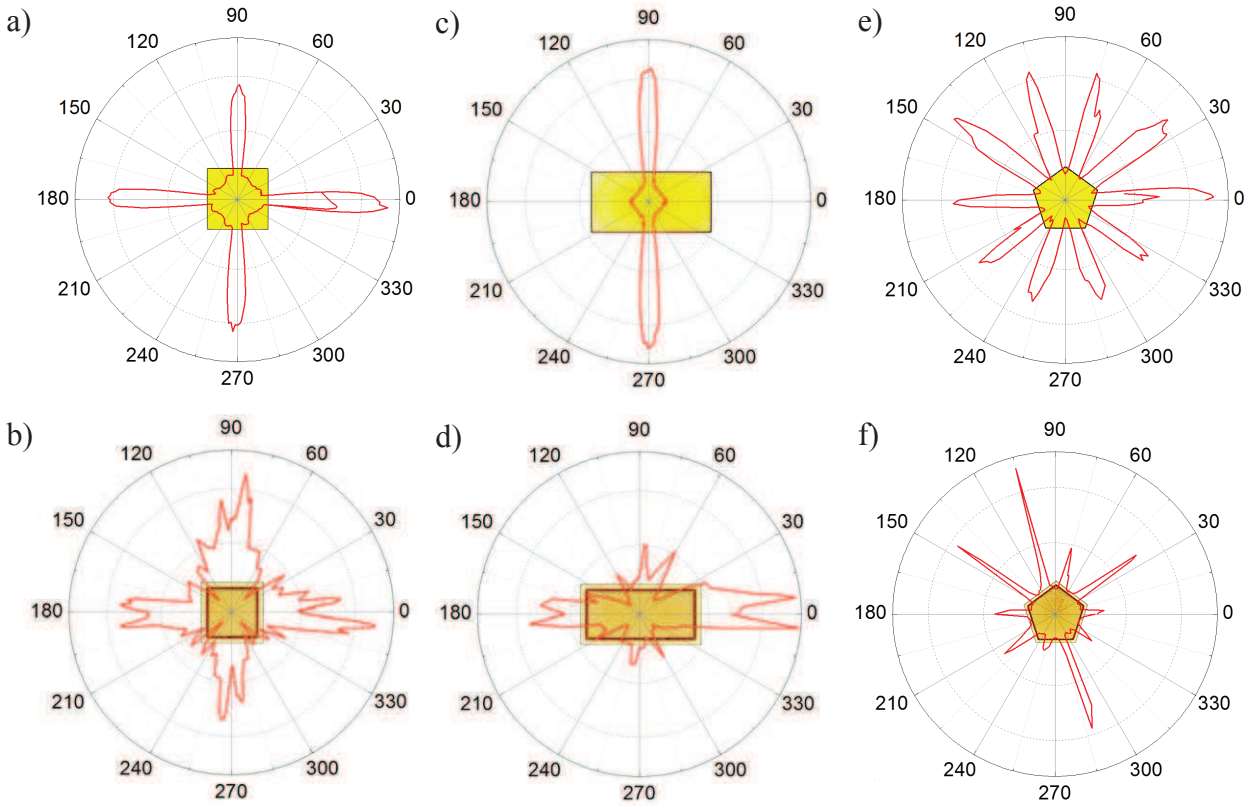

Fig.5-11. Experimental angular emission diagrams of microlasers with (b, d, f) and without (a, c, e) a pedestal under circularly polarized pump beam just above lasing threshold. Photographs of the cavities are superimposed to point out the orientation. (a, b) Square with side 150µm; (c, d) rectangle with length/width ration of two, width 75µm; (e, f) pentagon with side 90µm.

achieve deeper insight into nature of resonances and light out-coupling processes in cavities of various shapes.

5.3. *Pedestal influence on sensitivity.*

In order to understand, how the pedestal geometry will influence the refractive index sensitivity of microlasers we have analyzed the expected spectral shift in response to the variation of refractive index of surrounding medium. In the 2D-model used in Chapter 4, the presence of the underetch is not expected to influence the phase of the wave upon reflection at the cavity borders, therefore only contribution coming from effective refractive index is considered. However, the presence of a pedestal makes the problem more complicated than in the case of substrate-supported cavities, studied in the previous chapter. The impact on effective refractive index may change drastically depending on the resonator shape, region of mode localization and underetch depth: if the mode is localized in the free-standing cavity part, it is significantly more sensitive to medium index changes and vice versa. Therefore, at the beginning we will consider a simpler case of a Fabry-Perot cavity, whose single and understandable periodic orbit makes quantitative analysis easier and then we will move to whispering gallery mode cavities, were analysis is mostly carried out numerically.

5.3.1. *Effective refractive index in pedestal geometry.*

While for the substrate supported cavities the Eq. (4-3) used to calculate the mode effective refractive index can be applied directly, it will not work for pedestal cavities, as it is valid only in the case of infinite claddings surrounding a waveguiding layer. An assumption has been made, that the optical length of the pedestal cavity can be represented as a sum of two terms: the optical length of the part of a cavity supported by a substrate and the optical length of a free-standing part, both calculated with the appropriate effective refractive indices obtained from Eq. (4-3).

This approximation can be easily applied in the case of a Fabry-Perot cavity, where the wave propagates perpendicularly to the cavity walls and therefore the percentage of the cavity mode, localized in a free-hanging part and in the part supported by a substrate can be calculated. The lasing condition in a Fabry-Perot cavity in the pedestal case becomes:

$$\frac{2\pi}{\lambda}\left(n'_{eff}\cdot 2(L-d)+n''_{eff}\cdot 2d\right)=2\pi m \qquad (5\text{-}1)$$

where L is the length of the cavity, $d=2x$ is the total length of the underetch part, n'_{eff} and n''_{eff} are the effective refractive indices for the part of the cavity supported by the substrate and free-standing one correspondingly, calculated using Eq. (4-3).

In order to verify the correctness of this assumption a set of experiments was carried out. We observed the evolution of a Fabry-Perot microlaser spectrum during the HF etching process, by recording the emission of the same cavity before the first etch and then after each etching step. If we write the Eq. (5-1) for a cavity on a substrate and for a cavity with an underetch $d=2x$, the wavelength shift between the two spectra can be expressed as:

$$\frac{\lambda_2-\lambda_1}{\lambda_1}=\frac{d}{L}\left(\frac{n''_{eff}}{n'_{eff}}-1\right)<0 \qquad (5\text{-}2)$$

where λ_1, λ_2 are the positions of spectral peaks for a substrate supported cavity and a cavity with underetch d correspondingly. It turns out that the shift is negative, i.e a blue-shift should be observed in the experiment, as the underetch depth increases. The experimental spectra for a 200µm wide Fabry-Perot resonator ($h/\lambda=1$) fabricated in PMMA+DCM 5% with 3 different underetch depths are presented on Fig.5-12a, where we indeed observe a notable blue-shift of the peaks for each subsequent HF etching step. The comparison between experiment, calculation by Eq. (5-2) as well as numerical 2D FDTD simulation is shown on Fig.5-12b, where spectral shift $\Delta\lambda$ is plotted as a function of the underetch depth, while the spectral peak position for a substrate supported cavity (before etching) is taken as zero. The experiment shows that the blue-shift increases linearly with the underetch, as predicted by calculations, however the slopes of experimental and calculated curves are different, which evidences a presence of a systematic error. The 2D FDTD simulation was performed similarly as described in Annex 1 (§1.1), for a 200µm long Fabry-Perot cavity ($h/\lambda=1$) with different underetch depths and a good agreement with calculations was found, as shown in Fig.5-12b.

Multiple factors may be a cause of an error and difference between the experimental and theoretical curves. The calculation error consists of the error of determination of refractive index of DCM doped PMMA polymer (±0.01; value of n=1.54 taken for calculation) and the error of measurement of underetch depth with optical microscope (±0.2µm). The error in the value of polymer refractive index has the highest impact, considerably changing the slope of the curve.

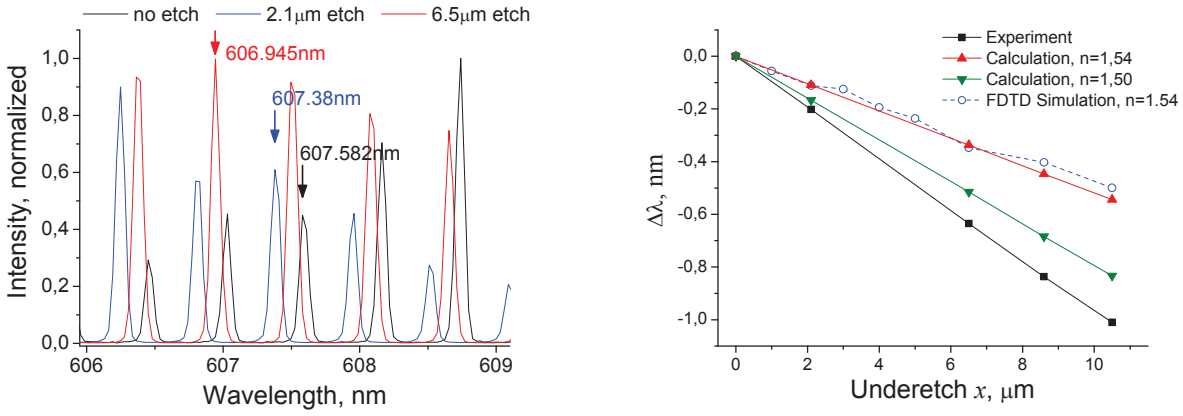

(a) (b)

Fig.5-12. a) Shift of the emitted spectrum depending on the etch depth for a Fabry-Perot microlaser and three underetch depths (width = 200μm, pump = 0.47μJ) Arrows point at peak positions.b) Comparison of experimental blue-shift with theoretical prediction (Eq. (5.3)) and FDTD simulation.

For comparison, the calculation for the polymer index of n=1.50 has been performed and plotted on Fig.5-12b, resulting in a closer correspondence with the experiment. Though refractive index of the polymer may be slightly decreased during e-beam exposure, it is unlikely to be so much different for the initial one. The source of discrepancies may be hidden in experimental values. First of all, it is a blue-shift due to the dye degradation that, summed up with the blue shift caused by underetch presence increases the slope of experimental curve. The blue-shift due to dye degradation, as was already mentioned, is hard to quantify precisely and no corrections were applied to the experimental data. The second very important issue is the transverse modes. The 2D calculation of effective indices by Eq.(4-3) is performed for a fundamental mode of an infinite layer, however in a real cavity a family of transverse modes with lower effective indices may exist, similar to what is displayed on Fig.5-3(c-4). The 2D FDTD simulation performed here also doesn't account for the presence of transverse modes. Taking into account the mode calculation results presented on Fig.5-3 and described in part 5.1.1, the cavity mode that exists both in substrate-supported part of a cavity and in the part with the underetch is very likely to have an effective index lower than the one obtained from Eq.(4-3). The difference in effective indices may be entirely responsible for observed discrepancies between experimental and predicted blue- shift values, however most probably, all of the abovementioned error sources play their role to a bigger or smaller extent.

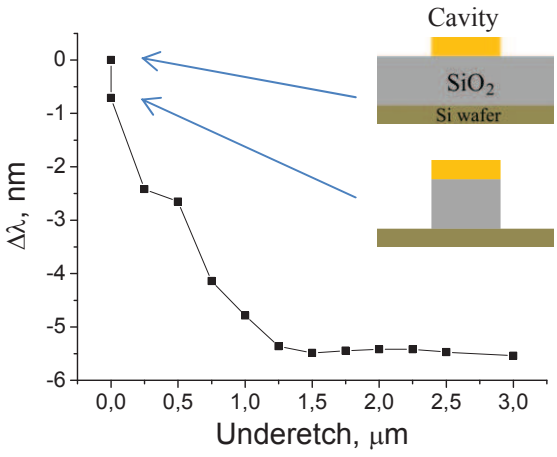

Fig.5-13. Dependence of numerically calculated blue-shift of the stadium cavity spectrum on the etch depth. Shift of the spectral peak at ~600nm is followed.

While we cannot unambiguously name the cause of discrepancy, we may conclude that effective index approximation remains

robust even in the non-trivial case of pedestal cavities as shown on Fig.5-12 and adequately describes the behavior of a system despite the difference in numerical values.

To further verify the validity of approach for whispering gallery mode cavities, we performed a 3-dimensional FDTD simulation for a stadium shaped cavity (r=2l=5µm, h/λ=1), while gradually changing the underetch depth and observed evolution of the resonance spectrum. Obtained result (Fig.5-13) confirms the qualitative explanation of the processes occurring in a pedestal cavity: for small underetch depths, an increasing blue shift is seen in the spectrum, similarly to Fig.5-12b. As the underetch increases further, the blue-shift reaches saturation which means that primary part of the mode energy is now localized in the free-standing section of the cavity, and according to accepted approximation, the resonance spectrum is now mostly determined by the effective index of a mode in a free-standing cavity part. Similarly to the simulation of pedestal cavity sensitivity, there are two points on the graph that correspond to the underetch of 0µm: the first one is related to the cavity on the infinitely wide substrate and the second one to the pillar configuration. The saturation is observed for the underetch depth $x \geq 1.5$µm, which is consistent with the refractive index sensitivity simulation, performed in the section 5.3.3. No quantitative calculation has been performed for this case as well as no experimental verification has been carried out for the WGM cavities.

5.3.2. *Sensitivity of a Fabry-Perot cavity*

Having obtained the proofs of validity of effective index approach, we may now analyze the spectral shift due to variation of the medium refractive index, which can now be approximately expressed as:

$$\Delta\lambda\big|_{\Delta\phi=0} = \frac{\lambda}{n'_{eff}\cdot\left(1-d/L\right)+n''_{eff}\cdot d/L}\cdot\left(\left(1-d/L\right)\cdot\frac{\partial n'_{eff}}{\partial n_e}+d/L\cdot\frac{\partial n''_{eff}}{\partial n_e}\right)\Delta n_e \qquad (5\text{-}3)$$

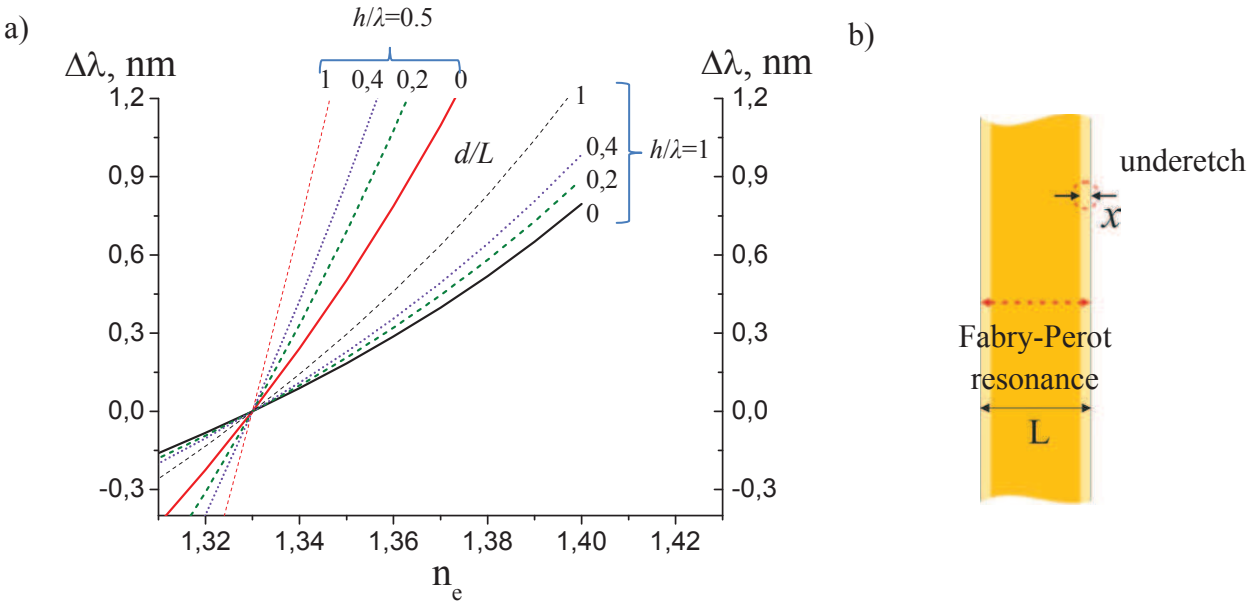

Fig.5-14. Calculated influence of the medium index variation (n_e) on the Fabry-Perot cavity spectral shift due to effective refractive index change for several d/L ratios. b) Illustration of a Fabry-Perot cavity on a pedestal (view from the top), showing the underetch.

where n_e is the refractive index of the medium surrounding the cavity. If the cavity is fully supported by the substrate (underetch depth d =0), Eq. (5-3) transforms into Eq. (4-4). Generally, we would expect the abovementioned approach to be adequate if the underetch d is longer than a wavelength in the cavity material.

In order to illustrate the influence of the underetch on the cavity sensitivity, a family of $\Delta\lambda = f(n_e)$ curves is plotted on Fig.5-14 for TE mode, h/λ=1; 0.5 geometries and several d/L ratios (0, 0.2, 0.4, 1). The ratios d/L =0 and d/L =1 are the limit cases when the cavity is either fully supported by the substrate (same as Fig.4-13a) or entirely free-standing, therefore pedestal influence on the spectral shift is limited by these two boundaries. In fabricated samples, d was usually $\leq 20\mu m$ ($x \leq 10\mu m$) while Fabry-Perot cavity dimensions lie within 100÷250μm, meaning $d/L \leq 0.2$.

Comparing the calculated data, we can conclude, that at h/λ=1 geometry presence of the pedestal with $d/L = 0.2$ increases the spectral shift $\Delta\lambda$ approximately 1.12 times and in $h/\lambda = 0.5$ geometry – 1.37 times in response to the medium index variation of $\Delta n_e = 0.01$. Hence, we conclude that the sensitivity of Fabry-Perot cavities is moderately enhanced by the presence of the underetch: in the fabricated samples, the free-hanging part constitutes only a fraction of the total cavity length (which in turn means that the cavity mode is mostly localized in the part supported by the substrate) and the ratios $d/L > 0.2$ are hardly achievable, for the reasons described in § 3.5.2. On the contrary, for the whispering gallery mode cavities, where entire mode is localized along the cavity edge, the underetch part is expected to significantly influence the spectral shift. For this reason, sensing experiments have been performed immediately with the stadium-shaped cavities.

5.3.3. *Sensitivity of stadium-shaped cavities.*

For the whispering gallery mode cavities the approach similar to the one described above may be attempted: the ratios d/L and $1 - d/L$ in Eq. (5-3) should be replaced by the weighting factors, corresponding to the spatial localization of the mode (percentage of the mode energy in a free-hanging part and in a substrate supported part). Qualitatively, this would mean the following: we expect spectral shift to increase gradually as the underetch becomes deeper and reach a saturation level after a certain depth, which would mean that the mode is primarily localized in the free-standing cavity party and is virtually not affected by subsequent etching. However such approach is hardly useful in practice, as the weighting factors cannot be determined from geometrical dimensions of the cavity. While for the Fabry-Perot resonator, the width and underetch depth explicitly define the percentage of the mode energy in both cavity parts, for the whispering gallery mode cavities, the exact volume occupied by the mode remains unknown, it may vary depending on the cavity dimensions and can be found, for instance, from numerical simulation. Therefore, we analyzed the sensitivity of a stadium shaped WGM cavity using a 3D FDTD simulation.

The simulation was performed for a stadium cavity with dimensions r=2l=5μm and two thicknesses: 600nm and 300nm (ie. h/λ=1 and h/λ=0.5). The underetch depth x was varied and for each value of x we swept medium refractive index in the range 1.330 ÷ 1.340 thus obtaining a set of curves $\Delta\lambda = f(n_e)$. From the distribution of electric field of cavity modes we can visually determine that for the substrate-supported cavity the maximum electric field intensity is observed in the band of approximately 1.5μm wide along the circumference of the cavity. Example of

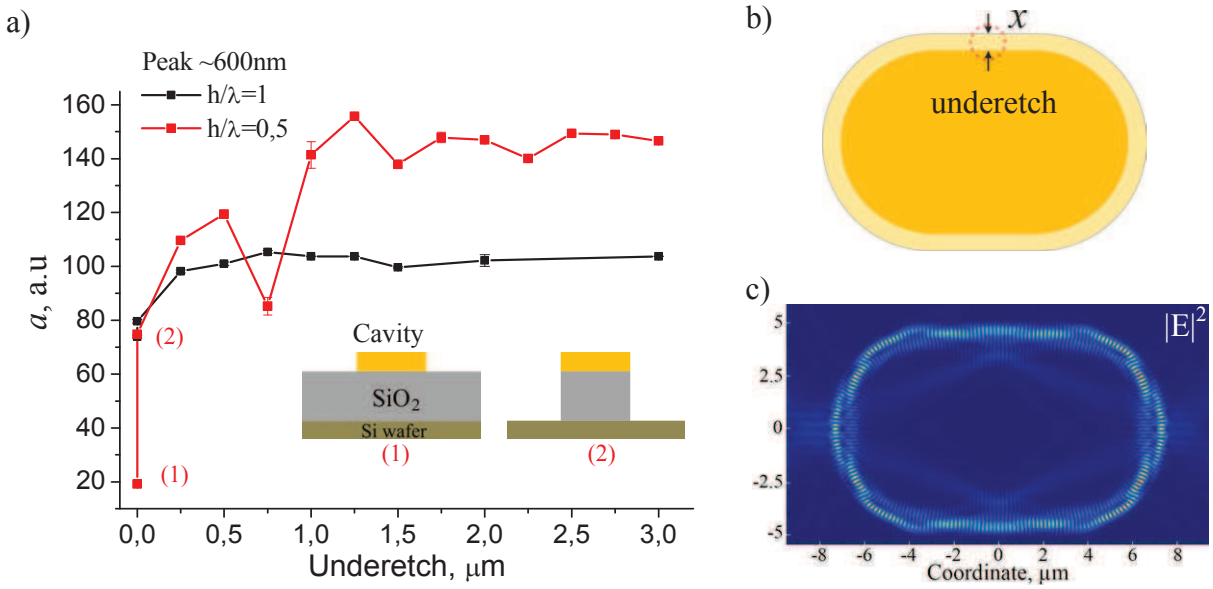

Fig.5-15. Simulated influence of underetch depth x on the stadium cavity spectral shift. b) Illustration of a stadium cavity on a pedestal (view from the top), showing the underetch. c) Electric field intensity distribution of a cavity mode in a substrate supported stadium.

electric field distribution for one of the resonances close to λ=600nm is shown on Fig.5-15c. Therefore, we can expect, that while the underetch depth x is lower than 1.5μm, the spectral shift will strongly depend on x. Once underetch becomes deeper than 1.5μm, the dependence should become weaker and finally reach certain saturation level.

As in the previous chapter, we assumed that the wavelength shift is linear in the selected range of indices and therefore can be represented as $\Delta\lambda = a(x)\cdot\Delta n_e$, where $a(x)$ is the slope for each underetch depth x, which takes into account both influence of the phase incursion and effective refractive index change. The $a(x)$ dependency is plotted on Fig.5-15a and agrees well with our qualitative expectations: the saturation of sensitivity is achieved for underetches $x \geq 1.5$μm. However, this result shouldn't be generalized: as we see from the plot, the mode in a stadium cavity has a complex distribution of electromagnetic field, and one cannot assert without additional study that the field distribution will be preserved for different cavity dimensions. It is probable, that for larger stadium sizes, as the ones used in experiment, the mode extends inside the cavity deeper than for 1.5μm, and therefore sensitivity saturation may be observed at different (larger) underetch depths.

An interesting feature is observed in simulated dependencies for the zero underetch depth (x=0μm): there are two points plotted on the graph, both corresponding to the substrate-supported cavity, but in the first case (called (1) in Fig.5-15a), the substrate is infinitely wide and in the second case (called (2) in Fig.5-15a), it has the lateral dimensions equal to that of the cavity (so-called pillar configuration). A drastic change in spectral shift is observed for h/λ=0.5 ratio when the cavity passes from the infinite substrate to pillar geometry. This effect cannot be predicted in our theoretical estimate, based on 2D effective index model, but is clearly evidenced in simulations. We could not fabricate the pillar cavities on a silica substrate with facilities available to us in order to verify the sensitivity increase experimentally. This effect however paves the ground for the pillar cavities on low-index CYTOP substrate, whose manufacturing

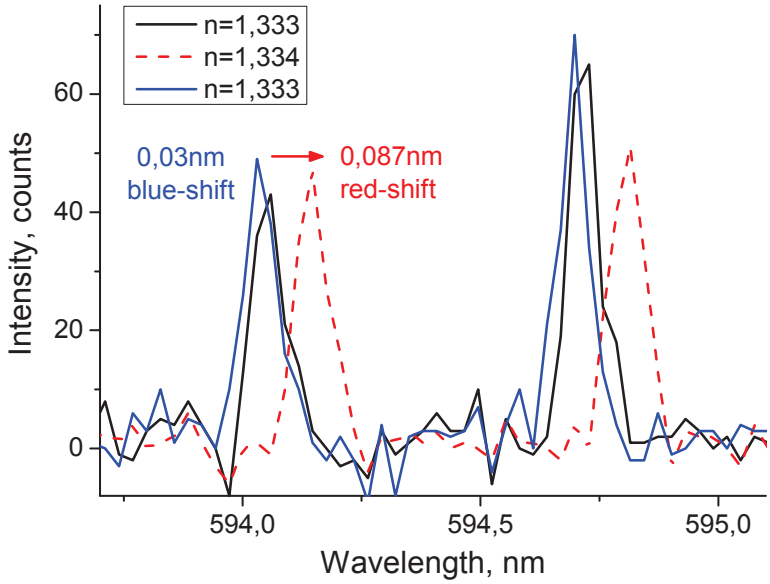

Fig.5-16. Refractive index sensing with a stadium-shaped PMMA pedestal microlaser. A red shift of approx. 0.09nm is observed for the analyte refractive index change of Δn=0.001 units. The spectrum restores its initial state with a slight blue-shift upon analyte removal (blue). Pump energy is 1.55μJ.

technology was described in Chapter 3: being more robust and safer in fabrication than the silica pedestal cavities, their sensitivity is expected to be of the same order of magnitude.

5.4. *Refractive index variation sensing with pedestal cavities.*

For the pedestal cavities, the sensing experiments were performed immediately with the stadium shaped microlasers, which have proven to exhibit the highest sensitivity. Moreover, to further boost the performance, we fabricated the cavites with h/λ=0.5 ratio: after immersion in HF acid solution for 90 minutes that created a 15μm deep underetch, another oxygen plasma etching was performed, that reduced the thickness of cavities to approximately 300nm. It should be noted, that 15μm was the maximum underetch depth that we could achieve with wet etching for a 600nm thick PMMA cavities. The attempts to create a deeper underetch always resulted in a collapse of a free-standing part.

The experiment was performed on a stadium microlaser with the dimensions r=2l=50μm, fabricated with UV-lithography in PMMA polymer doped with 5% Pyrromethene 605 dye. The experimental setup and measurement protocol were exactly the same as for the substrate-supported cavity. The cavities are sealed inside the microfluidic chip and a series of spectra is recorded inside the solutions with different refractive indices. As we expected the sensitivity of pedestal stadium to be superior, the glucose concentration was chosen in order to create a solution with the refractive index of 1.334 (that would give a Δn=0.001 in comparison with distilled water). The experimental lasing spectra presented on Fig.5-16 demonstrate a red-shift of approximately 0.09nm for the variation of analyte refractive index of 0.001 units. This value is almost 6 times higher than the shift registered for the substrate supported cavity: the approximate extrapolated sensitivity of a pedestal stadium microlaser reaches 90nm/RIU while for the

substrate-supported stadium it was 13nm/RIU. Though the energy of pump beam was decreased to the minimum, a blue-shift was observed in all the recorded spectra.

Due to the very high memory requirements, the FDTD simulation cannot be run for the cavity sizes used in experiment, but nevertheless an attempt to estimate the pedestal cavity sensitivity using the data of 2D and 3D simulations may be undertaken. We expect, that the effective refractive index contribution to sensitivity ($\Delta\lambda^{index}$) does not depend on the cavity dimensions. The latter is taken into account by the phase-dependent contribution ($\Delta\lambda^{phase}$). Therefore, we may estimate the $\Delta\lambda^{index}$ for the pedestal stadium from a 3D simulation, performed for a small cavity and then account for the cavity size by taking the appropriate value for $\Delta\lambda^{phase}$ from a 2D simulation (Fig.4-24). For example, the 3D simulation performed above for a stadium cavity with $r = 5\mu m$ takes into account both effective index and phase incursion contributions. Therefore, the effective index contribution for the cavity of any size would be $a^{index} = a - a^{phase}_{r=5}$ = 145 – 44 = 101, where a is the slope in a linear dependency $\Delta\lambda = a \cdot \Delta n_e$; $a \approx 145$ is taken from the Fig.5-15a and $a^{phase}_{r=5} = 44$ is taken from Fig.4-24. Then, for the cavity with $r = 50\mu m$ used in the experiment we obtain: $a = 101 + a^{phase}_{r=50} = 101 + 8 = 109$, which gives $\Delta\lambda = 109 \cdot 0.001 = 0.109nm$, a value very close to the one obtained experimentally (0.087nm; may be underrated by the blue shift). Of course, multiple measurements for the cavities of different sizes need to be performed in order to claim a good agreement between the experiments and simulations, but at least we may see that such approach yields an approximately correct result.

Concluding the results, we have experimentally confirmed the enhanced sensitivity of pedestal whispering gallery mode microlasers to the medium index variation (90nm/RIU against 13nm/RIU for the substrate-supported). A good agreement with numerical simulation was achieved. If higher sensitivity is to be reached, several approaches may be considered. First of all, porous polymer may be utilized as an active medium. While attempts performed within this thesis with polystyrene based polymers didn't lead to any improvement in sensitivity, this may only mean that more research on porous materials should be carried out. Another approach that requires deeper study would consist in using systems of coupled resonators. Coupling efficiency may be strongly influenced by the medium refractive index thus remarkably increasing the overall system sensitivity. Finally, a more straightforward way would be to decrease the size of the stadium cavity: as simulation results on Fig.4-24 evidence, a phase-dependent sensitivity contribution for a stadium with the radius $r = 25\mu m$ should be two times higher, and for a stadium with $r = 5\mu m$ – 9 times higher than for the ones, used in experiments ($r = 50\mu m$). Smaller cavity sizes should be achievable if substrates with lower refractive index and/or more efficient laser dyes are used and also if more elaborate emission detection system is employed.

5.5. *Detection of heavy-metal ions with pedestal microcavity sensor.*

After obtaining the proofs of enhanced sensitivity of pedestal cavities, we have repeated the experiment of mercury ions detection in liquid solution. For this purpose a sample with h/λ=1 stadium-shaped cavities was fabricated in PMMA doped with 5% Pyrromethene 605. The sample was treated for 30min with HF acid to create an underetch of approximately 4.5μm. We have intentionally reduced the depth of the underetch for this experiment and didn't further thin the cavities to increase the mechanical durability. Actually during the functionalization step the cavity undergoes multiple immersions in liquids and some other manipulations that may

potentially collapse the fragile pedestal cavities. Afterwards, the cavities were functionalized as described in §4.3, and sealed into PDMS microfluidic chip.

Mercury sensing experiment was performed on a stadium cavity with the radius of r=2*l*=50μm, following the same measurement protocol as in the case of substrate supported cavity. We started with 10^{-6}M Hg^{2+} solution in MES buffer and the resulting lasing spectra are shown on Fig.5-17. First of all a spectrum in pure MES buffer was recorded. Afterwards, we injected 1ml of Hg^{2+} analyte, let it flow thorough the chip at 14ml/hour and recorded the first spectrum (not shown on the plot). A red-shift of 0.145nm was clearly detected. Once again 1ml of Hg analyte was injected at the same velocity and the second spectrum was recorded, exhibiting a red-shift of 0.174 with respect to the clean buffer reference. The injection was repeated two more times and each time a gradual increase of the red-shift was observed. The spectrum on Fig.5-17 demonstrates the resulting red-shift of 0.232nm after 4 injections of 1ml of mercury analyte.

Then the cavity was washed with 3ml of $5 \cdot 10^{-5}$M dimercaptopropanol solution, however the spectrum didn't restore to the initial position. Two more washing steps with the same concentration of dimercaptopropanol were performed, however we couldn't achieve a full restoration of the lasing spectrum, as it was with substrate-supported cavity – spectral peaks remained red-shifted for 0.116nm (blue curve on Fig.5-17). We therefore didn't proceed with lower mercury concentrations.

On the one hand we have successfully demonstrated the enhanced sensitivity of a functionalized pedestal cavity and detected the 10^{-6}M concentration of mercury solution. We demonstrated the gradual red-shift of the lasing spectrum after each analyte injection which may be probably explained by the increase of number of mercury ions captured by the ligands. On the other hand, the red-shift was not completely reversible and the spectrum didn't restore to the initial position. The only explanation we could think of is connected with the presence of the underetch: due to the worse circulation of the washing solution in the thin gap under the free-standing cavity part there may be remaining mercury ions bonded with the ligands. The circulation may be even more obstructed by microscopic air bubbles, which can be trapped within the gap near the pedestal.

Further experiments are needed in order to estimate the maximum achievable sensitivity with functionalized pedestal cavities and also to verify whether the irreversibility of lasing spectrum was a one-time problem or it is regularly persisting. Taking into account the large spectral shift observed, we may expect that at least 10^{-7}M mercury concentration can be detected with a pedestal stadium microlaser.

While showing promising results in terms of sensitivity, pedestal cavities possess inherent flaw connected with the presence of a thin gap, where liquid circulation may be complicated or completely obstructed by micrometer-scale air-bubbles or sediment particles. While air bubbles can be relatively easily released if their presence is discovered, the microscopic particles depending on their nature may be very hard to remove from the thin gap and once trapped inside, may permanently alter the spectrum of a microlaser. Moreover, taking into account higher fragility of pedestal cavities, a non-pedestal configuration is preferred for implementation in operational sensing systems. In the next section, we will see the implementation of a prospective pillar microcavity on a low-index polymer substrate, which due to a number of advantages may be preferable over the pedestal geometry.

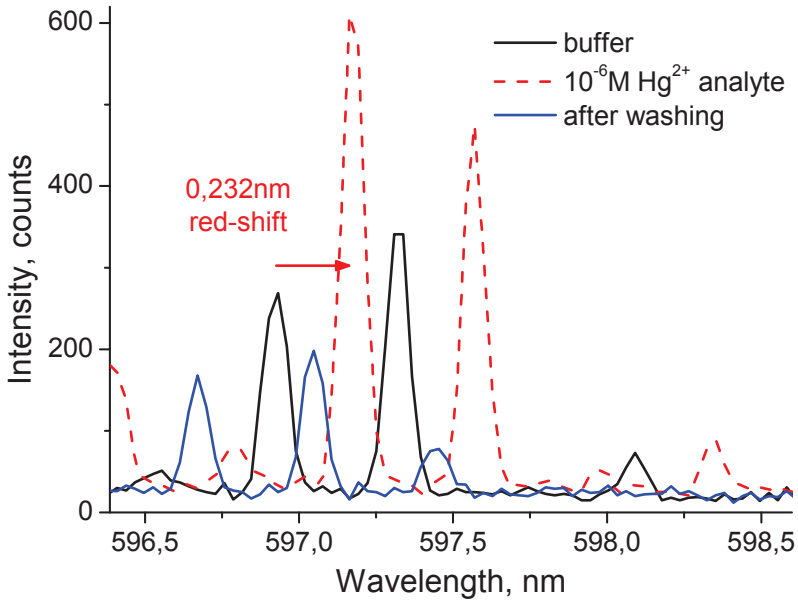

Fig.5-17. (a) Detection of a 10^{-6}M concentration of mercury ions in analyte solution with a pedestal stadium shaped microlaser. The resulting red-shift of 0.232nm is observed in the lasing spectrum after 4 injection of mercury solution.

5.6. *Pillar microcavities on low-index substrate*

The technology of fabrication of microcavities on a polymer pillar was explained in Chapter 3. Being safer in fabrication than pedestal microcavities, pillars are expected to exhibit the refractive index sensitivity of the same order of magnitude, basing on the results of numerical simulations performed in the previous paragraph. In this section we will introduce the advantages of pillar cavities over their silica-substrate predecessors and present the results of refractive index variation sensing.

5.6.1. *Pillar vs silica substrate cavities.*

The idea of a pillar microcavity (Fig.5-18a) came up and developed from the attempts to increase the refractive index contrast between the cavity and a substrate and so to increase mode confinement inside the active layer by reducing substrate coupling. There exist several polymer materials on the market, belonging to the class of fluoropolymers, which are compatible with spin-coating and have their refractive indices in the range 1.34 ÷ 1.36, significantly lower than that of the silica (n=1.45). Use of such a material as a substrate for PMMA resonators should lead to a better cavity mode confinement and as a consequence, lower lasing thresholds and higher emission intensities than in the case of a silica substrate. The CYTOP fluoropolymer was chosen as a substrate material due to its low refractive index, $n \approx 1.34$ at $\lambda = 600$nm and good compatibility with spin-coating technique.

The reduced index of a substrate changes the waveguiding properties of the PMMA layer: while still supporting only one vertical mode in h/λ=1 geometry, the cutoff thickness for a

fundamental TE mode is reduced to $h_{\min}^{TE} = 184\ nm$ (compared to 255nm for silica substrate), that may allow creating thin cavities ($h/\lambda < 0.5$) whose strong evanescent field, similarly to the pedestal case, will interact with the surrounding medium and lead to a higher sensitivity. It may happen though, that the minimal thickness at which the microlasers can function would be determined not by the cutoff thickness, but by the volume of the active medium, or in other words, by the gain/loss ratio. A small cavity volume may have insufficient gain for the laser generation to occur. Therefore the minimal thickness may be different for various lateral dimensions of the cavity. This question was not studied in details and further experiments are needed before any conclusions can be drawn.

It is during the first manufacturing attempts, that we realized that a pillar configuration can be easily created (see section 3.5.3). A pillar cavity may be a worth competitor to the silica pedestal configuration: it possesses some of the advantages of pedestal cavities while overcoming their major drawbacks. Firstly, diffractive coupling into the substrate at the edge of the cavity, which is the major source of losses influencing lasing, is eliminated in the pillar geometry. This effect cannot be predicted using the model based on effective refractive index which we developed for the analysis of the pedestal cavities, however was observed in the numerical simulations. Combined with the higher confinement of mode in the active cavity layer this should lead to lower lasing threshold and higher emission intensities than for the equivalent cavity on a silica pillar. Unfortunately, we cannot fabricate a cavity on a silica pillar in order to compare their characteristics, and comparison between a CYTOP pillar and a silica pedestal would be incorrect. Secondly, a dangerous HF etchant is eliminated from the technological process and, finally, the mechanical durability of pillar cavities is similar to that of the substrate supported analogues as the fragile free-standing part is absent here.

Among the weak points were pillar cavities lose to their pedestal competitors, are the impossibility to achieve quite the same confinement for the whispering gallery modes: while in the pedestal cavity with a sufficiently deep underetch we may expect a whispering gallery mode to be mostly localized in the free-standing cavity part, for the pillar cavities, the mode will always feel the presence of a substrate. Also, if we consider sensing applications, functionalized pedestal cavities of the same dimensions possess larger surface of contact with the analyte than the pillars, which may allow them to capture a larger number of analyte molecules and play a decisive role in their higher sensitivity. All of these drawbacks (though not the fragility) may be overcome in the pedestal CYTOP cavities, whose manufacturing technology we tried to implement (Chapter 3), however no measurements have been performed yet with the CYTOP pedestals except the experimental confirmation of their functioning: the pedestal stadium cavities with 2.7μm underetch described in §3.5.4 were generating laser emission.

While we haven't performed quantitative comparison of the pillar and pedestal cavity performance, we observed very similar tendencies: emission intensities for the micropillars are significantly stronger than for the substrate supported cavities and lasing spectra are observed at approximately the same pump energies as in the pedestal case which evidences a lower threshold. For example for the Fabry-Perot cavities, we observe a strong amplification of signal for a pillar cavity in comparison with a silica substrate-supported cavity of the same width (Fig.5-18b), similar as it was evidenced for pedestal microlasers. The results on Fig.5-18b should be treated rather illustrative than quantitative, as the spectra were recorded from the cavities on

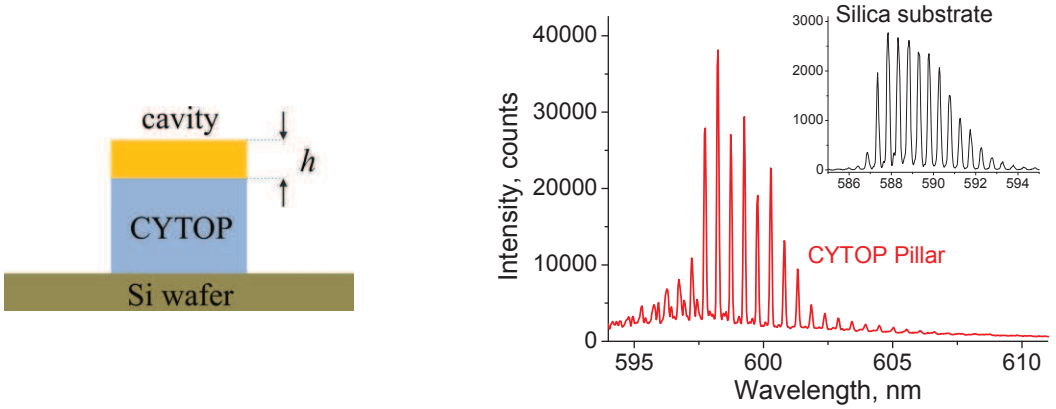

Fig.5-18. a) Illustration of a microcavity on a low-index polymer pillar. Scale not respected. b) Lasing spectrum of the same Fabry-Perot cavity (PMMA+Pyr605 5%, width = 200 µm) on the silica substrate (inset) and then on a CYTOP pillar at an equal pump energy of 0.4 µJ.

different samples at different time, which means that small variations in the dye concentration are possible and cavity thickness was slightly different.

Also, stadium cavities of a small size (r=2l=30µm), which do not normally function in the substrate-supported configuration, were emitting an intense spectrum, which paves the way of increasing the sensitivity to refractive index variation by reducing the cavity size. Once we obtained the proof of their functioning, we proceeded immediately with the refractive index sensing experiments with stadium-shaped cavities.

5.6.2. *Refractive index variation sensing with pillar microacvities.*

A sample containing stadium shaped pillar cavities was fabricated in PMMA + Pyr605 5% as described in Chapter 3 and an additional oxygen plasma etching was performed to further thin the cavities and boost the sensitivity: the final structure consisted of an approximately 360nm thick stadium microcavity supported by a 3.1µm thick CYTOP pillar. We intentionally did not approach too close to the cutoff thickness, as we were not sure whether the cavity will still function.

The sensing experiment was performed in exactly the same manner as previously. We have clearly detected a red-shift of approximately 0.06nm in the lasing spectrum of a stadium (r=2l=60µm), once the glucose solution with a refractive index of 1.334 was injected inside the microfluidic chip and the spectrum has restored to its initial position after washing with distilled water (Fig.5-19). The achieved sensitivity therefore reaches 60nm/RIU, which is almost 4 times higher than for the silica substrate-supported cavity (13nm/RIU) though slightly lower than for the pedestal cavity (90nm/RIU). Strictly speaking, we cannot compare the pedestal and pillar stadium cavities used in experiment due to their different thickness (approx. 300nm for the pedestal one and 360nm for the pillar one) and lateral dimensions, however most probably the sensitivity of the pillar cavity of the same dimensions will still be slightly lower due to a higher mode confinement and smaller surface of contact with the analyte.

The parameter a from $\Delta\lambda = a \cdot \Delta n_e$ dependency have been also calculated for CYTOP pillar cavities by FDTD method and was found to be $a \approx 105$. Doing similar calculation as in case with

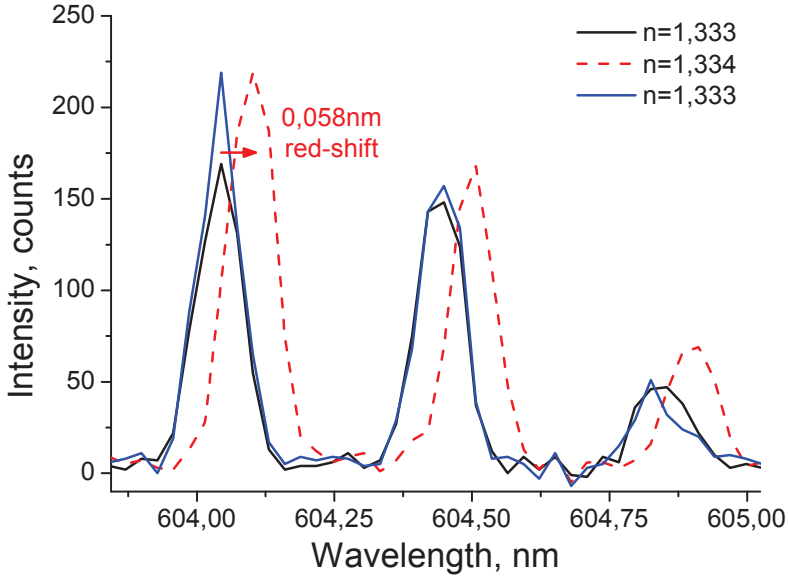

Fig.5-19. Refractive index variation sensing with a stadium-shaped PMMA microlaser on a CYTOP support. A red shift of approx. 0.058nm is observed for the analyte refractive index change of Δn=0.001 units (Sensitivity ≈60nm/RIU). The spectrum restores its initial state upon analyte removal (blue). Pump energy is 0.37μJ.

the pedestal cavities, spectral shift of $\Delta\lambda = 0.069$nm can be obtained for a $h/\lambda = 0.5$ cavity. This result is also in a good agreement with experimental measurement.

We have not yet performed the experiments with functionalized pillar cavities, as well as with pillar/pedestal cavities of smaller size, that may lead to significant increase in sensitivity to refractive index variation.

Conclusions

The novel cavity design – cavities on a pedestal and cavities on a pillar – have been studied and described in this chapter. A number of remarkable properties of the pedestal cavities have been discovered that enhances their performance both as a microlaser and as a sensor in comparison with the substrate supported cavities. From the fundamental point of view, diminution of lasing threshold, striking increase of emission intensity as well as enrichment of laser spectra, changes in angular emission diagrams and discovery of hot-spots present a great interest. These observations allow deeper understanding of processes occurring in complex (in the case of a stadium – chaotic) open electrodynamical systems and shed light on the out-coupling processes as well as diffraction at cavities' dielectric borders.

On the application end, pedestal cavities have demonstrated significantly enhanced sensitivity both to refractive index variation of the surrounding medium as well as to analyte ion concentration, once they are functionalized. A simple approach based on effective refractive index model has been proposed to predict the sensitivity of Fabry-Perot cavities on a pedestal. For the stadium cavities that support whispering gallery modes, the sensitivity to medium refractive index variation was increased up to 7 times and reached 90nm/RIU. Numerical simulation of the sensitivity of a pedestal stadium cavity to refractive index variation has been performed and a good agreement with experimental data was found. For the functionalized

stadium cavities, one order of magnitude in sensitivity was gained, and detection of 10^{-6}M concentration of Hg^{2+} in liquid solution was demonstrated, though lasing spectra were not completely reversible.

Finally, pillar microcavities on low-index CYTOP substrate have been fabricated and have demonstrated similar enhanced performance both in terms of laser characteristics (increased intensity and lower thresholds) as well as sensitivity to refractive index variation – spectral shift up to 60nm/RIU have been obtained.

Conclusions

In this thesis we have studied the application of polymer microcavity lasers for chemical sensing, more precisely, for the detection of heavy metal ions in water for environmental monitoring purposes. The goal of the work was to fabricate a prototype of a Lab-on-Chip sensor capable of detecting traces of heavy metal (Hg^{2+}, Pb^{2+}, Cd^{2+}) ions in drinking water through the change of the emission spectra of microlasers. We present the proofs of viability of such sensing approach.

The first two chapters lay out the scientific interest and novelty of the work, followed by a brief theoretical reminder of the principles of wave guiding and confinement. A rationale for the choice of polymer materials as cavity body is given, emphasizing the ease of functionalization with ligands, biocompatibility, low cost and simplicity of technological processes, easy integration with microfluidics. Experimental setup for emission spectra recording of microlasers is described and data processing techniques are explained.

The fabrication technique of microlasers is detailed in chapter 3, explaining the fabrication of conventional silicon substrate-supported cavities, pedestal cavities, and cavities on a low-index CYTOP polymer substrate that opens the way to all-polymer Lab-on-Chip design. The description of the used polymers – PMMA and porous polystyrene based polymers (PS-b-PAA, PS-Co-PAA, PS-P4VP) is given followed by the study of laser dye photostability in polymer matrices. Performance of porous polymers was inferior to that of PMMA: we observed fast dye degradation during storage in ambient conditions and ligand grafting led to reticulation of polymer layers (§4.3). Preliminary fabrication attempts of microcavities by laser ablation and 2-photon polymerization are reported, performed in cooperation with Laser Centrum Hannover, demonstrating poor suitability of laser ablation for polymer structuring and promising results of 2-photon polymerization.

Two applications of laser microcavities have been studied: detection of the refractive index variation of the medium by the non-functionalized cavities and detection of heavy metal ions in liquid by functionalized cavities. For this purpose the microfluidic chip has been developed that allows optical pumping and recording of the emission spectra of microlasers immersed in liquids (§4.2).

We have experimentally demonstrated for the first time the wavelength shift in the lasing spectra of the non-functionalized active microcavities in response to variation of the refractive index of the medium, surrounding the cavity. Two cavity types have been studied: polygonal cavities and stadium-shaped cavities which support whispering gallery modes. The analytical (for polygonal cavities) and numerical FDTD analysis (for WGM cavities) of the influence of the cavity shape on sensitivity to index variation were performed and obtained results are in a good agreement with the experiments. Experimentally observed sensitivity to refractive index variation is approximately 14nm/RIU for the substrate-supported microlasers of both types. Meanwhile, the proof of mercury ions detection in liquid with functionalized stadium-shaped microcavity (PMMA+Pyrromethene 605) have also been obtained – a 10^{-5}M

Hg^{2+} concentration has been detected via a red-shift in the lasing spectrum, which is reversible after the cavities are washed with dimercaptopropanol, that releases mercury from ligands.

The ways of sensitivity improvement have been proposed and explored in Chapter 5 with pedestal and pillar microcavities supporting whispering gallery modes, which have demonstrated significantly enhanced sensitivity both to refractive index variation of the surrounding medium as well as to analyte ion concentration, once they are functionalized. Almost 7 times higher sensitivity to refractive index variation was registered with pedestal cavities (~90nm/RIU) and almost 5 times higher with pillar cavities on CYTOP substrate (~60nm/RIU). Obtained sensitivity values are comparable with reported in literature [19, 79] for microspheres and planar microcavities. The FDTD numerical modeling of pedestal and pillar cavities yielded sensitivity values very close to experimental. The functionalized stadium cavities demonstrated a gain of one order of magnitude in sensitivity and detection of 10^{-6}M concentration of Hg^{2+} in liquid solution is reported, though spectral shift was not entirely reversible.

Alongside with enhanced sensitivity, pedestal microcavities were discovered to possess a number of interesting properties in comparison with substrate supported cavity: reduced lasing threshold, stronger emission intensity, unexpected angular emission patterns. Explanation attempt of the observed effects is undertaken in §5.2

While successfully proving the possibility of chemical sensing with functionalized microlasers, this work lays down a basis for future research, both fundamental and applied. On the fundamental end, the problem of emission of pedestal microlasers may be studied. Diffraction on the dielectric edge of a microcavity, a problem yet unsolved analytically, is thought to play an important role in shaping the microlaser angular emission patterns. Recording of full 3D angular emission diagrams may shed light on the outcoupling processes and help develop theoretical models describing emission of different cavity shapes. On the more applied end, many problems still need to be solved. First of all, the ways of sensitivity enhancement proposed here (§5.4) may be explored (reduction of cavity size for stadiums, further work on functionalization of porous materials, coupled microcavities). Question of sensor selectivity in multicomponent solutions need to be studied and ligands for other heavy metals (Cd^{2+}, Pb^{2+}) need to be tested with microlasers. Influence of temperature on microlaser spectra, casually mentioned here, should be evaluated more deeply. Secondly, creation of an integrated LOC on the basis of microlasers may be continued. For this purpose, a miniaturized detection system needs to be developed, compatible with microfluidics, which excludes the need for a spectrometer and can be integrated on the same substrate with the microlasers. Finally, parallelization capacity may be studied, for simultaneous operation of multiple microlasers, functionalized with various types of ligands.

Annex 1

Numerical Simulations

In this annex more detailed description of the numerical modeling methods that were used in this thesis will be given. We will explain how the simulations that are presented in the chapters 4 and 5 were performed, which information can be extracted from a numerical simulation and what are the sources of errors. The annex is split in two parts: in the first part, the principle of the Finite Difference Time Domain method (FDTD) will be explained. Simulations of the cavity spectrum sensitivity to the medium index variation, performed by FDTD, as well as visualization of electromagnetic field distribution of the resonant modes will be described. The second part is devoted to the Finite Element method (FEM), which is used to calculate the mode profiles in waveguiding polymer layer and effective refractive indices.

1. *FDTD simulations.*

The Finite-Difference Time-Domain (FDTD) method is perhaps the most general method of modeling the electromagnetic wave propagation, as in the essence, it numerically solves Maxwell's equations. The finite-difference schemes has been long used for the solution of various partial differential equation problems, however its first application in electrodynamics was realized by Yee in 1966 [146]. Later on the method was continuously developed and refined by other researcher, for example [147, 148].

The FDTD simulation provides a solution of Maxwell's equations for all six components of electric and magnetic fields at each mesh point. The main point of the method is the following: the simulated domain is meshed with a spatial grid and discretized in time with a step Δt. Therefore, we transform a continuous dependence on the time and coordinates of an electromagnetic field component into a discrete one: $A = f(x, y, z, t) \rightarrow A' = f(i\Delta x, j\Delta y, k\Delta z, n\Delta t)$, where $\Delta x, \Delta y, \Delta z$ and Δt are the corresponding spatial and time discretization steps. The spatial resolution of the grid (Δx, Δy, Δz) is connected with the temporal step Δt by the numerical stability criterion (Courant criterion):

$$\Delta t \leq \frac{1}{c}\left(\frac{1}{\Delta x^2} + \frac{1}{\Delta y^2} + \frac{1}{\Delta z^2}\right)^{-1/2} \qquad (1)$$

After the discretization, the approximate values of field components are calculated using a leapfrog scheme, where first the electric fields, then the magnetic are computed at each step in time (Fig.1). Any time-dependent signal can be used, in general, as an initial excitation; however most often Gaussian-shaped pulses are used. The properties of the medium are usually defined by dielectric and magnetic permittivities.

The main advantage of FDTD method for simulations of cavities, is the possibility to

- follow mode evolution in time
- obtain a response in a wide frequency band

in a single simulation, which is impossible with frequency-domain methods. The frequency spectra of the cavity can be easily calculated from the temporal field dependency by applying a Fourier Transform. On the contrary, to simulate the cavity resonant spectrum with frequency-domain methods, multiple calculations must be performed at each frequency of interest, with a fine frequency step in order to accurately trace the spectrum. The task becomes even more complicated in the case of high Q-factor cavities that exhibit wide spectra (in frequency domain) with thin, sharp peaks.

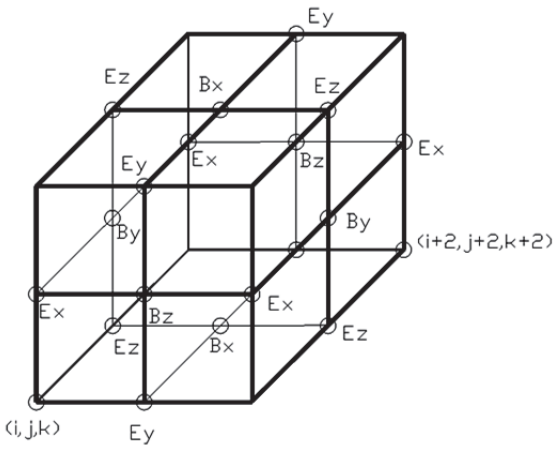

Fig.1. A single Yee cell.

Alongside with its beneficial features, there exist a number of weak points that may limit the applicability of FDTD method and precision of the obtained results. The simulation area is discretized with a Cartesian grid; therefore it is impossible to precisely describe the curved surfaces or boundaries. After discretization any curved interface will have a staircase shape, with the step size defined by the spatial mesh step that introduces an error in the calculated result. Various algorithms exist to minimize the meshing error: the nonlinear mesh may be utilized, where the cell size varies from smaller in the vicinity of small objects or object boundaries to larger in other domains with uniform properties. Various averaging techniques are employed, that calculate the mean value of permittivity inside a mesh cell, if there is more than one material present in the cell. More sophisticated conformal meshing technique [148] may be implemented that should further reduce the meshing error. Normally, the mesh precision of at least 10 cells per the smallest wavelength used in simulation should be used to obtain reasonable results.

Another source of errors may be connected with the boundary conditions of the simulation domain. To simulate the vanishing of the electromagnetic fields at the infinity, the simulation domain is truncated with the so called Perfectly Matched Layers (PML). The PMLs should entirely absorb all the emission falling on them and produce no reflections. However in the practical realizations, the PMLs absorbance is usually maximal at the normal incidence, and decreases as a square function of the incidence angle. Parasitic reflections may contribute to the calculation mistake, as well as the distortions of the wave front in case the wave propagates close to the PMLs.

In the work we used a commercial FDTD software package from Lumerical – FDTD Solutions. The FDTD is a computationally intensive method and, in case when large structures need to be modeled in 3 dimensions, requires large amounts of computer memory. In our case, when a typical cavity size reaches hundred microns, the 3D simulation at optical frequencies requires tremendous amounts of memory and becomes impossible with a desktop computer. Therefore, all the simulations were performed on down-scaled structures with a reasonable compromise between mesh precision and simulation time/memory requirements.

1.1. Simulation of spectral shift in response to effective refractive index change.

Simulation of the cavity response to the external medium index change via effective refractive index model was performed on a passive Fabry-Perot cavity in 2D configuration, as displayed on Fig.2a. The cavity, which is reduced cross-section of a real structure, is formed by a 15µm long slab with a thickness of either h=600nm or h=300nm (h/λ=1 or h/λ=0.5) and a refractive index of n=1.54, lying on the 2µm SiO_2 buffer layer (n=1.45) on top of a Si wafer. For a Si wafer the index dependency on the wavelength is taken into account by fitting the experimental $n = f(k)$ data [149] in the desired wavelength range (performed internally by the software). The bottom of the Si wafer and the SiO_2 layer on the left and right are extended through the PMLs surrounding the domain and shown in dark violet. The distance between the top side of the cavity and the upper PML is chosen to be several times larger than the wavelength, so that the evanescent wave tail present above the cavity in the case h/λ=0.5 doesn't feel the presence of the border. The excitation is performed with a plane wave source, placed at the left border of the cavity, either TE or TM polarized as shown on the scheme. The source injects a Gaussian-shaped pulse into the cavity, with a FWHM of τ = 3fs in the temporal domain and centered at 0.6µm with a span of 0.18µm in the spectral domain. A non-uniform mesh is set up with 20 cells/wavelength resolution, resulting in the total mesh size of 3205x405 cells for n_e=1 and 3205x461 cells for n_e=1.4. The simulation is run for 800 femtoseconds which correspond to approximately 5 complete round-trips of the mode in the cavity.

We study the Fabry-Perot resonance, formed by the wave which is confined within the cavity layer and propagates there and back, reflecting on the left and right boundaries, while varying the refractive index n_e of the surrounding medium in the range from 1.30 to 1.40. A

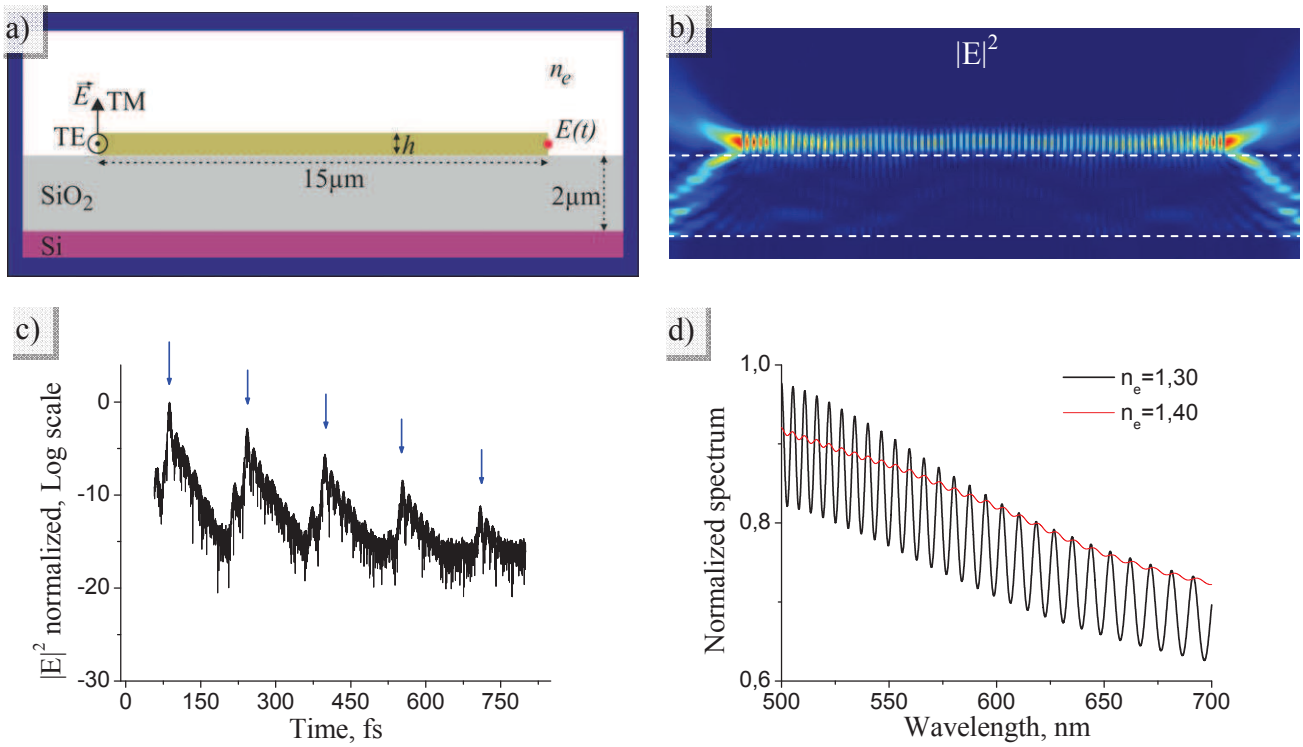

Fig.2. a) Layout of the simulation domain used in FDTD modeling; b) Visualisation of the Fabry-Perot mode – electric field intensity inside the simulation domain cavity; c) Temporal dependence of normalized electric field intensity, recorded by the monitor at the right cavity border; d) Cavity spectrum for n_e=1 (black) and n_e=1.4 (red).

mode is visualized on Fig.2b, where the nodes of the mode are clearly seen in the cavity. A time monitor, that records the time dependency of electromagnetic fields – $\vec{E}(t)$ and $\vec{H}(t)$, is placed in the middle of the right boundary of the cavity (red point on the scheme). The normalized electric field intensity $\left|E(t)^2\right|$ is plotted on a logarithmic scale on Fig.2c and features clearly distinguishable peaks upon each passage of the mode through the cavity border. The weak parasitic peaks in between the main ones appear due to the fact that part of the mode propagates inside the SiO_2 substrate and experiences numerous reflections on the Si/SiO_2 and SiO_2/PMMA interfaces. The logarithmic scale is taken because the cavity has high losses: with the reflection coefficient of ≈0.04 at each boundary, the mode loses almost two orders of magnitude in intensity upon each reflection. Afterwards, the chirped Z-transform is applied to all the field components recorded by the time monitor. The Z-transform is a generalization of the discrete-time Fourier transform (DTFT) that converts a discrete time-domain signal into a discrete frequency-domain signal at each desired angular frequency:

$$E_{\omega}[m] = \sum_{n} E[n] \cdot e^{i \cdot t[n] \omega[m]} \tag{2}$$

where E[n] are the discrete values of, for instance, electric field at discrete time steps t[n] and ω is the angular frequency. We used the Z-transform realization implemented by Lumerical, which returns the cavity spectrum shown on Fig.2d (for n_e=1 and n_e=1.4). To plot the $\Delta\lambda = f(n_e)$ dependency on Fig.4-13a in the main text, we followed the red-shift of the spectral peak at approximately 600 nm as n_e was increasing.

Due to the broadness of the peaks, only upper parts of the peaks are seen in the spectrum, while all the lower parts overlap. Once the n_e increase and approaches 1.4 the mode becomes even less confined, the spectral peaks widen up to the point when it is hardly possible to determine the peak maxima. Calculation of the 2nd derivative of the spectra allowed precise recovery of the peak position. However, this creates another source of error: agreement between the calculation and the simulation data is expected to be worse for the higher values of n_e. In some distinct cases it was impossible to determine the peak position for $n_e \geq 1.38$.

In order to calculate the spectra with the "infinite" SiO_2 buffer thickness, the Si layer was removed, the thickness of SiO_2 was increased to 5μm and the layer was extended through the PML boundary.

One should keep in mind that in the active microcavity (microlaser) the gain compensates the losses and thus leads to narrow peaks in the lasing spectrum. However in the simulation we deal with a passive cavity, and therefore observe fast resonance decay and very wide spectral peaks.

1.2. Simulation of the spectral shift in response to phase incursion.

In order to simulate the sensitivity of the cavity spectrum to the external medium index change vie phase incursion at the cavity facets, we modeled an 2D octagonal-shaped cavity, as shown on Fig.3a. Such 2D layout excludes the influence via effective refractive index variation, as the medium index changes only around the cavity and not above its surface. The cavity mode should certainly feel the "effective index" once it approaches the cavity perimeter, but this influence is considered insignificant and was neglected.

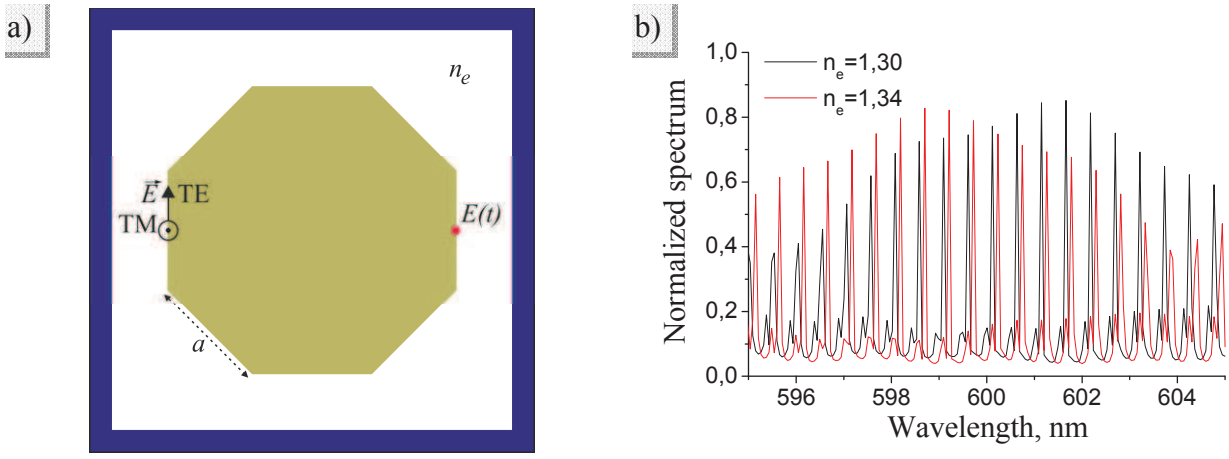

Fig.3. a) Layout of the simulation domain for an octagonal cavity. b) Spectrum of the octagon with a=60μm at n_e=1.30 and n_e=1.34 demonstrating a red-shift.

We simulated octagonal cavities of two sizes, with the side length of $a = 60$ μm and $a = 30$ μm, in order to verify the expected dependence of the spectral shift on the periodic orbit length. The excitation in this case is performed by a point dipole source with the same temporal and spectral characteristics as in the previous case, placed in the middle of one of the cavity facets. The mesh precision was 10 cells/wavelength for both cavity sizes, and the simulation time was chosen to allow 8 - 9 complete roundtrips for the octagonal orbit. Though the moderate mesh resolution may lead to the systematic error in the absolute values of resonance wavelengths, it should not significantly influence the relative spectral shift related to the medium index variation that interests us.

The temporal field dependence was recorded by the time monitor, denoted by red point on the scheme, and treated in the similar manner as above. The calculated spectra in this case exhibit much narrower, clearly defined peaks. Indeed, the octagonal orbit, opposite to the Fabry-Perot one, is well-confined by total internal reflection, therefore featuring resonances with higher Q-factor. The red-shift of the peak at approximately 600 nm was followed and plotted on the Fig.4-13b in the main text. The error bars on Fig.4-13 are therefore defined as $\Delta\lambda/2$, where $\Delta\lambda$ is the wavelength step in the spectra obtained by Z-transform.

1.3. Visualization of the mode profiles

To obtain a plot of the electromagnetic field distribution inside the cavity, corresponding to a certain resonance frequency, a 2D field profile monitor is used. A monitor, which is a rectangle of user-defined dimensions, performs a Z-transform of the temporal field dependencies at each mesh point, lying in the plane of the monitor at a certain angular frequency, defined before the beginning of the simulation. Therefore, two simulations are required: during the first one the resonance spectrum is calculated as was described above. For the second simulation, the field profile monitor is set up to perform Z-transform at a certain resonance frequency of interest. In this case, the electromagnetic field values at all the time steps, from t=0 till the end of the simulation are taken into account. For the leaky cavities, where the field intensity decays rapidly with time, transient processes occurring at the very beginning of the simulation will be seen in the plotted electromagnetic field pattern as well as the source dipole which manifests itself as a bright spot. To avoid the influence of the source and to obtain a clear picture of the cavity mode

an apodization function is applied to the temporal field dependency, with the FWHM τ in temporal domain corresponding to the width of resonant peak in the spectral domain (Fig.4c). This means, that the Z-transform will be performed not for a single chosen frequency value, but in a certain range of frequencies, determined by the width τ of the apodization filter and centered at the chosen value. The width τ must be selected so that the range of frequencies contains the resonance peak of interest and does not overlap with neighboring peaks in the spectrum. This is illustrated in the following example of a microdisc cavity.

One more interesting consequence of time-dependent simulation and temporal apodization is the possibility to follow the mode evolution in time. The modes with weak confinement in a leaky dielectric cavity may completely decay during the simulation time; while others possessing higher quality factor will dominate. The electromagnetic field configuration of one mode may evolve with time until it is transformed into another mode, having the same resonance frequency.

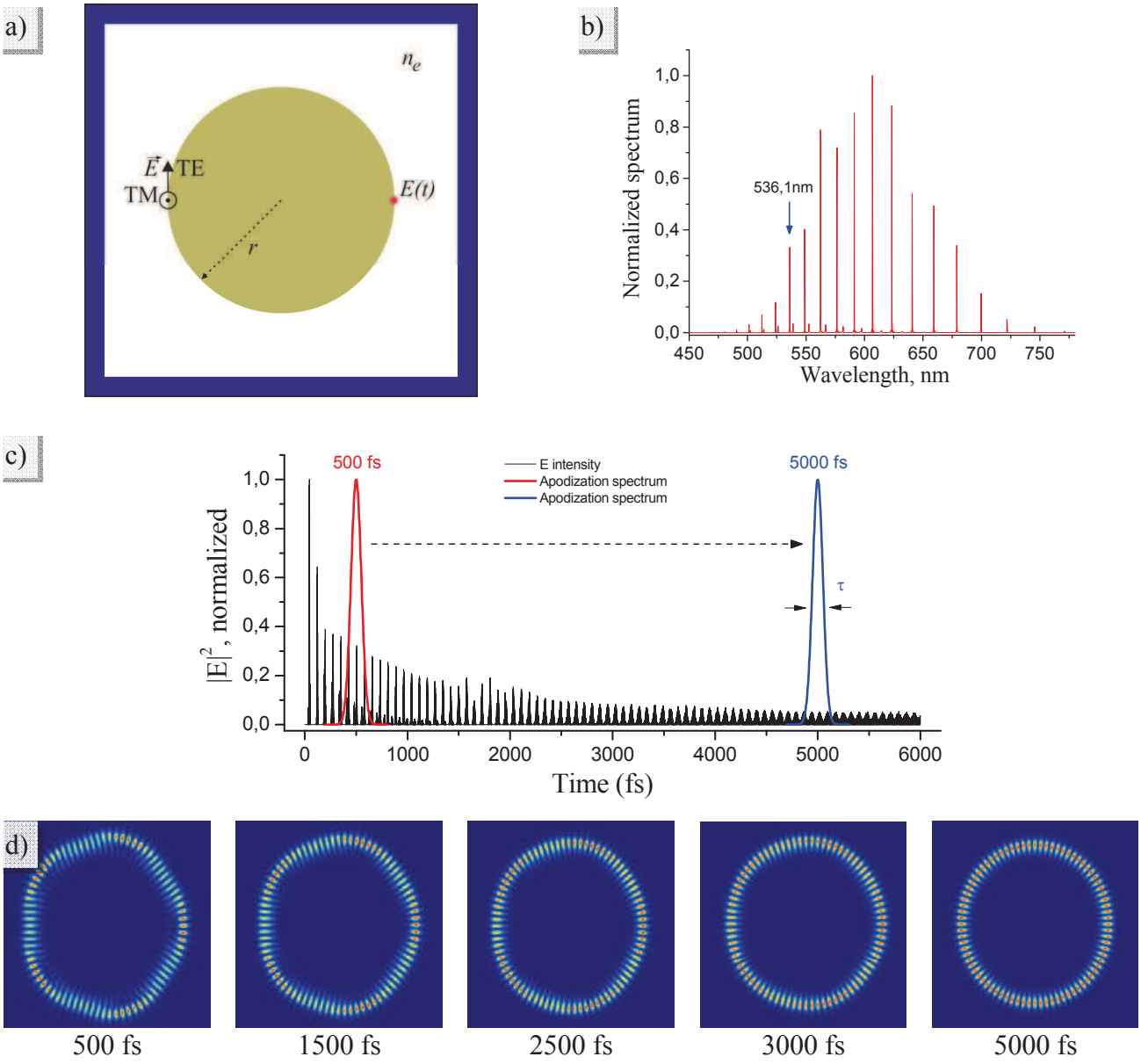

Fig.4. a) The simulation layout for a microdisk cavity, r=2.5μm; b) Calculated spectrum, the blue arrow marks the investigated resonance at 536.1nm; c) Time dependence of the normalized electric field intensity recorded by the time monitor; d) Electric field intensity $|E|^2$ for the selected resonance at different observation times.

That is what was observed for certain resonances of a microdisk cavity: if we follow in time the electric field intensity pattern for a resonance peak at 536.1nm (Fig.4b) of a microdisk with r=2.5μm (Fig.4a), we evidence its gradual evolution (Fig.4c) from an inscribed pentagon orbit at the beginning of the simulation (time ≤3000fs) to a certain eigenmode of a microdisk (time ≥4000fs), whose field distribution corresponds to that of a whispering gallery mode. The simulation here is performed for a TM mode (Fig.4a), similar as was described above, for a medium index n_e=1.

2. *Finite Element Method.*

The Finite Element Method (FEM) is a method of approximate numerical solution of partial differential equations (PDE) as well as integral equations. The first mathematical treatment of FEM was introduced by Richard Courant in 1943 [150, 151]. The detailed explanation of the method is rather complicated and is definitely out of the scope of this thesis; therefore we will just give a short schematic outline of the modeling steps.

- First of all, the solution domain is partitioned into a set of mesh elements which are typically either square or triangular in 2D and cubic or tetrahedron in 3D.
- The dependent variables of PDE are approximated with functions that can be described with a finite number of parameters. For a single variable u:

$$u = \sum_i U_i \varphi_i$$

  where U_i (so-called degrees of freedom) are the values of u in the node points of the mesh and φ_i are the basis functions.
- Assembling a system of equations for all the elements in the solution domain and solving it numerically.

To perform FEM modeling we have used COMSOL Multiphysics software which is a powerful tool for solving various kinds of physical (chemical, mechanical, etc.) problems where the phenomenon under investigation can be described with a system of PDEs.

In a FEM simulation as opposed to FDTD the calculation is performed at one single frequency defined before the beginning of a simulation. Therefore to obtain, for example, a spectrum of resonant frequencies of a cavity, multiple simulations need to be performed in a certain range of frequencies with a small step. The narrower are the resonance peaks of the cavity, the smaller should be the frequency step, therefore FDTD simulation is preferable for such calculations. At the same time, FDTD only solves a set of Maxwell equations for electric and magnetic field components, therefore problems, where a propagation constant or effective index of a guided mode needs to be found require different solution methods and FEM is convenient for this purposes.

Another advantage of finite element method is the intrinsic support of non-orthogonal meshes. Rectangular mesh, which is the only possibility in FDTD[1], cannot precisely discretize the curved boundaries of objects and leads to numerical errors. In FEM, on the contrary, triangular mesh can be used with large difference in size between the adjacent mesh elements which therefore allows more precise description of curved interfaces.

1.4. Effective refractive index calculation

In order to calculate the effective refractive index of the TE mode propagating in the active layer while taking into account the finite thickness of the SiO_2 buffer layer (presence of Si substrate) the simulation schematically depicted on Fig.5c was set-up. In our connotation, for a TE mode electric field lies in the plane of the cavity. A simulation domain consists of a stack of

[1] There exist works in literature where FDTD implementation on triangular [151] and non-orthogonal meshes [152] is demonstrated. However, majority of commercial FDTD packages only support rectangular meshes.

4 layers: Si (2µm) / SiO_2 (2µm) / PMMA (0.6µm or 0.3µm) / medium (4µm) with the width of 6um. The refractive indices are the following: Si – n=3.94 (crystalline silicon, λ=600nm [149]), SiO_2 – n=1.45, PMMA – n=1.54, medium - n_e. The equation solved is the Helmholtz equation for the E_z field component (propagation perpendicular to the plane of drawing):

$$\nabla^2 E_z + (\beta^2 - n^2 k_0^2) E_z = 0 \tag{3}$$

where β is the propagation constant, k_0 is the free-space wavenumber. Once the value of propagation constant is known, the effective index is calculated as:

$$n_{eff} = \beta / k_0 \tag{4}$$

The initial value of n_{eff} is given to COMSOL and afterwards software searches for converging solutions of Eq.(3) in the vicinity of this initial value. The result of the simulation is the list of the effective indices of the modes that may propagate in the structure and corresponding distributions of electric field E_z.

The simulation domain is truncated by a "perfect magnetic conductor" boundary condition, meaning that the tangential component of the magnetic field and normal component of the electric field are equal to zero:

$$\vec{n} \times \vec{H} = 0 \,,\; \vec{n} \cdot \vec{E} = 0 \tag{5}$$

where $\vec{n}$ is the normal vector to the boundary. This boundary condition allows correct representation of infiniteness of dielectric layers along the x axis when only E_z component of electric field is non-zero. The domain is meshed with a non-uniform triangular mesh reaching 15÷30 mesh cells/wavelength resolution. The initial guess value of n_{eff} is given to COMSOL and afterwards it searches for the converging solutions of Eq. (3) in the vicinity of this value.

The refractive index of the surrounding medium n_e is varied in the range $1 \div 1.4$ and the calculated effective refractive index values are used to plot Fig.4-14 in the main text. It was found that the effective index of the guided mode in the case of 2µm SiO_2 layer is lower than the one calculated analytically for infinite buffer layer thickness. The calculation errors in this case would arise due to the finite size of the mesh cells and, more important, due to the limited

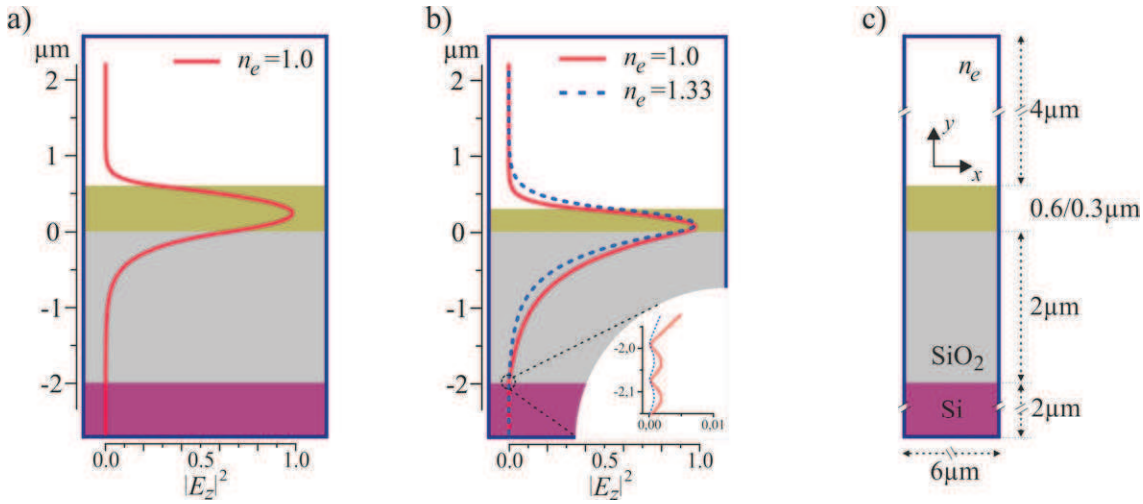

Fig.5. The E_z component of a field of a TE mode propagating in the cavity layer for a) h/λ=1 and b) h/λ=0.5 geometries and two different values of medium index; Inset shows stronger electric field intensity in the Si wafer layer in case when n_e=1. c) The layout of simulation.

thickness of the Si layer, which was chosen in order to balance a fine mesh resolution with reasonable memory consumption.

The modulus squared of the E_z electric field component is plotted for $h/\lambda = 1$ geometry on Fig.5a ($h = 0.6\mu m$) and $h/\lambda = 0.5$ on Fig.5b ($h = 0.3\mu m$) so that it is possible to visually estimate the mode localization in the cavity and claddings. In the case of a thicker cavity (h/λ=1), the mode is mostly confined within the active layer, electric field extends into the silica buffer but diminishes to zero at the interface with Si substrate, so that the mode is not influenced by its presence. However in the case of a twice thinner cavity ($h/\lambda = 0.5$) the mode is mostly localized at the cavity/SiO_2 interface, extends deeply into the buffer layer and, as the inset on Fig.5b shows, there exist part of the mode propagating inside the Si substrate. The effective index in this case is slightly different from the predicted by Eq. (4-3). Once the index of the medium above the cavity rises, the mode shifts closer to the cavity/medium interface and the influence of the Si substrate decreases.

For a TM mode it was found that while in h/λ=1 case the confinement is rather strong and mode effective index is not influenced by a silicon substrate, but in h/λ=0.5 case the mode extends significantly into the substrate leading to the difference of the order 10^{-3} between the analytical and numerical effective index calculations.

Bibliography

1. Ishikawa, D., A. Okamoto, S. Honma, T. Ito, K. Shimayabu, and K. Sato, *All-Optical Multifunctional Logic Gates for Image Information Using Photorefractive Two-Wave Mixing.* Optical Review, 2007. **14**(4): p. 246-251.
2. Liang, T.K., L.R. Nunes, M. Tsuchiya, K.S. Abedin, T. Miyazaki, D. Van Thourhout, W. Bogaerts, P. Dumon, R. Baets, and H.K. Tsang, *High speed logic gate using two-photon absorption in silicon waveguides.* Optics Communications, 2006. **265**(1): p. 171-174.
3. Zaghloul, Y.A. and A.R. Zaghloul, *Complete all-optical processing polarization-based binary logic gates and optical processors.* Opt Express, 2006. **14**(21): p. 9879-95.
4. Hill, M.T., H.J. Dorren, T. De Vries, X.J. Leijtens, J.H. Den Besten, B. Smalbrugge, Y.S. Oei, H. Binsma, G.D. Khoe, and M.K. Smit, *A fast low-power optical memory based on coupled micro-ring lasers.* Nature, 2004. **432**(7014): p. 206-9.
5. Liu, L., R. Kumar, K. Huybrechts, T. Spuesens, G. Roelkens, E.-J. Geluk, T. de Vries, P. Regreny, D. Van Thourhout, R. Baets, and G. Morthier, *An ultra-small, low-power, all-optical flip-flop memory on a silicon chip.* Nature Photonics, 2010. **4**(3): p. 182-187.
6. Nagamura, T., *Optical Memory by Novel Photoinduced Electrochromism.* Molecular Crystals and Liquid Crystals, 1993. **224**: p. 75-83.
7. Soares, B.F., F. Jonsson, and N.I. Zheludev, *All-optical phase-change memory in a single gallium nanoparticle.* Physical Review Letters, 2007. **98**(15).
8. Almeida, V.R., C.A. Barrios, R.R. Panepucci, and M. Lipson, *All-optical control of light on a silicon chip.* Nature, 2004. **431**(7012): p. 1081-4.
9. Hiroshi Nishihara, M.H., Toshiaki Suhara, *Optical Integrated Circuits*2011: Lightning Source Inc.
10. Kaminow, I.P., *Optical integrated circuits: A personal perspective.* Journal of Lightwave Technology, 2008. **26**(9-12): p. 994-1004.
11. Xu, Q.F. and R. Soref, *Reconfigurable optical directed-logic circuits using microresonator-based optical switches.* Optics Express, 2011. **19**(6): p. 5244-5259.
12. Daw, R. and J. Finkelstein, *Lab on a chip.* Nature, 2006. **442**(7101): p. 367-367.
13. Whitesides, G.M., *The origins and the future of microfluidics.* Nature, 2006. **442**(7101): p. 368-73.
14. DeMello, A.J., *Control and detection of chemical reactions in microfluidic systems.* Nature, 2006. **442**(7101): p. 394-402.
15. Noto, M., D. Keng, I. Teraoka, and S. Arnold, *Detection of protein orientation on the silica microsphere surface using transverse electric/transverse magnetic whispering gallery modes.* Biophys J, 2007. **92**(12): p. 4466-72.
16. Chen, X., L. Zhang, K. Zhou, E. Davies, K. Sugden, I. Bennion, M. Hughes, and A. Hine, *Real-time detection of DNA interactions with long-period fiber-grating-based biosensor.* Opt Lett, 2007. **32**(17): p. 2541-3.
17. Zhu, H., I.M. White, J.D. Suter, P.S. Dale, and X. Fan, *Analysis of biomolecule detection with optofluidic ring resonator sensors.* Opt Express, 2007. **15**(15): p. 9139-46.
18. Swann, M.J., L.L. Peel, S. Carrington, and N.J. Freeman, *Dual-polarization interferometry: an analytical technique to measure changes in protein structure in real time, to determine the stoichiometry of binding events, and to differentiate between specific and nonspecific interactions.* Anal Biochem, 2004. **329**(2): p. 190-8.
19. Xudong Fan, I.M.W., Hongying Zhu, Jonathan D. Suter, and Hesam Oveys, *Overview of novel integrated optical ring resonator bio/chemical sensors*, 2007, University of Missouri.
20. Chou, S.Y., P.R. Krauss, and P.J. Renstrom, *Imprint Lithography with 25-Nanometer Resolution.* Science, 1996. **272**(5258): p. 85-87.
21. Haisma, J., *Mold-assisted nanolithography: A process for reliable pattern replication.* Journal of Vacuum Science & Technology B: Microelectronics and Nanometer Structures, 1996. **14**(6): p. 4124.

22. Chou, S.Y., *Sub-10 nm imprint lithography and applications.* Journal of Vacuum Science & Technology B: Microelectronics and Nanometer Structures, 1997. **15**(6): p. 2897.
23. Gates, B.D., Q. Xu, M. Stewart, D. Ryan, C.G. Willson, and G.M. Whitesides, *New approaches to nanofabrication: molding, printing, and other techniques.* Chem Rev, 2005. **105**(4): p. 1171-96.
24. Becker, H. and C. Gärtner, *Polymer microfabrication methods for microfluidic analytical applications.* Electrophoresis, 2000. **21**(1): p. 12-26.
25. Chung-yen Chao, L.J.G., *Polymer Microring Resonators fabricated by nanoimprint technique.* J. Vac. Sci. Technol., 2002. **20**(6): p. 2862 - 2866.
26. EFSA Panel on Contaminants in the Food Chain (CONTAM), *Scientific Opinion on Lead in Food.* EFSA Journal, 2010. **8**(4).
27. *Scientific Opinion of the Panel on Contaminants in the Food Chain on a request from the European Commission on cadmium in food.* The EFSA Journal, 2009(980): p. 1-139.
28. *Opinion of the Scientific Panel on contaminants in the food chain [CONTAM] related to mercury and methylmercury in food.* The EFSA Journal, 2004. **34**: p. 1-14.
29. Fan, A.M., *Public Health Goal for Inorganic Mercury In Drinking Water*, 1999, California Environmental Protection Agency.
30. *Council Directive 98/83/EC of 3 November 1998 on the quality of water intended for human consumption.* Official Journal of the European Communities, 1998. **41**(L330).
31. Reay, R.J., A.F. Flannery, C.W. Storment, S.P. Kounaves, and G.T.A. Kovacs, *Microfabricated electrochemical analysis system for heavy metal detection.* Sensors and Actuators B: Chemical, 1996. **34**(1-3): p. 450-455.
32. Nolan, E.M. and S.J. Lippard, *MS4, a seminaphthofluorescein-based chemosensor for the ratiometric detection of Hg(ii).* Journal of Materials Chemistry, 2005. **15**(27-28): p. 2778.
33. Cherian, L. and V.K. Gupta, *A simple field test for the detection of mercury in polluted water, air and soil samples.* Fresenius' Journal of Analytical Chemistry, 1990. **336**(5): p. 400-402.
34. Melanie, L., *Chaos quantique et micro-lasers organiques*, 2007, Université Paris XI.
35. Nadia, D., *Vers le contrôle géométrique de l'émission de microcavités laser à base de polymères*, 2009, ENS Cachan.
36. Armani, A.M., R.P. Kulkarni, S.E. Fraser, R.C. Flagan, and K.J. Vahala, *Label-free, single-molecule detection with optical microcavities.* Science, 2007. **317**(5839): p. 783-7.
37. Luppa, P.B., L.J. Sokoll, and D.W. Chan, *Immunosensors—principles and applications to clinical chemistry.* Clinica Chimica Acta, 2001. **314**(1-2): p. 1-26.
38. De Vos, K.M., I. Bartolozzi, P. Bienstman, R. Baets, and E. Schacht, *Optical biosensor based on silicon-on-insulator microring cavities for specific protein binding detection.* 2007. **6447**: p. 64470K-64470K-8.
39. Vollmer, F., D. Braun, A. Libchaber, M. Khoshsima, I. Teraoka, and S. Arnold, *Protein detection by optical shift of a resonant microcavity.* Applied Physics Letters, 2002. **80**(21): p. 4057.
40. Araci, I.E., S.B. Mendes, N. Yurt, S. Honkanen, and N. Peyghambarian, *Highly sensitive spectroscopic detection of heme-protein submonolayer films by channel integrated optical waveguide.* Optics Express, 2007. **15**(9): p. 5595.
41. Yalcin, A., K.C. Popat, J.C. Aldridge, T.A. Desai, J. Hryniewicz, N. Chbouki, B.E. Little, K. Oliver, V. Van, C. Sai, D. Gill, M. Anthes-Washburn, M.S. Unlu, and B.B. Goldberg, *Optical sensing of biomolecules using microring resonators.* IEEE Journal of Selected Topics in Quantum Electronics, 2006. **12**(1): p. 148-155.
42. De Vos, K., I. Bartolozzi, E. Schacht, P. Bienstman, and R. Baets, *Silicon-on-Insulator microring resonator for sensitive and label-free biosensing.* Opt Express, 2007. **15**(12): p. 7610-5.
43. White, I.M., H. Oveys, X. Fan, T.L. Smith, and J. Zhang, *Integrated multiplexed biosensors based on liquid core optical ring resonators and antiresonant reflecting optical waveguides.* Applied Physics Letters, 2006. **89**(19): p. 191106.
44. Barrios, C.A., M.J. Banuls, V. Gonzalez-Pedro, K.B. Gylfason, B. Sanchez, A. Griol, A. Maquieira, H. Sohlstrom, M. Holgado, and R. Casquel, *Label-free optical biosensing with slot-waveguides.* Opt Lett, 2008. **33**(7): p. 708-10.

45. Freeman, N.J., L.L. Peel, M.J. Swann, G.H. Cross, A. Reeves, S. Brand, and J.R. Lu, *Real time, high resolution studies of protein adsorption and structure at the solid–liquid interface using dual polarization interferometry.* Journal of Physics: Condensed Matter, 2004. **16**(26): p. S2493-S2496.
46. Berney, H. and K. Oliver, *Dual polarization interferometry size and density characterisation of DNA immobilisation and hybridisation.* Biosens Bioelectron, 2005. **21**(4): p. 618-26.
47. Ricard-Blum, S., L.L. Peel, F. Ruggiero, and N.J. Freeman, *Dual polarization interferometry characterization of carbohydrate-protein interactions.* Anal Biochem, 2006. **352**(2): p. 252-9.
48. Shan, X., K.J. Foley, and N. Tao, *A label-free optical detection method for biosensors and microfluidics.* Applied Physics Letters, 2008. **92**(13): p. 133901.
49. Shew, B.Y., Y.C. Cheng, and Y.H. Tsai, *Monolithic SU-8 micro-interferometer for biochemical detections.* Sensors and Actuators A: Physical, 2008. **141**(2): p. 299-306.
50. Chung-Yen, C., W. Fung, and L.J. Guo, *Polymer microring resonators for biochemical sensing applications.* IEEE Journal of Selected Topics in Quantum Electronics, 2006. **12**(1): p. 134-142.
51. Chao, C.-Y. and L.J. Guo, *Biochemical sensors based on polymer microrings with sharp asymmetrical resonance.* Applied Physics Letters, 2003. **83**(8): p. 1527.
52. Mappes, T., C. Vannahme, M. Schelb, U. Lemmer, and J. Mohr, *Design for optimized coupling of organic semiconductor laser light into polymer waveguides for highly integrated biophotonic sensors.* Microelectronic Engineering, 2009. **86**(4-6): p. 1499-1501.
53. Cho, S.Y. and N.M. Jokerst, *A Polymer Microdisk Photonic Sensor Integrated Onto Silicon.* IEEE Photonics Technology Letters, 2006. **18**(20): p. 2096-2098.
54. Chen, Y., L. Lei, K. Zhang, J. Shi, L. Wang, H. Li, X.M. Zhang, Y. Wang, and H.L.W. Chan, *Optofluidic microcavities: Dye-lasers and biosensors.* Biomicrofluidics, 2010. **4**(4): p. 043002.
55. Francois, A. and M. Himmelhaus, *Whispering gallery mode biosensor operated in the stimulated emission regime.* Applied Physics Letters, 2009. **94**(3): p. 031101.
56. He, L., S.K. Ozdemir, J. Zhu, W. Kim, and L. Yang, *Detecting single viruses and nanoparticles using whispering gallery microlasers.* Nat Nanotechnol, 2011. **6**(7): p. 428-32.
57. Christiansen, M.B., J.M. Lopacinska, M.H. Jakobsen, N.A. Mortensen, M. Dufva, and A. Kristensen, *Polymer photonic crystal dye lasers as Optofluidic Cell Sensors.* Optics Express, 2009. **17**(4): p. 2722.
58. Lu, M., S.S. Choi, U. Irfan, and B.T. Cunningham, *Plastic distributed feedback laser biosensor.* Applied Physics Letters, 2008. **93**(11): p. 111113.
59. Lu, M., S.S. Choi, C.J. Wagner, J.G. Eden, and B.T. Cunningham, *Label free biosensor incorporating a replica-molded, vertically emitting distributed feedback laser.* Applied Physics Letters, 2008. **92**(26): p. 261502.
60. Li, H., L. Shang, X. Tu, L. Liu, and L. Xu, *Coupling variation induced ultrasensitive label-free biosensing by using single mode coupled microcavity laser.* J Am Chem Soc, 2009. **131**(46): p. 16612-3.
61. Nylander, C., B. Liedberg, and T. Lind, *Gas detection by means of surface plasmon resonance.* Sensors and Actuators, 1982. **3**: p. 79-88.
62. Liedberg, B., C. Nylander, and I. Lunström, *Surface plasmon resonance for gas detection and biosensing.* Sensors and Actuators, 1983. **4**: p. 299-304.
63. Nenninger, G.G., M. Piliarik, and J. Homola, *Data analysis for optical sensors based on spectroscopy of surface plasmons.* Measurement Science and Technology, 2002. **13**(12): p. 2038-2046.
64. Karlsson, R., Fält A., *Experimental design for kinetic analysis of protein-protein interactions with surface plasmon resonance biosensors.* Journal of Immunological Methods, 1997. **200**(1-2): p. 121-133.
65. Hastings, J.T., J. Guo, P.D. Keathley, P.B. Kumaresh, Y. Wei, S. Law, and L.G. Bachas, *Optimal self-referenced sensing using long- and short- range surface plasmons.* Optics Express, 2007. **15**(26): p. 17661.

66. Dostálek, J. and J. Homola, *Surface plasmon resonance sensor based on an array of diffraction gratings for highly parallelized observation of biomolecular interactions.* Sensors and Actuators B: Chemical, 2008. **129**(1): p. 303-310.
67. Sadowski, J.W., J. Lekkala, and I. Vikholm, *Biosensors based on surface plasmons excited in non-noble metals.* Biosensors and Bioelectronics, 1991. **6**(5): p. 439-444.
68. Homola, J., *Surface plasmon resonance sensors for detection of chemical and biological species.* Chem Rev, 2008. **108**(2): p. 462-93.
69. Forzani, E.S., H. Zhang, W. Chen, and N. Tao, *Detection of Heavy Metal Ions in Drinking Water Using a High-Resolution Differential Surface Plasmon Resonance Sensor.* Environmental Science & Technology, 2005. **39**(5): p. 1257-1262.
70. Chen, C.D., S.F. Cheng, L.K. Chau, and C.R. Wang, *Sensing capability of the localized surface plasmon resonance of gold nanorods.* Biosens Bioelectron, 2007. **22**(6): p. 926-32.
71. Haes, A.J. and R.P. Van Duyne, *A Nanoscale Optical Biosensor: Sensitivity and Selectivity of an Approach Based on the Localized Surface Plasmon Resonance Spectroscopy of Triangular Silver Nanoparticles.* J Am Chem Soc, 2002. **124**(35): p. 10596-10604.
72. Hall, W.P., S.N. Ngatia, and R.P. Van Duyne, *LSPR Biosensor Signal Enhancement Using Nanoparticle-Antibody Conjugates.* J Phys Chem C Nanomater Interfaces, 2011. **115**(5): p. 1410-1414.
73. Wang, T.-J. and P.-C. Ho, *Localized surface plasmon resonance biosensing by electro-optic modulation with sensitivity and resolution tunability.* Journal of Applied Physics, 2011. **109**(6): p. 064703.
74. Xiang, G., N. Zhang, and X. Zhou, *Localized surface plasmon resonance biosensing with large area of gold nanoholes fabricated by nanosphere lithography.* Nanoscale Res Lett, 2010. **5**(5): p. 818-22.
75. Murray, W.A., B. Auguié, and W.L. Barnes, *Sensitivity of Localized Surface Plasmon Resonances to Bulk and Local Changes in the Optical Environment.* The Journal of Physical Chemistry C, 2009. **113**(13): p. 5120-5125.
76. Shao, Y., S. Xu, X. Zheng, Y. Wang, and W. Xu, *Optical Fiber LSPR Biosensor Prepared by Gold Nanoparticle Assembly on Polyelectrolyte Multilayer.* Sensors, 2010. **10**(4): p. 3585-3596.
77. McFarland, A.D. and R.P. Van Duyne, *Single Silver Nanoparticles as Real-Time Optical Sensors with Zeptomole Sensitivity.* Nano Letters, 2003. **3**(8): p. 1057-1062.
78. Hao, F., Y. Sonnefraud, P. Van Dorpe, S.A. Maier, N.J. Halas, and P. Nordlander, *Symmetry breaking in plasmonic nanocavities: subradiant LSPR sensing and a tunable Fano resonance.* Nano Lett, 2008. **8**(11): p. 3983-8.
79. Fan, X., I.M. White, S.I. Shopova, H. Zhu, J.D. Suter, and Y. Sun, *Sensitive optical biosensors for unlabeled targets: a review.* Anal Chim Acta, 2008. **620**(1-2): p. 8-26.
80. Barrios, C.A., *Optical Slot-Waveguide Based Biochemical Sensors.* Sensors, 2009. **9**(6): p. 4751-4765.
81. Dell'Olio, F. and V.M. Passaro, *Optical sensing by optimized silicon slot waveguides.* Optics Express, 2007. **15**(8): p. 4977.
82. Almeida, V.R., Q. Xu, C.A. Barrios, and M. Lipson, *Guiding and confining light in void nanostructure.* Opt Lett, 2004. **29**(11): p. 1209.
83. Robinson, J.T., L. Chen, and M. Lipson, *On-chip gas detection in silicon optical microcavities.* Optics Express, 2008. **16**(6): p. 4296.
84. Hübner, J.r., K.B. Mogensen, A.M. Jorgensen, P. Friis, P. Telleman, and J.r.P. Kutter, *Integrated optical measurement system for fluorescence spectroscopy in microfluidic channels.* Review of Scientific Instruments, 2001. **72**(1): p. 229.
85. Mogensen, K.B., J. El-Ali, A. Wolff, and J.P. Kutter, *Integration of Polymer Waveguides for Optical Detection in Microfabricated Chemical Analysis Systems.* Applied Optics, 2003. **42**(19): p. 4072.
86. Mazurczyk, R., J. Vieillard, A. Bouchard, B. Hannes, and S. Krawczyk, *A novel concept of the integrated fluorescence detection system and its application in a lab-on-a-chip microdevice.* Sensors and Actuators B: Chemical, 2006. **118**(1-2): p. 11-19.

87. Yin, D., D.W. Deamer, H. Schmidt, J.P. Barber, and A.R. Hawkins, *Single-molecule detection sensitivity using planar integrated optics on a chip.* Opt Lett, 2006. **31**(14): p. 2136.
88. Yin, D., E.J. Lunt, M.I. Rudenko, D.W. Deamer, A.R. Hawkins, and H. Schmidt, *Planar optofluidic chip for single particle detection, manipulation, and analysis.* Lab Chip, 2007. **7**(9): p. 1171-5.
89. Psaltis, D., S.R. Quake, and C. Yang, *Developing optofluidic technology through the fusion of microfluidics and optics.* Nature, 2006. **442**(7101): p. 381-6.
90. Monat, C., P. Domachuk, and B.J. Eggleton, *Integrated optofluidics: A new river of light.* Nature Photonics, 2007. **1**(2): p. 106-114.
91. Levy, U. and R. Shamai, *Tunable optofluidic devices.* Microfluidics and Nanofluidics, 2007. **4**(1-2): p. 97-105.
92. Chen, Y., K. Huang, and Y. Lan, *Quantum manifestations of classical periodic orbits in a square billiard: Formation of vortex lattices.* Physical Review E, 2002. **66**(6).
93. B. E. A. Saleh, M.C.T., *Fundamentals of Photonics*, ed. J.W. Goodman1991: John Wiley & Sons, Inc.
94. Lebental, M., N. Djellali, C. Arnaud, J.S. Lauret, J. Zyss, R. Dubertrand, C. Schmit, and E. Bogomolny, *Inferring periodic orbits from spectra of simply shaped microlasers.* Physical Review A, 2007. **76**(2).
95. Dubertrand, R., E. Bogomolny, N. Djellali, M. Lebental, and C. Schmit, *Circular dielectric cavity and its deformations.* Physical Review A, 2008. **77**(1).
96. Robertson, R., E. Tentzeris, M. Krumpholz, and L.P.B. Katehi, *Modelling of dielectric cavity structures using multiresolution time-domain analysis.* International Journal of Numerical Modelling: Electronic Networks, Devices and Fields, 1998. **11**(1): p. 55-68.
97. Taflove, A. and K.R. Umashankar, *Review of FD-TD numerical modeling of electromagnetic wave scattering and radar cross section.* Proceedings of the IEEE, 1989. **77**(5): p. 682-699.
98. Lee, J.F., *Finite element analysis of lossy dielectric waveguides.* IEEE Transactions on Microwave Theory and Techniques, 1994. **42**(6): p. 1025-1031.
99. Rahman, B.M.A. and J.B. Davies, *Finite-Element Analysis of Optical and Microwave Waveguide Problems.* IEEE Transactions on Microwave Theory and Techniques, 1984. **32**(1): p. 20-28.
100. Rayleigh, L., *The Problem of the Whispering Gallery.* Phil. Mag., 1910(20): p. 1001-1004.
101. Richtmyer, R.D., *Dielectric Resonators.* Journal of Applied Physics, 1939. **10**(6): p. 391.
102. Savchenkov, A.A., A.B. Matsko, V.S. Iichenko, and L. Maleki, *Optical whispering gallery mode resonators with Q > 1011 and F > 107.* 2007: p. 1-2.
103. Peterson, O.G., *Organic Dye Laser Threshold.* Journal of Applied Physics, 1971. **42**(5): p. 1917.
104. Alain Orszag, G.H., *Les lasers et leurs applications*1980: Masson.
105. Crosby, G.A. and J.N. Demas, *Measurement of photoluminescence quantum yields. Review.* The Journal of Physical Chemistry, 1971. **75**(8): p. 991-1024.
106. Tagaya, A., T. Kobayashi, S. Nakatsuka, E. Nihei, K. Sasaki, and Y. Koike, *High Gain and High Power Organic Dye-Doped Polymer Optical Fiber Amplifiers: Absorption and Emission Cross Sections and Gain Characteristics.* Japanese Journal of Applied Physics, 1997. **36**(Part 1, No. 5A): p. 2705-2708.
107. Lill, Y. and B. Hecht, *Single dye molecules in an oxygen-depleted environment as photostable organic triggered single-photon sources.* Applied Physics Letters, 2004. **84**(10): p. 1665.
108. Zondervan, R., F. Kulzer, M.A. Kol'chenk, and M. Orrit, *Photobleaching of Rhodamine 6G in Poly(vinyl alcohol) at the Ensemble and Single-Molecule Levels.* The Journal of Physical Chemistry A, 2004. **108**(10): p. 1657-1665.
109. Dubois, A., M. Canva, A. Brun, F. Chaput, and J.-P. Boilot, *Photostability of dye molecules trapped in solid matrices.* Applied Optics, 1996. **35**(18): p. 3193.
110. Popov, S., *Dye Photodestruction in a Solid-State Dye Laser with a Polymeric Gain Medium.* Applied Optics, 1998. **37**(27): p. 6449.
111. Sorokin, P., *Flashlamp-pumped organic dye lasers.* IEEE Journal of Quantum Electronics, 1968. **4**(5): p. 315-315.
112. Grossmann, T., M. Hauser, T. Beck, C. Gohn-Kreuz, M. Karl, H. Kalt, C. Vannahme, and T. Mappes, *High-Q conical polymeric microcavities.* Applied Physics Letters, 2010. **96**(1): p. 013303.

113. Bilenberg, B., S. Jacobsen, M. Schmidt, L. Skjolding, P. Shi, P. Boggild, J. Tegenfeldt, and A. Kristensen, *High resolution 100kV electron beam lithography in SU-8.* Microelectronic Engineering, 2006. **83**(4-9): p. 1609-1612.
114. Campo, A.d. and C. Greiner, *SU-8: a photoresist for high-aspect-ratio and 3D submicron lithography.* Journal of Micromechanics and Microengineering, 2007. **17**(6): p. R81-R95.
115. Kudryashov, V., X.C. Yuan, W.C. Cheong, and K. Radhakrishnan, *Grey scale structures formation in SU-8 with e-beam and UV.* Microelectronic Engineering, 2003. **67-8**: p. 306-311.
116. Balslev, S., T. Rasmussen, P. Shi, and A. Kristensen, *Single mode solid state distributed feedback dye laser fabricated by gray scale electron beam lithography on a dye doped SU-8 resist.* Journal of Micromechanics and Microengineering, 2005. **15**(12): p. 2456-2460.
117. Bhuvana, T. and G.U. Kulkarni, *Polystyrene as a zwitter resist in electron beam lithography based electroless patterning of gold.* Bulletin of Materials Science, 2008. **31**(3): p. 201-206.
118. Ovsianikov, A., A. Gaidukeviciute, B.N. Chichkov, M. Oubaha, B.D. MacCraith, I. Sakellari, A. Giakoumaki, D. Gray, M. Vamvakaki, M. Farsari, and C. Fotakis, *Two-Photon Polymerization of Hybrid Sol-Gel Materials for Photonics Applications.* Laser Chemistry, 2008. **2008**: p. 1-7.
119. Smart, B.E., A.E. Feiring, C.G. Krespan, Z.-Y. Yang, M.-H. Hung, P.R. Resnick, W.R. Dolbier, and X.X. Rong, *New industrial fluoropolymer science and technology.* Macromolecular Symposia, 1995. **98**(1): p. 753-767.
120. Scheirs, J., *Modern fluoropolymers : high performancepolymers for diverse applications*, ed. Wiley1997. 660.
121. Katz, H.E.O.M., MD, US), Dhar, Bal Mukund (Baltimore, MD, US), *PATTERNING DEVICES USING FLUORINATED COMPOUNDS*, 2010, THE JOHNS HOPKINS UNIVERSITY (Baltimore, MD, US): United States.
122. Jeffrey A. Hrivnak; Waiter Mahler, W.G.O.B., Viacheslav and R.C.W. Alexandrovich Petrov, *Solvents for amorphous fluoropolymers*, 2001, E. I. du Pont de Nemours and Company, Wilmington, DE (US).
123. Claes, T., W. Bogaerts, and P. Bienstman, *Experimental characterization of a silicon photonic biosensor consisting of two cascaded ring resonators based on the Vernier-effect and introduction of a curve fitting method for an improved detection limit.* Optics Express, 2010. **18**(22): p. 22747.
124. Duffy, D.C., J.C. McDonald, O.J. Schueller, and G.M. Whitesides, *Rapid Prototyping of Microfluidic Systems in Poly(dimethylsiloxane).* Anal Chem, 1998. **70**(23): p. 4974-84.
125. Sia, S.K. and G.M. Whitesides, *Microfluidic devices fabricated in poly(dimethylsiloxane) for biological studies.* Electrophoresis, 2003. **24**(21): p. 3563-76.
126. McDonald, J.C. and G.M. Whitesides, *Poly(dimethylsiloxane) as a Material for Fabricating Microfluidic Devices.* Accounts of Chemical Research, 2002. **35**(7): p. 491-499.
127. Whitesides, G.M., J.C. McDonald, D.C. Duffy, J.R. Anderson, D.T. Chiu, H.K. Wu, and O.J.A. Schueller, *Fabrication of microfluidic systems in poly(dimethylsiloxane).* Electrophoresis, 2000. **21**(1): p. 27-40.
128. Chang-Yen, D.A., R.K. Eich, and B.K. Gale, *A monolithic PDMS waveguide system fabricated using soft-lithography techniques.* Journal of Lightwave Technology, 2005. **23**(6): p. 2088-2093.
129. Zhao, L., T. Wu, J.P. Lefevre, I. Leray, and J.A. Delaire, *Fluorimetric lead detection in a microfluidic device.* Lab Chip, 2009. **9**(19): p. 2818-23.
130. Soibinet, M., V. Souchon, I. Leray, and B. Valeur, *Rhod-5N as a fluorescent molecular sensor of cadmium(II) ion.* J Fluoresc, 2008. **18**(6): p. 1077-82.
131. Ha-Thi, M.H., M. Penhoat, V. Michelet, and I. Leray, *Highly selective and sensitive phosphane sulfide derivative for the detection of Hg2+ in an organoaqueous medium.* Org Lett, 2007. **9**(6): p. 1133-6.
132. Ros-Lis, J.V., R. Casasus, M. Comes, C. Coll, M.D. Marcos, R. Martinez-Manez, F. Sancenon, J. Soto, P. Amoros, J. El Haskouri, N. Garro, and K. Rurack, *A mesoporous 3D hybrid material with dual functionality for Hg2+ detection and adsorption.* Chemistry, 2008. **14**(27): p. 8267-78.

133. Walcarius, A. and C. Delacote, *Mercury(II) binding to thiol-functionalized mesoporous silicas: critical effect of pH and sorbent properties on capacity and selectivity.* Anal Chim Acta, 2005. **547**(1): p. 3-13.
134. Halliwell, C.M. and A.E.G. Cass, *A Factorial Analysis of Silanization Conditions for the Immobilization of Oligonucleotides on Glass Surfaces.* Anal Chem, 2001. **73**(11): p. 2476-2483.
135. Bogomolny, E., R. Dubertrand, and C. Schmit, *Trace formula for dielectric cavities: General properties.* Physical Review E, 2008. **78**(5).
136. Bogomolny, E., N. Djellali, R. Dubertrand, I. Gozhyk, M. Lebental, C. Schmit, C. Ulysse, and J. Zyss, *Trace formula for dielectric cavities. II. Regular, pseudointegrable, and chaotic examples.* Physical Review E, 2011. **83**(3).
137. Lebental, M., J.S. Lauret, R. Hierle, J. Zyss, C. Schmit, and E. Bogomolny, *Dielectric stadium shaped microlasers.* 2006: p. 1-2.
138. Lebental, M., J. Lauret, J. Zyss, C. Schmit, and E. Bogomolny, *Directional emission of stadium-shaped microlasers.* Physical Review A, 2007. **75**(3).
139. Djellali, N., I. Gozhyk, D. Owens, S. Lozenko, M. Lebental, J. Lautru, C. Ulysse, B. Kippelen, and J. Zyss, *Controlling the directional emission of holey organic microlasers.* Applied Physics Letters, 2009. **95**(10): p. 101108.
140. Cariou, J.M., J. Dugas, L. Martin, and P. Michel, *Refractive-index variations with temperature of PMMA and polycarbonate.* Applied Optics, 1986. **25**(3): p. 334.
141. Toyoda, T. and M. Yabe, *The temperature dependence of the refractive indices of fused silica and crystal quartz.* Journal of Physics D: Applied Physics, 1983. **16**(5): p. L97-L100.
142. Hawkes, J.B. and R.W. Astheimer, *The Temperature Coefficient of the Refractive Index of Water.* Journal of the Optical Society of America, 1948. **38**(9): p. 804.
143. Schwefel, H.G.L., N.B. Rex, H.E. Tureci, R.K. Chang, and A.D. Stone, *Dramatic shape sensitivity of emission patterns for similarly deformed cylindrical polymer lasers.* 2002: p. 24-25.
144. Dettmann, C.P., G.V. Morozov, M. Sieber, and H. Waalkens, *Unidirectional emission from circular dielectric microresonators with a point scatterer.* Physical Review A, 2009. **80**(6).
145. Wang, Q.J., C. Yan, N. Yu, J. Unterhinninghofen, J. Wiersig, C. Pflugl, L. Diehl, T. Edamura, M. Yamanishi, H. Kan, and F. Capasso, *Whispering-gallery mode resonators for highly unidirectional laser action.* Proc Natl Acad Sci U S A, 2010. **107**(52): p. 22407-12.
146. Kane, Y., *Numerical solution of initial boundary value problems involving maxwell's equations in isotropic media.* IEEE Transactions on Antennas and Propagation, 1966. **14**(3): p. 302-307.
147. Allen Taflove, S.H., *Computational Electromagnetics: The Finite-Difference Time-Domain Method*. 3rd Revised edition ed2005.
148. Wenhua, Y. and R. Mittra, *A conformal finite difference time domain technique for modeling curved dielectric surfaces.* IEEE Microwave and Wireless Components Letters, 2001. **11**(1): p. 25-27.
149. Palik, E.D., *Handbook of optical constants of solids*1991: Academic Press. 1096.
150. Pelosi, G., *The finite-element method, Part I: R. L. Courant [Historical Corner].* IEEE Antennas and Propagation Magazine, 2007. **49**(2): p. 180-182.
151. M. Krizek, P.N., Rolf Stenberg, *Finite Element Methods: Fifty Years of the Courant Method*1994. 536.
152. Liu, Y.X., C.D. Sarris, and G.V. Eleftheriades, *Triangular-mesh-based FDTD analysis of two-dimensional plasmonic structures supporting backward waves at optical frequencies.* Journal of Lightwave Technology, 2007. **25**(3): p. 938-945.
153. Liu, J., M. Brio, and J.V. Moloney, *Overlapping Yee FDTD Method on Nonorthogonal Grids.* Journal of Scientific Computing, 2008. **39**(1): p. 129-143.
154. Ha-Thi, M.-H., *Nouvelles architectures supramoléculaires à base de ligands phosphorés fluorescents: Synthèse, études photophysiques et applications*, 2007, ENS Cachan.